Autophagy Proteins Direct STING Trafficking and Innate Immune Signaling Independently of Canonical Autophagy

Thesis by

Kent Leslie

In Partial Fulfillment of the Requirements for the degree of

Doctor of Philosophy

CALIFORNIA INSTITUTE OF TECHNOLOGY

Pasadena, California

2026

(Defended April 21st, 2026)

Kent Lee Leslie
ORCID: 0009-0000-8680-6459

ACKNOWLEDGEMENTS

This thesis would not exist without the support of many people, and I am grateful to all of them.

First, to my advisor, Tsui-Fen Chou. Thank you for your guidance and confidence in me. Your mentorship shaped not only this work but the kind of scientist I hope to be. I am also grateful to the members of my thesis committee for their time, sharp questions, and thoughtful feedback throughout this process.

To my family, thank you for a lifetime of love and encouragement, and for believing in this path long before I could see it clearly myself. To my friends, the ones who pitched in at the bench, talked through ideas over coffee, and reminded me that there was life outside lab, you made these years not just survivable but genuinely joyful. I am lucky to have all of you.

To my wife, Bianca, thank you for your patience through the late nights, for celebrating every small win along the way, and for every act of love along the way. You have been my source of strength. I could not have done this without you.

Finally, to my late father, Scott, who loved Caltech and would have loved this day most of all: your lifelong curiosity is what set me on this path and it has stayed with me through every step of this process. This is for you.

ABSTRACT

Autophagy is a conserved lysosome-mediated degradation pathway that maintains cellular homeostasis by recycling cytoplasmic components and responding to metabolic stress. Initiation of autophagy is coordinated by the ULK1 complex, comprising ULK1, FIP200, ATG13, and ATG101, which is regarded as the earliest regulatory node controlling autophagosome formation. Emerging evidence, however, suggests that components of this complex also function in signaling processes beyond canonical autophagy. This thesis identifies and describes a previously unrecognized role of the ATG9A–ATG13–ATG101 module in mediating a Golgi-to-lysosome trafficking pathway essential for the degradation and signal termination of STING, a central adaptor in the cGAS–STING innate immune pathway. We demonstrate that loss of ATG13, ATG101, or the Golgi-resident membrane protein ATG9A impairs STING turnover, resulting in constitutive and cell-autonomous interferon activation. Mechanistically, STING exiting the Golgi recruits ATG9A-positive vesicles that depend on the ATG13–ATG101 subcomplex to enable entry into the endolysosomal pathway. Notably, this function is separable from canonical autophagy initiation, revealing a noncanonical trafficking role for autophagy-associated proteins in immune signal regulation. Complementing these findings, we identify Heat Shock Factor Binding Protein 1 (HSBP1) as a direct interactor of FIP200 that associates with coiled-coil scaffolds and vesicle-tethering factors, including ATG16L1 and EEA1, suggesting a role in organizing multimeric membrane trafficking assemblies. HSBP1 is intrinsically short-lived and undergoes rapid proteasome-dependent degradation during metabolic stress, indicating a regulatory mechanism independent of lysosomal autophagy. Together, this thesis describes previously unrecognized functions of autophagy initiation machinery in coordinating vesicular trafficking and innate immune regulation, establishing ATG9A–ATG13–ATG101 as a Golgi-to-lysosome trafficking module for STING.

TABLE OF CONTENTS

Chapter 1: Introduction

AUTOPHAGY: MECHANISM, IMMUNE CROSSTALK, AND THE AUTOPHAGY INITIATION COMPLEX

1.1 INTRODUCTION

Autophagy is a conserved cellular recycling process present from unicellular organisms to mammals[1]. During nutrient starvation or cellular stress, double-membrane-bound vacuoles known as autophagosomes form, expand, and sequester cytoplasmic cargo for delivery to lysosomes[2,3]. The phagophore, also called the isolation membrane, is the nascent, cup-shaped structure that elongates to form an autophagosome. Fusion of autophagosomes with lysosomes leads to degradation of the sequestered cargoes (**Figure 1**). Under basal conditions, autophagy contributes to cellular homeostasis by recycling long-lived proteins and removing damaged organelles. During periods of starvation, autophagy provides cells with essential metabolites, such as amino acids and fatty acids, to maintain metabolism.

Autophagy can be broadly classified into bulk or selective forms, depending on the substrates targeted. Bulk autophagy is triggered by nutrient starvation and is regulated by key signaling pathways, including mTORC1 and AMP kinase (AMPK)[4]. In contrast, selective autophagy targets specific substrates, including protein aggregates (aggrephagy)[5,6] and mitochondria (mitophagy)[7]. Impaired clearance of autophagic cargo, such as damaged mitochondria and protein aggregates, is implicated in neurodegenerative diseases including Parkinson's disease and amyotrophic lateral sclerosis (ALS)[8,9].

Given the conserved nature of autophagy, autophagy-related genes (ATGs) have been identified that are required for autophagosome formation[10]. These genes were first discovered in *S. cerevisiae* (yeast)[11,12], and extensive efforts have confirmed these proteins are highly conserved from lower eukaryotes to humans[13]. To date, eighteen core ATG proteins have been defined that coordinate autophagy initiation, phagophore nucleation and elongation, and ultimately the closure of the phagophore to form an autophagosome[14–16].

Genetic disruption of ATG genes typically results in stalled autophagosome accumulation and a loss of autophagic flux[17]. *In vivo*, loss of essential ATGs results in embryonic lethality or early postnatal death in mice, highlighting the critical importance of autophagy for cellular and organism viability[18,19].

In addition to the canonical roles in autophagy, components of the autophagy machinery have been increasingly recognized as performing autophagy-independent functions[20–22]. This thesis builds on these observations by identifying and characterizing novel, autophagy-independent functions of essential ATG proteins.

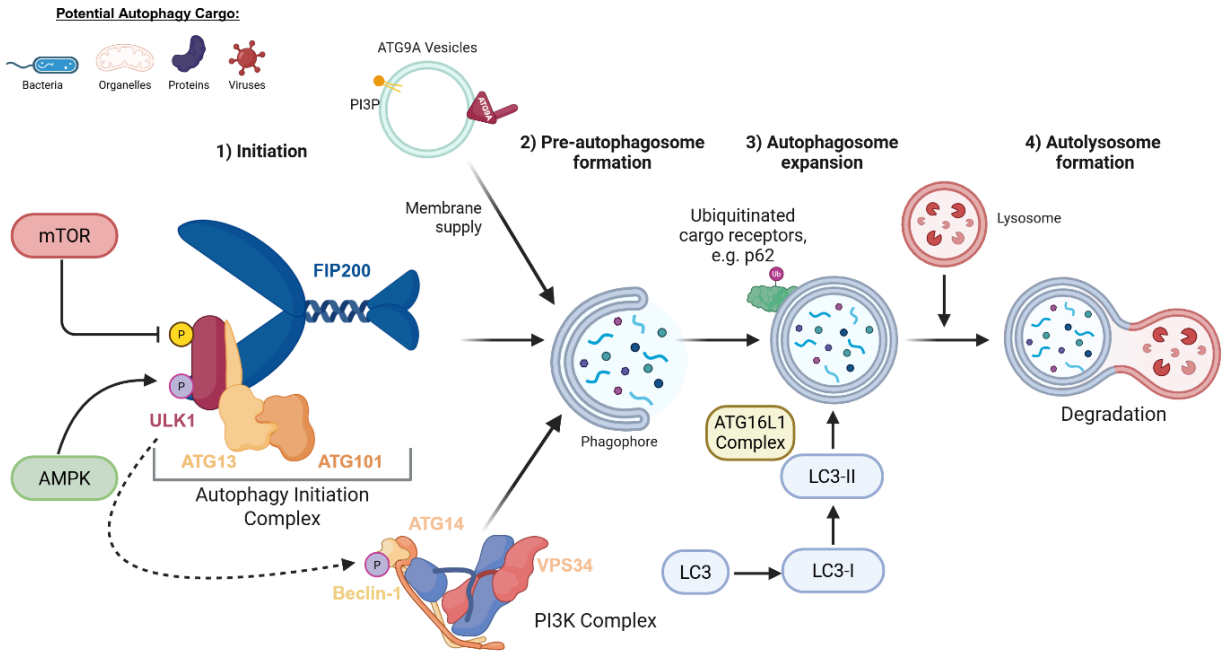

Figure 1. Overview of the mammalian autophagy pathway. *Autophagy proceeds through four sequential stages.* ***(1) Initiation:*** *Under nutrient-replete conditions, mTORC1 phosphorylates and inhibits the Autophagy Initiation Complex (AIC), comprising ULK1, FIP200, ATG13, and ATG101. During starvation, mTORC1 is inactivated, AMPK phosphorylates ULK1, activating the complex. The activated AIC phosphorylates components of the class III PI3K complex, including Beclin-1, VPS34, ATG14).* ***(2) Pre-autophagosome formation:*** *The PI3K complex generates phosphatidylinositol 3-phosphate (PI3P) on nascent membranes, while ATG9A vesicles supply membrane lipids to the expanding phagophore.* ***(3) Autophagosome expansion****:*

The ATG12-ATG5-ATG16L1 complex catalyzes LC3 lipidation and selective autophagy receptors recruit ubiquitinated cargo. ***(4) Autolysosome formation****: The mature autophagosome fuses with a lysosome for cargo degradation and recycling. Potential autophagy substrates include bacteria, damaged organelles, misfolded proteins, and viruses (top left). P, phosphate group; Ub, ubiquitin.*

1.2 MECHANISM AND PHYSIOLOGICAL FUNCTION

1.2.1 INITIATION AND REGULATION OF AUTOPHAGY - THE ULK1/ATG1 COMPLEX

Autophagy initiation is regulated by the evolutionarily conserved Atg1/ULK1 (unc-51 like autophagy activating kinase) complex, which integrates upstream signals to nucleate the phagophore[23]. I refer to the ULK1 complex as the Autophagy Initiation Complex (AIC) moving forward. I adopt this nomenclature because this thesis demonstrates that individual subunits of this complex perform distinct cellular roles outside of their shared role in autophagy initiation, making a function-neutral name more precise.

1.2.1.1 YEAST ATG1 COMPLEX

In yeast, autophagosome formation is coordinated by the Atg1 complex, a modular assembly of kinase and scaffold proteins at the pre-autophagosomal structure (PAS), the site of autophagosome formation and organization[24]. The core components are Atg1, Atg13, and the ternary scaffold complex Atg17-Atg29-Atg31[25–28]. Atg17 forms a dimeric, crescent-shaped scaffold that recruits Atg13 and downstream Atg proteins, while Atg29 and Atg31 stabilize the assembly[29,30]. Hierarchical mapping of Atg proteins identified Atg17 as the fundamental scaffold protein within the PAS. The Atg17-Atg29-Atg31 complex forms in equimolar amounts[29] and the dimerization of these complexes is critical for PAS formation and autophagy[30]. Atg29 and Atg31 are unique to budding yeast[31]. Atg13 binds the tips of the Atg17, utilizing the unique structure of Atg17 to form the supramolecular assembly of Atg1 complexes required for autophagy initiation[32,33]. The structure and function of Atg13 is discussed in greater depth below.

A related complex, in which the scaffolding protein Atg11 replaces Atg17-Atg31-Atg29, functions in selective autophagy initiation[34]. Atg11 is larger than Atg17 and adopts a parallel coiled-coil architecture, whereas Atg17 forms an anti-parallel coiled-coil architecture[35].

1.2.1.2 MAMMALIAN ULK1 COMPLEX

The mammalian ULK1 complex performs analogous functions to the yeast Atg1 complex, orchestrating autophagy initiation through ULK1, FIP200 (focal adhesion kinase family interacting protein of 200kDa), ATG13, and ATG101, assembled in a 1:2:1:1 stoichiometry(ULK1:FIP200:ATG13:ATG101)[36–40].

1.2.1.3 ULK1 AND ULK2 KINASES

Mammals have four Atg1 homologs, with ULK1 and ULK2 showing the highest conservation in their kinase and C-terminal domains[41]. These kinases are largely redundant, as knockout (KO) of both is required to robustly inhibit autophagy[42,43]. However, ULK1 and ULK2 have distinct binding partners and transcriptional regulators, suggesting potential nonredundant functions[44]. ULK1/2 double knockout (DKO) mice die within 24 hours of birth due to respiratory distress[43].

ULK1/2 is the homologue of unc-51, a gene essential for neuronal development in *C. elegans*[45]. ULK1 consists of an N-terminal kinase domain (KD), a serine-proline-rich region, and a C-terminal tandem microtubule-interacting and transport (MIT) domain. The human ULK1 structure resolved in 2015 confirmed the KD similarity to yeast Atg1[46]. This structural elucidation also identified an autophosphorylation site at Thr180, crucial for autophagy activation and the development of potent ULK1 complex inhibitors[46]. The tandem MIT domains mediate binding to FIP200 and ATG13[39,40,47].

ULK1 phosphorylates several downstream targets, including VPS34[48], ATG14[49], and BECN (in association with ATG14)[50], facilitating autophagy progress. Beyond autophagy[51], ULK1 phosphorylates substrates such as STING[52], a negative regulator of innate immune signaling and the focus of Chapter 3.

1.2.1.4 FIP200 – CENTRAL SCAFFOLD AND ADAPTOR OF THE ULK1 COMPLEX

FIP200 (focal adhesion kinase family-interacting protein of 200 kDa[53,54]) is the defining scaffold of the mammalian ULK1 complex[55,56] and the functional counterpart to yeast Atg17, though with a substantially expanded regulatory architecture. Conserved across metazoa, fungi, plants and protists as part of the Atg11/FIP200 family[57], FIP200 is a large protein composed of a C-shaped N-terminal domain (NTD), an intrinsically disordered region (IDR), a long coiled-coil (CC) domain, and a C-terminal Claw domain.

The NTD dimerizes to form an assembly platform for ULK1, ATG13, and ATG101[39], and FIP200 forms a long, flexible homodimer via interactions within its coiled-coil domain[39]. FIP200 shares conserved features with Atg11 and contains an Atg17-like domain in its N-terminus, suggesting Atg11/FIP200 and Atg17 represent evolutionarily diverged homologs[13,23,57]. Consistent with its evolutionary relationship, both yeast Atg17 and the Atg17-like region of FIP200 bind ATG13 and form dimeric assemblies, although their overall architectures differ[30,58,59]. Deletion of FIP200 leads to mid-gestation embryonic death, consistent with a severe autophagy phenotype and its role as the structural backbone of the AIC[60].

The complete molecular architecture of FIP200, its interactions with selective autophagy receptors and downstream autophagy machinery, and the characterization of a novel FIP200-interacting protein are explored in Chapter 4.

1.2.1.5 ATG13 AND ATG101 – CORE ADAPTORS OF THE AIC

ATG13 directly interacts with membranes, connecting the ULK complex to isolation membranes, mediating interactions between the PI3K complex and ULK complex at the endoplasmic reticulum (ER) in response to autophagy induction[61]. ATG101, absent in *S. cerevisiae* but essential in metazoans, was identified by two groups in 2009 as an ATG13 stabilizer[62–64]. ATG101 interaction with the broader ULK1 complex is stable, occurring both absent and during autophagy activation. Together, ATG13 and ATG101 function as central adaptors that coordinate autophagosome nucleation. These proteins are the focus of Chapter 2, where their structure, function, and interactions are examined in detail.

1.2.2 REGULATION OF AUTOPHAGY BY MTORC1 AND AMPK

Under nutrient-rich conditions, the mammalian Target of Rapamycin complex I (mTORC1), containing the central autophagy inhibitor mTOR kinase, interacts with ULK1 and ULK2, phosphorylating them and suppressing their kinase activity. This phosphorylation inhibits autophagy initiation by preventing ULK1 from activating downstream targets. During nutrient starvation, mTORC1 activity is inhibited, relieving repression of ULK1/ULK2, which then phosphorylate key downstream proteins[32,65,66]. Phosphorylation of ULK1 is a key molecular switch required for autophagy induction[11,25,67,68]. In yeast, TORC1 phosphorylates Atg13, a key step in regulating Atg1 complex activity[69–71]. Atg17, with its rigid helical structure, functions as a scaffold for the Atg1 complex during autophagosome formation[24,30].

Specific regulators of the Atg1 complex have been described. Recently, a phosphate metabolite sensor, Pho81, was found to interact with Atg1 complex adaptor Atg11 to modulate pexophagy[72]. Core Atg1 complex components are dispensable for phosphate-starvation induced autophagy, revealing a functional plasticity of the Atg1 complex in response to distinct cell stress and starvation signals. These findings indicate that the Atg1/ULK1 complexes contain subunits capable of sensing metabolic information directly to modulate autophagy regulation.

In response to mTOR inhibition and activation by AMP kinase[37], the ULK1 complex interacts with the nascent isolation membrane, PAS, and the PI3K complex, which adds phosphatidylinositol 3-phosphate (PI(3)P) to promote expansion of the isolation membrane to generate the autophagosome[42,73].

1.2.3 PHAGOPHORE FORMATION AND EXPANSION - PI3K COMPLEXES

The class III phosphatidylinositol 3-kinase complexes (PI3KC3) are critical for phagophore assembly. The complex exists in two distinct forms, complexes I and II. Each complex contains a class-III PI3K VPS34, the pseudo-kinase VPS15, Beclin-1 (BECN1, the yeast Atg6 homolog). Complex I uniquely incorporates ATG14[74–77] while complex II contains UVRAG[74]. Complex I is involved in autophagy initiation,[78] and complex II is involved in endosomal sorting and late stages of autophagy.

PI3KC3 generates the lipid, phosphatidylinositol-3-phosphate, PI(3)P, which is recognized by WIPI proteins. WIPI proteins then recruit the needed conjugation machinery to add LC3, an autophagosomal marker protein to expanding autophagosomal membranes[79].

Structures of activated PI3KC3-C1 were resolved in 2019 and 2021, respectively[80,81]. The inactive state of PI3KC1 is maintained through inhibitory contacts between VPS15 and VPS34 that restrict the activation of VPS34.

In 2025, the structure of core ULK1 complex in complex with the PI3KC1 complex was resolved. The two complexes co-assemble via multiple contact points between FIP200 of the AIC and VPS15, ATG14, and BECN1. Structural studies revealed that, in the presence of the PI3KC1 complex, the AIC undergoes a stoichiometric rearrangement from 1:2:1:1 to 2:2:2:2[40].

1.2.4 ATG8/LC3 CONJUGATION MACHINERY

Conjugation of Atg8 to the autophagosomal membrane is a hallmark of autophagy[82]. The ATG8/LC3 conjugation system is a ubiquitin-like lipidation cascade essential for autophagosome biogenesis[83]. This pathway was elucidated through yeast genetic studies that identified Atg8, Atg4, and the Atg12–Atg5 conjugation system as core autophagy components[82,83]. In most species, the ATG8 C-terminus must be cleaved by ATG4 proteases before lipid conjugation[83,84]. Metazoan Atg8 proteins are divided into two families, GABARAP and LC3, which differ in sequence and structure[85]. ATG4 also deconjugates LC3/GABARAPs from lipids[86]. As a cysteine protease, Atg4 cleaves Atg8 to expose the C-terminal glycine and releases Atg8 from autophagosome membranes for recycling[87]. In humans, ATG4B is the primary enzyme that processes all LC3 and GABARAP proteins[88,89].

Processed ATG8 is activated by C-terminal adenylation through the E1-like enzyme ATG7 and transferred to the E2-like enzyme ATG3, paralleling canonical ubiquitin conjugation[90]. Simultaneously, ATG12 is covalently conjugated to ATG5 through ATG7 and the E2-like enzyme ATG10, and the resulting ATG12–ATG5 complex associates non-covalently with ATG16L1 to form a multimeric E3-like ligase complex[91,92]. This complex localizes to autophagosome formation sites, directing ATG8 lipidation, conferring spatial control over autophagosome membrane expansion[93,94]. Deletion of components in the ATG12-ATG5-

ATG16L1 complex result in the formation of stalled autophagosomes[18,95]. This complex also has non-canonical functions in immune signaling and cellular homeostasis[96].

1.2.5 ATG9A VESICLES AND MEMBRANE SOURCES

ATG9A is the sole transmembrane component of the core autophagy machinery and an evolutionarily conserved lipid scramblase essential for autophagosome biogenesis[97,98]. Under nutrient-replete conditions, ATG9A localizes primarily to the trans-Golgi network (TGN) and late endosomes; upon starvation, it redistributes to early autophagosomal structures[99]. Autophagosome formation requires the addition of phospholipid membranes from diverse cellular sources, including the ER[100–103], Golgi[104,105], mitochondria[106,107], and endosomes[108–111], coordinated in part through ATG9A vesicle trafficking. The diameter of an autophagosome is between 400nm and 1μm, requiring millions of lipids to form[112]. Critically, ATG13 and ATG101, core AIC components, interact directly with the C-terminal domain of ATG9A to form the ATG9A–ATG13–ATG101 complex[113]. The structure, vesicle biology, and non-canonical immunological functions of this complex are examined in Chapter 2.

1.2.6 CARGO RECOGNITION AND SELECTIVITY - UBIQUITIN-RECEPTOR SYSTEM

A common autophagy initiating signal is ubiquitin decoration of cargo, marking "self" material as a recognizable substrate for degradation. Ubiquitin is attached by E3 ligases to proteins embedded in damaged organelle membranes or within insoluble protein assemblies to promote recruitment of ubiquitin-binding autophagy receptors. A well-characterized example is mitophagy. Following mitochondrial depolarization, PINK1 (PTEN-induced kinase 1) stabilization on the outer mitochondrial membrane (OMM) leads to the recruitment and activation of Parkin, triggering ubiquitination of OMM proteins to promote mitophagy sequestration[114–116]. This ubiquitin driven cascade generalizes to other specialized cargo classes (aggregates, pathogens, endomembranes) as a "tag-and-destroy" strategy using ubiquitin as the signal to concentrate receptors leading to local autophagosome formation[117].

Selective autophagy utilizes cargo receptors that read ubiquitin signals and engage ATG8/LC3 proteins to promote autophagosome engulfment. Canonical receptors include p62/SQSTM1[118]

and NBR1[119], the first vertebrate factors shown to couple ubiquitinated aggregates to the autophagic machinery[120,121]. In host defense, NDP52/CALCOCO2[122–124] and OPTN[125,126] function as ubiquitin-directed receptors during xenophagy, coordinating pathogen restriction with recruitment of LC3-positive membranes. TAX1BP1 participates in ubiquitin-dependent targeting of cytosolic bacteria and other substrates, highlighting the redundancy among receptors[127]. An investigation of NBR1 revealed that three distinct classes of autophagy binding patterns, ATG8-family proteins, FIP200, and TAX1BP1, bind to distinct yet overlapping regions within the protein[128]. This highlighted that autophagy receptors intersect with multiple critical complexes required for autophagy.

Most autophagy cargo receptors contain a ubiquitin-binding domain (UBD) enabling recognition of polyubiquitin chains on cargo. Many also encode oligomerization modules (e.g., p62 PB1) that promote receptor clustering and avidity for ubiquitinated substrates, favoring formation of receptor-rich assemblies that are efficiently captured by nascent phagophores[129]. In parallel, receptors carry one or more LC3-interacting regions (LIR motifs), short linear motifs that bind hydrophobic pockets on ATG8-family proteins, providing the direct molecular link to the autophagosome membrane.

1.2.7 SELECTIVE AUTOPHAGY PATHWAYS AND MECHANISMS

Selective autophagy targets specific substrates, such as protein aggregates (aggrephagy), mitochondria, or ER, for targeted degradation[5]. The ubiquitin–receptor–LC3 paradigm provides a shared mechanistic backbone for diverse organellophagy and quality-control autophagy pathways. Aggrephagy targets ubiquitin-positive protein aggregates (classically p62/NBR1-driven), whereas mitophagy removes damaged mitochondria via PINK1/Parkin-dependent ubiquitination[114,115,126,130] and subsequent receptor recruitment (often including OPTN, NDP52, TAX1BP1, and others depending on context). Xenophagy eliminates cytosolic microbes or damaged pathogen-containing vacuoles through ubiquitin coating and recruitment of receptors such as NDP52, OPTN, and TAX1BP1. Beyond these, specialized forms such as ER-phagy, pexophagy, lysophagy, and ribophagy use related logic (sometimes with non-ubiquitin “eat-me” signals or dedicated receptors), but converge on ATG8-family engagement to drive

selective encapsulation[131]. In this way, receptor-mediated selectivity allows the autophagy machinery to function as a broadly programmable degradation platform while preserving stringent cargo discrimination.

1.2.8 AUTOPHAGY RECEPTORS AS SUBSTRATES

p62/SQSTM1 and NBR1 are not only receptors, they are selective autophagy substrates normally delivered to lysosomes together with their bound cargo[132]. Consequently, when autophagy is genetically or pharmacologically impaired (e.g., defects in ATG7-dependent conjugation or autophagosome maturation), p62-positive bodies and ubiquitinated inclusions accumulate because receptor–cargo assemblies are formed but cannot be cleared. This phenomenon is robust in vivo: conditional loss of ATG7 leads to defective ATG conjugation systems and prominent accumulation of p62 and ubiquitin-positive inclusions in tissues such as liver and brain, and p62 has been implicated as a driver of pathology under autophagy-deficient conditions. Thus, p62 (and often NBR1) levels are widely used as a flux-sensitive marker: increased abundance frequently indicates impaired autophagic turnover, although interpretation benefits from pairing with lysosomal inhibitors and orthogonal flux assays.

1.2.9 AUTOPHAGOSOME-LYSOSOME FUSION

Autophagosome-lysosome fusion is the final step of autophagy, enabling the recycling of cellular cargo within autolysosomes[133]. This process relies on the coordinated action of membrane trafficking systems, tethering factors, and fusion machinery[134]. Autophagosomes mature by remodeling their membranes and acquiring key proteins such as SNAREs, Rab GTPases, and phosphoinositide signals that facilitate their docking and fusion with lysosomes. Rab GTPases orchestrate autophagosome positioning and tethering to lysosomes. RAB7, a key player, localizes to late autophagosomes and recruits effectors like RILP to link autophagosomes with microtubule motors, directing transport toward lysosome-rich areas[135–137]. Other Rabs, including RAB2, RAB9, and RAB33B, assist in specialized trafficking, while GEFs and GAPs regulate their activity for precise timing.

Tethering complexes such as HOPS (homotypic fusion and protein sorting) physically connect autophagosomes to lysosomes and recognize specific membrane lipids like phosphatidylinositol 3-phosphate (PI3P)[138,139]. Fusion is driven by SNARE proteins forming trans-SNARE complexes; syntaxin 17 (STX17) on autophagosomes teams with SNAP29 and lysosomal SNARE VAMP8 to catalyze membrane fusion[140,141]. This process is tightly regulated by proteins including ATG14[142] and the PI3KC3 complex[143].

Accessory proteins like PLEKHM1[144] and UVRAG[145] refine fusion by scaffolding tethering and promoting membrane curvature. Lipid composition, including PI4P and cholesterol, supports fusion and lysosomal enzyme function[146,147]. After fusion, cargo is degraded in the acidic lysosomal lumen, maintained by V-ATPase activity[148].

Defects in fusion or lysosomal function lead to accumulation of undegraded material and cellular stress, contributing to diseases such as Parkinson's[149–152], Alzheimer's[153–155], ALS[156,157], and lysosomal storage disorders like Niemann-Pick type C[158] and Gaucher disease[159,160].

1.3 AUTOPHAGY-IMMUNE CROSSTALK

Immune signaling pathways often have a high degree of overlap with autophagy. Immune activation can induce autophagy, and autophagy and non-canonical autophagy pathways can function to clear the machinery that regulates immune responses[161].

1.3.1 XENOPHAGY

Xenophagy is a selective form of autophagy that targets invading pathogens for lysosomal degradation. Ruptured pathogen-containing vacuoles are sensed by galectin-8[162], triggering rapid recruitment of ubiquitin-binding autophagy receptors including NDP52, OPTN, p62, and TAX1BP1, which bridge ubiquitinated pathogens to LC3-family proteins on nascent autophagosomal membranes[125,163]. TBK1 is recruited and activated at sites of bacterial invasion, phosphorylating these receptors to enhance their antimicrobial function while simultaneously integrating xenophagic clearance with interferon and inflammatory signaling pathways[126,164].

1.3.2 CGAS-STING PATHWAY

Cytosolic DNA triggers an immune response[165], specifically an IRF3 (interferon regulatory factor 3)-dependent innate immune response (**Figure 2**)[166]. cGAS (cyclic GMP-AMP synthase), following dsDNA binding, undergoes a conformational shift that produces cyclic GMP-AMP (cGAMP) from ATP and GMP[167–171]. cGAMP is then detected by cyclic GMP-AMP receptor stimulator of interferon genes (STING), a transmembrane cyclic-dinucleotide sensor located at the ER[172–175]. STING binding cGAMP results in its activation, oligomerization, and translocation to the Golgi where it activates TANK-binding kinase 1 (TBK1)[167,176]. TBK1 phosphorylates itself, STING, and IRF3, resulting in IRF3 dimerization and subsequent localization to the nucleus where it activates the transcription of interferon-stimulated genes (ISGs)[177]. This pathway, termed the cGAS-STING pathway, relies on the precise spatial localization of each component as key regulatory mechanisms[178]. The focus of Chapter 3 is the discovery of ATG9A-ATG13-ATG101 as a subcomplex mediating the trafficking of activated STING between the Golgi, the site of its role mediating TBK1-STING-IRF3 activation, and the lysosome, the site of its degradation. The subcellular trafficking of STING will be explained in greater depth in Chapter 3.

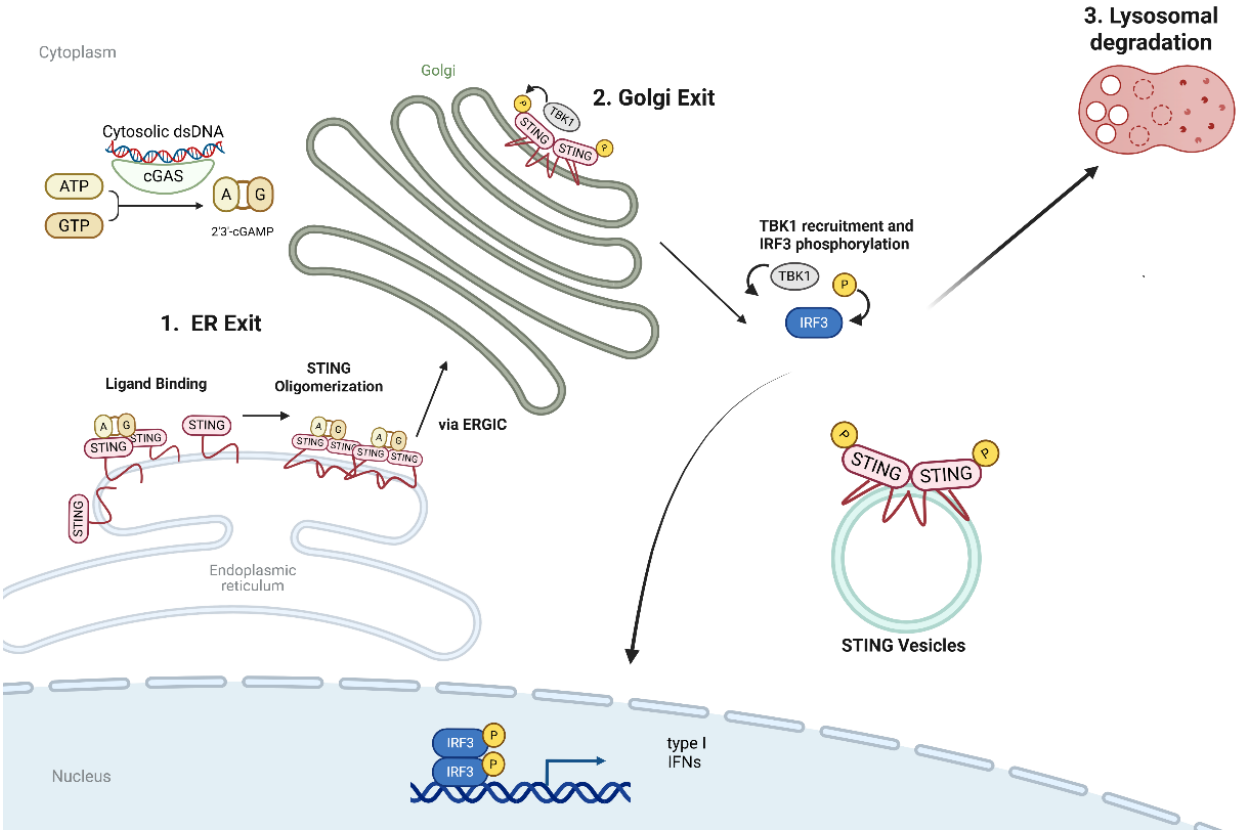

Figure 2. Overview of the cGAS–STING innate immune signaling pathway. *The cGAS–STING pathway mediates cytosolic DNA sensing and type I interferon responses. Cytosolic double-stranded DNA (dsDNA) is detected by cyclic GMP–AMP synthase (cGAS), which catalyzes the synthesis of the second messenger 2'3'-cGAMP from ATP and GTP. cGAMP binds STING, an endoplasmic reticulum (ER)-resident transmembrane protein, inducing its oligomerization.* ***(1) ER exit:*** *Activated STING oligomers translocate from the ER via the ER–Golgi intermediate compartment (ERGIC) to the Golgi apparatus.* ***(2) Golgi exit:*** *At the Golgi, STING recruits and activates TANK-binding kinase 1 (TBK1), which phosphorylates STING and the transcription factor interferon regulatory factor 3 (IRF3). Phosphorylated IRF3 dimerizes and translocates to the nucleus, where it induces transcription of type I interferons (IFNs). Following activation, STING is sorted into STING-containing vesicles for downstream trafficking.* ***(3) Lysosomal degradation:*** *STING vesicles are delivered to lysosomes, where degradation of STING terminates signaling. P, phosphorylation.*

1.3.3 AIC AND INNATE IMMUNITY

Cyclic dinucleotides trigger ULK phosphorylation of STING to prevent sustained innate immune signaling. After autophagy-dependent STING delivery of TBK1 to endosomal/lysosomal compartments and activation of transcription factors interferon regulatory factor 3 (IRF3) and NF-κB, STING is subsequently phosphorylated by serine/threonine UNC-51-like kinase (ULK1/ATG1), and IRF3 function is suppressed[52].

A recent case report reported on the connection between rare, deleterious FIP200 mutations and impaired SARS-CoV-2 immunity. Cell lines expressing the FIP200 patient variants exhibited elevated SARS-CoV-2 replication and impaired autophagic flux. The authors report on a novel lysosomal degradation pathway for SARS-CoV-2 virions that are directly targeted to single-membrane LC3B-positive vesicles for degradation[179]. This pathway, independent of canonical autophagy, directly connects FIP200 to antiviral immunity.

1.4 THESIS OVERVIEW

Despite research establishing the AIC as the master regulator of autophagy initiation, fundamental questions about the individual subunits remain. The four components have been studied primarily as an ensemble, with their non-redundant contributions to cellular physiology largely inferred from phenotypic differences between KO lines rather than from mechanistic dissection of subunit-specific interactions and substrates. Can individual AIC subunits regulate cellular processes entirely independently of canonical autophagy? Do the proteomic consequences of their loss reveal pathway connections that genetics alone cannot?

The thesis utilizes genetic, proteomic, and cell biological approaches to address these questions, and the findings support a model of the AIC as a modular platform rather than a unified complex. Quantitative proteomics of all four AIC KO lines revealed an unexpected innate immune signature, upregulation of type I interferon pathway components and NF-κB signaling proteins, selectively in ATG101 and ATG13 KO cells but not in ULK1/2 or FIP200 KO cells. Chapter 2 links this phenotype to the ATG9A-ATG13-ATG101 subcomplex, establishing it as a non-canonical regulator of innate immune activation independent of autophagy. Chapter 3

identifies cGAS-STING as the relevant signaling pathway and demonstrates that ATG9A-ATG13-ATG101 mediate the Golgi-to-lysosome trafficking of activated STING, termed GLAD. Chapter 4 turns to FIP200, where proteomic analysis of its interactome identifies HSBP1 as a rapidly degraded, proteasomally regulated coiled-coil scaffold that interacts with FIP200 independent of other AIC components. Together, these findings demonstrate that core autophagy initiation machinery performs functionally independent roles in trafficking and innate immune regulation.

1.5 REFERENCES

1. Feng, Y., He, D., Yao, Z. & Klionsky, D. J. The machinery of macroautophagy. *Cell Res.* **24**, 24–41 (2014).
2. Simonsen, A. & Tooze, S. A. Coordination of membrane events during autophagy by multiple class III PI3-kinase complexes. *J. Cell Biol.* **186**, 773–782 (2009).
3. Seglen, P. O., Gordon, P. B. & Holen, I. Non-selective autophagy. *Semin. Cell Biol.* **1**, 441–448 (1990).
4. Sabatini, D. M. Twenty-five years of mTOR: Uncovering the link from nutrients to growth. *Proc. Natl. Acad. Sci.* **114**, 11818–11825 (2017).
5. Lamark, T. & Johansen, T. Aggrephagy: Selective Disposal of Protein Aggregates by Macroautophagy. *Int. J. Cell Biol.* **2012**, 736905 (2012).
6. Rubinsztein, D. C. The roles of intracellular protein-degradation pathways in neurodegeneration. *Nature* **443**, 780–786 (2006).
7. Wang, S. *et al.* The mitophagy pathway and its implications in human diseases. *Signal Transduct. Target. Ther.* **8**, 304 (2023).
8. Lynch-Day, M. A., Mao, K., Wang, K., Zhao, M. & Klionsky, D. J. The Role of Autophagy in Parkinson's Disease. *Cold Spring Harb. Perspect. Med.* **2**, a009357 (2012).
9. Dikic, I. & Elazar, Z. Mechanism and medical implications of mammalian autophagy. *Nat. Rev. Mol. Cell Biol.* **19**, 349–364 (2018).
10. Klionsky, D. J. Autophagy: from phenomenology to molecular understanding in less than a decade. *Nat. Rev. Mol. Cell Biol.* **8**, 931–937 (2007).
11. Tsukada, M. & Ohsumi, Y. Isolation and characterization of autophagy-defective mutants of *Saccharomyces cerevisiae*. *FEBS Lett.* **333**, 169–174 (1993).
12. Thumm, M. *et al.* Isolation of autophagocytosis mutants of Saccharomyces cerevisiae. *FEBS Lett.* **349**, 275–280 (1994).
13. Zhang, S., Hama, Y. & Mizushima, N. The evolution of autophagy proteins – diversification in eukaryotes and potential ancestors in prokaryotes. *J. Cell Sci.* **134**, jcs233742 (2021).
14. Ohsumi, Y. Historical landmarks of autophagy research. *Cell Res.* **24**, 9–23 (2014).
15. Noda, N. N. Structural view on autophagosome formation. *FEBS Lett.* **598**, 84–106 (2024).

16. Nishimura, T. & Tooze, S. A. Emerging roles of ATG proteins and membrane lipids in autophagosome formation. *Cell Discov.* **6**, 32 (2020).
17. Kishi-Itakura, C., Koyama-Honda, I., Itakura, E. & Mizushima, N. Ultrastructural analysis of autophagosome organization using mammalian autophagy-deficient cells. *J. Cell Sci.* **127**, 4089–4102 (2014).
18. Kuma, A. *et al.* The role of autophagy during the early neonatal starvation period. *Nature* **432**, 1032–1036 (2004).
19. Kojima, T. *et al.* Role of the *Atg9a* gene in intrauterine growth and survival of fetal mice. *Reprod. Biol.* **15**, 131–138 (2015).
20. Bestebroer, J., V'kovski, P., Mauthe, M. & Reggiori, F. Hidden Behind Autophagy: The Unconventional Roles of ATG Proteins. *Traffic Cph. Den.* **14**, 1029–1041 (2013).
21. Cadwell, K. & Debnath, J. Beyond self-eating: The control of nonautophagic functions and signaling pathways by autophagy-related proteins. *J. Cell Biol.* **217**, 813–822 (2017).
22. Galluzzi, L. & Green, D. R. Autophagy-Independent Functions of the Autophagy Machinery. *Cell* **177**, 1682–1699 (2019).
23. Mizushima, N. The role of the Atg1/ULK1 complex in autophagy regulation. *Curr. Opin. Cell Biol.* **22**, 132–139 (2010).
24. Suzuki, K., Kubota, Y., Sekito, T. & Ohsumi, Y. Hierarchy of Atg proteins in pre-autophagosomal structure organization. *Genes Cells* **12**, 209–218 (2007).
25. Matsuura, A., Tsukada, M., Wada, Y. & Ohsumi, Y. Apg1p, a novel protein kinase required for the autophagic process in *Saccharomyces cerevisiae*. *Gene* **192**, 245–250 (1997).
26. Kamada, Y. *et al.* Tor-Mediated Induction of Autophagy via an Apg1 Protein Kinase Complex. *J. Cell Biol.* **150**, 1507–1513 (2000).
27. Kabeya, Y. *et al.* Atg17 Functions in Cooperation with Atg1 and Atg13 in Yeast Autophagy. *Mol. Biol. Cell* **16**, 2544–2553 (2005).
28. Cheong, H., Nair, U., Geng, J. & Klionsky, D. J. The Atg1 Kinase Complex Is Involved in the Regulation of Protein Recruitment to Initiate Sequestering Vesicle Formation for Nonspecific Autophagy in Saccharomyces cerevisiae. *Mol. Biol. Cell* https://doi.org/10.1091/mbc.e07-08-0826 (2007) doi:10.1091/mbc.e07-08-0826.

29. Kabeya, Y. *et al.* Characterization of the Atg17–Atg29–Atg31 complex specifically required for starvation-induced autophagy in *Saccharomyces cerevisiae*. *Biochem. Biophys. Res. Commun.* **389**, 612–615 (2009).
30. Ragusa, M. J., Stanley, R. E. & Hurley, J. H. Architecture of the Atg17 Complex as a Scaffold for Autophagosome Biogenesis. *Cell* **151**, 1501–1512 (2012).
31. Yamamoto, H., Zhang, S. & Mizushima, N. Autophagy genes in biology and disease. *Nat. Rev. Genet.* **24**, 382–400 (2023).
32. Fujioka, Y. *et al.* Structural basis of starvation-induced assembly of the autophagy initiation complex. *Nat. Struct. Mol. Biol.* **21**, 513–521 (2014).
33. Yamamoto, H. *et al.* The Intrinsically Disordered Protein Atg13 Mediates Supramolecular Assembly of Autophagy Initiation Complexes. *Dev. Cell* **38**, 86–99 (2016).
34. Zientara-Rytter, K. & Subramani, S. Mechanistic insights into the role of Atg11 in selective autophagy. *J. Mol. Biol.* **432**, 104–122 (2020).
35. Suzuki, H. & Noda, N. N. Biophysical characterization of Atg11, a scaffold protein essential for selective autophagy in yeast. *FEBS Open Bio* **8**, 110–116 (2018).
36. Ganley, I. G. *et al.* ULK1·ATG13·FIP200 Complex Mediates mTOR Signaling and Is Essential for Autophagy. *J. Biol. Chem.* **284**, 12297–12305 (2009).
37. Hosokawa, N. *et al.* Nutrient-dependent mTORC1 association with the ULK1-Atg13-FIP200 complex required for autophagy. *Mol. Biol. Cell* **20**, 1981–1991 (2009).
38. Jung, C. H. *et al.* ULK-Atg13-FIP200 Complexes Mediate mTOR Signaling to the Autophagy Machinery. *Mol. Biol. Cell* **20**, 1992–2003 (2009).
39. Shi, X. *et al.* ULK complex organization in autophagy by a C-shaped FIP200 N-terminal domain dimer. *J. Cell Biol.* **219**, e201911047 (2020).
40. Chen, M. *et al.* Structure and activation of the human autophagy-initiating ULK1C:PI3KC3-C1 supercomplex. *Nat. Struct. Mol. Biol.* **32**, 1596–1605 (2025).
41. Chan, E. Y. & Tooze, S. A. Evolution of Atg1 function and regulation. *Autophagy* **5**, 758–765 (2009).
42. McAlpine, F., Williamson, L. E., Tooze, S. A. & Chan, E. Y. W. Regulation of nutrient-sensitive autophagy by uncoordinated 51-like kinases 1 and 2. *Autophagy* **9**, 361–373 (2013).

43. Cheong, H. *et al.* Analysis of a lung defect in autophagy-deficient mouse strains. *Autophagy* **10**, 45–56 (2014).
44. Demeter, A. *et al.* ULK1 and ULK2 are less redundant than previously thought: computational analysis uncovers distinct regulation and functions of these autophagy induction proteins. *Sci. Rep.* **10**, 10940 (2020).
45. Pareek, G. & Kundu, M. Physiological functions of ULK1/2. *J. Mol. Biol.* **436**, 168472 (2024).
46. Lazarus, M. B., Novotny, C. J. & Shokat, K. M. Structure of the Human Autophagy Initiating Kinase ULK1 in Complex with Potent Inhibitors. *ACS Chem. Biol.* **10**, 257–261 (2015).
47. Caballe, A. *et al.* ULK3 regulates cytokinetic abscission by phosphorylating ESCRT-III proteins. *eLife* **4**, e06547 (2015).
48. Mercer, T. J. *et al.* Phosphoproteomic identification of ULK substrates reveals VPS15-dependent ULK/VPS34 interplay in the regulation of autophagy. *EMBO J.* **40**, e105985 (2021).
49. Wold, M. S., Lim, J., Lachance, V., Deng, Z. & Yue, Z. ULK1-mediated phosphorylation of ATG14 promotes autophagy and is impaired in Huntington's disease models. *Mol. Neurodegener.* **11**, 76 (2016).
50. Park, J.-M. *et al.* ULK1 phosphorylates Ser30 of BECN1 in association with ATG14 to stimulate autophagy induction. *Autophagy* **14**, 584–597 (2018).
51. Mercer, T. J. & Tooze, S. A. The ingenious ULKs: expanding the repertoire of the ULK complex with phosphoproteomics. *Autophagy* **17**, 4491–4493 (2021).
52. Konno, H., Konno, K. & Barber, G. N. Cyclic Dinucleotides Trigger ULK1 (ATG1) Phosphorylation of STING to Prevent Sustained Innate Immune Signaling. *Cell* **155**, 688–698 (2013).
53. Gan, B. & Guan, J.-L. FIP200, a key signaling node to coordinately regulate various cellular processes. *Cell. Signal.* **20**, 787–794 (2008).
54. Chen, S. *et al.* Distinct roles of autophagy-dependent and -independent functions of FIP200 revealed by generation and analysis of a mutant knock-in mouse model. *Genes Dev.* **30**, 856–869 (2016).
55. Hara, T. *et al.* FIP200, a ULK-interacting protein, is required for autophagosome formation in mammalian cells. *J. Cell Biol.* **181**, 497–510 (2008).

56. Mizushima, N., Yoshimori, T. & Ohsumi, Y. The Role of Atg Proteins in Autophagosome Formation. *Annu. Rev. Cell Dev. Biol.* **27**, 107–132 (2011).
57. Pan, Z.-Q. *et al.* Atg1 kinase in fission yeast is activated by Atg11-mediated dimerization and cis-autophosphorylation. *eLife* **9**, e58073 (2020).
58. Farré, J.-C. & Subramani, S. Mechanistic insights into selective autophagy pathways: lessons from yeast. *Nat. Rev. Mol. Cell Biol.* **17**, 537–552 (2016).
59. Li, F., Chung, T. & Vierstra, R. D. AUTOPHAGY-RELATED11 Plays a Critical Role in General Autophagy- and Senescence-Induced Mitophagy in Arabidopsis. *Plant Cell* **26**, 788–807 (2014).
60. Gan, B. *et al.* Role of FIP200 in cardiac and liver development and its regulation of TNFalpha and TSC-mTOR signaling pathways. *J. Cell Biol.* **175**, 121–133 (2006).
61. Karanasios, E. *et al.* Autophagy initiation by ULK complex assembly on ER tubulovesicular regions marked by ATG9 vesicles. *Nat. Commun.* **7**, 12420 (2016).
62. Hosokawa, N. *et al.* Atg101, a novel mammalian autophagy protein interacting with Atg13. *Autophagy* **5**, 973–979 (2009).
63. Mercer, C. A., Kaliappan, A. & Dennis, P. B. A novel, human Atg13 binding protein, Atg101, interacts with ULK1 and is essential for macroautophagy. *Autophagy* **5**, 649–662 (2009).
64. Suzuki, H., Kaizuka, T., Mizushima, N. & Noda, N. N. Structure of the Atg101–Atg13 complex reveals essential roles of Atg101 in autophagy initiation. *Nat. Struct. Mol. Biol.* **22**, 572–580 (2015).
65. Jung, C. H. *et al.* ULK-Atg13-FIP200 Complexes Mediate mTOR Signaling to the Autophagy Machinery. *Mol. Biol. Cell* **20**, 1992–2003 (2009).
66. Kim, J., Kundu, M., Viollet, B. & Guan, K.-L. AMPK and mTOR regulate autophagy through direct phosphorylation of Ulk1. *Nat. Cell Biol.* **13**, 132–141 (2011).
67. Mizushima, N. The role of the Atg1/ULK1 complex in autophagy regulation. *Curr. Opin. Cell Biol.* **22**, 132–139 (2010).
68. Egan, D. F. *et al.* Phosphorylation of ULK1 (hATG1) by AMP-Activated Protein Kinase Connects Energy Sensing to Mitophagy. *Science* **331**, 456–461 (2011).
69. Funakoshi, T., Matsuura, A., Noda, T. & Ohsumi, Y. Analyses of *APG13* gene involved in autophagy in yeast, *Saccharomyces cerevisiae*. *Gene* **192**, 207–213 (1997).

70. Yamamoto, H. *et al.* The Intrinsically Disordered Protein Atg13 Mediates Supramolecular Assembly of Autophagy Initiation Complexes. *Dev. Cell* **38**, 86–99 (2016).
71. Hu, Z. *et al.* Multilayered Control of Protein Turnover by TORC1 and Atg1. *Cell Rep.* **28**, 3486-3496.e6 (2019).
72. Gross, A. S. *et al.* A metabolite sensor subunit of the Atg1/ULK complex regulates selective autophagy. *Nat. Cell Biol.* **26**, 366–377 (2024).
73. Jaber, N. & Zong, W.-X. Class III PI3K Vps34: essential roles in autophagy, endocytosis, and heart and liver function. *Ann. N. Y. Acad. Sci.* **1280**, 48–51 (2013).
74. Itakura, E., Kishi, C., Inoue, K. & Mizushima, N. Beclin 1 Forms Two Distinct Phosphatidylinositol 3-Kinase Complexes with Mammalian Atg14 and UVRAG. *Mol. Biol. Cell* **19**, 5360–5372 (2008).
75. Sun, Q. *et al.* Identification of Barkor as a mammalian autophagy-specific factor for Beclin 1 and class III phosphatidylinositol 3-kinase. *Proc. Natl. Acad. Sci.* **105**, 19211–19216 (2008).
76. Ohashi, Y., Tremel, S. & Williams, R. L. VPS34 complexes from a structural perspective. *J. Lipid Res.* **60**, 229–241 (2019).
77. Bilanges, B., Posor, Y. & Vanhaesebroeck, B. PI3K isoforms in cell signalling and vesicle trafficking. *Nat. Rev. Mol. Cell Biol.* **20**, 515–534 (2019).
78. Zhong, Y. *et al.* Distinct regulation of autophagic activity by Atg14L and Rubicon associated with Beclin 1–phosphatidylinositol-3-kinase complex. *Nat. Cell Biol.* **11**, 468–476 (2009).
79. Dooley, H. C. *et al.* WIPI2 Links LC3 Conjugation with PI3P, Autophagosome Formation, and Pathogen Clearance by Recruiting Atg12–5-16L1. *Mol. Cell* **55**, 238–252 (2014).
80. Young, L. N., Goerdeler, F. & Hurley, J. H. Structural pathway for allosteric activation of the autophagic PI 3-kinase complex I. *Proc. Natl. Acad. Sci. U. S. A.* **116**, 21508–21513 (2019).
81. Tremel, S. *et al.* Structural basis for VPS34 kinase activation by Rab1 and Rab5 on membranes. *Nat. Commun.* **12**, 1564 (2021).
82. Mizushima, N. *et al.* A protein conjugation system essential for autophagy. *Nature* **395**, 395–398 (1998).

83. Ichimura, Y. *et al.* A ubiquitin-like system mediates protein lipidation. *Nature* **408**, 488–492 (2000).
84. Kirisako, T. *et al.* The Reversible Modification Regulates the Membrane-Binding State of Apg8/Aut7 Essential for Autophagy and the Cytoplasm to Vacuole Targeting Pathway. *J. Cell Biol.* **151**, 263–276 (2000).
85. Jatana, N., Ascher, D. B., Pires, D. E. V., Gokhale, R. S. & Thukral, L. Human LC3 and GABARAP subfamily members achieve functional specificity via specific structural modulations. *Autophagy* **16**, 239–255 (2020).
86. Nakatogawa, H., Ishii, J., Asai, E. & Ohsumi, Y. Atg4 recycles inappropriately lipidated Atg8 to promote autophagosome biogenesis. *Autophagy* **8**, 177–186 (2012).
87. Maruyama, T. & Noda, N. N. Autophagy-regulating protease Atg4: structure, function, regulation and inhibition. *J. Antibiot. (Tokyo)* **71**, 72–78 (2018).
88. Agrotis, A. *et al.* Human ATG4 autophagy proteases counteract attachment of ubiquitin-like LC3/GABARAP proteins to other cellular proteins. *J. Biol. Chem.* **294**, 12610–12621 (2019).
89. Skytte Rasmussen, M. *et al.* ATG4B contains a C-terminal LIR motif important for binding and efficient cleavage of mammalian orthologs of yeast Atg8. *Autophagy* **13**, 834–853 (2017).
90. Tanida, I. *et al.* Apg7p/Cvt2p: A Novel Protein-activating Enzyme Essential for Autophagy. *Mol. Biol. Cell* **10**, 1367–1379 (1999).
91. Mizushima, N. *et al.* Mouse Apg16L, a novel WD-repeat protein, targets to the autophagic isolation membrane with the Apg12-Apg5 conjugate. *J. Cell Sci.* **116**, 1679–1688 (2003).
92. Hanada, T. *et al.* The Atg12-Atg5 Conjugate Has a Novel E3-like Activity for Protein Lipidation in Autophagy. *J. Biol. Chem.* **282**, 37298–37302 (2007).
93. Fujita, N. *et al.* The Atg16L Complex Specifies the Site of LC3 Lipidation for Membrane Biogenesis in Autophagy. *Mol. Biol. Cell* **19**, 2092–2100 (2008).
94. Walczak, M. & Martens, S. Dissecting the role of the Atg12–Atg5-Atg16 complex during autophagosome formation. *Autophagy* **9**, 424–425 (2013).
95. Phillips, A. R., Suttangkakul, A. & Vierstra, R. D. The ATG12-Conjugating Enzyme ATG10 Is Essential for Autophagic Vesicle Formation in Arabidopsis thaliana. *Genetics* **178**, 1339–1353 (2008).

96. Hamaoui, D. & Subtil, A. ATG16L1 functions in cell homeostasis beyond autophagy. *FEBS J.* **289**, 1779–1800 (2022).
97. Matoba, K. *et al.* Atg9 is a lipid scramblase that mediates autophagosomal membrane expansion. *Nat. Struct. Mol. Biol.* **27**, 1185–1193 (2020).
98. Maeda, S. *et al.* Structure, lipid scrambling activity and role in autophagosome formation of ATG9A. *Nat. Struct. Mol. Biol.* **27**, 1194–1201 (2020).
99. Young, A. R. J. *et al.* Starvation and ULK1-dependent cycling of mammalian Atg9 between the TGN and endosomes. *J. Cell Sci.* **119**, 3888–3900 (2006).
100. Hamasaki, M. *et al.* Autophagosomes form at ER–mitochondria contact sites. *Nature* **495**, 389–393 (2013).
101. Axe, E. L. *et al.* Autophagosome formation from membrane compartments enriched in phosphatidylinositol 3-phosphate and dynamically connected to the endoplasmic reticulum. *J. Cell Biol.* **182**, 685–701 (2008).
102. Hayashi-Nishino, M. *et al.* A subdomain of the endoplasmic reticulum forms a cradle for autophagosome formation. *Nat. Cell Biol.* **11**, 1433–1437 (2009).
103. Ylä-Anttila, P., Vihinen, H., Jokitalo, E. & Eskelinen, E.-L. 3D tomography reveals connections between the phagophore and endoplasmic reticulum. *Autophagy* **5**, 1180–1185 (2009).
104. Ge, L., Melville, D., Zhang, M. & Schekman, R. The ER–Golgi intermediate compartment is a key membrane source for the LC3 lipidation step of autophagosome biogenesis. *eLife* **2**, e00947 (2013).
105. Guo, Y. *et al.* AP1 is essential for generation of autophagosomes from the trans-Golgi network. *J. Cell Sci.* **125**, 1706–1715 (2012).
106. Young, A. R. J. *et al.* Starvation and ULK1-dependent cycling of mammalian Atg9 between the TGN and endosomes. *J. Cell Sci.* **119**, 3888–3900 (2006).
107. Hailey, D. W. *et al.* Mitochondria Supply Membranes for Autophagosome Biogenesis during Starvation. *Cell* **141**, 656–667 (2010).
108. Puri, C., Renna, M., Bento, C. F., Moreau, K. & Rubinsztein, D. C. Diverse Autophagosome Membrane Sources Coalesce in Recycling Endosomes. *Cell* **154**, 1285–1299 (2013).
109. Molino, D., Zemirli, N., Codogno, P. & Morel, E. The Journey of the Autophagosome through Mammalian Cell Organelles and Membranes. *J. Mol. Biol.* **429**, 497–514 (2017).

110. Imai, K. *et al.* Atg9A trafficking through the recycling endosomes is required for autophagosome formation. *J. Cell Sci.* **129**, 3781–3791 (2016).
111. Zhou, C. *et al.* Recycling of autophagosomal components from autolysosomes by the recycler complex. *Nat. Cell Biol.* **24**, 497–512 (2022).
112. Schmitt, D. *et al.* Lipid and protein content profiling of isolated native autophagic vesicles. *EMBO Rep.* **23**, EMBR202153065 (2022).
113. Nguyen, A. *et al.* Metamorphic proteins at the basis of human autophagy initiation and lipid transfer. *Mol. Cell* **83**, 2077–2090 (2023).
114. Narendra, D., Tanaka, A., Suen, D.-F. & Youle, R. J. Parkin is recruited selectively to impaired mitochondria and promotes their autophagy. *J. Cell Biol.* **183**, 795–803 (2008).
115. Matsuda, N. *et al.* PINK1 stabilized by mitochondrial depolarization recruits Parkin to damaged mitochondria and activates latent Parkin for mitophagy. *J. Cell Biol.* **189**, 211–221 (2010).
116. Geisler, S. *et al.* The PINK1/Parkin-mediated mitophagy is compromised by PD-associated mutations. *Autophagy* **6**, 871–878 (2010).
117. Grumati, P. & Dikic, I. Ubiquitin signaling and autophagy. *J. Biol. Chem.* **293**, 5404–5413 (2018).
118. Pankiv, S. *et al.* p62/SQSTM1 Binds Directly to Atg8/LC3 to Facilitate Degradation of Ubiquitinated Protein Aggregates by Autophagy. *J. Biol. Chem.* **282**, 24131–24145 (2007).
119. Kirkin, V. *et al.* A Role for NBR1 in Autophagosomal Degradation of Ubiquitinated Substrates. *Mol. Cell* **33**, 505–516 (2009).
120. Zheng, Y. T. *et al.* The Adaptor Protein p62/SQSTM1 Targets Invading Bacteria to the Autophagy Pathway. *J. Immunol.* **183**, 5909–5916 (2009).
121. Lamark, T., Kirkin, V., Dikic, I. & Johansen, T. NBR1 and p62 as cargo receptors for selective autophagy of ubiquitinated targets. *Cell Cycle* **8**, 1986–1990 (2009).
122. Thurston, T. L. M., Ryzhakov, G., Bloor, S., von Muhlinen, N. & Randow, F. The TBK1 adaptor and autophagy receptor NDP52 restricts the proliferation of ubiquitin-coated bacteria. *Nat. Immunol.* **10**, 1215–1221 (2009).
123. Ravenhill, B. J. *et al.* The Cargo Receptor NDP52 Initiates Selective Autophagy by Recruiting the ULK Complex to Cytosol-Invading Bacteria. *Mol. Cell* **74**, 320-329.e6 (2019).

124. Vargas, J. N. S. *et al.* Spatiotemporal Control of ULK1 Activation by NDP52 and TBK1 during Selective Autophagy. *Mol. Cell* **74**, 347-362.e6 (2019).
125. Wild, P. *et al.* Phosphorylation of the Autophagy Receptor Optineurin Restricts Salmonella Growth. *Science* **333**, 228–233 (2011).
126. Richter, B. *et al.* Phosphorylation of OPTN by TBK1 enhances its binding to Ub chains and promotes selective autophagy of damaged mitochondria. *Proc. Natl. Acad. Sci.* **113**, 4039–4044 (2016).
127. Tumbarello, D. A. *et al.* The Autophagy Receptor TAX1BP1 and the Molecular Motor Myosin VI Are Required for Clearance of Salmonella Typhimurium by Autophagy. *PLOS Pathog.* **11**, e1005174 (2015).
128. North, B. J., Ohnstad, A. E., Ragusa, M. J. & Shoemaker, C. J. The LC3-interacting region of NBR1 is a protein interaction hub enabling optimal flux. *J. Cell Biol.* **224**, e202407105 (2025).
129. Rogov, V., Dötsch, V., Johansen, T. & Kirkin, V. Interactions between autophagy receptors and ubiquitin-like proteins form the molecular basis for selective autophagy. *Mol. Cell* **53**, 167–178 (2014).
130. Lazarou, M. *et al.* The ubiquitin kinase PINK1 recruits autophagy receptors to induce mitophagy. *Nature* **524**, 309–314 (2015).
131. Vargas, J. N. S., Hamasaki, M., Kawabata, T., Youle, R. J. & Yoshimori, T. The mechanisms and roles of selective autophagy in mammals. *Nat. Rev. Mol. Cell Biol.* **24**, 167–185 (2023).
132. Komatsu, M. *et al.* Loss of autophagy in the central nervous system causes neurodegeneration in mice. *Nature* **441**, 880–884 (2006).
133. Nakamura, S. & Yoshimori, T. New insights into autophagosome–lysosome fusion. *J. Cell Sci.* **130**, 1209–1216 (2017).
134. Diao, J., Yip, C. K. & Zhong, Q. Molecular structures and function of the autophagosome-lysosome fusion machinery. *Autophagy Rep.* **3**, 2305594 (2024).
135. Jordens, I. *et al.* The Rab7 effector protein RILP controls lysosomal transport by inducing the recruitment of dynein-dynactin motors. *Curr. Biol.* **11**, 1680–1685 (2001).
136. Johansson, M. *et al.* Activation of endosomal dynein motors by stepwise assembly of Rab7–RILP–p150Glued, ORP1L, and the receptor βlll spectrin. *J. Cell Biol.* **176**, 459–471 (2007).

137. Guerra, F. & Bucci, C. Multiple Roles of the Small GTPase Rab7. *Cells* **5**, 34 (2016).
138. Jiang, P. *et al.* The HOPS complex mediates autophagosome–lysosome fusion through interaction with syntaxin 17. *Mol. Biol. Cell* **25**, 1327–1337 (2014).
139. Shvarev, D. *et al.* Structure of the HOPS tethering complex, a lysosomal membrane fusion machinery. *eLife* **11**, e80901 (2022).
140. Itakura, E., Kishi-Itakura, C. & Mizushima, N. The Hairpin-type Tail-Anchored SNARE Syntaxin 17 Targets to Autophagosomes for Fusion with Endosomes/Lysosomes. *Cell* **151**, 1256–1269 (2012).
141. Li, Y. *et al.* Decoding three distinct states of the Syntaxin17 SNARE motif in mediating autophagosome–lysosome fusion. *Proc. Natl. Acad. Sci.* **117**, 21391–21402 (2020).
142. Liu, R., Zhi, X. & Zhong, Q. ATG14 controls SNARE-mediated autophagosome fusion with a lysosome. *Autophagy* **11**, 847–849 (2015).
143. Cheng, X. *et al.* Pacer Mediates the Function of Class III PI3K and HOPS Complexes in Autophagosome Maturation by Engaging Stx17. *Mol. Cell* **65**, 1029-1043.e5 (2017).
144. McEwan, D. G. *et al.* PLEKHM1 Regulates Autophagosome-Lysosome Fusion through HOPS Complex and LC3/GABARAP Proteins. *Mol. Cell* **57**, 39–54 (2015).
145. Liang, C. *et al.* Beclin1-binding UVRAG targets the class C Vps complex to coordinate autophagosome maturation and endocytic trafficking. *Nat. Cell Biol.* **10**, 776–787 (2008).
146. Wetzel, L. *et al.* TECPR1 promotes aggrephagy by direct recruitment of LC3C autophagosomes to lysosomes. *Nat. Commun.* **11**, 2993 (2020).
147. Ballabio, A. & Bonifacino, J. S. Lysosomes as dynamic regulators of cell and organismal homeostasis. *Nat. Rev. Mol. Cell Biol.* **21**, 101–118 (2020).
148. Mindell, J. A. Lysosomal Acidification Mechanisms. *Annu. Rev. Physiol.* **74**, 69–86 (2012).
149. Zimprich, A. *et al.* Mutations in *LRRK2* Cause Autosomal-Dominant Parkinsonism with Pleomorphic Pathology. *Neuron* **44**, 601–607 (2004).
150. Sidransky, E. *et al.* Multicenter Analysis of Glucocerebrosidase Mutations in Parkinson's Disease. *N. Engl. J. Med.* **361**, 1651–1661 (2009).
151. Mazzulli, J. R. *et al.* Gaucher Disease Glucocerebrosidase and α-Synuclein Form a Bidirectional Pathogenic Loop in Synucleinopathies. *Cell* **146**, 37–52 (2011).

152. Usenovic, M., Tresse, E., Mazzulli, J. R., Taylor, J. P. & Krainc, D. Deficiency of ATP13A2 Leads to Lysosomal Dysfunction, α-Synuclein Accumulation, and Neurotoxicity. *J. Neurosci.* **32**, 4240–4246 (2012).
153. Cataldo, A. M., Paskevich, P. A., Kominami, E. & Nixon, R. A. Lysosomal hydrolases of different classes are abnormally distributed in brains of patients with Alzheimer disease. *Proc. Natl. Acad. Sci.* **88**, 10998–11002 (1991).
154. Lee, J.-H. *et al.* Lysosomal Proteolysis and Autophagy Require Presenilin 1 and Are Disrupted by Alzheimer-Related PS1 Mutations. *Cell* **141**, 1146–1158 (2010).
155. Lee, J.-H. *et al.* Faulty autolysosome acidification in Alzheimer's disease mouse models induces autophagic build-up of Aβ in neurons, yielding senile plaques. *Nat. Neurosci.* **25**, 688–701 (2022).
156. Zhu, Q. *et al.* Reduced C9ORF72 function exacerbates gain of toxicity from ALS/FTD-causing repeat expansion in C9orf72. *Nat. Neurosci.* **23**, 615–624 (2020).
157. Beckers, J. *et al.* A toxic gain-of-function mechanism in C9orf72 ALS impairs the autophagy-lysosome pathway in neurons. *Acta Neuropathol. Commun.* **11**, 151 (2023).
158. Elrick, M. J., Yu, T., Chung, C. & Lieberman, A. P. Impaired proteolysis underlies autophagic dysfunction in Niemann–Pick type C disease. *Hum. Mol. Genet.* **21**, 4876–4887 (2012).
159. Settembre, C. *et al.* A block of autophagy in lysosomal storage disorders. *Hum. Mol. Genet.* **17**, 119–129 (2008).
160. Platt, F. M., d'Azzo, A., Davidson, B. L., Neufeld, E. F. & Tifft, C. J. Lysosomal storage diseases. *Nat. Rev. Dis. Primer* **4**, 27 (2018).
161. Deretic, V. & Lazarou, M. A guide to membrane atg8ylation and autophagy with reflections on immunity. *J. Cell Biol.* **221**, e202203083 (2022).
162. Thurston, T. L. M., Wandel, M. P., von Muhlinen, N., Foeglein, Á. & Randow, F. Galectin 8 targets damaged vesicles for autophagy to defend cells against bacterial invasion. *Nature* **482**, 414–418 (2012).
163. Tumbarello, D. A. *et al.* The Autophagy Receptor TAX1BP1 and the Molecular Motor Myosin VI Are Required for Clearance of Salmonella Typhimurium by Autophagy. *PLOS Pathog.* **11**, e1005174 (2015).
164. Pilli, M. *et al.* TBK-1 promotes autophagy-mediated antimicrobial defense by controlling autophagosome maturation. *Immunity* **37**, 223–234 (2012).

165. Rotem, Z., Cox, R. A. & Isaacs, A. Inhibition of Virus Multiplication by Foreign Nucleic Acid. *Nature* **197**, 564–566 (1963).
166. Stetson, D. B. & Medzhitov, R. Recognition of Cytosolic DNA Activates an IRF3-Dependent Innate Immune Response. *Immunity* **24**, 93–103 (2006).
167. Zhang, X. *et al.* Cyclic GMP-AMP Containing Mixed Phosphodiester Linkages Is An Endogenous High-Affinity Ligand for STING. *Mol. Cell* **51**, 226–235 (2013).
168. Ablasser, A. *et al.* cGAS produces a 2′-5′-linked cyclic dinucleotide second messenger that activates STING. *Nature* **498**, 380–384 (2013).
169. Gao, P. *et al.* Cyclic [G(2′,5′)pA(3′,5′)p] Is the Metazoan Second Messenger Produced by DNA-Activated Cyclic GMP-AMP Synthase. *Cell* **153**, 1094–1107 (2013).
170. Diner, E. J. *et al.* The innate immune DNA sensor cGAS produces a non-canonical cyclic-di-nucleotide that activates human STING. *Cell Rep.* **3**, 1355–1361 (2013).
171. Sun, L., Wu, J., Du, F., Chen, X. & Chen, Z. J. Cyclic GMP-AMP synthase is a cytosolic DNA sensor that activates the type I interferon pathway. *Science* **339**, 786–791 (2013).
172. Ishikawa, H. & Barber, G. N. STING is an endoplasmic reticulum adaptor that facilitates innate immune signalling. *Nature* **455**, 674–678 (2008).
173. Zhong, B. *et al.* The Adaptor Protein MITA Links Virus-Sensing Receptors to IRF3 Transcription Factor Activation. *Immunity* **29**, 538–550 (2008).
174. Sun, W. *et al.* ERIS, an endoplasmic reticulum IFN stimulator, activates innate immune signaling through dimerization. *Proc. Natl. Acad. Sci.* **106**, 8653–8658 (2009).
175. Burdette, D. L. *et al.* STING is a direct innate immune sensor of cyclic di-GMP. *Nature* **478**, 515–518 (2011).
176. Gao, P. *et al.* Structure-Function Analysis of STING Activation by c[G(2′,5′)pA(3′,5′)p] and Targeting by Antiviral DMXAA. *Cell* **154**, 748–762 (2013).
177. Fitzgerald, K. A. *et al.* IKKε and TBK1 are essential components of the IRF3 signaling pathway. *Nat. Immunol.* **4**, 491–496 (2003).
178. Jeltema, D., Abbott, K. & Yan, N. STING trafficking as a new dimension of immune signaling. *J. Exp. Med.* **220**, e20220990 (2023).

179. Hu, L. et al. Deleterious variants in the autophagy-related gene RB1CC1/FIP200 impair immunity to SARS-CoV-2. *Nat. Commun*. **16**, 10618 (2025).

Chapter 2

THE ATG9A–ATG13–ATG101 COMPLEX SUPPRESSES CONSTITUTIVE INNATE IMMUNE SIGNALING INDEPENDENT OF CANONICAL AUTOPHAGY

2.1 ABSTRACT

ATG13 and ATG101, HORMA domain-containing subunits of the Autophagy Initiation Complex (AIC), form a complex with transmembrane protein ATG9A via its C-terminal HORMA Dimer-Interacting Region (HDIR). While their canonical role in autophagy is established, their full cellular function remains unclear. Unbiased proteomics of AIC KO cell lines revealed that loss of ATG101 or ATG13, but not FIP200 or ULK1/2, causes constitutive upregulation of type I interferon-stimulated genes (ISGs) including IFIT1, IFIT2, IFIT3, OASL, and ISG15, across multiple cell types and reversible upon protein re-expression. Mutagenesis demonstrated that ATG101's interaction with ATG9A, but not its autophagy function or WPF finger, is required for ISG suppression. ATG13's FIP200-binding domain is dispensable, further highlighting that this function is fully independent of canonical autophagic flux. ATG9A KO phenocopied these effects in an HDIR-dependent manner. These findings establish the ATG9A-ATG13-ATG101 subcomplex as a non-canonical regulator of innate immune homeostasis, operating independently of the broader AIC.

2.2 INTRODUCTION

Chapter 1 provides a comprehensive review of autophagy mechanisms and the canonical functions of the AIC and its individual subunits. Building on this framework, this chapter investigates whether AIC subunits perform functions entirely independent of canonical autophagy. ATG13 and ATG101 are HORMA domain-containing subunits of the AIC that additionally form a biochemically distinct complex with ATG9A, the sole transmembrane ATG protein, through direct interactions with the intrinsically disordered C-terminal HORMA Domain Interacting Region (HDIR) of ATG9A. This ATG9A–ATG13–ATG101 complex is assembled independently of FIP200 and ULK1 and has structural and functional characteristics that are distinct from the AIC.

This chapter first examines the molecular biology of ATG13, ATG101, and ATG9A individually, and then explores their assembly and function as the ATG9A–ATG13–ATG101 complex. To establish a functional baseline, CRISPR-Cas9 KO lines were generated for each AIC component and characterized by autophagy flux and selective mitophagy assays, revealing that each subunit makes distinct and non-redundant contributions to autophagic activity. Unbiased proteomic profiling of these AIC KO cell lines described below revealed a striking observation: deletion of ATG101 or ATG13, but not FIP200 or ULK1/2, leads to constitutive upregulation of type I ISGs across multiple cell types, independently of canonical autophagy. These results dissociate the immune regulatory function of the complex from its established role in autophagosome nucleation. Mutagenesis and reconstitution experiments show that this phenotype depends specifically on the intact interaction among ATG9A, ATG13, and ATG101, identifying the complex as a non-canonical regulatory module that maintains innate immune homeostasis.

Chapter 3 examines the underlying mechanism of this immune regulation, focusing on the complex's role in Golgi-to-lysosome trafficking of the innate immune adaptor STING.

2.2.1 ATG13

2.2.1.1 ATG13 DISCOVERY AND CONSERVATION

ATG13 is a highly conserved autophagy protein that was among the first identified genes required for autophagy[1]. The yeast homolog, Atg13, was identified as a genetic interactor and phosphorylation target of Atg1 (yeast homolog of ULK1)[2,3]. Atg13 is required for cytoplasmic vesicle formation, the process later defined as autophagosome formation[4]. Formation of the complete Atg1 complex, comprising Atg1-Atg13-Atg17-Atg29-Atg31, is required for PAS localization[5–7]. Atg1 and Atg13 are constitutive binders, however the interaction is enhanced following Atg13 dephosphorylation[8–10]. Mice lacking ATG13 die *in utero*, underscoring its essential and non-redundant role[11].

2.2.1.2 ATG13 STRUCTURE

Atg13 consists of an N-terminal HORMA (Hop1, Rev7, and Mad2) domain and C-terminal IDR and MIT domains that mediate interactions with Atg1 and Atg17[10]. The HORMA domain mediates interactions with PI3K[12], ATG101[13,14], and ATG9A[15–18]. The C-terminal IDR of Atg13 is the central scaffold of interactions with Atg1 and Atg17, utilizing multivalent interactions to promote the assembly of supramolecular Atg1 complexes[19–21].

ATG13 also contains an LC3-interacting region (LIR) that permits direct complex formation with ATG8 family proteins[22,23].

2.2.1.3 HORMA DOMAINS

HORMA domains are protein modules that act as conserved conformational switches in a range of cellular checkpoints[24]. HORMA domains were first identified in three divergent proteins in *S. cerevisiae*: the meiotic regulator Hop1, the DNA repair factor Rev7, and the spindle assembly checkpoint Mad2[25]. ATG13 and ATG101 are HORMA domain-containing proteins[13]. The HORMA domain is a ~200 amino acid fold

consisting of a β-sheet core flanked by α-helices and a flexible C-terminal 'safety belt' region[26].

The defining feature of a HORMA domain is its capacity to adopt distinct conformations that control binding to partner proteins. HORMA domains recognize short closure motifs in their partner proteins, wrapping around those motifs to form a locked complex. In one conformation (open), the domain cannot form a stable interaction with partner motifs, whereas in the closed conformation the domain topologically embraces the closure motif to form a long-lived complex[27]. Closure motif binding involves a 'safety belt' segment that wraps around the ligand, creating a topological interaction that is unusually stable and often requires remodeling factors for release. The highly specific and long-lived nature of HORMA domain interactions make them ideal hubs for protein-protein interactions[28].

2.2.1.4 ATG13 REGULATION

ATG13 activity is tightly regulated through phosphorylation in response to nutrient status. In yeast, Atg13 is phosphorylated by multiple upstream regulators of autophagy, including TORC1[29], PKA[30], and Atg1[31]. Phosphorylation of Atg13 by TORC1 negatively regulates autophagy by preventing Atg13 from bridging Atg17-Atg29-Atg31, resulting in failure to form PAS[29,32,33]. This signaling cascade is mirrored in mammals, with ATG13 being directly phosphorylated by mTOR on Ser-258 and by AMPK on Ser-224[10,34].

During nutrient starvation, TORC1 activity is inhibited and Atg13 is dephosphorylated by PP2C-like phosphatases Ptc2 and Ptc3, promoting the multivalent interaction with Atg17 and driving PAS formation[35]. Overall, ATG13 can be extensively modified post-translationally via 48 distinct phosphorylation events. Disrupting this dynamic regulation of ATG13 can lead to insufficient or excessive autophagy[36].

2.2.1.5 ATG13 FUNCTION

The primary function of ATG13 is to act as a scaffold of the ULK1 initiation complex, bridging the kinase subunit Atg1/ULK1 to downstream Atg17-Atg29-Atg31 subcomplex in yeast and to FIP200 and ATG101 in mammals.

Importantly, disruption of the ULK1-ATG13 interaction in mammals does not entirely inhibit autophagy, highlighting ULK1-independent autophagy functions of ATG13[37–39]. This may be due to the ability of ATG13 to bind both ULK1 and ULK2[40]. Consistent with this, ATG13-deficient mice die in utero with myocardial growth defects, a phenotype shared with FIP200 loss but not ULK1/2 deletion, suggesting a non-autophagic developmental function mediated through the ATG13-FIP200 axis independent of ULK1[11]. As discussed in greater depth in Chapter 4, the IDR of ATG13 directly interacts with FIP200[21].

In a study in HEK cells, ATG13 positively regulates type I interferon signaling in response to viral infection and innate immune ligands[41]. ATG13 knockdown reduced interferon-stimulated gene expression and its overexpression conferred viral resistance. This function appeared to operate through the RLR-MAVS-TBK1 axis and through physical interaction with TRAF3 and TRAF6, rather than through any autophagic degradation mechanism. This suggests that ATG13 has evolved functional versatility beyond its role as an autophagy initiator. Notably, this positive regulatory role for ATG13 in IFN signaling contrasts with findings presented later in this chapter (**Section 2.3.3**) and is discussed further in Section 2.4.

Beyond its role within the AIC, ATG13 forms a direct interaction with ATG9A through its HORMA domain, contributing to the assembly of the ATG9A–ATG13–ATG101 complex. The function and significance of this complex is explored in depth in the ATG9A section below.

2.2.2 ATG101

2.2.2.1 ATG101 DISCOVERY AND CONSERVATION

ATG101 was identified in 2009 by two independent groups as a novel ATG13-interacting protein required for autophagy in mammals[42,43]. ATG101 is unique among ATG proteins in that it lacks a known *S. cerevisiae* homolog[44], yet is an essential autophagy protein conserved in filamentous fungi (*S. pombe*)[45], *Drosophila*[46], *C. elegans*[47], *Arabidopsis thaliana*[47], and all metazoans[44]. Deletion of the ATG101 *C. elegans* homolog EPG9 leads to a loss of autophagy function[47]. ATG101 KO in *Drosophila* results in failure to form autophagosomes and accumulation of ubiquitin[48,49]. SpAtg101 cannot substitute for the function of *S. cerevisiae* Atg29 and Atg31, components of the Atg1 complex described in Chapter 1, *in vivo,* indicating clear evolutionary divergence between these proteins[50].

ATG101 was first discovered as an ATG13 interactor and stabilizer[43] and was later shown to facilitate recruitment of the autophagic transmembrane protein ATG9A to the AIC[51]. ATG101 interacts with the AIC via direct interaction with ATG13, rather than with FIP200 or ULK1 directly.

2.2.2.2 ATG101 STRUCTURE

Structures of yeast (SpATG101) and human ATG101, alone and in complex with partner proteins, including ATG13 and ATG9A, have been resolved.[13,14,51–53] Initial resolution of the SpATG101 structure revealed that the protein is composed of three α-helices and six β-strands[14]. The three α-helices (αA-C) align with a β-sheet composed of four β-strands (β1 and β4–β6) and are flanked by an antiparallel β-sheet of β2/β3 on the opposing side.

SpAtg101 contains a protruding loop between β4 and β5 harboring a Trp-Phe or Trp-Pro-Phe motif, termed the WPF finger. The WPF is conserved among ATG101 homologs and, due to its variable conformation, was predicted to mediate interactions with other proteins. Mutations to the WPF finger do not impact ATG13 binding. Although initially described as sequestered[13], subsequent studies found that the WPF finger is exposed and recruits downstream machinery, such as LC3, WIPI1, and ZFYVE/DFCP1, to autophagosomes.[14]

The ATG13-ATG101 binding interface has been resolved and is composed of αA, αC, β3 and the αA-β2 loop of SpATG101, which interact with αC, β8′ and the αA-αB loops of SpAtg13. *In vitro* pulldown assays with purified recombinant proteins identified SpATG101 mutations that abrogate interactions with ATG13, including the F29R/H30R (equivalent to L30/H31R in humans) and V134R/N138R mutants. Crystal structures of full-length human ATG101 with a truncated ATG13 consisting of its HORMA domain, $ATG13^{HORMA}$, confirmed the ATG13-ATG101 binding region observed in *S. pombe* is conserved in humans and is mediated via the HORMA domain[13,52]. Evidence from Suzuki et al. highlights that the region of interaction between ATG101 and ATG13 is partially conserved between SpATG101 and the mouse homolog, mATG101[14].

In addition to the ATG13-binding region and WPF finger, another structure of full length ATG101 and $ATG13^{HORMA}$ reveals a flexible and exposed C-terminal domain capable of interacting with downstream autophagy machinery[53].

2.2.2.3 ATG101 FUNCTION

The primary function of ATG101 is to stabilize ATG13. Supporting this, overexpression of ATG101 prevents proteasomal degradation of ATG13[43]. While ULK1, FIP200, ATG13, and ATG101 form a stable complex, size-exclusion chromatography (SEC) studies highlight that the ATG13-ATG101 complex and monomeric ATG101 also exist in large amounts[42]. The existence of ATG13-ATG101 complex independent of the ULK1 complex points to a potential AIC-independent role of this complex.

ATG13 mutants incapable of binding ATG101 due to mutations in the HORMA domain are significantly autophagy impaired, highlighting the importance of this interaction.[54] Consistent with this, mutating the human ATG13-binding region (L30R/H31R) abolished the interaction with ATG101, excluding ATG101 from the ULK1 complex leading to a strong autophagy defect[14,54].

ATG13 forms a constitutive dimer with ATG101 through their respective HORMA domains. Structures of the ATG13:ATG101 dimer complexed with the PI3P-binding protein WIPI2 and WIPI3 have been resolved. Bound to WIPI2 or WIPI3, the

ATG13:ATG101 aligns with the membrane to insert the ATG101 WPF finger into the membrane surface. This alignment stabilizes the complex on membranes, explaining the essential role of the WPF residues in autophagy. The interaction between ATG13-ATG101 and WIPIs is required for ATG16L1 phosphorylation by ULK1, ATG13 puncta formation, and bulk autophagic flux, establishing a stepwise pathway for recruitment of the AIC to the membrane downstream of PI3KC3-C1[55].

Overall, the prevailing model is that Atg13 is stabilized by Atg101 and recruits downstream autophagy factors to the autophagosome-formation site, with the WPF finger mediating downstream interactions, but not ATG13 binding.

2.2.2.4 ATG101-CONTAINING COMPLEXES

In addition to its role in the AIC and ATG9A-ATG13-ATG101 complex, ATG101 is a component of a multiprotein complex containing Smith-Magenis syndrome chromosomal region candidate gene 8 (SMCR8), WDR41, and chromosome 9 open reading frame 72 (C9orf72)[56]. This complex interacts with the AIC and has a role in the regulation and expression of ULK1. C9orf72 is a prevalent genetic cause of frontotemporal dementia (FTD) and amyotrophic lateral sclerosis (ALS)[57], indicating a potential connection between ATG101-mediated autophagy defects and neurodegenerative disease.

2.2.2.5 ATG101 IN DISEASE AND PHYSIOLOGY

Deletion of ATG101 in human pancreatic carcinoma cell line leads to reduced survival and an inability to promote autophagy during nutrient starvation[58]. This indicates that ATG101 may play a role in cancer cell adaptation to metabolic stress and therefore represent a potential therapeutic target.

ATG101 has been shown to directly interact with STING, a connection explored in greater depth in Chapter 3. Bovine Herpesvirus 1 tegument protein UL3 suppresses innate antiviral immune response to promote viral replication. UL3 upregulates ATG101 to promote autophagic degradation of STING, thereby inhibiting the cGAS-STING

pathway. Co-IP experiments point to a direct interaction between ATG101 and STING[59]. This is the first described connection between ATG101 and STING in the literature.

2.2.3 ATG9A

2.2.3.1 ATG9A DISCOVERY AND CONSERVATION

ATG9A is an integral membrane protein first identified in *S. cerevisiae,* where it was recognized as essential for vesicle formation and autophagy.[60,61] Most species contain only a single paralog, but a gene multiplication event in vertebrates led to the rise of two homologs, ATG9A and ATG9B[62,63]. ATG9A is ubiquitously expressed in all tissue types, but ATG9B is only highly expressed in the placenta and pituitary[64,65]. This may indicate a specialized function of ATG9B[63]. Although ATG9B is capable of functionally compensating for ATG9A loss, its limited expression means ATG9A is the dominant paralog in most cellular contexts[63].

The essentiality of ATG9 homologs for autophagy is conserved across evolution[63,66–69]. Atg9A-deficient *Drosophila* are sterile and display significant autophagy defects during development[70,71]. In mice, Atg9a KO is embryonic lethal[72–74].

2.2.3.2 ATG9A STRUCTURE

ATG9 is the sole transmembrane ATG protein and forms an obligate trimer[75]. Cryo-EM structures resolved across multiple species reveal evolutionarily conserved trimeric architecture with a central pore that opens laterally to accommodate lipid headgroups, providing the structural basis for its lipid scramblase activity[76–78]. ATG9A has cytosolic exposed N- and C-termini and a lumenal N-linked high mannose glycosylation site.

The C-terminus of ATG9A is intrinsically disordered and contains an HDIR at its extreme C-terminus. This motif is essential for interactions with the HORMA domain proteins ATG13 and ATG101[17,51,77,79] and is therefore critical for ATG9A's role in autophagy. The trafficking of ATG9A vesicles requires small guanosine triphosphate

(GTP)-binding Rab proteins, ADP-ribosylation factor (Arf) GTPases, and Arfaptins, which together coordinate membrane dynamics at ATG9A-positive vesicles[80].

2.2.3.3 ATG9A LOCALIZATION

In yeast, Atg9 is co-translationally inserted into the ER and shuttled to the Golgi in a Sec12-dependent manner[81]. In mammals, ATG9A localizes primarily to the trans-Golgi network (TGN) and late endosomes under nutrient-replete conditions, where it occupies a perinuclear compartment that is positive for TGN and endosomal markers[63,65,66,82,83]. Early studies revealed that Atg9 localization to the PAS is regulated by Atg1 and Atg13[15]. Atg9 cycles through pre-PAS and mitochondria, providing initial evidence that mitochondrial membranes supply lipids to nascent autophagosome[84].

In response to amino acid starvation, ATG9A redistributes from the TGN to LC3-positive autophagosomes[82,85]. ATG9A transiently interacts with autophagosomes as seen by partial colocalization between ATG9A and LC3B, with only small proportion of ATG9A being incorporated into mature autophagosomes[66,86,87]. Imaging and membrane fractionation experiments in ATG2 DKO cells confirm that ATG9A colocalizes and migrates with LC3B, consistent with a transient residence on lipidated membranes during autophagosome biogenesis[87]. ATG9A vesicles thus serve as seed membrane source rather than constitutive autophagosome components.

2.2.3.4 ATG9A VESICLES

ATG9A vesicles exist as two populations: a motile and a diffuse population[66,86]. While these vesicles carry fusion machinery including SNARE proteins and Rab GTPases[80], the vesicle protein content does not mirror that of the phagophore[79]. Rather, ATG9A vesicles are enriched for adaptor proteins, lipid kinases and trafficking regulators[80,88–90]. Among these are the BAR domain proteins Arfaptin 1 and 2, though only Arfaptin 2 controls ATG9A localization. Loss of Arfaptin 2 leads to a dispersal of ATG9A from its perinuclear compartment[80].

The importance of ATG9A vesicles is demonstrated by yeast reconstitution assays. Yeast Atg9-containing proteo-liposomes or immunopurified ATG9A vesicles are each sufficient to reconstitute autophagosome nucleation in vitro[91,92]. In these systems, Atg9-positive vesicles can be lipidated by the E3 complex and recruit autophagy proteins, including PI3KC3-C1 complex, to generate PI3P on the vesicle[91]. This establishes ATG9A vesicles not merely as lipid donors, but as active platforms for autophagy signaling.

2.2.3.5 ATG9A VESICLE TRAFFICKING

In yeast, budding of Atg9 vesicles from the TGN requires Atg23 and Atg27[93]. In mammals, this process requires the AP-4 (adaptor protein 4) complex[94–96]. In addition to ATG9A, the AP-4 complex also packages SERINC1 and SERINC3 into ATG9A vesicles.[95] The clinical relevance of this pathway is underscored by the finding that AP-4 mutations cause hereditary spastic paraplegia (HSP)[94]. These mutations result in ATG9A retention at the TGN and depletion of ATG9A at distal axons, causing defective axonal extension[97]. Beyond AP-4, ATG9A trafficking is regulated by AP-1[98], AP-2[99], BIF-1[100], and multiple kinases, including ULK1 and SRC[101].

Rab GTPases act as central regulators of ATG9A trafficking and are involved in multiple steps from autophagosome biogenesis to lysosomal fusion[102]. RAB1 is detected on ATG9A vesicles and its knockdown leads to ATG9A accumulation at the PAS and subsequent autophagy inhibition[103]. Loss of Rab1b specifically affects ATG9A trafficking from the ER to Golgi, leading to its accumulation and impaired autophagic flux[103]. Rab3c has also been found to influence ATG9A trafficking in a mechanism involving Rab12[104]. In yeast, the Arf-like-GTPase Arl1 is implicated in Atg9 anterograde transport, with Arl1 deletion leading to reduced Atg9 levels at the PAS[105].

ATG9A can be recycled from membranes following autophagosome maturation. The autophagosome component recycling complex of SNX4, SNX5 and SNX17 has been proposed to mediate the recycling of ATG9A from the autolysosome in a Rab32/38 dependent mechanism[106,107].

2.2.3.6 ATG9A FUNCTION

The core biochemical function of ATG9A is as a lipid scramblase that transfers phospholipids from inner and outer membrane leaflets[76,79,108]. The scramblase activity is required for its autophagic function. Mutations that disrupt scrambling lead to a block in autophagic flux, increase in p62 aggregates, and reduction in autophagic structure size[79].

Formation of autophagosomes requires the addition of phospholipid membranes from diverse sources including mitochondria,[82,109] ER,[110–113] Golgi,[98,114] plasma membranes[115], TGN, and endosomes[106,116–118], and ATG9A is found at these sites. ATG9A also interacts with ATG2, a lipid transfer protein that contains a hydrophobic cavity capable of transporting lipids between membrane sites, forming contact sites between the ER and the phagophore during early autophagosome formation[119–122].

Beyond its canonical role in autophagosome membrane expansion, ATG9A has broader selective autophagy function. Degradation of autophagy adaptor NBR1 is largely independent of ULK1 and several ATG factors required for LC3 lipidation, however it is entirely dependent on ATG9A and ATG101[123]. Consistently, ATG9A emerged as a top hit in a CRISPR/Cas9 screen for proteins required for p62/SQSTM1 degradation, while other core ATG proteins were not essential[124].

ATG9A also has roles beyond autophagy. In *C. elegans,* ATG-9 maintains lysosome homeostasis by promoting lysosomal biogenesis and maintaining lysosomal integrity[125]. In mice, Atg9A has been linked to a form of necrosis in developing bones; Atg9a-deficient mice lack this necrosis[126]. The authors of this study suggest a potential link to inflammation[73], however the mechanism linking Atg9A to bone necrosis is not understood.

2.2.3.7 ATG9A IN DISEASE AND PHYSIOLOGY

ATG9A loss has particularly severe consequences in neurons, cell types particularly reliant on intracellular trafficking. ATG9A KO leads to progressive degeneration of the

axons and impaired nerve fiber tract formation[127] and mutations in ATG9 can lead to neurodevelopmental or neurodegeneration phenotypes[97,128,129]. At the systemic level, Atg9a KO in mice is embryonic lethal[72–74] while AP-4 mutations that mislocalize ATG9A at the TGN cause HSP in humans[94], underscoring the role of ATG9A trafficking in the nervous system.

ATG9A has emerged as a critical regulator of immune signaling. In mice, ATG9A limits TBK1-STING cytosolic puncta formation in response to dsDNA-induced immune response and has been described as colocalized with STING and TBK1[73].

ATG9A has also been identified as a key mediator of an unconventional lysosomal targeting pathway that degrades activated TNFR1-associated signaling complexes. Mechanistically, TNF binding to TNFR1 drives formation of Complex I and Complex IIa, with the latter promoted by caspase-8 activation and RIPK1 M1-ubiquitination. TAX1BP1 binds Complex IIa and recruits FIP200 and ATG9A to facilitate its lysosomal degradation in an AIC-dependent, LC3-independent process. Loss of Atg9a in mice prevents this degradation, resulting in TNFR1-mediated embryonic lethality, while keratinocyte-specific deletion of Atg9a leads to an inflammatory skin disease, demonstrating an anti-inflammatory role for Atg9a[130]. ATG9A's anti-inflammatory properties appear to stem from its capacity to inhibit TNFR complex IIa-driven apoptosis by limiting TNFR-mediated cGAS/STING activation and subsequent ZBP1 cytotoxicity[131].

The function of the ATG9A-ATG13-ATG101 complex as a regulator of STING signaling is further elaborated in Chapter 3.

2.2.4 ATG9A-ATG13-ATG101 COMPLEX

BioID proximity-labelling[132] experiments in HEK293T cells expressing a C-terminal BirA fusion of ATG9A (ATG9A-BirA), revealed that ATG9A interacts with ATG101 and ATG13 in a HORMA domain-dependent manner[133]. Structural and biochemical analyses show that ATG13 and ATG101 individually interact with the C-terminal domain of ATG9[17] and together form a complex with a 3:6:3 stoichiometry

(ATG9A:ATG13:ATG101). Assembly of this complex is rate-limited by a metamorphosis of the ATG13-ATG101 dimer, which exhibits substantially more rapid binding kinetics than either component alone.

Increasing evidence points to the ATG9A-ATG13-ATG101 complex as the central interaction hub for recruitment of all autophagy initiation subcomplexes. ATG2A interacts with this complex together with WIPI4, cooperatively enhancing both vesicle tethering and lipid transfer activities[122,134,135]. Lipid transfer by ATG2 is accelerated by the ATG9A-ATG13-ATG101 complex, establishing a positive feedback loop that amplifies early autophagosome membrane expansion[17].

Upon autophagy induction, ATG9A and ATG13 engage in close temporal and spatial interactions on ER extensions and omegasomes, catalyzing phagophore formation[111,133,136,137]. Notably, this interaction is independent of ULK1[16,17,51,133]. Interestingly, siRNA KD or KO of ULK1 leads to ATG9A dispersal from Golgi to peripheral sites[82,101].

The ATG9A-ATG13-ATG101 complex functions as an independent autophagy initiation node that coordinates with the AIC to supply the membrane dynamics needed for phagophore nucleation.

2.3 RESULTS

2.3.1 DELETION OF AIC COMPONENTS YIELDS DISTINCT GENERAL AUTOPHAGY AND SELECTIVE AUTOPHAGY DEFECTS.

The AIC comprises ULK1, FIP200, ATG13, and ATG101 (**Figure 1A**). We used CRISPR-Cas9 editing to generate KO HeLa S3 cell lines for each component and validated deletion by western blot (**Figure 1B**). Loss of ATG13 or ATG101 reciprocally destabilized each other, as previously observed[14,43]. ATG101 KO increased FIP200, whereas ATG13 KO uniquely reduced ULK1 (**Figure 1B-C**). All KOs impaired autophagy as indicated by altered NBR1, p62/SQSTM1, and LC3B-II/I ratios detected by western blot (**Figure 1D-E**)[138].

FIP200 and ATG101 KO caused the strongest p62 and NBR1 accumulation, followed by ATG13 KO. ULK1/2 double KO (DKO) showed minimal effects. All KOs demonstrated reduced LC3B-II/I ratio, consistent with impaired autophagy flux. Notably, ATG101 KO displayed greater accumulation of LC3B-II than ATG13 KO. To directly assess autophagy flux, we used the quantitative HaloTag-LC3B processing assay under basal conditions and with mTOR inhibition[139]. HaloTag is protease-resistant; upon delivery to autolysosomes, HaloTag-LC3B is cleaved generating a stable "processed HaloTag" band. The ratio of the lower "processed" HaloTag band divided by the upper HaloTag-LC3B band provides an internally controlled, quantitative readout of autophagy flux. All KO lines exhibited lower basal autophagy and Torin1-induced autophagy flux compared to WT. ATG101 and FIP200 KO demonstrated the strongest reduction in autophagy flux, followed by ATG13 KO and ULK1/2 DKO (**Figure 1F-G**). Interestingly, autophagy flux in the ULK1/2 DKO was sensitive to mTOR inhibition, indicating that mTOR can suppress autophagy independently of ULK1/2.

We next investigated the role of each AIC component on PINK1/Parkin selective mitophagy. We stably expressed Parkin and the mitochondrially targeted pH-sensitive fluorescent reporter mito-Keima (mtKeima) in all KO lines[140]. mtKeima excitation shifts from ~ 405 nm (neutral) to ~555 nm (acidic) during mitophagy; we quantified the 555/405 (acidic/neutral) ratio. Mitophagy was induced by oligomycin A/antimycin A (O/A) plus the pan-caspase inhibitor Q-VD-OPh (QVD). FIP200 KO nearly abolished mitophagy, whereas ATG101 and ATG13 KO, and to a lesser extent ULK1/2 DKO, led to partial mitophagy impairment (**Figure 1H-I**).

These results indicate that each component of the AIC is important for autophagy. Strikingly, ATG101 KO caused more severe defects than ATG13 KO in both general and selective autophagy, suggesting ATG101 function beyond ATG13 stabilization.

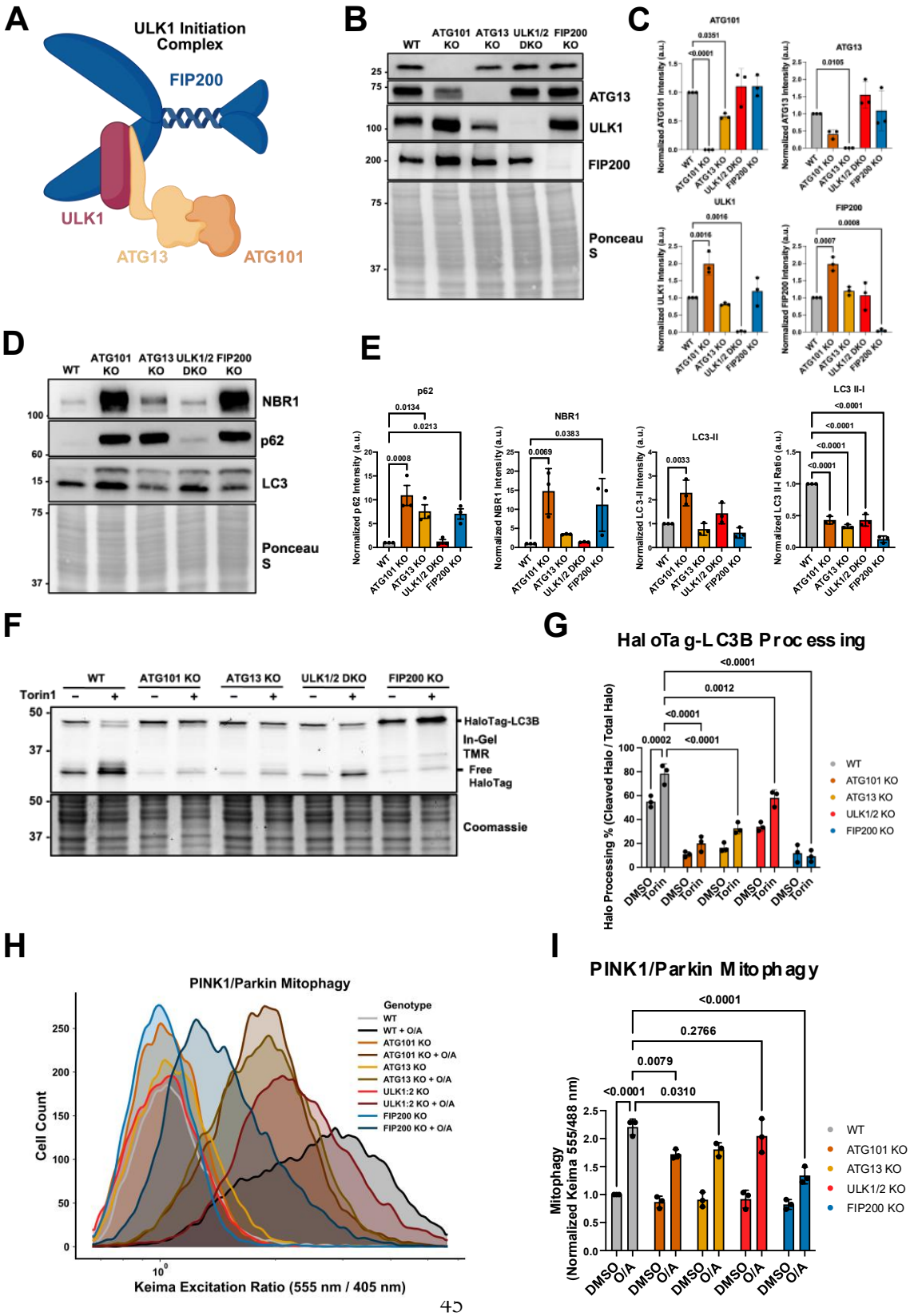
A
ULK1 Initiation Complex
FIP200
ULK1
ATG13
ATG101
B
WT
ATG101 KO
ATG13 KO
ULK1/2 DKO
FIP200 KO
ATG13
ULK1
FIP200
Ponceau S
C
ATG101
ATG13
ULK1
FIP200
Normalized ATG101 Intensity (a.u.)
Normalized ATG13 Intensity (a.u.)
Normalized ULK1 Intensity (a.u.)
Normalized FIP200 Intensity (a.u.)
D
NBR1
p62
LC3
Ponceau S
E
p62
NBR1
LC3-II
LC3 II-I
Normalized p62 Intensity (a.u.)
Normalized NBR1 Intensity (a.u.)
Normalized LC3-II Intensity (a.u.)
Normalized LC3 II-I Ratio (a.u.)
F
Torin1
HaloTag-LC3B
In-Gel TMR
Free HaloTag
Coomassie
G
HaloTag-LC3B Processing
Halo Processing % (Cleaved Halo / Total Halo)
DMSO
Torin
H
PINK1/Parkin Mitophagy
Genotype
WT
WT + O/A
ATG101 KO
ATG101 KO + O/A
ATG13 KO
ATG13 KO + O/A
ULK1:2 KO
ULK1:2 KO + O/A
FIP200 KO
FIP200 KO + O/A
Cell Count
Keima Excitation Ratio (555 nm / 405 nm)
I
PINK1/Parkin Mitophagy
Mitophagy (Normalized Keima 555/488 nm)
DMSO
O/A

Figure 1. Deletion of each member of the Autophagy Initiation Complex (AIC) leads to distinct defects in general and selective autophagy. ***(A)*** *Cartoon diagram of the AIC based on structural studies.* ***(B)*** *Western blot of HeLa S3 cell lines with CRISPR mediated KO of each AIC member. Ponceau S stain is the loading control.* ***(C)*** *Densitometry quantification of western blots in (B) to determine the effect of each member on the three other proteins of the complex. All expression data are first normalized by Ponceau S stain and normalized to the WT HeLa S3. Here and elsewhere: WT (grey), ATG101 KO (orange), ATG13 KO (yellow), ULK1/2 KO (red), and FIP200 KO (blue).* ***(D)*** *Western blot of autophagy markers NBR1, p62, and LC3B in AIC KO lines.* ***(E)*** *Densitometry quantification of western blots in (D).* ***(F)*** *In-gel TMR fluorescence of a HaloTag-LC3 processing assay for each of the WT and AIC KO lines with or without Torin1 (250 nM) for 16 hours. The upper band is composed of HaloTag-LC3 both unlipidated (LC3B-I) and the faster-migrating lipidated band (LC3B-II). The lower set of bands is HaloTag alone cleaved from LC3B within the autophagolysosomes. Coomassie stain is the loading control.* ***(G)*** *Quantification of HaloTag-LC3B processing assay shown in (F). For each condition, the intensity of the lower band (processed) is divided by the intensity of the total HaloTag intensity (lower and upper band combined) to determine the % of HaloTag processed.* ***(H)*** *Representative flow cytometry histograms of HeLa cells expressing Flag-Parkin and mtKeima treated with DMSO (light) or O/A (10 μM/ 5 μM) (dark). All cells were treated with 10 μM QVD. The x-axis is the ratio of Keima emission stimulated with 555 nm laser (pH 5) over the emission stimulated with the 405 nm laser (pH 7.4).* ***(I)*** *Quantification of the median mtKeima 555/405 nm ratio shown in (H) across experiments. In each biological replicate, the mtKeima ratio is normalized to WT DMSO. Western blots shown are representative of at least three biological replicates. Data are presented as mean ± SD across at least N = 3 biological replicates; (C, E: one-way ANOVA; G, I: two-way ANOVA).*

2.3.2 PROTEOMIC ANALYSIS OF AIC KO LINES REVEALS SUBUNIT-SPECIFIC CELLULAR SIGNATURES.

To identify cellular processes uniquely regulated by individual AIC components, we performed DIA-based quantitative proteomics on whole-cell lysates from all four KO lines and WT HeLa controls. Differentially abundant proteins were subjected to GO biological process enrichment analysis using clusterProfiler (**Figure 2A-B**).

GO terms related to autophagy were enriched across multiple KO lines in the upregulated protein sets, consistent with accumulation of autophagy cargo receptors and substrates observed in Figure 1D. Selective autophagy and mitophagy were among the most significantly enriched terms in ATG101 KO and FIP200 KO, in agreement with mtKeima experiments (**Figure 1H**). Autophagosome assembly and macroautophagy were particularly prominent in the ATG101 KO upregulated set, consistent with impaired autophagy flux.

The four AIC KO lines diverged substantially in their non-autophagy GO signatures, supporting subunit-specific functions. Innate immune signaling terms were specifically enriched in ATG101 KO and ATG13 KO (**Figure 2A**). These enrichments were not observed in ULK1/2 DKO or FIP200 KO, suggesting that this signature may reflect a function specific to the ATG13-ATG101 module. These observations motivated the further investigation of ATG101 and ATG13 in innate immune regulation (**Section 2.3.3**).

Analysis of proteins decreased in abundance revealed additional subunit-specific signatures (**Figure 2B**). ATG101 KO cells showed enrichment for post-Golgi vesicle-mediated transport and glucose metabolic processes. ATG13 KO cells showed enrichment of unfolded protein response-related terms, including regulation of IRE1-mediated ER stress. This enrichment was not observed for other AIC KO lines, suggesting a potential role for ATG13 in ER homeostasis.

FIP200 KO exhibited a distinct downregulated proteomic signature, with enrichment of protein phosphorylation, extracellular matrix organization, and cell motility-related processes. These terms suggest that FIP200 loss impacts kinase signaling networks and

adhesion pathways, consistent with its prior identification as a focal adhesion kinase interacting protein. FIP200 KO upregulated proteins showed enrichment for DNA damage terms alongside autophagy pathways. These observations motivated further analysis of FIP200-specific interactions (**Chapter 4**).

ULK1/2 DKO exhibited comparatively modest proteomic changes. Downregulated proteins were enriched for transport and exocytosis-related processes, while upregulated proteins were related to negative regulation of TORC1 signaling. Together, these data confirm a broad role for ULK1 in metabolic sensing rather than a highly discrete cellular pathway.

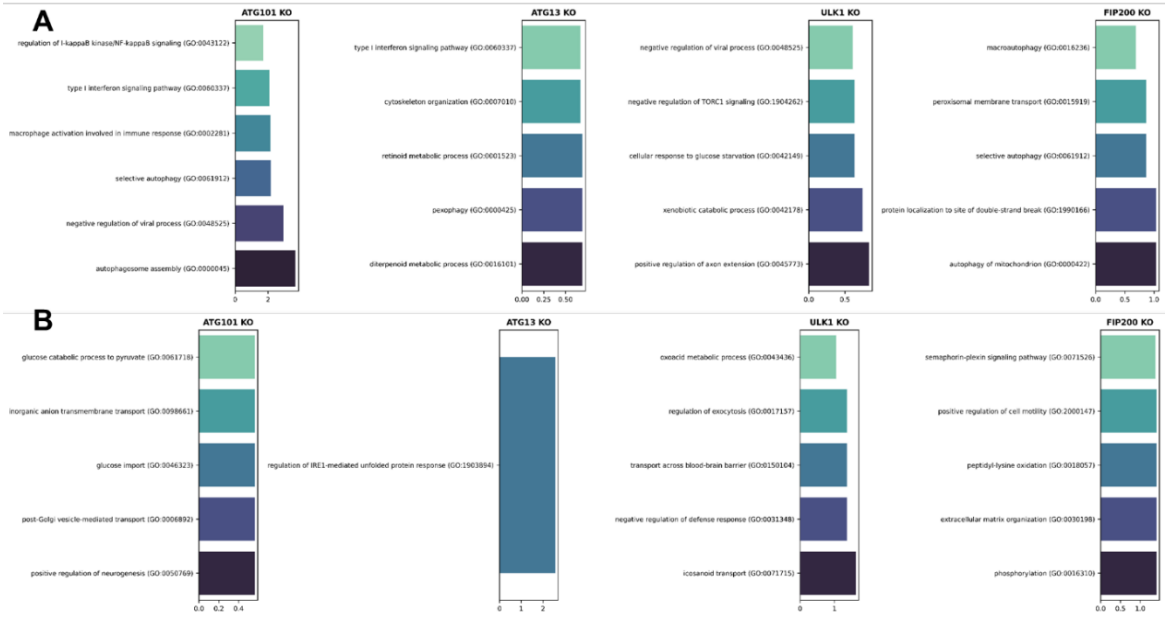

Figure 2. Quantitative proteomics of autophagy initiation complex (AIC) KO lines reveals subunit-specific cellular signatures. *DIA-based quantitative proteomics was performed on whole-cell lysates from ATG101, ATG13, ULK1/2, and FIP200 KO HeLa S3 cells and WT controls. Differentially abundant proteins were subjected to GO biological process enrichment analysis. Bar plots show the top enriched GO terms for each KO line, ranked by --log10(FDR-adjusted P-value).* ***(A)*** *Upregulated GO terms per*

KO line relative to WT. ***(B)*** *Downregulated GO terms per KO line relative to WT. Data represent N = 4 biological replicates per genotype.*

2.3.3 ATG13 AND ATG101 SUPPRESS A CONSTITUTIVE INNATE IMMUNE SIGNALING AXIS

DIA-MS proteomic profiling of AIC KO lines revealed an unexpected enrichment of innate immune GO terms specifically in ATG101 and ATG13 KO proteomes, but not in FIP200 or ULK1/2 KO. Principal component analysis (PCA) confirmed separation of each KO line, indicating distinct alterations to the proteome (**Figure 3A**). Differential protein expression analysis demonstrated varying levels of autophagy receptor accumulation in all four KO lines, consistent with western blot results (**Figure 3C**). Unexpectedly, ATG101 KO showed upregulation of terms related to anti-viral processes (**Figure 3D**). Among the most altered proteins were interferon-stimulated genes (ISG) including interferon-induced proteins with tetratricopeptide repeats 1/2/3 (IFIT1, IFIT2, IFIT3), oligoadenylate synthase-like (OASL) protein, and ISG15 (**Figure 3B-E**). Type I ISGs were elevated in ATG13, though to a lesser extent than ATG101 KO. A modest elevation was also observed in ULK1/2 DKO cells, though this did not reach significance in GO enrichment analysis (**Figure 3F-G**). Despite obvious defects in autophagy, FIP200 KO displayed no ISG activation, consistent with prior proteomics analyses of FIP200 KO cells[141]. We also observed changes in the parallel NF-κB-related genes in ATG101 and ATG13 KO cells, but not in ULK1/2 DKO or FIP200 KO (**Figure 3E**). Upregulation of ISGs in ATG101 KO and ATG13 KO were confirmed by western blot (**Figure 3F-G**).

Next, we confirmed that the Type I IFN response was consistently upregulated across multiple ATG101 and ATG13 KO clones (**Figure S1A-B**). We generated ATG101 rescue cells by adding N- or C-terminal GFP-tagged ATG101 to the KO. Addition of C-terminal tagged ATG101-GFP rescued autophagy defects and suppression of the IFN response (**Figure 3H**). Addition of N-terminal tagged GFP-ATG13 rescued accumulation of the autophagy marker p62 and the IFN response (**Figure 3I**).

To determine whether this phenotype was a general cellular pathway, we generated ATG101 KOs in K562 (leukemia) and THP-1 (monocyte) lines, where ISG levels and autophagy markers p62/NBR1 were similarly increased (**Figure 3J, Figure 4A**). MCF-7 breast cancer cells lacked detectable ATG101 expression and exhibited basal induction of ISGs and autophagy receptors higher than WT HeLa (**Figure 3J**). This was consistent in two independently sourced MCF-7 clones (**Figure 4B**). Ectopic expression of ATG101-GFP in MCF-7 cells suppressed ISG signaling and autophagy receptor levels (**Figure 4C-D**).

To directly test whether ATG101's role in ISG suppression requires FIP200 or functional autophagy, we generated ATG101/FIP200 DKO cells. Loss of ATG101 in FIP200 KO cells elevated ISG levels without additional accumulation of p62 (**Figure 4E**), demonstrating that ATG101 suppresses ISG expression through a pathway that is fully independent of FIP200 and of canonical autophagic flux. Consistent with this, re-expression of ATG101-GFP in ATG101/FIP200 DKO cells restored IFIT3 to near-WT levels but left p62 accumulation unremedied (**Figure 4F**), confirming that ATG101's ISG-suppressive function is mechanistically separable from its role in autophagy.

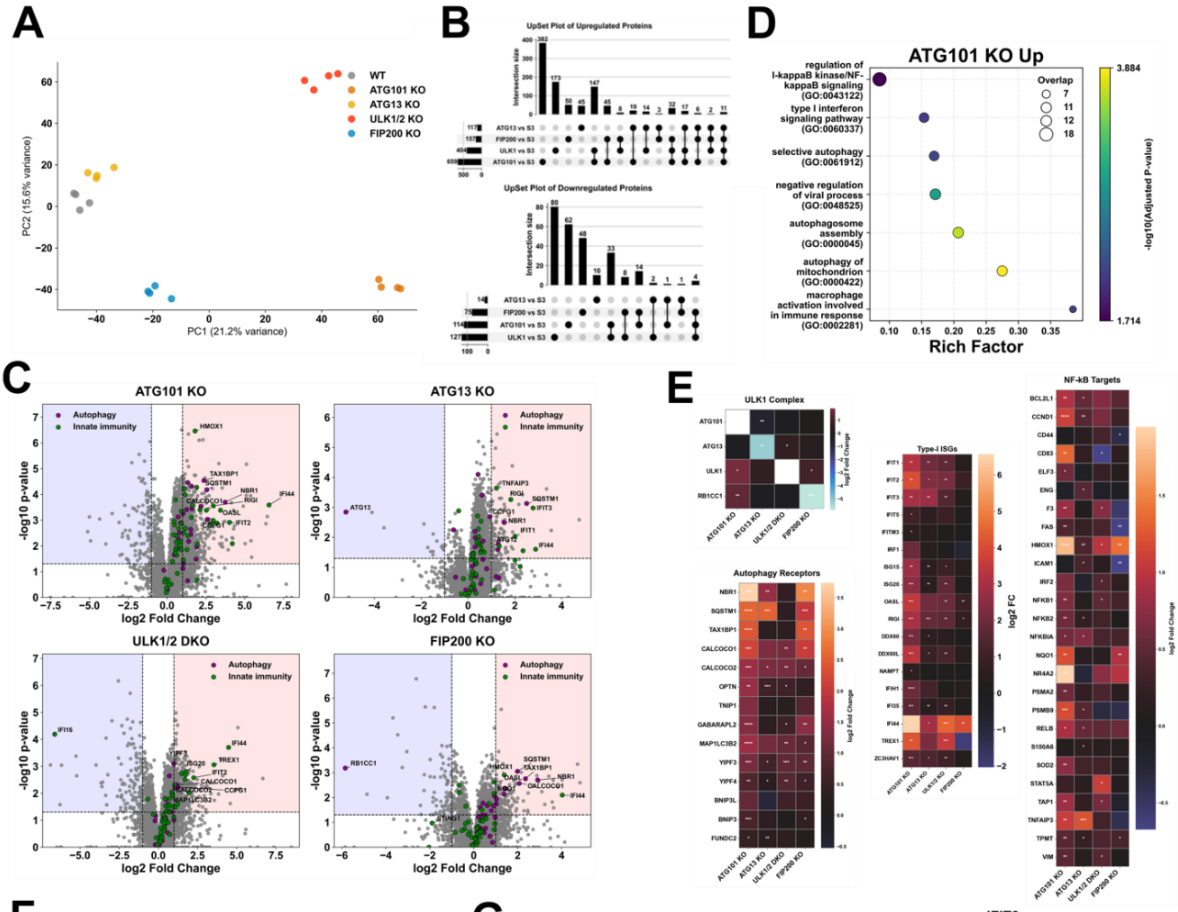
A
WT
ATG101 KO
ATG13 KO
ULK1/2 KO
FIP200 KO
PC2 (15.6% variance)
PC1 (21.2% variance)
B
UpSet Plot of Upregulated Proteins
Intersection size
ATG13 vs S3
FIP200 vs S3
ULK1 vs S3
ATG101 vs S3
UpSet Plot of Downregulated Proteins
D
ATG101 KO Up
regulation of I-kappaB kinase/NF-kappaB signaling (GO:0043122)
type I interferon signaling pathway (GO:0060337)
selective autophagy (GO:0061912)
negative regulation of viral process (GO:0048525)
autophagosome assembly (GO:0000045)
autophagy of mitochondrion (GO:0000422)
macrophage activation involved in immune response (GO:0002281)
Overlap
-log10(Adjusted P-value)
Rich Factor
C
ATG101 KO
ATG13 KO
ULK1/2 DKO
FIP200 KO
Autophagy
Innate immunity
-log10 p-value
log2 Fold Change
E
ULK1 Complex
Autophagy Receptors
Type-I ISGs
NF-kB Targets
log2 FC
F
WT
ATG101 KO
ATG13 KO
ULK1/2 DKO
FIP200 KO
IFIT1
IFIT2
IFIT3
ISG15
Ponceau S
G
IFIT1
IFIT2
IFIT3
0.0033
<0.0001
0.0002
0.0014
<0.0001
Normalized IFIT1 Intensity (a.u.)
Normalized IFIT2 Intensity (a.u.)
Normalized IFIT3 Intensity (a.u.)
H
ATG101 Rescue
ATG13 Rescue
+ ATG101-GFP
+ GFP-ATG13
ATG101
ATG13
IFIT3
p62
Ponceau S
I
ATG101 Rescue
ATG13 Rescue
J
ATG101 KO Across Cell Lines
S3 HeLa
MCF-7
K562
THP-1
ATG101 gRNA
ATG101
IFIT2
IFIT3
p62
p97
Ponceau S

Figure 3. Label-free data-independent acquisition (DIA) proteomics identifies ATG101 and ATG13 as suppressors of a constitutive innate immune signaling axis. ***(A)*** *PCA plot of proteomics data collected for four biological replicates of each AIC KO and WT HeLa. Here and elsewhere: WT (grey), ATG101 KO (orange), ATG13 KO (yellow), ULK1/2 KO (red), and FIP200 KO (blue).* ***(B)*** *UpSet plot detailing the overlap of upregulated (top) and downregulated (bottom) proteins across the AIC KOs compared to WT cells. The total number of differentially expressed proteins is given as the horizontal bar plot to the left of each upset plot.* ***(C)*** *Proteomic volcano plots for each AIC KO cell line compared to WT. Significantly upregulated proteins are shown with a red shaded region, with significantly downregulated proteins shown in the blue shaded region. Top differentially expressed proteins are labeled by gene name. Select proteins related to autophagy are highlighted in purple with innate immune related proteins highlighted in green.* ***(D)*** *Bubble plot detailing differentially upregulated GO term pathways altered in ATG101 KO cells.* ***(E)*** *Heatmap of protein expression differences and significant for select autophagy and innate immune pathways.* ***(F)*** *Western blot validation of interferon-stimulated gene products in each AIC KO line.* ***(G)*** *Densitometry quantification of western blots in (F).* ***(H)*** *Western blot of ATG101 and ATG13 KO lines rescued with ATG101-GFP or GFP-ATG13.* ***(I)*** *Densitometry quantification of western blots in (H).* ***(J)*** *Western blot of autophagy and interferon related proteins in parent and pooled gRNA KOs of ATG101 across various cancer cell lines. Here, housekeeping genes p97 and GAPDH, as well as Ponceau stain is used to assess protein loading across different cell lines. Western blots shown are representative of at least three biological replicates. Data are presented as mean ± SD across at least N = 3 biological replicates; *P ≤ 0.05, **P ≤ 0.01, ***P ≤ 0.001, ****P ≤ 0.0001 (G, I: one-way ANOVA). All expression data are first normalized by protein loading (Ponceau S Stain) and then to the WT line set at 1.*

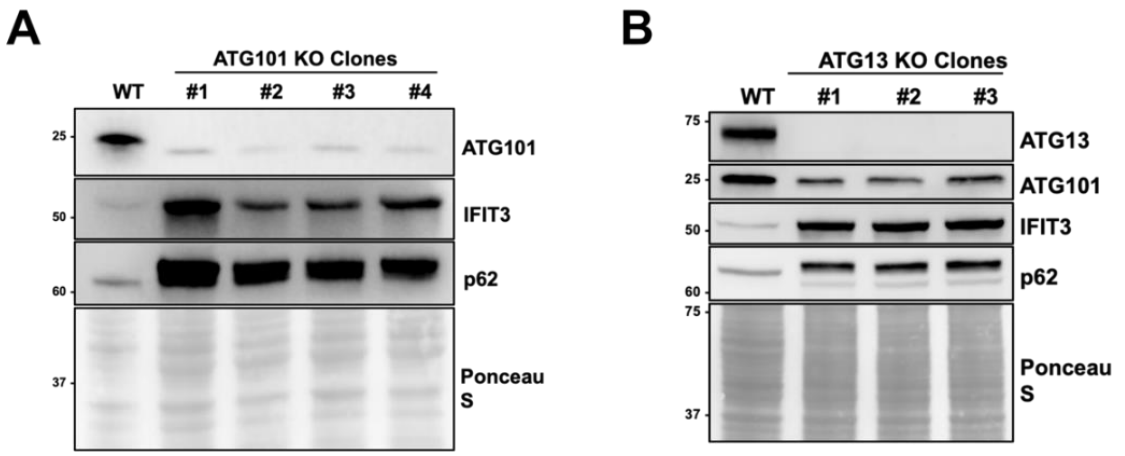

Figure S1. Loss of ATG101 and ATG13 leads to a robust ISG expression. ***(A)*** *Western blot of WT HeLa and three separate ATG101 KO clonal lines. Ponceau stain is used as a loading control.* ***(B)*** *Western blot of WT HeLa and three separate ATG13 KO clonal lines. Ponceau stain is used as a loading control.*

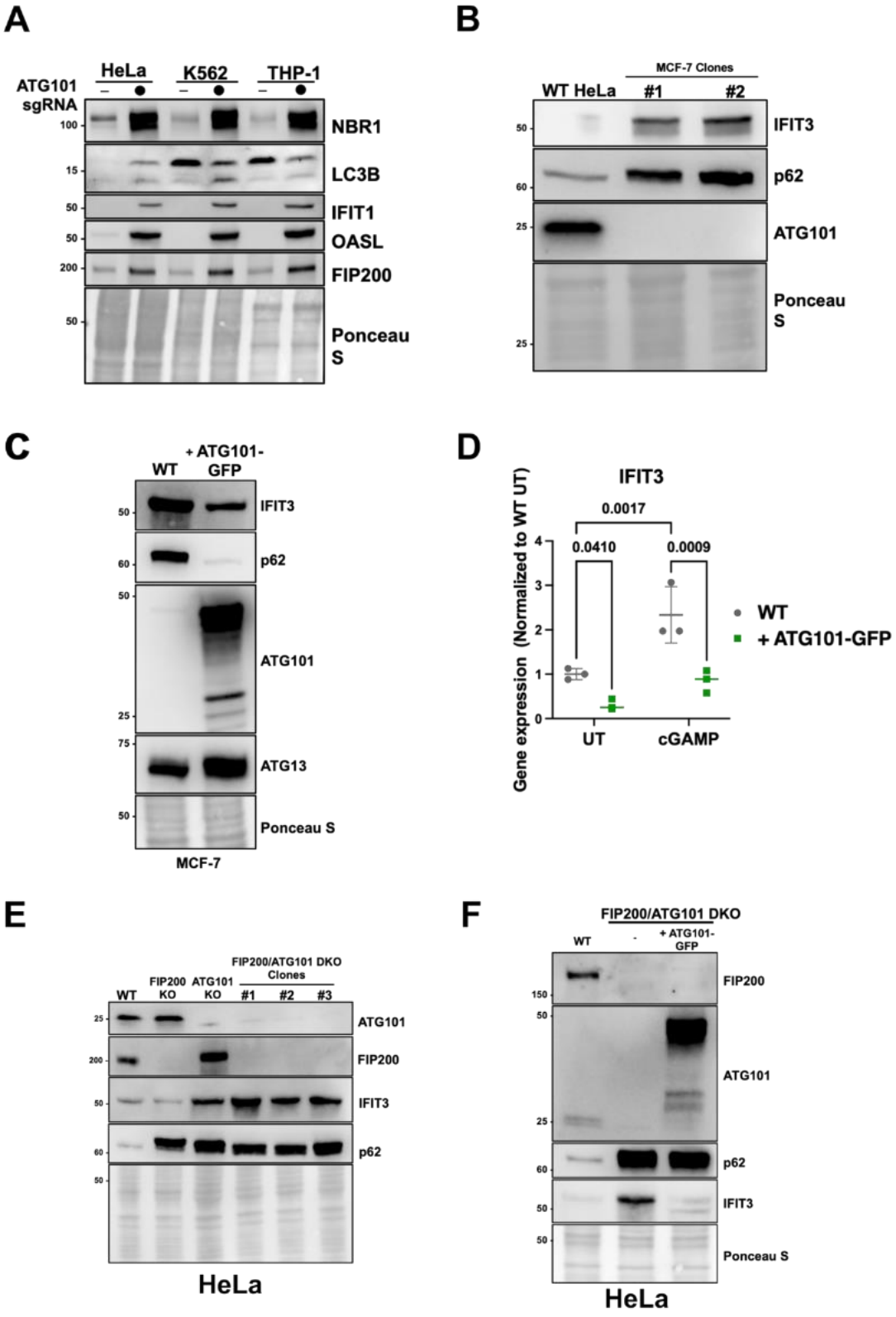
A
HeLa
K562
THP-1
ATG101 sgRNA
NBR1
LC3B
IFIT1
OASL
FIP200
Ponceau S
B
MCF-7 Clones
WT HeLa
#1
#2
IFIT3
p62
ATG101
Ponceau S
C
+ ATG101-GFP
WT
IFIT3
p62
ATG101
ATG13
Ponceau S
MCF-7
D
IFIT3
0.0017
0.0410
0.0009
Gene expression (Normalized to WT UT)
WT
+ ATG101-GFP
UT
cGAMP
E
FIP200/ATG101 DKO Clones
WT
FIP200 KO
ATG101 KO
#1
#2
#3
ATG101
FIP200
IFIT3
p62
HeLa
F
FIP200/ATG101 DKO
WT
-
+ ATG101-GFP
FIP200
ATG101
p62
IFIT3
Ponceau S
HeLa

Figure 4. Loss of ATG101 induces ISG expression across diverse cell types and in FIP200 KO cells. (A) *Western blots of WT and ATG101 KO pooled cell lines across multiple cell types. Loss of ATG101 leads to accumulation of p62 and induction of interferon-stimulated gene (ISG) products.* ***(B)*** *Western blots of two independent MCF-7 cell lines obtained from external sources showing loss of detectable ATG101 and accumulation of p62 and IFIT3.* ***(C)*** *Western blot of MCF-7 cells expressing ATG101–GFP demonstrating rescue of p62 and IFIT3 accumulation.* ***(D)*** *RT-qPCR analysis of ISG expression in indicated genotypes. Gene expression is first normalized to actin and then to WT control cells. N = 3 biological replicates.* ***(E)*** *Western blot of WT, FIP200 KO, ATG101 KO, and FIP200/ATG101 DKO clones generated in the FIP200 KO background. Loss of ATG101 in FIP200 KO cells induces IFIT3 expression but does not further increase p62 accumulation.* ***(F)*** *Western blot of HeLa cells confirming induction of ISG products upon ATG101 loss. Data are presented as mean ± SD across at least N = 3 biological replicates; *P ≤ 0.05, **P ≤ 0.01, ***P ≤ 0.001 (D: one-way ANOVA). All expression data are normalized by protein loading (Ponceau S stain) and then normalized to WT.*

2.3.4 THE ATG9A-ATG13-ATG101 COMPLEX SUPPRESSES BASAL TYPE I IFN SIGNALING

Recent evidence demonstrated that the ATG9A-ATG13-ATG101 subcomplex can exist independent of FIP200, and is required for autophagy[51,133]. ATG9A has been implicated in STING signaling, and its loss parallels elevated Type I IFN signaling observed in ATG101 and ATG13 KO cells. Structural studies have characterized the assembly of this subcomplex, identifying critical regions and residues for each interaction (**Figure 5A**).

To define the ATG101 domains and interactors required for regulating Type I IFN signaling, we tested whether ATG101 mutant re-expression could rescue the ISG phenotype in ATG101 KO cells. ATG101 KO cells were reconstituted with wild-type ATG101 or previously characterized point mutants: ATG13-binding mutant

(L30R/H31R), ATG9A-binding mutant (Y45D), and tryptophan-proline-phenylalanine "WPF finger" triple mutant, which disrupts downstream autophagy interactions or membrane binding[13,16,51,53]. Autophagy was assessed by LC3B-II/I ratio and p62 levels, while ISG expression was analyzed by IFIT3 expression (**Figure 5B,D**).

ATG101-Y45D mutant, ATG9A-binding defect, was unable to restore autophagy or rescue ISG expression. The L30R/H31R ATG13-binding mutant showed no rescue of autophagy and a modest reduction in ISG expression. The WPF finger mutant did not restore autophagy, however it completely rescued ISG expression. These data indicate that ATG101 interaction with ATG9A, and to a lesser extent ATG13, is critical for suppressing a constitutive innate immune signaling axis. The WPF domain appears critical for autophagy, but dispensable to ISG suppression. Consistent findings were obtained with an ATG13 mutant lacking the C-terminal FIP200 binding domain (ΔFBD). ATG13 ΔFBD was able to rescue the ISG defect, but not autophagy (**Figure 5C,E**). These results demonstrate that the ATG9A-ATG13-ATG101 complex, but not FIP200 or canonical autophagy, is required for suppressing Type I IFN signaling.

2.3.5 ATG9A KO PHENOCOPIES ATG13 AND ATG101 KO

We next generated an ATG9A KO HeLa line and found, using DIA-MS proteomics, that they also exhibited strong basal ISG expression (**Figure 5F**). Basal ISG induction and autophagy impairment were comparable to ATG101 and ATG13 KO (**Figure 5G**). ATG9A KO cells exhibited elevated ISG induction following cGAMP treatment, similar to the previously reported elevated ISG response to dsDNA (**Figure 5H**). The kinetics of this sustained response are examined in Chapter 3.

ATG9A binds to the ATG13-ATG101 HORMA domain dimer via a short sequence on its C-terminus, the so-called HORMA Domain Interacting Region (HDIR). We found that defects in ISG expression and autophagy in the ATG9A KO line could be rescued with N-terminally tagged GFP-ATG9A, but not with an ATG9A ΔHDIR mutant (**Figure 5I**). Reciprocal results with ATG9A and ATG101 rescue indicate that the interaction

between ATG9A and ATG101/ATG13 are critical for both autophagy and suppression of Type I IFN signaling.

2.3.6 ATG9A-ATG13-ATG101 ALTER IFN SIGNALING IN IMMUNE CELLS

To determine whether type I IFN dynamics were altered in an immune-relevant context, we analyzed IFN signaling in a THP-1 monocyte line. While it was possible to create pooled THP-1 ATG101 KO samples, we were unable to culture single-cell clones. Instead, we utilized doxycycline-inducible knockdowns (KD) of ATG101, ATG9A, and ATG13, which demonstrated robust KD, basal IFIT3 induction, and p62 accumulation (**Figure 5J**). We performed DIA MS proteomics in the KD cell lines compared to the NT-shRNA (**Figure S2A-B**). Differential expression analysis revealed the widespread alteration of immune related proteins in all ATG9A subcomplex compared to NT-shRNA control (**Figure 5K**, **Figure S2C).** Induction of Type-I ISG and NF-κB response was robust (**Figure 5L**, **Figure S2D**). Gene set enrichment analysis (GSEA) demonstrated strong induction of the Interferon alpha and inflammatory response across each KD (**Figure S2E**). These data indicate that ATG101, ATG9A, and ATG13 are critical for suppression of an active inflammatory response within a bona fide immune cell context.

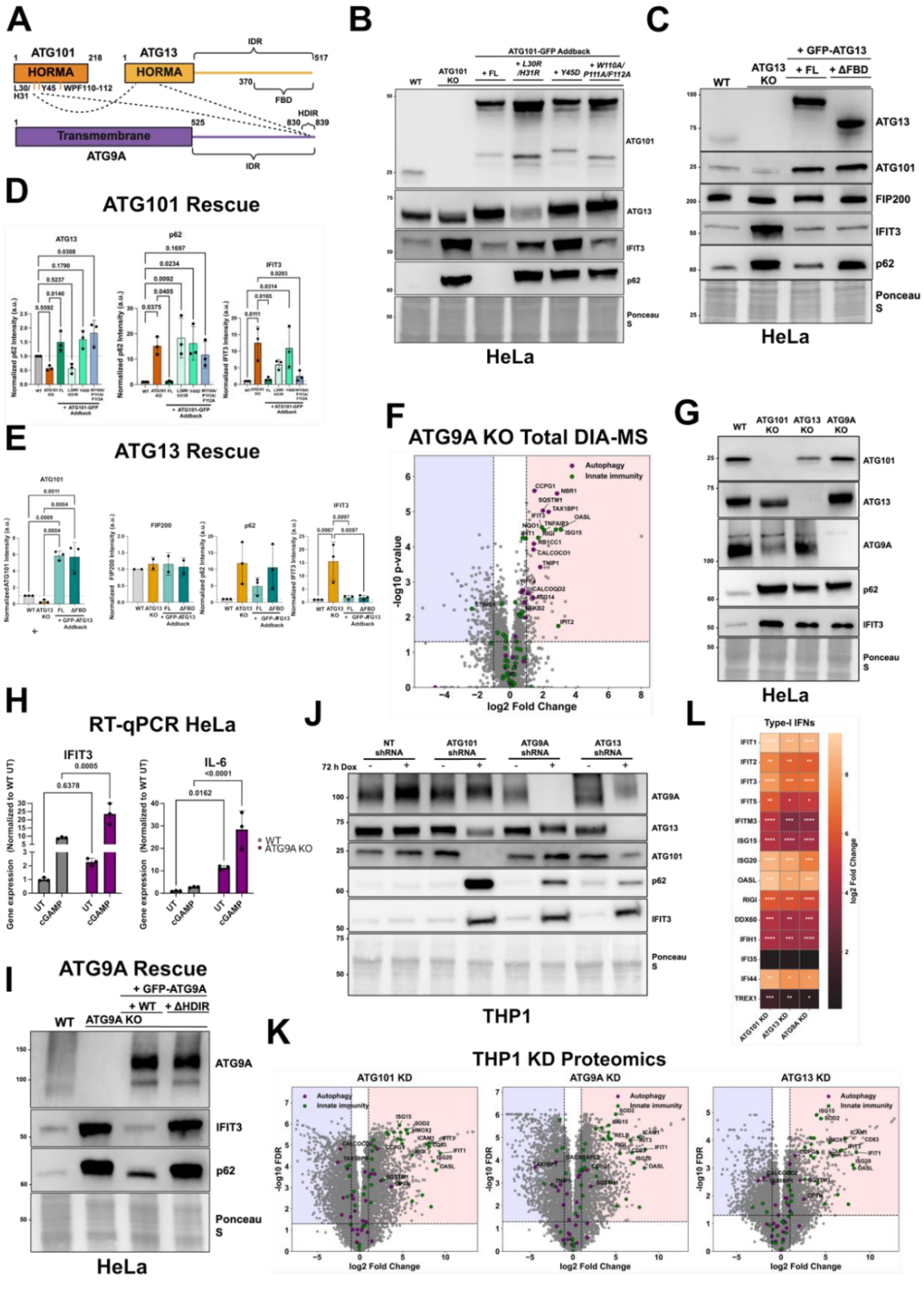
A
ATG101
HORMA
ATG13
HORMA
IDR
FBD
HDIR
Transmembrane
ATG9A
B
ATG101-GFP Addback
WT
ATG101 KO
+ FL
+ L30R /H31R
+ Y45D
+ W110A/ P111A/F112A
ATG101
ATG13
IFIT3
p62
Ponceau S
HeLa
C
+ GFP-ATG13
WT
ATG13 KO
+ FL
+ ΔFBD
ATG13
ATG101
FIP200
IFIT3
p62
Ponceau S
HeLa
D
ATG101 Rescue
ATG13
p62
IFIT3
+ ATG101-GFP Addback
E
ATG13 Rescue
ATG101
FIP200
p62
IFIT3
+ GFP-ATG13 Addback
F
ATG9A KO Total DIA-MS
Autophagy
Innate immunity
-log10 p-value
log2 Fold Change
G
WT
ATG101 KO
ATG13 KO
ATG9A KO
ATG101
ATG13
ATG9A
p62
IFIT3
Ponceau S
HeLa
H
RT-qPCR HeLa
IFIT3
IL-6
Gene expression (Normalized to WT UT)
UT
cGAMP
WT
ATG9A KO
I
ATG9A Rescue
+ GFP-ATG9A
+ WT
+ ΔHDIR
WT
ATG9A KO
ATG9A
IFIT3
p62
Ponceau S
HeLa
J
NT shRNA
ATG101 shRNA
ATG9A shRNA
ATG13 shRNA
72 h Dox
ATG9A
ATG13
ATG101
p62
IFIT3
Ponceau S
THP1
K
THP1 KD Proteomics
ATG101 KD
ATG9A KD
ATG13 KD
Autophagy
Innate immunity
-log10 FDR
log2 Fold Change
L
Type-I IFNs
IFIT1
IFIT2
IFIT3
IFIT5
IFITM3
ISG15
ISG20
OASL
RIGI
DDX60
IFIH1
IFI35
IFI44
TREX1
log2 Fold Change
ATG101 KD
ATG13 KD
ATG9A KD

Figure 5. The ATG9A-ATG13-ATG101 subcomplex suppresses constitutive ISG expression. ***(A)*** *Diagram of the domains and interactions of ATG101 (orange), ATG13 (yellow), and ATG9A (purple). Dotted lines connecting segments indicate experimentally determined interaction sites. HORMA: Hop1p, Rev7p and MAD2 domain. IDR: Intrinsically Disordered Region. FBD: FIP200-Binding Domain. HDIR: HORMA-Domain Interacting Region.* ***(B)*** *Western blot of WT HeLa, ATG101 KO, and ATG101 KO lines stably expressing WT or mutated ATG101-GFP.* ***(C)*** *Western blot of WT HeLa, ATG13 KO, and ATG13 KO lines stably expressing WT or mutated GFP-ATG13.* ***(D)*** *Densitometry quantification of western blots shown in (B).* ***(E)*** *Densitometry quantification of western blots shown in (C).* ***(F)*** *Volcano plot DIA-MS analysis of ATG9A KO HeLa compared to WT. Significantly upregulated proteins are shaded in red, and significantly downregulated proteins are shaded in blue. Autophagy related proteins are indicated in purple, whereas innate immune related proteins are colored green.* ***(G)*** *Western blot of WT, ATG13, ATG101, and ATG9A KO HeLa lines for autophagy and ISGs.* ***(H)*** *RT-qPCR for STING activation marker genes in WT and ATG9A KO HeLa cells treated with or without cGAMP (60 μg/mL) for 8 hours. Gene expression is first normalized to actin and then to WT untreated cells. N = 3 biological replicates.* ***(I)*** *Western blot of WT HeLa, ATG9A KO, and ATG9A KO lines rescued with WT or HDIR mutant GFP-ATG9A.* ***(J)*** *Western blot of THP-1 cells stably expressing a dox-inducible nontargeting (NT) shRNA (shNT), or shRNA directed against ATG101 (shATG101), ATG9A (shATG9A), and ATG13 (shATG13). Cells were treated with or without dox for 72 hours and ATG101, ATG9A, and ATG13 as well as autophagy and IFN markers were analyzed via western blot.* ***(K)*** *Volcano plots of DIA MS proteomics analysis of shRNA expressing THP-1 cells treated with 72 hours dox treatment. Each gene KD is relative to the NT shRNA control. Autophagy related proteins are indicated in purple and immune related proteins are indicated in green.* ***(L)*** *Heatmap of Type-I ISGs in each of the THP-1 KD experiments. Data are presented as mean ± SD. *P ≤ 0.05, **P ≤ 0.01, ***P ≤ 0.001, ****P ≤ 0.0001 (H: two-way ANOVA; D, E: one-way ANOVA). Ponceau stain is used as a loading control.*

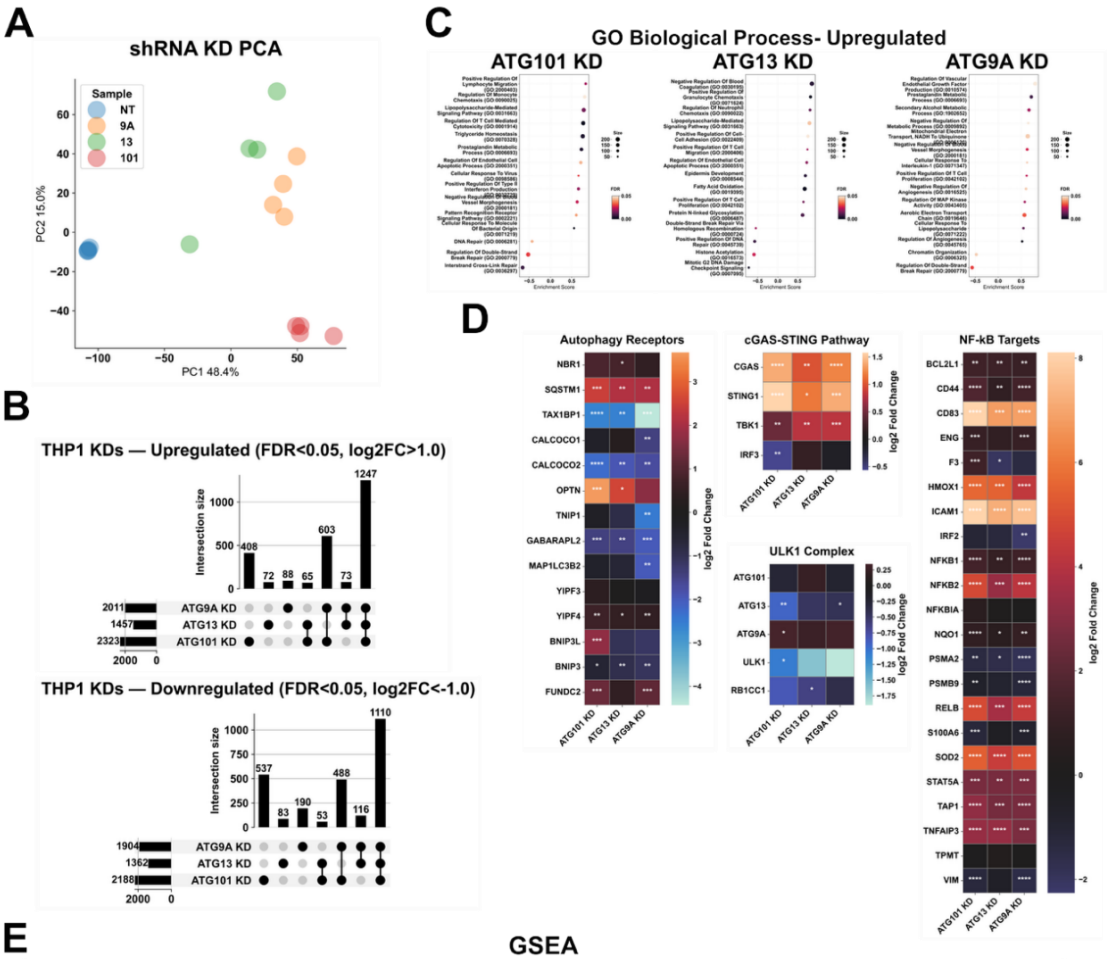
A
shRNA KD PCA
Sample
NT
9A
13
101
PC2 15.0%
PC1 48.4%
B
THP1 KDs — Upregulated (FDR<0.05, log2FC>1.0)
Intersection size
1247
603
408
72
88
65
73
2011
1457
2323
ATG9A KD
ATG13 KD
ATG101 KD
THP1 KDs — Downregulated (FDR<0.05, log2FC<-1.0)
1110
537
488
190
83
53
116
1904
1362
2188
C
GO Biological Process- Upregulated
ATG101 KD
ATG13 KD
ATG9A KD
D
Autophagy Receptors
NBR1
SQSTM1
TAX1BP1
CALCOCO1
CALCOCO2
OPTN
TNIP1
GABARAPL2
MAP1LC3B2
YIPF3
YIPF4
BNIP3L
BNIP3
FUNDC2
log2 Fold Change
cGAS-STING Pathway
CGAS
STING1
TBK1
IRF3
ULK1 Complex
ATG101
ATG13
ATG9A
ULK1
RB1CC1
NF-kB Targets
BCL2L1
CD44
CD83
ENG
F3
HMOX1
ICAM1
IRF2
NFKB1
NFKB2
NFKBIA
NQO1
PSMA2
PSMB9
RELB
S100A6
SOD2
STAT5A
TAP1
TNFAIP3
TPMT
VIM
E
GSEA
ATG101 shRNA
ATG9A shRNA
ATG13 shRNA
Interferon Alpha Response
Inflammatory Response
Interferon α
Inflammation
Enrichment Score
Ranked metric
Gene Rank
NES: 2.779
Pval: 0.000e+00
FDR: 0.000e+00
Zero score at 4360
NES: 2.324
Pval: 0.000e+00
FDR: 7.447e-05
Zero score at 4619
NES: 3.117
Pval: 0.000e+00
FDR: 0.000e+00
Zero score at 4763
NES: 2.726
Pval: 0.000e+00
FDR: 0.000e+00
Zero score at 4360
NES: 2.495
Pval: 0.000e+00
FDR: 0.000e+00
Zero score at 4619
NES: 2.753
Pval: 0.000e+00
FDR: 0.000e+00
Zero score at 4763

Figure S2. Label-free data-independent acquisition (DIA) proteomics of ATG9A, ATG13, ATG101 knockdowns in the THP-1 monocyte line. (A) *PCA plot of proteomics data collected for four biological replicates of each ATG9A subcomplex shRNA KD and NT shRNA.* ***(B)*** *UpSet plot detailing the overlap of upregulated (top) and downregulated (bottom) proteins across the ATG9A subcomplex member KDs compared to NT-shRNA treated cells. The total number of differentially expressed proteins is given as the horizontal bar plot to the left of each upset plot.* ***(C)*** *Bubble plot detailing differentially regulated GO term pathways altered in each ATG9A subcomplex KD.* ***(D)*** *Heatmap of protein expression differences and significant for select autophagy and innate immune pathways.* ***(E)*** *Gene-set enrichment analysis (GSEA) of the Interferon alpha and inflammatory response in each ATG9A subcomplex KD compared to NT-shRNA treated cells. *P ≤ 0.05, **P ≤ 0.01, ***P ≤ 0.001, ****P ≤ 0.0001.*

2.3.7 SUBCELLULAR LOCALIZATION OF ATG101 IS SPECIFICALLY ALTERED IN ATG9A KO CELLS

To assess how loss of ATG9A would affect ATG101, we imaged ATG101-GFP in AIC KO lines and ATG9A KO. In WT cells, ATG101 was distributed in the cytoplasm with a higher density localizing to perinuclear foci. Only ATG9A KO caused a clear redistribution of ATG101, resulting in large ATG101-GFP puncta (**Figure 6A-B**). These puncta were positive for Ub, p62, and the autophagy receptor TNIP1, indicating they are likely stalled autophagy initiation sites (**Figure 6C-D**). ATG101-GFP showed higher density at the perinuclear region in proximity to the Golgi body as indicated by the marker TGN46 (**Figure 6E**). ATG101 puncta in the ATG9A KO were not positive for TGN46 or the late endosomal marker RAB7A (**Figure 6E**).

These data indicate that ATG101 localization is selectively dependent on ATG9A but not on other AIC components. The accumulation of ATG101 at ubiquitin-, p62-, and TNIP1-positive puncta in ATG9A KO cells suggests that in the absence of ATG9A, ATG101 is retained at stalled autophagy initiation intermediates that cannot progress

through the normal membrane trafficking pathway. The absence of TGN46 and RAB7A staining indicates that these structures do not represent Golgi fragments or late endosomal compartments, but rather an intermediate compartment upstream of both. Together, these observations support a model in which ATG9A is required for the trafficking of ATG101-associated membranes and are consistent with a functional interdependence between these proteins beyond their shared role in canonical autophagy.

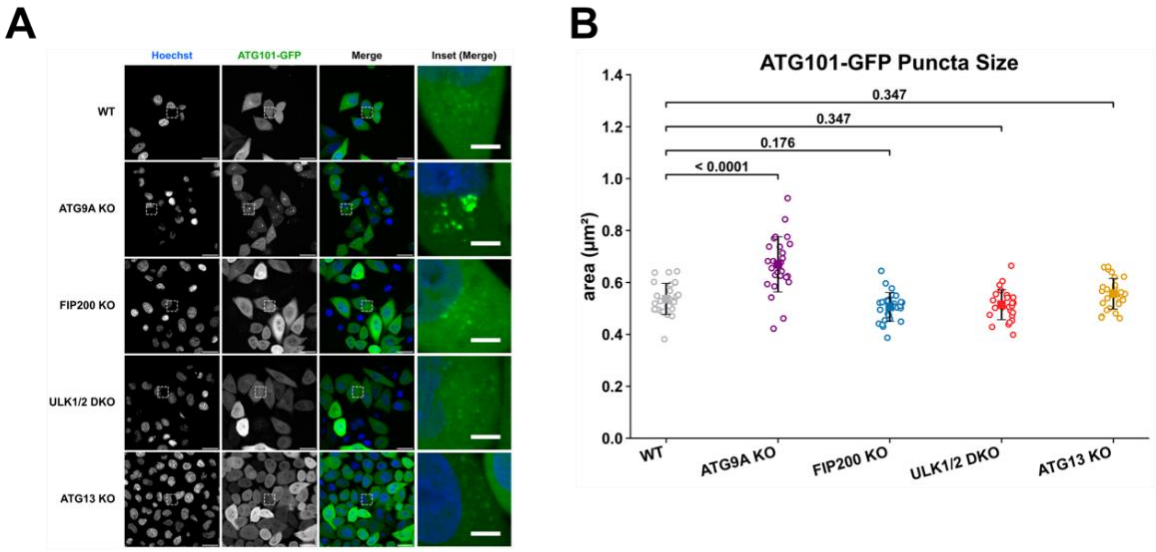
A
Hoechst
ATG101-GFP
Merge
Inset (Merge)
WT
ATG9A KO
FIP200 KO
ULK1/2 DKO
ATG13 KO
B
ATG101-GFP Puncta Size
area (µm²)
0.347
0.347
0.176
< 0.0001
WT
ATG9A KO
FIP200 KO
ULK1/2 DKO
ATG13 KO
C
p62
ATG101-GFP
DAPI
Merge
Insets
WT
ATG9A KO
D
TNIP1
Ubiquitin
ATG101-GFP
DAPI
Merge
Insets
WT
ATG9A KO
E
RAB7A
TGN46
ATG101-GFP
DAPI
Merge
Insets
WT
ATG9A KO

Figure 6. Loss of ATG9A results in ATG101 accumulation at stalled autophagic puncta. (A) *Representative microscopy images of WT and AIC component KO cells expressing ATG101-GFP. ATG101 is observed in the cytosol, nucleus, and accumulated at perinuclear foci. Main scale bar, 20 µm; inset, 4 µm.* ***(B)*** *Quantification of ATG101-GFP puncta size in (A). Data are represented as mean and standard deviation for 27 sites taken across three biological replicates. A one-way ANOVA was used to calculate significance.* ***(C-E)*** *Representative spinning disk microscopy of WT and ATG9A KO cells expressing ATG101-GFP and immunostained for various markers. Red channels are stained with Alexa Fluor568 conjugated secondary antibodies and Purple channels are stained with Alexa Fluor647 conjugated secondary antibodies. Main scale bar, 20 µm; inset, 4 µm.*

2.4 DISCUSSION

This chapter reveals a previously unrecognized function of the ATG9A–ATG13–ATG101 complex in suppressing basal innate immune signaling. Proteomic profiling of AIC KO cell lines showed that deletion of ATG101 or ATG13, but not FIP200 or ULK1/2, led to upregulation of type I interferon-stimulated genes (ISGs), including IFIT1, IFIT2, IFIT3, OASL, and ISG15. This ISG signature was observed across multiple cell lines, such as HeLa, K562, THP-1, and MCF-7, and was reversed by re-expression of ATG101 or ATG13, confirming that the immune activation is cell-autonomous and intrinsic to the ATG101–ATG13 submodule. The absence of this phenotype in FIP200 KO cells, despite impaired autophagy, provides evidence that ISG regulation is independent of canonical autophagy flux. The modest, non-significant ISG elevation in ULK1/2 DKO cells is consistent with the known role of ULK1 in phosphorylating STING to attenuate interferon signaling[52]. However, the substantially greater ISG phenotype observed in ATG101 and ATG13 KO cells indicates that the ATG9A-ATG13-ATG101 trafficking function, rather than ULK1 kinase activity toward STING, is the dominant mechanism suppressing basal ISG expression. Interestingly, ATG101 KO produced more severe defects than ATG13 KO in both autophagy and ISG

induction. For autophagy, the WPF finger likely accounts for this difference, as it mediates downstream interactions dispensable for ISG suppression. For ISG regulation, a plausible explanation is that ATG101 retains partial ATG9A binding independently of ATG13, as ATG101 can homodimerize and engage the ATG9A HDIR motif[17]. In this model, ATG13 KO cells would retain ATG101-ATG9A function sufficient to partially suppress STING signaling, whereas ATG101 KO eliminates this activity entirely.

Mutagenesis experiments demonstrated that the interaction between ATG9A, ATG13, and ATG101 is essential for this regulatory function. The ATG101 Y45D mutation, which disrupts ATG9A binding, abolished ISG rescue, whereas the WPF finger mutant, which selectively impairs autophagy while preserving ATG9A binding, fully restored ISG suppression. The ATG13 ΔFBD mutant similarly rescued ISGs but not autophagy. Reciprocal ATG9A KO experiments reinforced that the intact trimeric complex is required for immune homeostasis, with rescue dependent on the HDIR motif. The results define that ATG101's interaction surface with ATG9A, rather than its autophagy-effector interface, is the critical determinant of ISG suppression.

The requirement for ATG9A is consistent with emerging evidence linking it to innate immune signaling. ATG9A limits STING-TBK1 puncta formation in response to dsDNA[73], mediates unconventional lysosomal targeting of TNFR1 complexes, and restrains TNFR1-driven STING activation[130,131]. Our findings extend this by showing that ATG9A's immune role requires ATG13 and ATG101, positioning the complex as the functional unit.

These findings should be considered alongside a prior report that ATG13 positively regulates type I IFN signaling in HEK293T cells through the RLR-MAVS-TBK1 axis, an opposing phenotype to what we report here[41]. Notably, Du et al. interrogated the RLR-MAVS-TBK1 axis using siRNA knockdown, whereas the ISG phenotype described here arises in genetic knockouts. The upstream pathways driving ISG induction in ATG13 and ATG101 KO cells is investigated in Chapter 3.

Imaging revealed that ATG9A loss uniquely caused ATG101 redistribution into puncta positive for ubiquitin, p62, and TNIP1, but negative for TGN46 and RAB7A, consistent

with stalled autophagy initiation sites. The selective dependence of ATG101 localization on ATG9A has not previously been reported but mirrors the genetic specificity of the ISG phenotype. The finding that MCF-7 cells naturally lack detectable ATG101 protein, confirmed across two independently sourced lines, and exhibit constitutive ISG induction, reversible by ectopic ATG101-GFP, further validates these results and raises the possibility that ATG101 loss in tumors may contribute to a constitutively inflamed microenvironment.

In summary, this chapter establishes the ATG9A-ATG13-ATG101 complex as a non-canonical regulator of innate immune homeostasis independent of FIP200, ULK1/2, and canonical autophagy flux. Constitutive regulation of ISG expression by this complex has important implications for cancer and inflammatory diseases. Limitations include reliance on cancer-derived cell lines and the absence of a defined molecular mechanism. How this complex suppresses ISG expression is addressed in Chapter 3.

2.5 METHODS

Cell culture

HeLa S3 cells (ATCC CCL-2.2; RRID:CVCL_0058), HEK293T (ATCC CRL-3216), MCF-7, K562, and THP-1 cells were used in this study. HeLa S3, HEK293T, and MCF-7 cells were cultured at 37°C in a humidified 5% CO^2 atmosphere in Dulbecco's Modified Eagle Medium (DMEM; Sigma-Aldrich) supplemented with 10% non-heat-inactivated fetal bovine serum (FBS; R&D Systems) and 1% penicillin-streptomycin (Gibco). Adherent cells were passaged every 2–3 days using 1× TrypLE Express (phenol red-free; Gibco). THP-1 and K562 cells were cultured under identical conditions in RPMI-1640 medium (Corning) supplemented with 10% non-heat-inactivated FBS, 1% penicillin-streptomycin, and 2 mM L-glutamine. THP-1 cells were maintained at a density of 3×10^5 cells/mL at each passage without differentiation induction. All cell lines were used below passage 8. STR authentication was not performed. All cell lines were tested monthly for mycoplasma contamination using the MycoAlert Mycoplasma Detection Kit (Lonza) and consistently tested negative.

Generation of stable cell lines

Stable cell lines were generated using lentiviral and retroviral transduction. For lentiviral production, HEK293T cells were seeded in 6-well plates and transfected with pHDM-G (0.2 µg), CAG4RTR2 (0.6 µg), CAGGHIVgpco (0.6 µg), and the plasmid construct containing the gene of interest using polyethyleneimine (PEI; Polysciences) at a 3:1 PEI:DNA ratio (w/w) in serum-free DMEM. For retroviral production, HEK293T cells were similarly transfected with pUMVC (0.4 µg) and VSV-G (0.8 µg) alongside the gene of interest construct using the same PEI:DNA ratio. In both cases, 9 µg PEI was diluted in 150 µL serum-free DMEM prior to addition to cells. Media were replaced 16 hours post-transfection, and viral supernatants were harvested 48 h post-transfection and filtered through 0.45 µm syringe filters (WHA9914-2504, Cytiva) to remove contaminating cells. Viral supernatants were used crude without further concentration.

Target cells were seeded at 50,000 cells/well in 12-well plates and transduced by spinfection with 500 µL virus-containing media supplemented with 8 µg/mL polybrene (Sigma-Aldrich) at 800 × *g* for 45 minutes at 16°C. Transduced cells were selected with 5 µg/mL puromycin (Thermo Scientific) for 72 hours to establish stable integrants. The cells were then expanded and sorted by fluorescence-activated cell sorting (FACS) to additionally select for infected cells and normalize protein expression across individual cells.

Plasmids used in this study included: pMXs-IP-eGFP-hATG13 (Addgene #38191), p-eGFP-C1-hATG101 (Addgene #22876), pMXs-puro-RFP-ATG9A, pMXs-puro-HaloTag7-ATG9A, pMRX-IP-HaloTag7-LC3 (Addgene #184899; gift from Noboru Mizushima), ATG101-GFP (generated by Gibson assembly), pHAGE-Flag-Parkin, and pHAGE-mtKeima. GFP-ATG9A was generated by replacing RFP in pMXs-puro-RFP-ATG9A (Addgene #60609) with GFP.

CRISPR-Cas9 genome editing

Knockout (KO) cell lines were generated in-house using CRISPR-Cas9. Cells were either transfected with a Cas9 plasmid encoding the appropriate sgRNA and carrying a puromycin resistance marker, followed by selection with 5 µg/mL puromycin, or transfected with a GFP-tagged Cas9 plasmid encoding the appropriate sgRNA, after which GFP-positive cells were isolated by single-cell fluorescence-activated cell sorting (FACS) 48 h post-transfection. In both cases, 20 clones per target were screened. KO cell lines for ULK1, FIP200, ATG13, ATG101, and ATG9A were generated in HeLa S3 cells. The ULK1/2 double knockout (DKO) was generated by sequential CRISPR-Cas9 editing of ULK2 in the ULK1 KO background. The FIP200/ATG101 DKO was similarly generated by sequential editing in the FIP200 KO background. ATG101 KO lines were also generated in K562 and THP-1 cells. All KO cell lines were validated by Western blot.

Doxycycline-inducible shRNA knockdown

Doxycycline (dox)-inducible shRNA knockdown was performed in THP-1 cells using the pLKO-Tet-On lentiviral vector (Addgene #98398). shRNA sequences targeting ATG101, ATG9A, and ATG13 were cloned into the vector by restriction cloning. A non-targeting (NT) shRNA was used as a control. THP-1 cells were transduced and selected as described above. For knockdown induction, cells were treated with doxycycline for 72 hours before collection.

Mutagenesis

Site-directed mutagenesis was performed using Q5® Hot Start High-Fidelity DNA Polymerase (NEB) according to the manufacturer's protocol with primer pairs designed to introduce point mutations or domain deletions. ATG101-GFP mutants generated included L30R/H31R (ATG13-binding deficient), Y45D (ATG9A-binding deficient), T63R, and W110P111F112A (WPF finger mutant). GFP-ATG13 mutants included a FIP200-binding domain deletion (ΔFBD). GFP-ATG9A HDIR mutant was similarly generated. Briefly, PCR reactions (50 µL) contained 1× Q5 reaction mix, 0.5 µM each primer, 1 ng of plasmid template, and 1 U of Q5 Hot Start polymerase. Thermocycling conditions were optimized according to primer T_m values, typically involving an initial denaturation at 98 °C for 30 s, followed by 25 cycles of 98 °C for 10 s, 55–65 °C for 15 s, and 72 °C for 30 s per kb, with a final extension at 72 °C for 2 min. Following amplification, 1 µL of the PCR product was treated with 1× KLD enzyme mix (NEB) containing T4 polynucleotide kinase, T4 DNA ligase, and DpnI for 15–60 min at room temperature to simultaneously phosphorylate, ligate, and digest parental methylated DNA. The reaction mixture was then transformed into chemically competent *E. coli* (NEB 5-alpha), and positive clones were verified by Sanger sequencing.

Genomic PCR for CRISPR knockout validation

Genomic DNA was extracted from cell pellets using the QuickExtract DNA Extraction Solution (Qiagen) according to the manufacturer's instructions. PCR was performed using Q5 High-Fidelity DNA Polymerase (New England Biolabs) with primers flanking

the CRISPR-targeted region, designed to amplify a ~500–1000 bp product. Each 25 µL reaction contained 12.5 µL of 2× Q5 Master Mix, 0.5 µM each primer, and ~50 ng of genomic DNA. PCR cycling conditions were: initial denaturation at 98 °C for 30 s, followed by 30 cycles of 98 °C for 10 s, 58 °C for 20 s, and 72 °C for 30 s, with a final extension at 72 °C for 2 min. Products were run on a 1.5% agarose gel stained with SYBR Safe, purified by gel clean-up, and sent for Sanger sequencing of the amplified product containing indels.

Quantitative PCR

Total RNA was extracted from 800,000 cells using the Direct-zol RNA MicroPrep kit (R2062, Zymo Research). One microgram of total RNA was used for cDNA synthesis via the High-Capacity cDNA Reverse Transcription Kit (4368814, Thermo Fisher Scientific) as per the manufacturer's protocol. Quantitative PCR was performed using Power SYBR Green PCR Master Mix (4368577, Thermo Fisher Scientific). Fold changes in RNA expression were calculated using the ΔΔCt method compared to actin as a loading control. Where indicated, cells were treated with cGAMP (60 µg/mL; MedChemExpress) for 8 hours prior to RNA extraction.

mt-Keima assay via flow cytometry

Stable cell lines expressing mt-Keima and Flag-Parkin were seeded in 12-well plates at 200,000 cells per well and treated the following day with DMSO or 1 µM oligomycin A/antimycin A (O/A; MedChemExpress/USB Corporation) combined with 10 µM pan-caspase inhibitor Q-VD-OPh (QVD; Abochem) for 24 hours. The cells were then trypsinized and resuspended in sorting buffer [145 mM NaCl, 5 mM KCl, 1.8 mM $CaCl_2$, 10 mM HEPES, 10 mM glucose, and 0.1% bovine serum albumin (BSA)]. The cells were filtered through 35-µm strainer caps into 5-mL polystyrene FACS tubes (FSC-9005, Stellar Scientific) to eliminate large clumps. Analysis was performed using CytExpert software version 2.6 on a Beckman Coulter CytoFLEX flow cytometer. Measurements of lysosomal mt-Keima were taken by calculating the ratio of mt-Keima

emission at 610 nm after excitation by a 555-nm (pH 4) laser over mt-Keima emission at 610 nm after excitation by a 470-nm (pH 7) laser. For each sample, at least 20,000 events were collected and subsequently gated for live, single cells expressing mt-Keima. Three biological replicates were performed.

Protein gels and Western blots

Cells were plated in six-well plates at a density of 400,000 cells per well and incubated overnight. Cells were harvested using TrypLE Express (12604-013, Thermo Fisher Scientific) and pelleted by centrifugation. Cell pellets were washed with phosphate-buffered saline (PBS) and lysed in radioimmunoprecipitation assay (RIPA) buffer (50 mM Tris, 150 mM NaCl, 0.1% SDS, 0.5% sodium deoxycholate, 1% Triton X-100) supplemented with EDTA-free broad-spectrum protease inhibitors (Thermo Fisher Scientific) for 15 minutes on ice. Lysates were cleared by centrifugation at 20,000 × *g* for 15 minutes at 4°C, and soluble fractions were collected. Protein concentration was determined using the BCA assay (Thermo Fisher Scientific). Samples were diluted 1:4 in 4× SDS loading buffer, denatured at 95°C for 5 minutes, and briefly centrifuged. Five to ten micrograms of protein per sample was resolved on 4–20% Mini-PROTEAN TGX gels (Bio-Rad) at 150 V for 60 minutes, or on 4–12% Bis-Tris gels in MOPS running buffer where indicated. Proteins were transferred to nitrocellulose membranes using the Trans-Blot Turbo Transfer System (Bio-Rad) for 10 minutes. Membranes were stained with Ponceau S (Thermo Scientific) for 5 minutes at room temperature, washed with deionized water, and imaged using a ChemiDoc MP Imaging System (Bio-Rad). Membranes were washed in TBS-T (Tris-buffered saline + 0.1% Tween-20) and blocked for 1 hour at room temperature in 5% nonfat milk in TBS-T. Primary antibody incubation was performed overnight at 4°C in 2.5% nonfat milk in TBS-T at the concentrations listed below. Membranes were washed three times for 5 minutes with TBS-T and incubated for 1 hour at room temperature with goat anti-mouse or goat anti-rabbit HRP-conjugated secondary antibodies (1706515 and 1706516, Bio-Rad; RRID:AB_11125142 and RRID:AB_11125547) diluted 1:3000 in 2.5% nonfat milk in

TBS-T. Membranes were washed three times with TBS-T and imaged using Immobilon ECL Ultra Western HRP Substrate (WBKLS0500, MilliporeSigma) and a ChemiDoc MP Imaging System (Bio-Rad). Densitometry analysis was performed using ImageLab version 6.1 (RRID:SCR_014210). All densitometry was first normalized to Ponceau S staining and then to the WT condition set at 1, unless otherwise noted.

HaloTag-LC3B processing assay

Cells stably expressing HaloTag7-LC3B were plated at 200,000 cells per well in 12-well plates. The next day, cells were incubated with media containing 100 nM Halo-TMR ligand (G8252A, Promega) for 20 minutes. Cells were washed three times with PBS before experimental treatments. Treatments included basal conditions and Torin1 (250 nM; MedChemExpress) for 16 hours. Following a PBS wash, cells were directly lysed on plate in 1× LDS sample buffer supplemented with cOmplete Protease Inhibitor cocktail (Roche), and boiled immediately at 99 °C for 10 min. Protein quantitation per sample was obtained using the Pierce BCA protein assay kit (Thermo Fisher). β-Mercaptoethanol (BME; Sigma) was added to each sample at 5% v/v with blue loading dye just before gel loading. Twenty micrograms of total protein per sample was loaded into wells of 4–12% Bis-Tris gels (GenScript) and separated in MOPS buffer run at 125 V until the dye front reached the bottom of the gel. Gels were directly imaged on a Bio-Rad ChemiDoc imaging system using the rhodamine channel. Gels were subsequently stained with Coomassie (Sigma) as a loading control. Autophagy flux was quantified by calculating the ratio of the processed HaloTag band (lower band) to the total HaloTag intensity (processed plus unprocessed bands).

Spinning disk microscopy and immunofluorescence

For live cell imaging, cells expressing ATG101-GFP were plated in P96-1.5H-N, Coverslip #1.5H 96-well imaging plates (Cellvis) and imaged on a Nikon Ti-2 CSU-W1 spinning disk confocal system operated by Nikon Elements AR microscope imaging software using a 40× water objective (NA 1.15) with the automated TI2-N-WID water

immersion dispenser. The microscope is equipped with a live cell chamber set to 37°C and 5% CO^2 with constant humidity.

For immunofluorescence, cells were seeded in 96-well imaging plates or 8-well chamber slides (Cellvis C8-1.5H-N), fixed with 4% warm paraformaldehyde (PFA) in PBS for 10 minutes, washed three times with PBS, permeabilized with 0.1% Triton X-100 in PBS for 5 minutes, and blocked with 3% goat serum and 1% BSA in PBS for one hour. Cells were then incubated overnight in 1:200 or 1:500 dilution of primary antibodies in blocking solution on a rocker at 4°C. Cells were washed three times, incubated with a 1:1000 dilution of Alexa Fluor 568- or Alexa Fluor 647-conjugated secondary antibodies for one hour at room temperature in blocking solution on a rocker, then washed three times before imaging. DAPI was used as a nuclear stain where indicated.

Colocalization and image analysis

Image analysis and colocalization quantification were performed using custom Python scripts. ATG101-GFP puncta size was measured from at least 27 imaging sites across three biological replicates. For colocalization of immunofluorescence markers, Pearson's correlation coefficient was calculated from images of at least 10 cells per condition per experiment across three biological replicates.

Label-free proteomics

Cells (10×10^7) were harvested and prepared with EasyPep Mini MS Sample Prep Kit (A4006, Thermo Fisher Scientific) according to the manufacturer's instructions in four biological replicates per genotype. Peptide concentration was measured with the Pierce Quantitative Fluorometric Peptide Assay (Cat #23290, Thermo Fisher Scientific).

Mass spectrometry sample preparation

For digestion, 25 µL of 50 mM HEPES was added to dilute 10 M urea, followed by 1 µL TCEP (500 mM) and 3 µL CAA (500 mM), incubated for 20 and 15 min shaking at 750 rpm at 37°C, respectively. Two microliters of Lys-C (100 ng/µL, Wako) was added

and incubated for 4 hours at 750 rpm at 37°C, followed by dilution with 375 µL HEPES buffer (50 mM) and 5 µL $CaCl_2$ (100 mM). Three microliters of trypsin (100 ng/µL, Thermo Scientific) was added and incubated overnight. Peptides were desalted with Pierce C18 spin columns (Thermo Fisher Scientific) and dried by vacuum centrifugation. Samples were reconstituted in Solvent A (97.8% H_2O, 2% ACN, 0.2% formic acid).

LC-MS/MS experiments were performed using an EASY-nLC 1000 (Thermo Fisher Scientific) connected to a QExactive HF mass spectrometer operated in data-independent acquisition (DIA) mode. The sample (1 µg) in 0.1% formic acid solution was loaded onto an Aurora UHPLC Column (25 cm × 75 µm, 1.6 µm C18, AUR225075C18A, IonOpticks) and separated over 136 min at a flow rate of 0.35 µL/min with the following gradient: 2–6% Solvent B (7.5 min), 6–25% B (82.5 min), 25–40% B (30 min), 40–98% B (1 min), and 98% B (15 min). Solvent A consisted of 97.9% H_2O, 2% ACN, and 0.1% formic acid, and Solvent B consisted of 19.9% H_2O, 80% ACN, and 0.1% formic acid. MS1 scans were acquired in the Orbitrap at 120,000 resolution with a scan range of 350–1500 *m/z*. Ion source settings were: ion source type, NSI; spray voltage, 2400 V; ion transfer tube temperature, 275 °C. System control and data collection were performed by Xcalibur software. The mass spectrometry proteomics data have been deposited to the ProteomeXchange Consortium via the PRIDE partner repository with the dataset identifier PXD058150.

Proteomic data analysis

Proteomic analysis was performed using Proteome Discoverer 3.5 (Thermo Scientific), the *H. sapiens* UniProt database, and SequestHT with Percolator validation. Percolator FDRs were 0.01 (strict) and 0.05 (relaxed). Peptide FDRs were 0.01 (strict) and 0.05 (relaxed), with medium confidence and a minimum peptide length of 6. Carbamidomethyl (C) was a static modification, while oxidation (M) was dynamic. Additional N-terminal modifications included acetyl (protein N-term), Met-loss (protein N-term M), and Met-loss + acetyl (protein N-term M). P-values were calculated using

independent t-tests, and data were sum-normalized to protein abundance, then normalized to bait protein abundance. GO biological process enrichment analysis was performed using clusterProfiler. Gene-set enrichment analysis (GSEA) was used to assess enrichment of interferon alpha and inflammatory response gene sets.

Antibodies and reagents

Primary antibodies used for Western blotting in this study included: ATG101 (13492S; CST, 1:1000; RRID:AB_2798234), ATG13 (13273, clone D1G9; CST, 1:1000; RRID:AB_2798169), ULK1 (8054, clone D9K4; CST, 1:1000; RRID:AB_11178668), ULK2 (PA5-76450; Thermo Fisher, 1:1000), FIP200/RB1CC1 (17250-1-AP; ProteinTech, 1:1000; RRID:AB_10666428), LC3B (PM036; MBL, 1:1000; RRID:AB_2274121), NBR1 (16004-1-AP; ProteinTech, 1:1000; RRID:AB_2251178), p62 (PM045; MBL, 1:1000; RRID:AB_1279301), IFIT1 (14769; CST, 1:1000; RRID:AB_2783869), IFIT2 (92633; CST, 1:1000; RRID:AB_3107027), IFIT3 (87781; CST, 1:1000; RRID:AB_3717248), OASL (36845; CST, 1:1000; RRID:AB_3712914), ISG15 (2743; CST, 1:1000; RRID:AB_2126201), ATG9A (ab108338; Abcam, 1:1000; RRID:AB_10863880), GFP (50430-2-AP; ProteinTech, 1:2000; RRID:AB_11042881), p97 (MA1-21412; Thermo Fisher, 1:1000; RRID:AB_557663), GAPDH (60004-1-Ig; ProteinTech, 1:10000), and GAPDH (2251-1; Abcam, 1:10000; RRID:AB_1267174).

Primary antibodies used for immunofluorescence included: ubiquitin/FK2, p62, TNIP1, TGN46 (ProteinTech), and RAB7A. Secondary antibodies for immunofluorescence were Alexa Fluor 568- and Alexa Fluor 647-conjugated antibodies used at 1:1000.

Secondary antibodies for Western blotting included goat anti-rabbit IgG-HRP conjugate (170-6515; Bio-Rad; RRID:AB_11125142) and goat anti-mouse IgG-HRP conjugate (170-6516; Bio-Rad; RRID:AB_11125547), diluted 1:3000.

The following reagents were used: Torin1 (HY-13003, MedChemExpress), oligomycin (HY-100558, MedChemExpress), antimycin A (1397-94-0, USB Corporation), Q-VD-OPh (AC982001, Abochem), cGAMP (HY-12512, MedChemExpress), bafilomycin A1 (S1413, Selleckchem), doxycycline, Halo-TMR ligand (G8252A, Promega), FuGENE 6

Transfection Reagent (E2691, Promega), Ponceau S stain (161470250, Thermo Scientific), and Coomassie stain (B-0630, Sigma).

Statistical analysis

Statistical analyses were performed and graphed using GraphPad Prism Version 10.2.3 (RRID:SCR_002798) or custom Python scripts. In most cases, significance was calculated with either a one-way or two-way ANOVA test with appropriate multiple comparison tests; an unpaired, two-tailed *t* test was performed when comparing two groups. Error bars are reported as mean ± SD. Images and blots shown are representative of at least three biological replicates unless otherwise noted in the figure legends. Significance levels are indicated as: *P ≤ 0.05, **P ≤ 0.01, ***P ≤ 0.001, ****P ≤ 0.0001.

2.6 REFERENCES

1. Tsukada, M. & Ohsumi, Y. Isolation and characterization of autophagy-defective mutants of *Saccharomyces cerevisiae*. *FEBS Lett.* **333**, 169–174 (1993).
2. Funakoshi, T., Matsuura, A., Noda, T. & Ohsumi, Y. Analyses of *APG13* gene involved in autophagy in yeast, *Saccharomyces cerevisiae*. *Gene* **192**, 207–213 (1997).
3. Kamada, Y. *et al.* Tor-Mediated Induction of Autophagy via an Apg1 Protein Kinase Complex. *J. Cell Biol.* **150**, 1507–1513 (2000).
4. Scott, S. V. *et al.* Apg13p and Vac8p Are Part of a Complex of Phosphoproteins That Are Required for Cytoplasm to Vacuole Targeting. *J. Biol. Chem.* **275**, 25840–25849 (2000).
5. Suzuki, K., Kubota, Y., Sekito, T. & Ohsumi, Y. Hierarchy of Atg proteins in pre-autophagosomal structure organization. *Genes Cells* **12**, 209–218 (2007).
6. Kabeya, Y. *et al.* Characterization of the Atg17–Atg29–Atg31 complex specifically required for starvation-induced autophagy in *Saccharomyces cerevisiae*. *Biochem. Biophys. Res. Commun.* **389**, 612–615 (2009).
7. Kawamata, T., Kamada, Y., Kabeya, Y., Sekito, T. & Ohsumi, Y. Organization of the Pre-autophagosomal Structure Responsible for Autophagosome Formation. *Mol. Biol. Cell* **19**, 2039–2050 (2008).
8. Kraft, C. *et al.* Binding of the Atg1/ULK1 kinase to the ubiquitin-like protein Atg8 regulates autophagy. *EMBO J.* **31**, 3691–3703 (2012).
9. Yeh, Y.-Y., Shah, K. H. & Herman, P. K. An Atg13 Protein-mediated Self-association of the Atg1 Protein Kinase Is Important for the Induction of Autophagy. *J. Biol. Chem.* **286**, 28931–28939 (2011).
10. Fujioka, Y. *et al.* Structural basis of starvation-induced assembly of the autophagy initiation complex. *Nat. Struct. Mol. Biol.* **21**, 513–521 (2014).
11. Kaizuka, T. & Mizushima, N. Atg13 Is Essential for Autophagy and Cardiac Development in Mice. *Mol. Cell. Biol.* **36**, 585–595 (2016).
12. Jao, C. C., Ragusa, M. J., Stanley, R. E. & Hurley, J. H. A HORMA domain in Atg13 mediates PI 3-kinase recruitment in autophagy. *Proc. Natl. Acad. Sci.* **110**, 5486–5491 (2013).

13. Qi, S., Kim, D. J., Stjepanovic, G. & Hurley, J. H. Structure of the Human Atg13-Atg101 HORMA Heterodimer: an Interaction Hub within the ULK1 Complex. *Structure* **23**, 1848–1857 (2015).
14. Suzuki, H., Kaizuka, T., Mizushima, N. & Noda, N. N. Structure of the Atg101–Atg13 complex reveals essential roles of Atg101 in autophagy initiation. *Nat. Struct. Mol. Biol.* **22**, 572–580 (2015).
15. Reggiori, F., Tucker, K. A., Stromhaug, P. E. & Klionsky, D. J. The Atg1-Atg13 Complex Regulates Atg9 and Atg23 Retrieval Transport from the Pre-Autophagosomal Structure. *Dev. Cell* **6**, 79–90 (2004).
16. Suzuki, S. W. *et al.* Atg13 HORMA domain recruits Atg9 vesicles during autophagosome formation. *Proc. Natl. Acad. Sci.* **112**, 3350–3355 (2015).
17. Nguyen, A. *et al.* Metamorphic proteins at the basis of human autophagy initiation and lipid transfer. *Mol. Cell* **83**, 2077–2090 (2023).
18. Rao, Y., Perna, M. G., Hofmann, B., Beier, V. & Wollert, T. The Atg1–kinase complex tethers Atg9-vesicles to initiate autophagy. *Nat. Commun.* **7**, 10338 (2016).
19. Chew, L. H. *et al.* Molecular interactions of the Saccharomyces cerevisiae Atg1 complex provide insights into assembly and regulatory mechanisms. *Autophagy* **11**, 891–905 (2015).
20. Köfinger, J., Ragusa, M. J., Lee, I.-H., Hummer, G. & Hurley, J. H. Solution Structure of the Atg1 Complex: Implications for the Architecture of the Phagophore Assembly Site. *Structure* **23**, 809–818 (2015).
21. Chen, M. *et al.* Structure and activation of the human autophagy-initiating ULK1C:PI3KC3-C1 supercomplex. *Nat. Struct. Mol. Biol.* **32**, 1596–1605 (2025).
22. Suzuki, H. *et al.* Structural Basis of the Autophagy-Related LC3/Atg13 LIR Complex: Recognition and Interaction Mechanism. *Structure* **22**, 47–58 (2014).
23. Alemu, E. A. *et al.* ATG8 Family Proteins Act as Scaffolds for Assembly of the ULK Complex: SEQUENCE REQUIREMENTS FOR LC3-INTERACTING REGION (LIR) MOTIFS. *J. Biol. Chem.* **287**, 39275–39290 (2012).

24. Gu, Y., Desai, A. & Corbett, K. D. Evolutionary Dynamics and Molecular Mechanisms of HORMA Domain Protein Signaling. *Annu. Rev. Biochem.* **91**, 541–569 (2022).
25. Aravind, L. & Koonin, E. V. The HORMA domain: a common structural denominator in mitotic checkpoints, chromosome synapsis and DNA repair. *Trends Biochem. Sci.* **23**, 284–286 (1998).
26. Mapelli, M., Massimiliano, L., Santaguida, S. & Musacchio, A. The Mad2 Conformational Dimer: Structure and Implications for the Spindle Assembly Checkpoint. *Cell* **131**, 730–743 (2007).
27. Luo, X., Tang, Z., Rizo, J. & Yu, H. The Mad2 Spindle Checkpoint Protein Undergoes Similar Major Conformational Changes Upon Binding to Either Mad1 or Cdc20. *Mol. Cell* **9**, 59–71 (2002).
28. Rosenberg, S. C. & Corbett, K. D. The multifaceted roles of the HORMA domain in cellular signaling. *J. Cell Biol.* **211**, 745–755 (2015).
29. Kamada, Y. *et al.* Tor Directly Controls the Atg1 Kinase Complex To Regulate Autophagy. *Mol. Cell. Biol.* **30**, 1049–1058 (2010).
30. Stephan, J. S., Yeh, Y.-Y., Ramachandran, V., Deminoff, S. J. & Herman, P. K. The Tor and PKA signaling pathways independently target the Atg1/Atg13 protein kinase complex to control autophagy. *Proc. Natl. Acad. Sci.* **106**, 17049–17054 (2009).
31. Matsuura, A., Tsukada, M., Wada, Y. & Ohsumi, Y. Apg1p, a novel protein kinase required for the autophagic process in *Saccharomyces cerevisiae*. *Gene* **192**, 245–250 (1997).
32. Yamamoto, H. *et al.* The Intrinsically Disordered Protein Atg13 Mediates Supramolecular Assembly of Autophagy Initiation Complexes. *Dev. Cell* **38**, 86–99 (2016).
33. Fujioka, Y. *et al.* Phase separation organizes the site of autophagosome formation. *Nature* **578**, 301–305 (2020).
34. Puente, C., Hendrickson, R. C. & Jiang, X. Nutrient-regulated Phosphorylation of ATG13 Inhibits Starvation-induced Autophagy. *J. Biol. Chem.* **291**, 6026–6035 (2016).

35. Memisoglu, G., Eapen, V. V., Yang, Y., Klionsky, D. J. & Haber, J. E. PP2C phosphatases promote autophagy by dephosphorylation of the Atg1 complex. *Proc. Natl. Acad. Sci.* **116**, 1613–1620 (2019).
36. Bhattacharya, A. *et al.* Decoding the function of Atg13 phosphorylation reveals a role of Atg11 in bulk autophagy initiation. *EMBO Rep.* **25**, 813–831 (2024).
37. Hieke, N. *et al.* Expression of a ULK1/2 binding-deficient ATG13 variant can partially restore autophagic activity in ATG13-deficient cells. *Autophagy* **11**, 1471–1483 (2015).
38. Zachari, M. *et al.* Selective Autophagy of Mitochondria on a Ubiquitin-Endoplasmic-Reticulum Platform. *Dev. Cell* **50**, 627-643.e5 (2019).
39. Alers, S. *et al.* Atg13 and FIP200 act independently of Ulk1 and Ulk2 in autophagy induction. *Autophagy* **7**, 1424–1433 (2011).
40. Jung, C. H. *et al.* ULK-Atg13-FIP200 Complexes Mediate mTOR Signaling to the Autophagy Machinery. *Mol. Biol. Cell* **20**, 1992–2003 (2009).
41. Du, J. *et al.* ATG13 restricts viral replication by induction of type I interferon. *J. Cell. Mol. Med.* **23**, 6508–6511 (2019).
42. Hosokawa, N. *et al.* Atg101, a novel mammalian autophagy protein interacting with Atg13. *Autophagy* **5**, 973–979 (2009).
43. Mercer, C. A., Kaliappan, A. & Dennis, P. B. A novel, human Atg13 binding protein, Atg101, interacts with ULK1 and is essential for macroautophagy. *Autophagy* **5**, 649–662 (2009).
44. Noda, N. N. & Mizushima, N. Atg101: Not Just an Accessory Subunit in the Autophagy-initiation Complex. *Cell Struct. Funct.* **41**, 13–20 (2016).
45. Bartoszewska, M. & Kiel, J. A. K. W. The Role of Macroautophagy in Development of Filamentous Fungi. *Antioxid. Redox Signal.* **14**, 2271–2287 (2011).
46. Bánréti, Á., Lukácsovich, T., Csikós, G., Erdélyi, M. & Sass, M. PP2A regulates autophagy in two alternative ways in Drosophila. *Autophagy* **8**, 623–636 (2012).
47. Liang, Q., Yang, P., Tian, E., Han, J. & Zhang, H. The C. elegans ATG101 homolog EPG-9 directly interacts with EPG-1/Atg13 and is essential for autophagy. *Autophagy* **8**, 1426–1433 (2012).

48. Hegedűs, K., Nagy, P., Gáspári, Z. & Juhász, G. The Putative HORMA Domain Protein Atg101 Dimerizes and Is Required for Starvation-Induced and Selective Autophagy in Drosophila. *BioMed Res. Int.* **2014**, 470482 (2014).
49. Guo, T. *et al.* The autophagy-related gene Atg101 in Drosophila regulates both neuron and midgut homeostasis. *J. Biol. Chem.* **294**, 5666–5676 (2019).
50. Nanji, T. *et al.* Conserved and unique features of the fission yeast core Atg1 complex. *Autophagy* **13**, 2018–2027 (2017).
51. Ren, X. *et al.* Structural basis for ATG9A recruitment to the ULK1 complex in mitophagy initiation. *Sci. Adv.* **9**, eadg2997 (2023).
52. Michel, M. *et al.* The mammalian autophagy initiator complex contains 2 HORMA domain proteins. *Autophagy* **11**, 2300–2308 (2015).
53. Kim, B.-W. *et al.* The C-terminal region of ATG101 bridges ULK1 and PtdIns3K complex in autophagy initiation. *Autophagy* **14**, 2104–2116 (2018).
54. Wallot-Hieke, N. *et al.* Systematic analysis of ATG13 domain requirements for autophagy induction. *Autophagy* **14**, 743–763 (2018).
55. Duan, Y. *et al.* Reconstitution of multistep recruitment of ULK1 to membranes in autophagy. *bioRxiv* 2025.11.07.687251 (2025) doi:10.1101/2025.11.07.687251.
56. Yang, M. *et al.* A C9ORF72/SMCR8-containing complex regulates ULK1 and plays a dual role in autophagy. *Sci. Adv.* **2**, e1601167 (2016).
57. Renton, A. E. *et al.* A hexanucleotide repeat expansion in C9ORF72 is the cause of chromosome 9p21-linked ALS-FTD. *Neuron* **72**, 257–268 (2011).
58. Lee, J. *et al.* ATG101 Degradation by HUWE1-Mediated Ubiquitination Impairs Autophagy and Reduces Survival in Cancer Cells. *Int. J. Mol. Sci.* **22**, 9182 (2021).
59. Sun, F., Ma, W., Wang, H. & He, H. Tegument protein UL3 of bovine herpesvirus 1 suppresses antiviral IFN-I signaling by targeting STING for autophagic degradation. *Vet. Microbiol.* **291**, 110031 (2024).
60. Noda, T. *et al.* Apg9p/Cvt7p Is an Integral Membrane Protein Required for Transport Vesicle Formation in the Cvt and Autophagy Pathways. *J. Cell Biol.* **148**, 465–480 (2000).

61. Lang, T., Reiche, S., Straub, M., Bredschneider, M. & Thumm, M. Autophagy and the cvt Pathway Both Depend on AUT9. *J. Bacteriol.* **182**, 2125–2133 (2000).
62. Zhang, S., Hama, Y. & Mizushima, N. The evolution of autophagy proteins – diversification in eukaryotes and potential ancestors in prokaryotes. *J. Cell Sci.* **134**, jcs233742 (2021).
63. Chiduza, G. N. *et al.* ATG9B is a tissue-specific homotrimeric lipid scramblase that can compensate for ATG9A. *Autophagy* **20**, 557–576 (2024).
64. Yamada, T. *et al.* Endothelial Nitric-oxide Synthase Antisense (*NOS3AS*) Gene Encodes an Autophagy-related Protein (APG9-like2) Highly Expressed in Trophoblast. *J. Biol. Chem.* **280**, 18283–18290 (2005).
65. Tamura, H., Shibata, M., Koike, M., Sasaki, M. & Uchiyama, Y. Atg9A Protein, an Autophagy-related Membrane Protein, Is Localized in the Neurons of Mouse Brains. *J. Histochem. Cytochem.* **58**, 443–453 (2010).
66. Orsi, A. *et al.* Dynamic and transient interactions of Atg9 with autophagosomes, but not membrane integration, are required for autophagy. *Mol. Biol. Cell* **23**, 1860–1873 (2012).
67. Yamamoto, H. *et al.* Atg9 vesicles are an important membrane source during early steps of autophagosome formation. *J. Cell Biol.* **198**, 219–233 (2012).
68. Thaprawat, P. *et al.* TgATG9 is required for autophagosome biogenesis and maintenance of chronic infection in Toxoplasma gondii. *Autophagy Rep.* **3**, 2418256 (2024).
69. Zhuang, X. *et al.* ATG9 regulates autophagosome progression from the endoplasmic reticulum in Arabidopsis. *Proc. Natl. Acad. Sci.* **114**, E426–E435 (2017).
70. Bader, C. A., Shandala, T., Ng, Y. S., Johnson, I. R. D. & Brooks, D. A. Atg9 is required for intraluminal vesicles in amphisomes and autolysosomes. *Biol. Open* **4**, 1345–1355 (2015).
71. Kiss, V. *et al.* Drosophila Atg9 regulates the actin cytoskeleton via interactions with profilin and Ena. *Cell Death Differ.* **27**, 1677–1692 (2020).
72. Kuma, A. *et al.* The role of autophagy during the early neonatal starvation period. *Nature* **432**, 1032–1036 (2004).

73. Saitoh, T. *et al.* Atg9a controls dsDNA-driven dynamic translocation of STING and the innate immune response. *Proc. Natl. Acad. Sci. U. S. A.* **106**, 20842–20846 (2009).
74. Kojima, T. *et al.* Role of the *Atg9a* gene in intrauterine growth and survival of fetal mice. *Reprod. Biol.* **15**, 131–138 (2015).
75. Holzer, E., Martens, S. & Tulli, S. The Role of ATG9 Vesicles in Autophagosome Biogenesis. *J. Mol. Biol.* **436**, 168489 (2024).
76. Matoba, K. *et al.* Atg9 is a lipid scramblase that mediates autophagosomal membrane expansion. *Nat. Struct. Mol. Biol.* **27**, 1185–1193 (2020).
77. Guardia, C. M. *et al.* Structure of Human ATG9A, the Only Transmembrane Protein of the Core Autophagy Machinery. *Cell Rep.* **31**, 107837 (2020).
78. Lai, L. T. F. *et al.* Subnanometer resolution cryo-EM structure of Arabidopsis thaliana ATG9. *Autophagy* **16**, 575–583 (2020).
79. Maeda, S. *et al.* Structure, lipid scrambling activity and role in autophagosome formation of ATG9A. *Nat. Struct. Mol. Biol.* **27**, 1194–1201 (2020).
80. Judith, D. *et al.* ATG9A shapes the forming autophagosome through Arfaptin 2 and phosphatidylinositol 4-kinase IIIβ. *J. Cell Biol.* **218**, 1634–1652 (2019).
81. Mari, M. *et al.* An Atg9-containing compartment that functions in the early steps of autophagosome biogenesis. *J. Cell Biol.* **190**, 1005–1022 (2010).
82. Young, A. R. J. *et al.* Starvation and ULK1-dependent cycling of mammalian Atg9 between the TGN and endosomes. *J. Cell Sci.* **119**, 3888–3900 (2006).
83. Lamb, C. A. *et al.* TBC1D14 regulates autophagy via the TRAPP complex and ATG9 traffic. *EMBO J.* **35**, 281–301 (2016).
84. Reggiori, F., Shintani, T., Nair, U. & Klionsky, D. J. Atg9 Cycles between Mitochondria and the Pre-Autophagosomal Structure in Yeasts. *Autophagy* **1**, 101–109 (2005).
85. Webber, J. L. & Tooze, S. A. Coordinated regulation of autophagy by p38α MAPK through mAtg9 and p38IP. *EMBO J.* **29**, 27–40 (2010).
86. Broadbent, D. G., Barnaba, C., Perez, G. I. & Schmidt, J. C. Quantitative analysis of autophagy reveals the role of ATG9 and ATG2 in autophagosome formation. *J. Cell Biol.* **222**, e202210078 (2023).

87. Olivas, T. J. *et al.* ATG9 vesicles comprise the seed membrane of mammalian autophagosomes. *J. Cell Biol.* **222**, e202208088 (2023).
88. Park, D. *et al.* Synaptic vesicle proteins and ATG9A self-organize in distinct vesicle phases within synapsin condensates. *Nat. Commun.* **14**, 455 (2023).
89. Binotti, B. *et al.* ATG9 resides on a unique population of small vesicles in presynaptic nerve terminals. *Autophagy* **20**, 883–901 (2024).
90. Kakuta, S. *et al.* Small GTPase Rab1B is associated with ATG9A vesicles and regulates autophagosome formation. *FASEB J* **31**, 3757–3773 (2017).
91. Sawa-Makarska, J. *et al.* Reconstitution of autophagosome nucleation defines Atg9 vesicles as seeds for membrane formation. *Science* **369**, eaaz7714 (2020).
92. Chang, C. *et al.* Reconstitution of cargo-induced LC3 lipidation in mammalian selective autophagy. *Sci. Adv.* **7**, eabg4922 (2021).
93. Backues, S. K. *et al.* Atg23 and Atg27 Act at the Early Stages of Atg9 Trafficking in S. cerevisiae. *Traffic* **16**, 172–190 (2015).
94. Mattera, R., Park, S. Y., De Pace, R., Guardia, C. M. & Bonifacino, J. S. AP-4 mediates export of ATG9A from the trans-Golgi network to promote autophagosome formation. *Proc. Natl. Acad. Sci.* **114**, E10697–E10706 (2017).
95. Davies, A. K. *et al.* AP-4 vesicles contribute to spatial control of autophagy via RUSC-dependent peripheral delivery of ATG9A. *Nat. Commun.* **9**, 3958 (2018).
96. Majumder, P. *et al.* AP-4 regulates neuronal lysosome composition, function, and transport via regulating export of critical lysosome receptor proteins at the trans-Golgi network. *Mol. Biol. Cell* **33**, ar102 (2022).
97. Ivankovic, D. *et al.* Axonal autophagosome maturation defect through failure of ATG9A sorting underpins pathology in AP-4 deficiency syndrome. *Autophagy* **16**, 391–407 (2020).
98. Guo, Y. *et al.* AP1 is essential for generation of autophagosomes from the trans-Golgi network. *J. Cell Sci.* **125**, 1706–1715 (2012).
99. Popovic, D. & Dikic, I. TBC1D5 and the AP2 complex regulate ATG9 trafficking and initiation of autophagy. *EMBO Rep.* **15**, 392–401 (2014).

100. Takahashi, Y. *et al.* Bif-1 regulates Atg9 trafficking by mediating the fission of Golgi membranes during autophagy. *Autophagy* **7**, 61–73 (2011).
101. Zhou, C. *et al.* Regulation of mATG9 trafficking by Src- and ULK1-mediated phosphorylation in basal and starvation-induced autophagy. *Cell Res.* **27**, 184–201 (2017).
102. Lu, Q., Wang, P.-S. & Yang, L. Golgi-associated Rab GTPases implicated in autophagy. *Cell Biosci.* **11**, 35 (2021).
103. Kakuta, S. *et al.* Small GTPase Rab1B is associated with ATG9A vesicles and regulates autophagosome formation. *FASEB J* **31**, 3757–3773 (2017).
104. Saffari, A. *et al.* High-content screening identifies a small molecule that restores AP-4-dependent protein trafficking in neuronal models of AP-4-associated hereditary spastic paraplegia. *Nat. Commun.* **15**, 584 (2024).
105. Yang, S. & Rosenwald, A. G. Autophagy in Saccharomyces cerevisiae requires the monomeric GTP-binding proteins, Arl1 and Ypt6. *Autophagy* **12**, 1721–1737 (2016).
106. Zhou, C. *et al.* Recycling of autophagosomal components from autolysosomes by the recycler complex. *Nat. Cell Biol.* **24**, 497–512 (2022).
107. Wu, Z. *et al.* Rab32 family proteins regulate autophagosomal components recycling. *J. Cell Biol.* **223**, e202306040 (2024).
108. Ghanbarpour, A., Valverde, D. P., Melia, T. J. & Reinisch, K. M. A model for a partnership of lipid transfer proteins and scramblases in membrane expansion and organelle biogenesis. *Proc. Natl. Acad. Sci.* **118**, e2101562118 (2021).
109. Hailey, D. W. *et al.* Mitochondria Supply Membranes for Autophagosome Biogenesis during Starvation. *Cell* **141**, 656–667 (2010).
110. Hamasaki, M. *et al.* Autophagosomes form at ER–mitochondria contact sites. *Nature* **495**, 389–393 (2013).
111. Axe, E. L. *et al.* Autophagosome formation from membrane compartments enriched in phosphatidylinositol 3-phosphate and dynamically connected to the endoplasmic reticulum. *J. Cell Biol.* **182**, 685–701 (2008).
112. Hayashi-Nishino, M. *et al.* A subdomain of the endoplasmic reticulum forms a cradle for autophagosome formation. *Nat. Cell Biol.* **11**, 1433–1437 (2009).

113. Ylä-Anttila, P., Vihinen, H., Jokitalo, E. & Eskelinen, E.-L. 3D tomography reveals connections between the phagophore and endoplasmic reticulum. *Autophagy* **5**, 1180–1185 (2009).
114. Ge, L., Melville, D., Zhang, M. & Schekman, R. The ER–Golgi intermediate compartment is a key membrane source for the LC3 lipidation step of autophagosome biogenesis. *eLife* **2**, e00947 (2013).
115. Ravikumar, B., Moreau, K., Jahreiss, L., Puri, C. & Rubinsztein, D. C. Plasma membrane contributes to the formation of pre-autophagosomal structures. *Nat. Cell Biol.* **12**, 747–757 (2010).
116. Puri, C., Renna, M., Bento, C. F., Moreau, K. & Rubinsztein, D. C. Diverse Autophagosome Membrane Sources Coalesce in Recycling Endosomes. *Cell* **154**, 1285–1299 (2013).
117. Molino, D., Zemirli, N., Codogno, P. & Morel, E. The Journey of the Autophagosome through Mammalian Cell Organelles and Membranes. *J. Mol. Biol.* **429**, 497–514 (2017).
118. Imai, K. *et al.* Atg9A trafficking through the recycling endosomes is required for autophagosome formation. *J. Cell Sci.* **129**, 3781–3791 (2016).
119. Osawa, T. *et al.* Atg2 mediates direct lipid transfer between membranes for autophagosome formation. *Nat. Struct. Mol. Biol.* **26**, 281–288 (2019).
120. Valverde, D. P. *et al.* ATG2 transports lipids to promote autophagosome biogenesis. *J. Cell Biol.* **218**, 1787–1798 (2019).
121. Maeda, S., Otomo, C. & Otomo, T. The autophagic membrane tether ATG2A transfers lipids between membranes. *eLife* **8**, e45777 (2019).
122. Gómez-Sánchez, R. *et al.* Atg9 establishes Atg2-dependent contact sites between the endoplasmic reticulum and phagophores. *J. Cell Biol.* **217**, 2743–2763 (2018).
123. Ohnstad, A. E. *et al.* Receptor-mediated clustering of FIP200 bypasses the role of LC3 lipidation in autophagy. *EMBO J.* **39**, EMBJ2020104948 (2020).
124. Goodwin, J. M. *et al.* Autophagy-Independent Lysosomal Targeting Regulated by ULK1/2-FIP200 and ATG9. *Cell Rep.* **20**, 2341–2356 (2017).
125. Peng, K., Zhao, G., Zhao, H., Noda, N. N. & Zhang, H. The autophagy protein ATG-9 regulates lysosome function and integrity. *J. Cell Biol.* **224**, e202411092 (2025).

126. Imagawa, Y., Saitoh, T. & Tsujimoto, Y. Vital staining for cell death identifies Atg9a-dependent necrosis in developmental bone formation in mouse. *Nat. Commun.* **7**, 13391 (2016).
127. Yamaguchi, J. *et al.* Atg9a deficiency causes axon-specific lesions including neuronal circuit dysgenesis. *Autophagy* **14**, 764–777 (2018).
128. Li, H. *et al.* A neuroprotective role of Ufmylation through Atg9 in the aging brain of Drosophila. *Cell. Mol. Life Sci.* **80**, 129 (2023).
129. Stavoe, A. K. H., Kargbo-Hill, S. E., Hall, D. H. & Colón-Ramos, D. A. KIF1A/UNC-104 Transports ATG-9 to Regulate Neurodevelopment and Autophagy at Synapses. *Dev. Cell* **38**, 171–185 (2016).
130. Huyghe, J. *et al.* ATG9A prevents TNF cytotoxicity by an unconventional lysosomal targeting pathway. *Science* **378**, 1201–1207 (2022).
131. Priem, D. *et al.* ATG9A-mediated autophagy prevents inflammatory skin disease by limiting TNFR1-driven STING activation and ZBP1-dependent cell death. *Immunity* **58**, 2972-2988.e6 (2025).
132. Roux, K. J., Kim, D. I., Burke, B. & May, D. G. BioID: A Screen for Protein-Protein Interactions. *Curr. Protoc. Protein Sci.* **91**, 19.23.1-19.23.15 (2018).
133. Kannangara, A. R. *et al.* BioID reveals an ATG9A interaction with ATG13-ATG101 in the degradation of p62/SQSTM1-ubiquitin clusters. *EMBO Rep.* **22**, e51136 (2021).
134. Wang, C.-W. *et al.* Apg2 Is a Novel Protein Required for the Cytoplasm to Vacuole Targeting, Autophagy, and Pexophagy Pathways. *J. Biol. Chem.* **276**, 30442–30451 (2001).
135. van Vliet, A. R. *et al.* ATG9A and ATG2A form a heteromeric complex essential for autophagosome formation. *Mol. Cell* **82**, 4324-4339.e8 (2022).
136. Karanasios, E. *et al.* Dynamic association of the ULK1 complex with omegasomes during autophagy induction. *J. Cell Sci.* **126**, 5224–5238 (2013).
137. Karanasios, E. *et al.* Autophagy initiation by ULK complex assembly on ER tubulovesicular regions marked by ATG9 vesicles. *Nat. Commun.* **7**, 12420 (2016).
138. Sankar, D. S. *et al.* The ULK1 effector BAG2 regulates autophagy initiation by modulating AMBRA1 localization. *Cell Rep.* **43**, (2024).

139. Yim, W. W.-Y., Yamamoto, H. & Mizushima, N. A pulse-chasable reporter processing assay for mammalian autophagic flux with HaloTag. *eLife* **11**, e78923 (2022).
140. Sun, N. *et al.* A fluorescence-based imaging method to measure in vitro and in vivo mitophagy using mt-Keima. *Nat. Protoc.* **12**, 1576–1587 (2017).
141. Hickey, K. L. *et al.* Proteome census upon nutrient stress reveals Golgiphagy membrane receptors. *Nature* **623**, 167–174 (2023).

Chapter 3

THE ATG9A–ATG13–ATG101 COMPLEX DIRECTS POST-GOLGI STING DEGRADATION

3.1 ABSTRACT

The cGAS–STING pathway is a central axis of innate immune defense whose activity is coupled to the subcellular trafficking of STING. Here, we identify the ATG9A–ATG13–ATG101 complex as a critical regulator of STING signal termination through a Golgi-to-lysosome degradation pathway we term GLAD (Golgi-to-Lysosome ATG9A–ATG13–ATG101-Dependent degradation). Loss of ATG101 or ATG13 impairs STING delivery to the lysosome after Golgi exit, resulting in the accumulation of activated STING in post-Golgi vesicles and sustained type I interferon signaling. Live-cell imaging and super-resolution microscopy demonstrate that the ATG9A–ATG13–ATG101 complex physically associates with activated STING vesicles in the post-Golgi compartment, forming trans-contact clusters that facilitate STING's entry into the endolysosomal system. These findings establish GLAD as a non-canonical membrane trafficking pathway through which core autophagy initiation proteins regulate innate immune homeostasis.

3.2 INTRODUCTION

Chapter 2 established that loss of ATG13 or ATG101 drives constitutive activation of ISGs through an ATG9A–ATG13–ATG101 complex-dependent mechanism independent of FIP200 and canonical autophagy. Two questions arise directly from this finding: which innate immune pathway is activated, and what is the molecular substrate whose dysregulation underlies the ISG phenotype? This chapter addresses both questions. The cGAS–STING pathway is identified as the relevant immune signaling axis, and STING, a transmembrane innate immune adaptor whose activity is coupled to its subcellular trafficking, is identified as the substrate whose post-Golgi lysosomal degradation requires the ATG9A–ATG13–ATG101 complex.

Because the spatiotemporal regulation of STING is inseparable from its function, this chapter provides a comprehensive introduction to the cGAS–STING pathway: its evolutionary origins, the structural basis of STING activation and function, the subcellular trafficking from ER through Golgi to lysosome, its canonical downstream signaling outputs, and its established connections to autophagy machinery and human disease. Interferon-stimulated genes, particularly IFIT family members that serve as the primary proteomics readout in Chapter 2, are also described and contextualized within the type I interferon response.

The chapter then presents genetic, biochemical, and imaging evidence addressing how the ATG9A–ATG13–ATG101 complex regulates STING trafficking and signal termination, and defines the relationship of this pathway to canonical autophagy and other known mechanisms of STING turnover.

3.2.1 EVOLUTIONARY ORIGINS OF THE CGAS-STING SIGNALING PATHWAY

The cGAS-STING pathway represents the most ancient pattern recognition receptor (PRR) system known, with its core architecture conserved from prokaryotes to vertebrates[1–3]. In bacteria, the pathway is a frontline antiphage defense mechanism. Upon phage infection, cyclic dinucleotide (CDN) synthetases, cGAS-like receptors (cGLRs), produce CDN second messengers in response to the detection of cytosolic

oligonucleotides, initiating a signaling cascade that activates effectors to block phage propagation. CDNs bind and activate bacterial STING, which often contains a Toll/interleukin-1 receptor (TIR) domain in place of the transmembrane domains present in vertebrate STING[2]. CDN binding to TIR-STING results in NAD+ signaling or cell death.[2] Bacteria encode multiple cGLRs that are capable of producing distinct CDNs that activate specific STING variants, highlighting the importance of this evolutionary conserved pathway[1,4].

The transition from bacteria to the metazoan system introduced structural and functional changes. Vertebrate STING abandoned the TIR domain architecture in favor of N-terminal transmembrane domains that embed it firmly within the endoplasmic reticulum (ER) membrane[2]. Additionally, vertebrate STING contains a C-terminal tail (CTT), absent in bacterial homologs[5], that is essential for the recruitment of TBK1 and IRF3, the primary downstream effectors of the vertebrate innate immune response.[6,7] These structural transitions repurposed the ancient CDN second messenger system into a spatially regulated immune signaling axis able to drive transcriptional interferon response[8].

3.2.2 CGAS-STING PATHWAY AND MECHANISM

Detection of cytosolic DNA is the primary upstream trigger of the cGAS-STING pathway[9], initiating an IRF3-dependent innate immune response. cGAS, following dsDNA recognition and binding, undergoes a conformational shift that synthesizes cGAMP from ATP and GMP[10–13]. cGAMP production following intracellular DNA detection is a critical upstream step for STING activation[14]. cGAMP serves as a second messenger and diffusible activator of STING, a transmembrane cyclic-dinucleotide sensor resident at the ER[15,16].

STING, originally discovered in two independent cDNA overexpression screens,[15,17] is a transmembrane protein with a cytosolic C-terminal region[18]. STING binding cGAMP induces a conformational change such that the ligand-binding region is rotated to be parallel with the transmembrane domain.[10,19] Activated STING translocates from the ER

to the Golgi apparatus, where it recruits TBK1 via its CTT. TBK1 undergoes autophosphorylation and phosphorylates STING at serine 366, as well as IRF3 at serine 396.[20] Phosphorylated IRF3 dimerizes, translocates to the nucleus, and drives the expression of interferon-stimulated genes (ISGs). Following Golgi-localized activity, STING is trafficked to the lysosome for degradation, which terminates immune signaling activation.

The sources of cytosolic DNA capable of activating cGAS are diverse and include foreign and self-derived nucleic acids. Pathogen-derived DNA is thought to be the canonical trigger, yet self-DNA released from damaged mitochondria[21,22], micronuclei[23], cytoplasmic chromatin[24,25], or age-related nuclear envelope breakdown can aberrantly activate the pathway[26]. Nuclear and plasma-membrane associated cGAS is thought to be sequestered from free cytosolic DNA under homeostatic conditions, providing a spatial self-tolerance mechanism[27–29]. Importantly, cGAS-STING is distinct from the dsRNA and AT-rich dsDNA sensing mediated by MDA5[30] and RIG-I[31–34].

3.2.3 STRUCTURAL BASIS OF STING FUNCTION

STING is a multi-pass transmembrane protein that is comprised of 4 N-terminal transmembrane domains anchored in the ER membrane and a cytosolic-facing C-terminal region containing a ligand-binding domain (LBD) and the CTT. At the ER, STING forms constitutive dimers such that the LBDs adopt a V-shaped ligand binding pocket that permits cGAMP binding[35–38]. Recent structural evidence has further shown that apo-STING at the ER exists in a bilayer assembly in which two ER membranes are held together through head-to-head and side-by-side LBD packing, autoinhibiting STING preventing ER exit and TBK1 recruitment[39].

cGAMP binding induces the closure of the LBD lid and results in a 180º rotation of the LBD relative to the transmembrane domain[10,40], transitioning STING from an autoinhibited state to an active conformation. This conformational rotation drives higher-order oligomerization through side-by-side packing of STING dimers, required for full signaling activity[40,41].

Multiple cryo-EM and crystal structures of apo and cGAMP-bound STING have been resolved[10,35–38], and full-length structures of chicken and human STING in apo and ligand-bound states have further defined STING's transmembrane architecture.[40] Structural studies of STING-TBK1 complexes have revealed that the CTT contains a conserved TBK1-binding motif and that the CTT adopts a β-strand-like conformation that inserts into a groove between the kinase domain of one TBK1 molecule and the dimerization domains of a neighboring TBK1[42,43]. Adjacent to the TBK1-binding motif is a pLxIS (phosphorylated leucine-any-isoleucine-serine) motif within the CTT that is required for IRF3 recruitment and phosphorylation.[44]

Structural insight into STING and STING-associated complexes have directly informed the development of pharmacological STING modulators. Small-molecule agonists acting orthogonally to cGAMP have been identified, including C53, a compound that binds a cryptic pocket in the STING transmembrane domain to promote oligomerization[45]. Additionally, NVS-STG2, a molecular glue, has been found to induce oligomerization of STING molecules through binding to a pocket between the transmembrane domains of adjacent STING dimers[46].

3.2.4 STING TRAFFICKING

The subcellular trafficking of STING is tightly coupled with its function, and as a result its spatial regulation is a critical check on immune activity. STING is constantly being cycled through the ER and Golgi, and dysregulation at any stage can lead to aberrant immune activity.

At the ER, STING is maintained in an inactive state through interactions with retention and stabilization factors. The calcium sensor stromal interaction molecule 1 (STIM1) directly binds STING and acts as an ER retention factor.[47] STIM1 deficiency leads to uncontrolled STING release from the ER and excessive type I interferon (IFN-I) signaling. *STIM1*-deficient patients present with autoimmunity due to elevated STING-IFN signaling.[48] Toll-interacting protein (TOLLIP) similarly stabilizes STING at the ER under steady-state conditions[49]. Further, IFI16 has been shown to facilitate STING-

TBK1 interaction[50]. Retrograde Golgi-to-ER trafficking of STING mediated by COP-I vesicles also contributes to ER retention and defects in COP-I mediated transport lead to immune dysregulation due to STING accumulation at the Golgi.[51–53]

ER exit of STING is mediated by COP-II vesicles. Loss of core COP-II components, including Sar1, Sec13, Sec24, and Sec31, prevent ER exit of STING, resulting in attenuated STING-mediated IFN signaling.[54,55] STING ER exit protein (STEEP) promotes ER membrane curvature and COPII vesicle formation to facilitate STING export.[56] Prior to ER exit, STING oligomerization following cGAMP binding activates TAK1 (Transforming Growth Factor Beta-Activated Kinase 1), which phosphorylates STING at serine 355, promoting its interaction with STEEP and leading to STING's translocation to the ER-Golgi intermediate compartment (ERGIC).[57] Additional ER exit factors include YIPF5, which facilitates COPII vesicle budding and STING vesicle recruitment,[58] and iRhom2, an ER protein that facilitates STING interaction with TRAPB, a component of the translocon complex required for ER exit.[59]

At the Golgi, STING signaling is tightly regulated by multiple post-translational modifications. STING is palmitoylated at cysteine 88 and 91 by acyltransferases DHHC3, DHHC7, and DHHC17, a modification required for STING oligomerization and downstream signaling.[60] Inhibition of STING palmitoylation prevents STING oligomerization and downstream signaling.[61] STING is ubiquitinated by multiple proteins at the Golgi, modulating its homeostasis by promoting STING degradation.[62] ARFGAP2 (ADP-ribosylation factor GTPase-activating protein 2) is a small GTPase regulator of vesicle transport in the Golgi that promotes STING proton channel activity, resulting in reduced Golgi acidity. Loss of ArfGAP2 disrupts cytokine trafficking and reduces STING-mediated inflammatory responses.[63]

Following TBK1-mediated phosphorylation at the Golgi, STING is rapidly sorted for lysosomal degradation. Adaptor protein complex-1 (AP-1) binds a dileucine motif and phosphoserine 366 within the STING CTT domain and packages phosphorylated STING into vesicles destined for lysosomes.[64] Niemann-Pick type 1 (NPC1) is a critical facilitator of Golgi-to-lysosome transit and in its absence, STING degradation is

impaired and immune signaling is amplified. In the absence of NPC1, STING signaling is 'primed' by its association with SREBP2 trafficking and 'boosted' due to impaired lysosomal degradation.[65] The ESCRT complex, specifically components HGS, VPS37A, and UBAP1, mediate STING sorting into multivesicular bodies (MVBs) that are trafficked to lysosomes for degradation following STING ubiquitination.[66] Loss of Golgin GCC2 (GRIP and coiled-coil domain containing protein 2) and certain RAB GTPases, specifically RAB14, result in altered STING degradation and continuous interferon signaling.[67] GCC2 is a Golgin involved in cargo trafficking in and out of the trans-Golgi network (TGN). Evidence that loss of Golgi-to-lysosome factors, which lead to elevated STING Golgi-dwell time, promote excessive interferon signaling points to a basal level of Golgi flux at homeostasis. This contrasts with a "trigger-release" mechanism in which cGAS and STING are inactive in the absence of a pathological trigger.

The siRNA screen run by Tu et al focused on 31 candidate genes and assessed STING trafficking following ligand activation (with dsDNA) and in tonic activation (in absence of dsDNA stimuli). Several proteins involved in post-Golgi STING trafficking, including RAB6B, NPC1, and GCC2, were identified as increasing ligand-mediated IFN response,[65] while proteins involved in STING ER-exit were identified as reducing ligand-mediated IFN response, specifically SEC24C and VAPB.[55,68] Certain RABs, RAB1B, RAB2A/B, among others, did not have an effect on downstream IFN response. Of note, knockdown of Arfgap1, required for COPI vesicle formation and Golgi-to-ER retrograde trafficking,[69] lead to increased tonic IFN signaling.[67]

Given STING's central role in immune signaling, it has also been shown that altering STING degradation can enhance anti-tumor immunity.[70]

Overall, the subcellular localization of STING is highly relevant to its function, with evidence that enhanced localization at the Golgi leads to upregulated downstream signaling. Aberrant Golgi-to-ER retrograde vesicular trafficking or lysosomal dysfunction can lead to sustained immune signal through STING, leading to tissue pathology, in particular neurodegeneration, in mice and humans[8].

3.2.5 CANONICAL STING FUNCTIONS

STING acts as a multifunctional signaling hub whose activation can lead to a range of distinct cellular outcomes. Four canonical functions of STING have been described: TBK1/IRF3-dependent immune activation, NF-κB activation, autophagy regulation, and lysosomal cell death.

The most well-characterized function of STING is its role in TBK1/IRF3-dependent type I interferon signaling. Although TBK1 is localized proximal to STING at the ER membrane, steric hindrance prevents phosphorylation under basal conditions. Following cGAMP binding, STING undergoes a conformational rotation that relieves this constraint, permitting TBK1 autophosphorylation and activation. The resulting TBK1-STING complex serves as a docking platform for IRF3 recruitment and phosphorylation, driving IRF3 dimerization, nuclear translocation, and downstream transcription of type I interferon genes. STING oligomerization and translocation from the ER to the Golgi apparatus via the ER-Golgi Intermediate Compartment (ERGIC) is dependent on STING palmitoylation[41,60]. Consistent with the importance of this modification, STING palmitoylation inhibitors have been developed and shown to prevent STING translocation and abrogate downstream immune activation[61].

In parallel, STING activates the NF-κB transcription factor to drive a pro-inflammatory cytokine production distinct from the interferon response. Two mechanisms have been described. First, active TBK1 can phosphorylate the IκB kinase (IKK) complex, triggering IκBα degradation and canonical NF-κB nuclear translocation.[7] Second, the ligand-binding domain of STING in its active, cGAMP-bound conformation can directly recruit IKK complex components independent of TBK1. The transcriptional output of this pathway, including TNF-α, IL-6, and IL-12, is distinct from the IRF3-driven interferon response and is thought to be shaped by the degree of STING oligomerization and the duration of upstream stimulation. The balance between NF-κB and IRF3 outputs is therefore an important determinant of the overall inflammatory character of the STING response.

STING performs a TBK1-independent function in autophagy regulation, and this role is mechanistically distinct from classical autophagy. Upon cytosolic dsDNA sensing, STING mediates LC3B lipidation on single-membrane perinuclear vesicles through a pathway requiring ATG16L1 and vacuolar ATPase (V-ATPase) activity, but not the ULK1 or PI3KC3 initiation complexes typically required for canonical autophagy, which proceeds via double-membrane autophagosomes.[71] Downstream autophagy effectors WIPI2 and ATG5 are required, indicating that STING engages a subset of the autophagy machinery. The ERGIC itself can additionally serve as a membrane source for autophagosome biogenesis, with cGAMP generation promoting LC3 lipidation through this TBK1-independent mechanism.[54] Beyond this noncanonical route, STING can directly activate autophagy through an ATG5-dependent but Beclin-1-, p62-, ATG9A-, and ULK1-independent mechanism to fine-tune the innate immune response.[72] Importantly, autophagy is thought to serve a regulatory function on STING signaling itself by targeting STING and its upstream activators for degradation. This may represent a negative feedback mechanism that prevents chronic inflammatory signaling.

Following Golgi processing, STING is trafficked to the lysosome. Sustained lysosomal localization is associated with lysosomal membrane permeabilization (LMP), release of cathepsins into the cytosol, and initiation of cell death.[73] This function is thought to represent a cellular failsafe, ensuring the elimination of cells sustaining prolonged cytosolic DNA sensing to limit chronic inflammatory signaling while potentially contributing to immunogenic cell death and downstream adaptive immune priming. Notably, the relative engagement of lysosomal cell death (LCD) versus the upstream signaling functions described above is highly context-dependent: in innate immune cells such as macrophages and dendritic cells, TBK1/IRF3-driven interferon production typically dominates, whereas in T cells, STING activation is more strongly coupled to apoptotic cell death. In tumor cells, STING expression is frequently suppressed or functionally skewed, with important consequences for immunosurveillance.

3.2.6 CONNECTIONS BETWEEN AUTOPHAGY AND CGAS-STING IMMUNE SIGNALING

The relationship between autophagy machinery and STING represents an important regulatory axis that prevents chronic innate immune activation. Following autophagy-dependent delivery of STING and TBK1 to endosomal and lysosomal compartments, and subsequent activation of IRF3 and NF-κB, STING is phosphorylated by the serine/threonine kinase ULK1, which suppresses additional IRF3 function and attenuates interferon signaling.[74] This negative feedback is mediated in part through TBK1-activated, p62-dependent selective autophagy, which drives degradation of STING signaling components to limit the duration of immune activation.[75] The use of selective autophagy as a rheostat for inflammatory signaling is not unique to the cGAS-STING axis. An analogous mechanism has been described for MAVS, the primary adaptor protein of the RIG-I RNA sensing pathway,[76] indicating that autophagic control of innate immune adaptors may represent a broad cellular strategy for preventing sustained inflammation.[77] The physiological importance of this connection is further bolstered by studies demonstrating that extracellular mycobacterial DNA can activate host DNA sensing pathways to direct bacteria toward autophagic clearance, coupling pathogen detection directly to autophagic effector function.[78] STING-dependent autophagy can also be activated in response to bacterial cyclic dinucleotides, independently of DNA sensing. cyclic-di-AMP, produced by live Gram-positive bacteria, engages STING as a vita-PAMP, triggering ER stress and subsequent mTOR inactivation. STING activation in this context induces ER-phagy to resolve stress and limit phagocyte death, while simultaneously repositioning STING to autophagosomes to amplify the interferon response.[79]

3.2.7 DISEASE RELEVANCE: AUTOIMMUNITY, NEURODEGENERATION, AND CANCER

Given the centrality of STING to innate immune homeostasis, perturbation in its activation, trafficking, and degradation are associated with human disease. Broadly, insufficient STING activity is relevant for cancer immune evasion while excessive or aberrant STING signaling underlying autoimmune and neurodegenerative disease pathology[80].

Mutations in TREX1, a cytosolic exonuclease, lead to the accumulation of self-DNA, leading to cGAS-STING mediated IFN-I production and severe auto-immune disease.[81,82] TREX1 deficiency is causally linked to Aicardi-Goutières syndrome (AGS) and systemic lupus erythematosus (SLE)[83,84], autoimmune conditions that require both cGAS and STING for pathological interferon production.

SPRTN, a protease involved in the cleaving DNA-protein crosslinks (DPC)[85], can cause Ruijs-Aalfs progeria syndrome (RJALS) when mutated[86,87]. Loss of SPRTN function leads to cytoplasmic DNA triggering cGAS-STING inflammatory signaling[88]. Genetic or pharmacological inhibition of cGAS-STING rescued all disease phenotypes.

STING-associated vasculopathy with onset in infancy (SAVI) is an autoinflammatory disease caused by gain-of-function mutations in STING that promote constitutive ER exit and Golgi translocation independently of cGAMP binding[89]. Patients present with severe systemic inflammation, interstitial lung disease, and cutaneous vasculopathy driven by chronic type I interferon production. The pathological mechanism, ligand-independent STING accumulation at the Golgi, is conceptually analogous to the post-Golgi STING accumulation observed upon loss of ATG9A–ATG13–ATG101 described in this chapter, underscoring that disruption of STING's ER-to-lysosome trafficking axis can drive pathological interferon signaling.

Aberrant STING trafficking is increasingly recognized as a cause of neurodegenerative disease. In Niemann-Pick type C (NPC), loss of NPC1 impairs lysosomal STING degradation, resulting in tonic amplification of STING signaling. Npc1-null mice display significant neurological impairment that is rescued with STING, but not cGAS,

deletion.[65] Pathogenic mutations in UBAP1, an ESCRT component required for STING lysosomal sorting, are linked to hereditary spastic paraplegia (HSP).[66] In ALS, C9orf72 mutant patients exhibit elevated type I interferons that can be suppressed with STING inhibition.[90] Further, cytoplasmic accumulation of TDP43 has been shown to drive cGAS-STING mediated neuroinflammation[91]. Collectively, trafficking-dependent regulation of STING is a contributor to neurodegenerative disease.

In oncology, STING expression is frequently downregulated in tumor cells, presumably to impair immunosurveillance[92,93]. Therapeutic strategies targeting STING activation and its degradation to prolong signaling has shown promise in enhancing anti-tumor immunity[94–99].

Together, these disease associations underscore the importance of precise spatial regulation of STING signaling. The continuous trafficking of STING through the secretory pathway, and the multiple checkpoints governing its ER retention, Golgi processing, and lysosomal degradation, represents both the mechanistic basis of STING-dependent immunity and potential therapeutic targets.

3.2.8 INTERFERON STIMULATED GENES

Host cells initiate antiviral response following the recognition of pathogen-associated molecular patterns (PAMPs) through PRRs[100]. In mammals, these include Toll-like receptors (TLR3, TLR7, TLR8, TLR9), cytosolic RNA sensors (RIG-I, MDA5), and cytosolic DNA sensors including cGAS[101]. Activation of these receptors triggers signaling cascades that induce pro-inflammatory cytokines, including type I interferons, which act to restrict virus replication. Type I IFNs, primarily IFNα and IFNβ[102], signal through the IFNAR1/2 receptor complex to activate the JAK/STAT pathway resulting in the formation of the ISGF3 complex (STAT1-STAT2-IRF9)[103]. This complex translocates to the nucleus and drives transcription of hundreds of interferon-stimulated genes (ISGs)[104].

3.2.9 ISG ANTI-VIRAL ACTIVITY

Among ISGs, IFN-induced proteins with tetratricopeptide repeats (IFITs) play key roles in antiviral defense through multiple mechanisms. IFITs are induced by type I IFN or IRF3 activation. Structurally, IFIT proteins contain multiple tetratricopeptides repeats (TPRs), each consisting of a ~34 amino-acid helix-turn-helix structure that mediates protein-protein interactions[105]. Early studies demonstrated that IFITs bind to the translation initiation complex eIF3, inhibiting protein translation[106], and that IFIT1 and IFIT2 are rapidly induced within 2 hours of IFNα exposure[107].

In human IFITs, four IFIT proteins, *IFIT1 (ISG56), IFIT2 (ISG54), IFIT3 (ISG60) and IFIT5 (ISG58),* are encoded on a gene cluster. IFIT5 does not precipitate with other IFIT family members, suggesting functional divergence[108]. IFIT homologs are conserved across vertebrates including mammals, birds, fish, and amphibians, with human and mouse IFITs sharing 50-60% sequence homology[109].

IFIT family members discriminate between self and non-self RNA based on 5'-end structures. For example, IFIT1 specifically recognizes RNAs lacking 2'O methylation of the 5' RNA cap. In the absence of IFIT1, viruses deficient in 2'-O methylation exhibit increased pathogenicity. IFIT2 preferentially binds RNA containing AU-rich elements[110]. Conversely, IFIT5 preferentially recognizes uncapped 5'-triphosphate RNA[111]. Distinct recognition motifs enable the detection of multiple classes of viral RNA. In addition to these individual functions, IFITs can assemble into multiprotein complexes that bind and sequester viral RNA, acting as effectors to limit viral replication and translation[108].

3.3 RESULTS

3.3.1 ATG101 AND ATG13 REGULATE THE CGAS-STING PATHWAY

Given the established role of cGAS-STING signaling in innate immunity and the involvement of STING and TBK1 in autophagy, we evaluated whether ISG levels in ATG101-deficient cells depended on this pathway. Double deletion of ATG101 with

cGAS, STING, or TBK1 abolished ISG induction, indicating dependence on the cGAS-STING pathway (**Figure 1A**). In ATG101 KO, and to a lesser extent ATG13 KO, we observed basal activation of STING indicated by phosphorylation of STING (Ser366), TBK1 (Ser172), and IRF3 (Ser396) (**Figure 1B**). pS172-TBK1 was elevated in FIP200 KO, as previously reported[112], but other markers of STING activation were not observed. Loss of ATG101 or ATG13 leads to sustained cell-autonomous cGAS-STING activation independent of extracellular DNA or canonical autophagy.

3.3.2 CGAMP PRODUCTION AND STING SIGNALING ATTENUATION IN ATG KO CELLS

Next, we assessed whether ATG101 or ATG13 KO cells had higher levels of cGAS activity by measuring cGAMP levels. cGAMP was quantified by ELISA in WT, ATG101 KO, ATG101 GFP rescue, ATG13 KO, and FIP200 KO HeLa following dsDNA or mock transfection (**Figure S1E**). Basal cGAMP levels were similar across all lines. Upon dsDNA treatment, all KO lines showed induced cGAMP levels, but to a lowered magnitude compared to WT. Two observations argue that this reduction reflects clonal selection rather than a direct consequence of AIC component loss. First, reduced cGAMP production was shared across all KO lines, including FIP200 KO, indicating it is not specific to the ATG13–ATG101 module. Second, ATG101-GFP re-expression rescued ISG levels but did not restore cGAMP production, separating the two phenotypes. Third, cGAS protein levels are not altered across KO lines (**Figure 1B**), ruling out loss of cGAS as an explanation. Clonal selection against tonic cGAS activity has been previously reported in CRISPR-edited cell lines, where sustained STING activation may impose a growth disadvantage during single-cell expansion[113]. We therefore conclude that reduced cGAMP production is not related to the observed alteration in STING signaling in ATG13 and ATG101 KO cells.

cGAMP treatment led to enhanced STING signaling in ATG101 and ATG13 KO, but not FIP200 KO, by RT-qPCR (**Figure 1C**). WT and ATG101 KO cells were transfected with cGAMP for up to 24 h. WT and ATG101 KO showed similar induction of the ISG

response, measured by the change in IFIT levels. However, while ISG induction is moderated 24 h following cGAMP in WT cells, ATG101 KO cells display a sustained increase in ISG production (**Figure 1D,E**). Active STING is terminated either via return to the ER or through degradation within endolysosomes[53,70].

ATG101 and ATG13 KO cells show normal basal cGAMP levels but a sustained ISG response upon cGAMP treatment. This indicates that a defective attenuation of STING signaling is a potential mechanistic explanation.

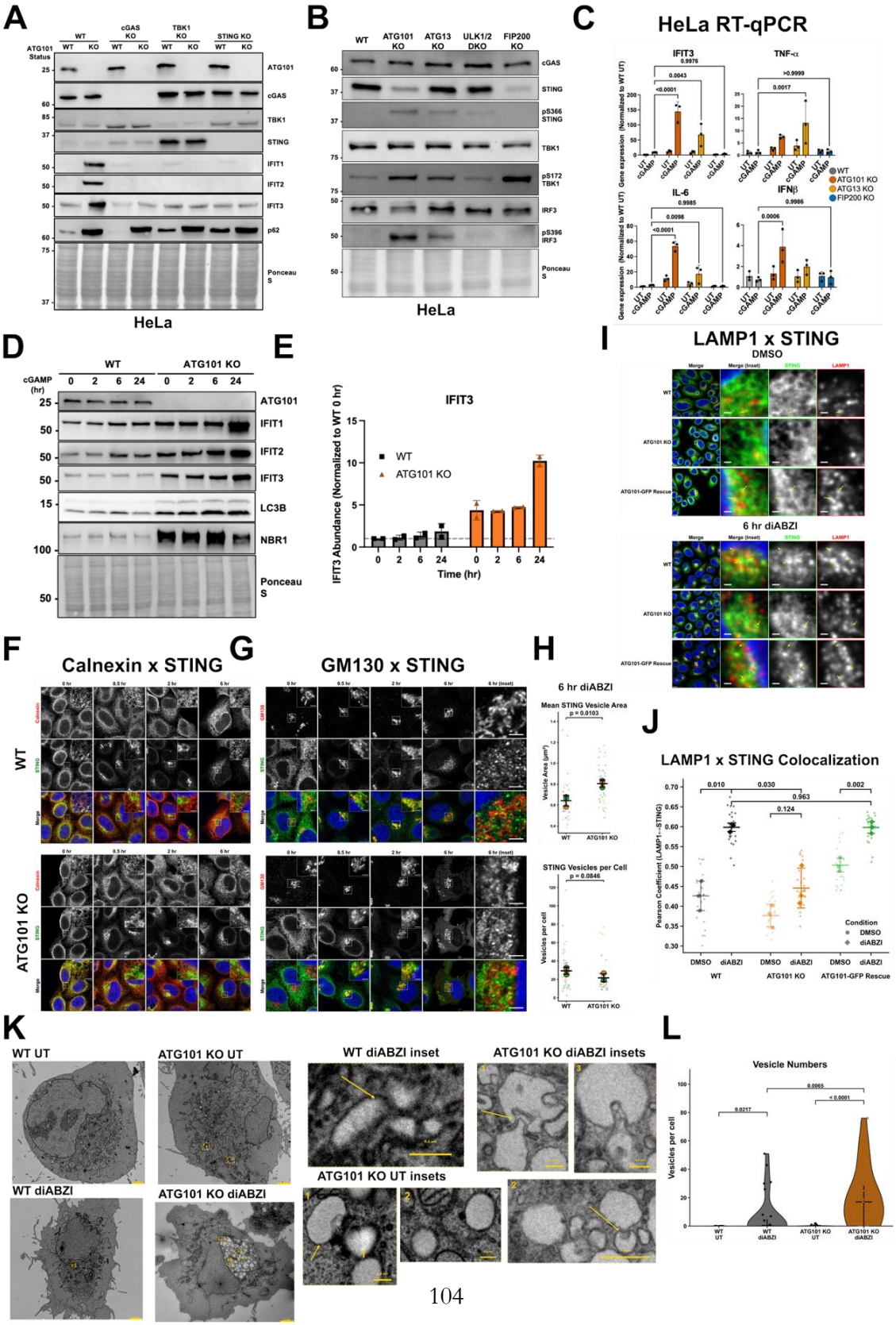
A
WT
cGAS KO
TBK1 KO
STING KO
ATG101 Status
ATG101
cGAS
TBK1
STING
IFIT1
IFIT2
IFIT3
p62
Ponceau S
HeLa
B
WT
ATG101 KO
ATG13 KO
ULK1/2 DKO
FIP200 KO
cGAS
STING
pS366 STING
TBK1
pS172 TBK1
IRF3
pS396 IRF3
Ponceau S
HeLa
C
HeLa RT-qPCR
IFIT3
TNF-α
IL-6
IFNβ
Gene expression (Normalized to WT UT)
UT
cGAMP
WT
ATG101 KO
ATG13 KO
FIP200 KO
D
WT
ATG101 KO
cGAMP (hr)
0 2 6 24 0 2 6 24
ATG101
IFIT1
IFIT2
IFIT3
LC3B
NBR1
Ponceau S
E
IFIT3
IFIT3 Abundance (Normalized to WT 0 hr)
WT
ATG101 KO
Time (hr)
I
LAMP1 x STING
DMSO
6 hr diABZI
Merge
Merge (Inset)
STING
LAMP1
WT
ATG101 KO
ATG101-GFP Rescue
F
Calnexin x STING
G
GM130 x STING
WT
ATG101 KO
0 hr
0.5 hr
2 hr
6 hr
6 hr (Inset)
Calnexin
GM130
STING
Merge
H
6 hr diABZI
Mean STING Vesicle Area
p = 0.0103
Vesicle Area (μm²)
STING Vesicles per Cell
p = 0.0846
Vesicles per cell
WT
ATG101 KO
J
LAMP1 x STING Colocalization
Pearson Coefficient (LAMP1 ~ STING)
0.010
0.030
0.963
0.124
0.002
Condition
DMSO
diABZI
WT
ATG101 KO
ATG101-GFP Rescue
K
WT UT
ATG101 KO UT
WT diABZI
ATG101 KO diABZI
WT diABZI inset
ATG101 KO diABZI insets
ATG101 KO UT insets
L
Vesicle Numbers
Vesicles per cell
0.0217
0.0065
< 0.0001
WT UT
WT diABZI
ATG101 KO UT
ATG101 KO diABZI

Figure 1. Loss of ATG101 or ATG13 results in sustained activation of the cGAS-STING pathway and impairs post-Golgi STING trafficking to the lysosome. *(A) Western blot of ATG101 KO in cell lines null for components of the cGAS-STING pathway. Ponceau S stain is used as a loading control.* ***(B)*** *Western blot of markers of the cGAS-STING pathway in the AIC KO lines.* ***(C)*** *RT-qPCR for STING activation marker genes in WT, ATG101 KO, ATG13 KO, and FIP200 KO lines treated with or without cGAMP (60 µg/mL) for 8 hours. Gene expression is first normalized to actin and then to WT untreated cells. Mean and standard deviation of N = 3 experimental replicates.* ***(D)*** *Western blot analysis of markers of STING and autophagy activity in WT and ATG101 KO cells treated with STING activator cGAMP (60 ug/mL) for the indicated period.* ***(E)*** *Densitometry quantification of western blots in (D). Data are normalized to T =0 h in the WT line. Ponceau stain is used as a loading control.* ***(F)*** *Representative AiryScan imaging of WT and ATG101 KO HeLa^{STING} with 1 µM diABZI for 0, 0.5, 2, and 6 hours, fixed, and immunostained for Calnexin and STING. Scale bar, 10 µm, 2 µm (inset)* ***(G)*** *Representative Airyscan imaging of WT and ATG101 KO HeLa^{STING} with 1 µM diABZI for 0, 0.5, 2, and 6 hours, fixed, and immunostained for GM130 and STING. Scale bar, 10 µm, 2 µm (inset)* ***(H)*** *Quantification of STING structures observed at 6 hours post diABZI treatment. The black line and whiskers represent the mean and standard deviation. Large colored symbols represent the average of each experiment (N=3) whereas smaller colored points represent individual sites. At least 300 cells were measured per genotype.* ***(I)*** *Representative spinning disk microscopy of WT, ATG101 KO, and ATG101-GFP rescue cells treated with DMSO or diABZI for 6 hours and immunostained for STING (green) and LAMP1 (red). Scale bar, 10 µm, 1 µm (inset).* ***(J)*** *Quantification of STING-LAMP1 overlap using the Pearson Coefficient. Large colored symbols represent the average of each replicate (N=3) whereas smaller colored points represent individual sites. At least 300 cells were measured for each genotype.* ***(K)*** *Representative TEM images of WT and ATG101 KO HeLa^{STING} without treatment or after 6 h diABZI. Zoomed in sections containing swollen vesicles in (K, insets).* ***(L)*** *Quantification of swollen vesicle per cell in (K) for at least*

20 cells collected in two biological replicates. Data are presented as mean ± SD; (C, H, J: two-way ANOVA; L: Student's T-Test).

In the absence of pathogens, cGAS-STING can be activated by nuclear or mitochondrial dsDNA, or by extracellular DNA.[21,23,114] cGAS-STING induction can also be triggered non-cell autonomously by endocytosis of DNA.[115] To determine whether extracellular DNA contributed to ISG induction in ATG101 KO cells, we tested whether conditioned media from ATG101 KO cells could trigger ISG expression in WT HeLa cells. No induction was observed (**Figure S1A**), suggesting that cGAS-STING activation occurs cell-autonomously. Nuclear DNA-induced cGAS activation often occurs when cells fail to repair DNA damage. ATG101 KO cells were not more susceptible to cell death induced by genotoxic agents' cisplatin, a DNA-PKc inhibitor (KU57788), or doxorubicin (**Figure S1B**). Further, AIC KO cell lines were not more prone to micronuclei accumulation basally or following doxorubicin treatment (**Figure S1C-D**).

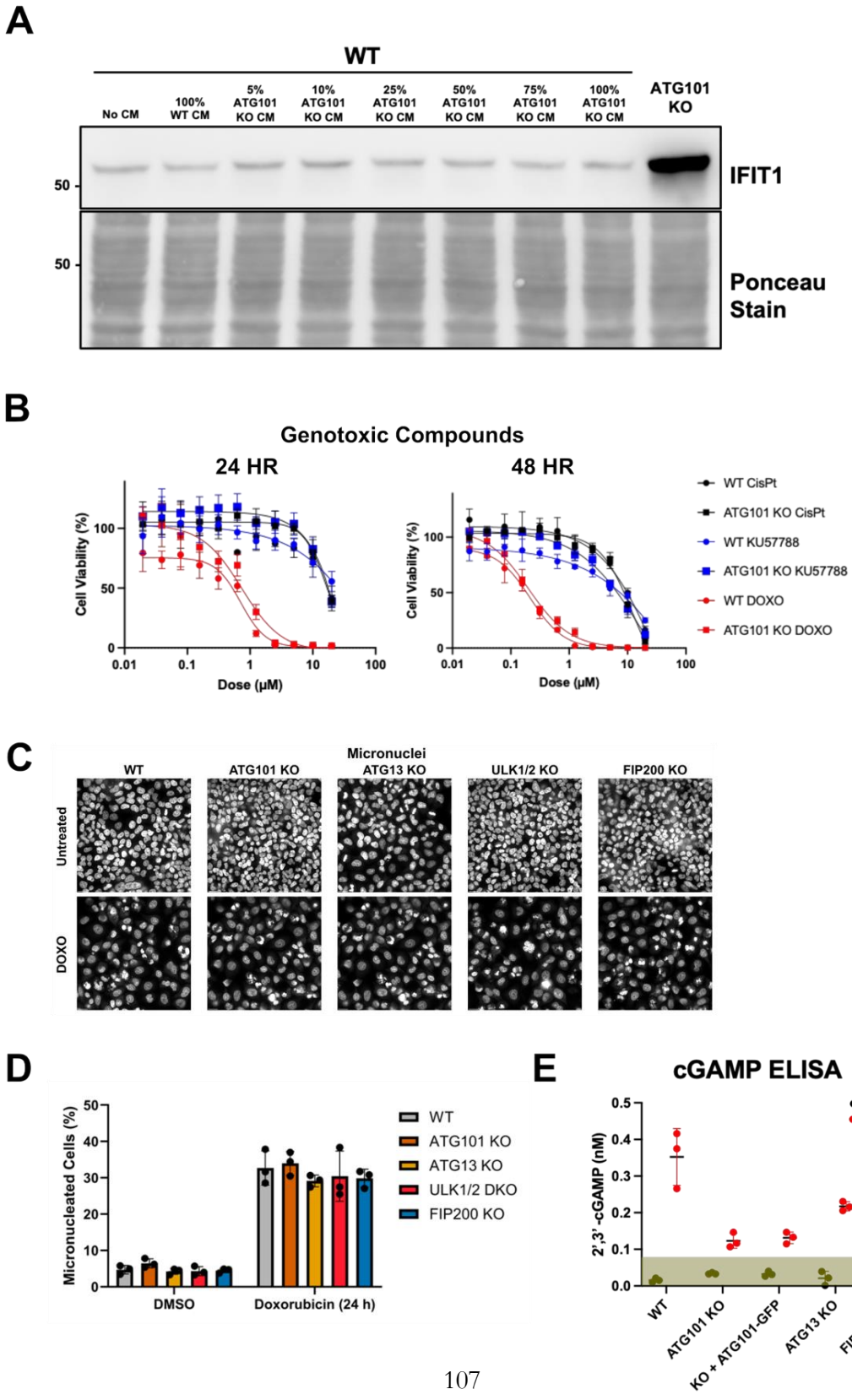
A
WT
No CM
100% WT CM
5% ATG101 KO CM
10% ATG101 KO CM
25% ATG101 KO CM
50% ATG101 KO CM
75% ATG101 KO CM
100% ATG101 KO CM
ATG101 KO
50
IFIT1
50
Ponceau Stain
B
Genotoxic Compounds
24 HR
48 HR
Cell Viability (%)
Dose (μM)
WT CisPt
ATG101 KO CisPt
WT KU57788
ATG101 KO KU57788
WT DOXO
ATG101 KO DOXO
C
Micronuclei
WT
ATG101 KO
ATG13 KO
ULK1/2 KO
FIP200 KO
Untreated
DOXO
D
Micronucleated Cells (%)
WT
ATG101 KO
ATG13 KO
ULK1/2 DKO
FIP200 KO
DMSO
Doxorubicin (24 h)
E
cGAMP ELISA
Mock
dsDNA
2',3'-cGAMP (nM)
WT
ATG101 KO
KO + ATG101-GFP
ATG13 KO
FIP200 KO

Figure S1. The ATG101 KO induced-immune response is cell-autonomous, and ATG101 KO cells are not sensitive to genotoxic stress. ***(A)*** *Western blot of WT HeLa cells cultured for 24 hours in varying levels of ATG101 KO conditioned media. Ponceau stain is used as a loading control.* ***(B)*** *CellTiter-Glo cell viability assay in WT (circles) and ATG101 KO (squares) cells exposed to varying doses of cisplatin (CisPt, black), KU57788 (DNA-PKc inhibitor, blue), or doxorubicin (DOXO, red) for 24 or 48 hours. Solid lines represent fits of the data to the hill equation. Data are presented as mean ± SD for N = 4 biological replicates.* ***(C)*** *Representative images of AIC complex mutant nuclei stained for DAPI untreated or with 24 hours of DOXO treatment.* ***(D)*** *Quantification of micronuclei occurrence in the AIC KO lines treated with or without DOXO. Data are presented as mean ± SD for N = 3 biological replicates.* ***(E)*** *ELISA assay for levels of 2',3'-cGAMP in WT, ATG101 KO, ATG101 KO + ATG101-GFP, ATG13 KO, and FIP200 KO.*

3.3.3 POST-GOLGI TRAFFICKING OF STING IS ALTERED IN ATG101 KO CELLS

To determine where STING accumulated in ATG101 KO cells, we monitored STING trafficking by immunofluorescence (IF) following diABZI treatment in HeLa^{STING} lines (HeLa stably expressing BFP-P2A-STING). In ATG101 KO, STING successfully trafficked out of the ER into the Golgi but accumulated in large peri-nuclear vesicle-like structures following 6 h of diABZI treatment (**Figure 1F,G**). In contrast, in WT cells following 6 h of diABZI, STING overlapped with enlarged LAMP1 structures, indicating late endosome or lysosomal localization (**Figure 1H-I**). ATG101 KO reduced STING-LAMP1 colocalization, which was rescued with addition of ATG101-GFP (**Figure 1J**). These findings suggest ATG101 KO leads to a defect in STING trafficking following Golgi exit, prior to delivery to the lysosome.

We next examined WT and ATG101 KO cells before and after diABZI treatment by transmission electron microscopy (TEM). In WT cells treated for 6 h, we observed electron-sparse vesicles in the perinuclear region (**Figure 1K-L**). In ATG101 KO cells, similar vesicles were observed at baseline and dramatically increased in number

following diABZI treatment. Many of the vesicles appeared to be connected, reminiscent of Golgi structures following ionophore treatment.[116,117] These results suggest that activated STING, a known proton channel, accumulates at the TGN or in post-TGN vesicles in ATG101 KO cells and that its proton channel activity leads to their swelling.[118,119]

In the absence of ATG101, STING accumulates in swollen post-Golgi vesicles due to impaired trafficking toward lysosomes.

3.3.4 THE ATG9A-ATG13-ATG101 SUBCOMPLEX ASSOCIATES WITH STING VESICLES

To understand the interplay of the ATG9A-subcomplex with STING, we performed live cell imaging of HaloTag-STING and RFP-ATG9A in ATG101 KO cells rescued with ATG101-GFP. Prior to diABZI treatment, ATG101 colocalized to ATG9A-positive vesicles, many of which localized to the perinuclear Golgi region, and, in some instances, overlapped with STING (**Figure 2A-B**). After diABZI treatment, STING translocated to the Golgi and showed increased colocalization with ATG9A (**Figure 2A-C**). ATG101 and STING also increased in colocalization, with all three proteins forming dense clusters in the perinuclear region (**Figure 2A-C**). At later timepoints, distinct STING-ATG9A-ATG101 containing puncta were present. We also observed endogenous ATG13 colocalization with STING puncta in WT cells (**Figure 2D**). In ATG101 KO cells, ATG13 localized to cytosolic puncta at baseline and to large STING vesicle clusters after diABZI treatment (**Figure 2D,E**). Addition of BafA, an inhibitor of V-ATPases and STING-induced-V-ATPase-ATG16L1-induced LC3B lipidation (VAIL), or a TBK1 inhibitor (GSK8612), did not prevent STING-ATG9A-ATG101 colocalization, however both inhibitors reduced the clustering of these vesicles in the perinuclear region (**Figure 2C, 3A-C**).

These data indicate that ATG101-ATG9A association to STING is independent of TBK1 activity or VAIL but indicate that the subcomplex is directly involved in STING's post-Golgi route that ends at the lysosome.

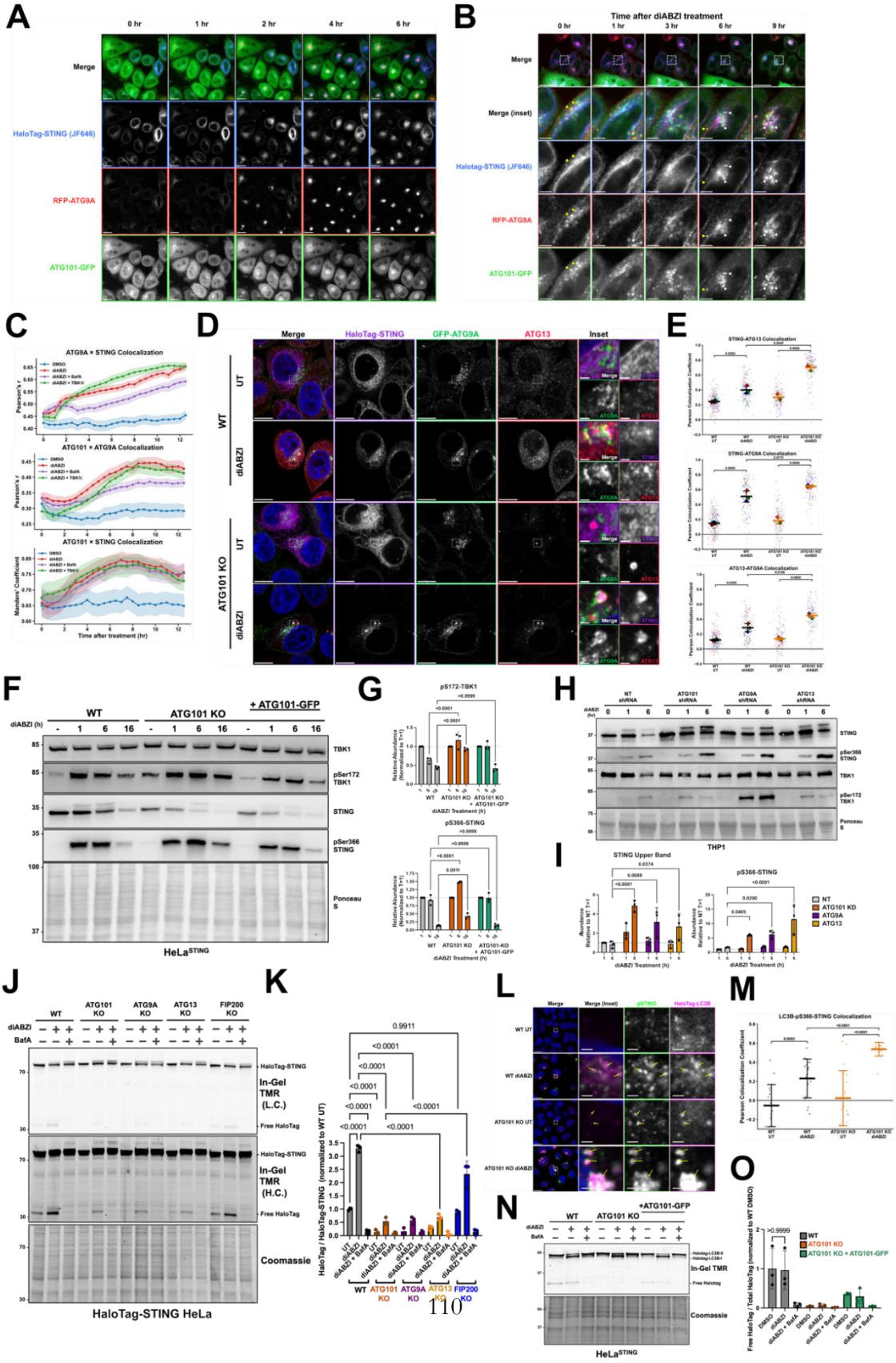
A
0 hr
1 hr
2 hr
4 hr
6 hr
Merge
HaloTag-STING (JF646)
RFP-ATG9A
ATG101-GFP
B
Time after diABZI treatment
0 hr
1 hr
3 hr
6 hr
9 hr
Merge
Merge (inset)
Halotag-STING (JF646)
RFP-ATG9A
ATG101-GFP
C
ATG9A × STING Colocalization
ATG101 × ATG9A Colocalization
ATG101 × STING Colocalization
Pearson's r
Manders' Coefficient
Time after treatment (hr)
DMSO
diABZI
diABZI + BafA
diABZI + TBK1i
D
Merge
HaloTag-STING
GFP-ATG9A
ATG13
Inset
WT
ATG101 KO
UT
diABZI
E
STING-ATG13 Colocalization
STING-ATG9A Colocalization
ATG13-ATG9A Colocalization
Pearson Colocalization Coefficient
F
WT
ATG101 KO
+ ATG101-GFP
diABZI (h)
TBK1
pSer172 TBK1
STING
pSer366 STING
Ponceau S
HeLaSTING
G
pS172-TBK1
pS366-STING
Relative Abundance (Normalized to T=0)
diABZI Treatment (h)
H
NT shRNA
ATG101 shRNA
ATG9A shRNA
ATG13 shRNA
STING
pSer366 STING
TBK1
pSer172 TBK1
Ponceau S
THP1
I
STING Upper Band
pS366-STING
Abundance Relative to NT (T=0)
NT
ATG101 KD
ATG9A
ATG13
J
WT
ATG101 KO
ATG9A KO
ATG13 KO
FIP200 KO
diABZI
BafA
HaloTag-STING
In-Gel TMR (L.C.)
Free HaloTag
In-Gel TMR (H.C.)
Coomassie
HaloTag-STING HeLa
K
HaloTag / HaloTag-STING (normalized to WT UT)
UT
diABZI
diABZI + BafA
WT
ATG101 KO
ATG9A KO
ATG13 KO
FIP200 KO
L
Merge
Merge (Inset)
pSTING
HaloTag-LC3B
WT UT
WT diABZI
ATG101 KO UT
ATG101 KO diABZI
M
LC3B-pS366-STING Colocalization
Pearson Colocalization Coefficient
N
WT
ATG101 KO
+ATG101-GFP
diABZI
BafA
In-Gel TMR
Free Halotag
Coomassie
HeLaSTING
O
Free HaloTag / Total HaloTag (normalized to WT DMSO)
WT
ATG101 KO
ATG101 KO + ATG101-GFP
DMSO
diABZI
diABZI + BafA

Figure 2. The ATG9A-ATG13-ATG101 subcomplex is recruited to mediate the selective degrading of active STING. ***(A)*** *Representative live cell spinning disk imaging of HeLa cells expressing ATG101-GFP, RFP-ATG9A, and HaloTag-STING. Cells were treated with diABZI (1 μM) and imaged every 60 minutes. Main scale bar, 20 μm; inset, 4 μm* ***(B)*** *Representative live cell spinning disk imaging of HeLa cells expressing ATG101-GFP, RFP-ATG9A, and HaloTag-STING at the subcellular level. Cells were treated with diABZI (1 μM) and imaged every 60 minutes. Yellow arrows indicate ATG9A-ATG101 double positive puncta. White arrows indicate STING-ATG9A-ATG101 triple positive puncta. Main scale bar, 20 μm; inset, 4 μm.* ***(C)*** *Colocalization quantifications of live cell imaging of ATG101-GFP, RFP-ATG9A, and HaloTag-STING HeLa cells treated with DMSO, diABZI, diABZI + BafA, or diABZI + TBK1i. Mander's threshold were automatically set by Otsu's method to find the fraction of STING or ATG9A overlapping ATG101 positive puncta. Pearson's correlation coefficient was used to determine the STING and ATG9A signal overlap. Colored dots and shaded region represent the mean and standard deviation N = 44 sites across four independent experiments, with at least 800 cells measured for each condition and time.* ***(D)*** *Representative AiryScan confocal microscopy of HaloTag-STING and GFP-ATG9A expressing WT or ATG101 KO HeLa cells. Cells were treated for 6 hours with 1 μM diABZI or untreated and immunostained for endogenous ATG13. Main scale bar, 20 μm; inset, 2 μm.* ***(E)*** *Colocalization quantification of markers for at least 10 cells per experiment in N=3 replicates.* ***(F)*** *Western blot analysis of diABZI (1 μM) induced STING degradation time-course in WT, ATG101 KO, and ATG101 KO + ATG101-GFP rescue in HeLa^{STING} cells.* ***(G)*** *Densitometry quantification of western blots in (F). Data are normalized to T = 1 h, for each cell line. Ponceau stain is used as a loading control.* ***(H)*** *Western blot analysis of a diABZI timecourse in shRNA expressing THP-1 cells. shRNA expressing THP-1 cells were treated with 72 hours dox treatment before adding diABZI for the indicated times before collection. Ponceau stain is used as a loading control* ***(I)*** *Densitometry quantification of western blots in (H). Data are normalized to shNT after 1 h diABZI treatment.* ***(J)*** *In-Gel fluorescence and western blots of a*

representative HaloTag-STING processing assay in WT, ATG101 KO, ATG9A KO, ATG13 KO, and FIP200 KO HeLa cells. Cells stably expressing HaloTag-STING were labelled with TMR-Halo before treatment with DMSO, diABZI (1 μM), or diABZI + BafA (100 nM) for 16 hours. Coomassie stain is used as a loading control. ***(K)*** *Quantification of in-gel TMR fluorescence from the HaloTag-STING processing assay in (J). The lower (processed) HaloTag is normalized to the corresponding upper HaloTag-STING (unprocessed) band.* ***(L)*** *Representative live cell spinning disk microscopy images of HaloTag-LC3B WT and ATG101 KO HeLa^{STING} cells control or exposed to diABZI for 6 hours and immunostained for pSTING (S366). Main scale bar, 10 μm; inset, 4 μm.* ***(M)*** *Pearson correlation coefficient of experiment in (L) for HaloTag-LC3B and pSTING overlap in N = 18 sites across two biological replicates.* ***(N)*** *In-gel fluorescence of Hela^{STING} WT, ATG101 KO, and ATG101-GFP rescue cells expressing HaloTag-LC3B. Cells were stained with Halo-TMR before treatment with DMSO, diABZI, or diABZI + BafA for 8 hours. Conversion of LC3B-I to LC3B-II (CASM) is observed upon diABZI treatment which is blocked by BafA in all cells. No accumulation of lysosomally processed free HaloTag is observed upon diABZI treatment. Coomassie stain is used as a loading control.* ***(O)*** *Quantification of HaloTag-LC3B processing in WT, ATG101, and ATG101-GFP rescues Hela^{STING} cells treated with diABZI or diABZI + BafA. N = 3 biological replicates. All data are normalized to the WT untreated sample. At least N = 3 biological replicates were measured for each condition. Data are presented as mean ± SD. (E, G, M, I, K,O: two-way ANOVA).*

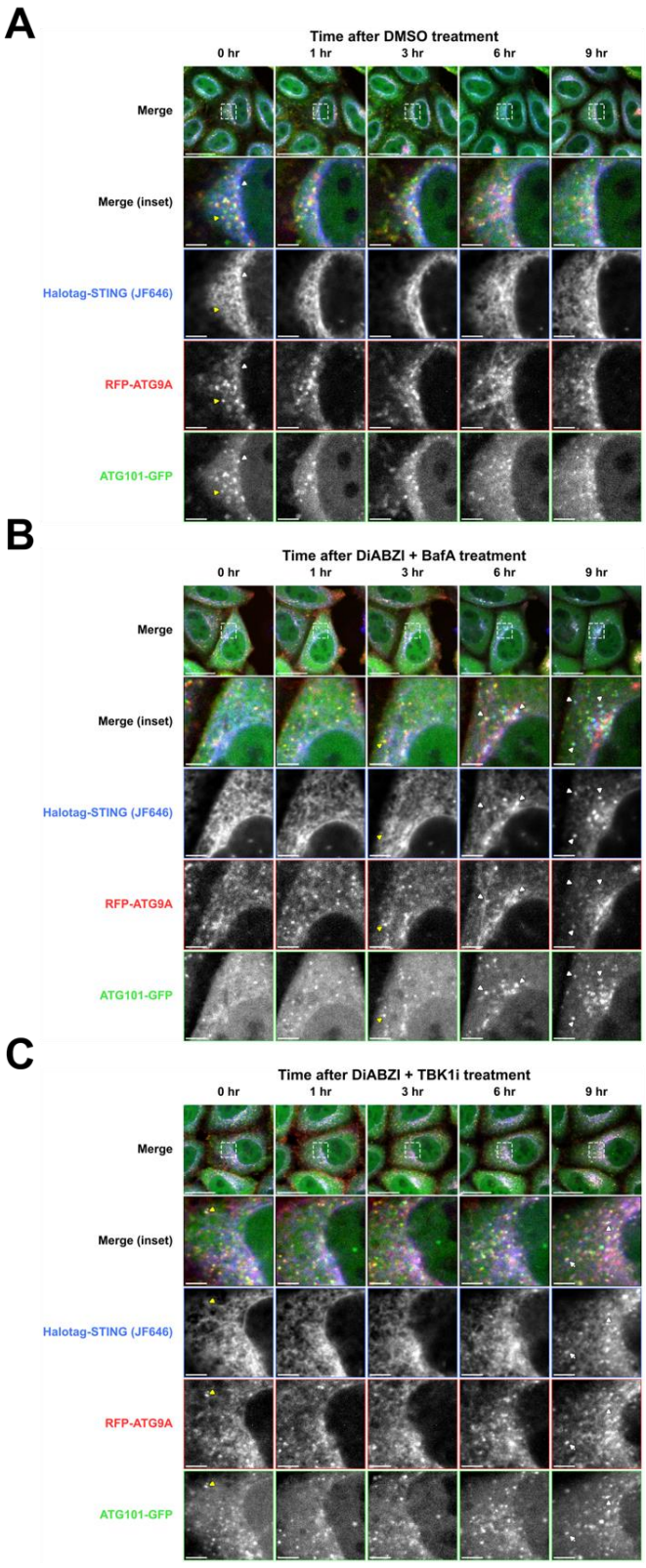
A
Time after DMSO treatment
0 hr
1 hr
3 hr
6 hr
9 hr
Merge
Merge (inset)
Halotag-STING (JF646)
RFP-ATG9A
ATG101-GFP
B
Time after DiABZI + BafA treatment
0 hr
1 hr
3 hr
6 hr
9 hr
Merge
Merge (inset)
Halotag-STING (JF646)
RFP-ATG9A
ATG101-GFP
C
Time after DiABZI + TBK1i treatment
0 hr
1 hr
3 hr
6 hr
9 hr
Merge
Merge (inset)
Halotag-STING (JF646)
RFP-ATG9A
ATG101-GFP

Figure 3. Inhibition of CASM or TBK1 does not prevent ATG9A or ATG101 recruitment to STING vesicles. ***(A)*** *Representative live cell spinning disk microscopy images of HaloTag-STING (JF646), RFP-ATG9A, ATG101-GFP rescue expressing cells over the course of the live cell imaging experiment. Yellow arrows indicate ATG9A-ATG101 containing vesicles. White arrows indicate STING^{+} ATG9A-ATG101 vesicles.* ***(B)*** *As in (A), time-course of cells exposed to diABZI + 100 nM BafA treatment.* ***(C)*** *As in (B), for cells exposed to diABZI + 10 μM TBK1i (GSK8612) for varying times. Images are quantified in Fig. 3C. Main scale bar, 10 μm; inset, 4 μm.*

3.3.5 THE ATG9A-ATG13-ATG101 SUBCOMPLEX MEDIATES THE GOLGI-TO-LYSOSOME DEGRADATION OF STING

To determine if STING termination was affected by ATG101 KO utilized our HeLa^{STING} lines. STING degradation was monitored following activation with the agonist diABZI[94]. pS366-STING (pSTING) and pS172-TBK1 (pTBK1) levels were normalized to peak activation (1 h post-diABZI) to assess degradation kinetics. In WT cells, pSTING and pTBK1 levels declined by 6 h and were substantially reduced by 16 h consistent with expected STING degradation. In contrast, ATG101 KO cells showed elevated pSTING and pTBK1 at baseline and sustained elevated at 6 and 16 h post-diABZI (**Figure 2F,G**), indicating impaired degradation of active STING. Re-expression of ATG101-GFP partially restored pSTING and pTBK1 degradation kinetics to near WT levels.

Following STING's trafficking with respect to ATG9A in WT cells, STING colocalized with ATG9A after 2 h diABZI, followed by reduced colocalization at 6 h (**Figure 4A-B**). In the ATG101 KO, STING and ATG9A have a higher basal overlap, a transient decrease, then increasing colocalization observed at 2-6 h post-activation. These post-Golgi STING vesicles also accumulate the immune regulator and autophagy adaptor TNIP1 (**Figure 4C-D**). We also found that pS366-STING strongly accumulates at and around the TGN in ATG101 KO cells (**Figure 4E-F**). As previously observed, STING colocalized with conjugated ubiquitin, as well as ATG13 in WT and ATG101 KO cells

(**Figure 4G-H**). These results indicate that in the absence of ATG101, active, ubiquitinated STING-vesicles are unable to be degraded.

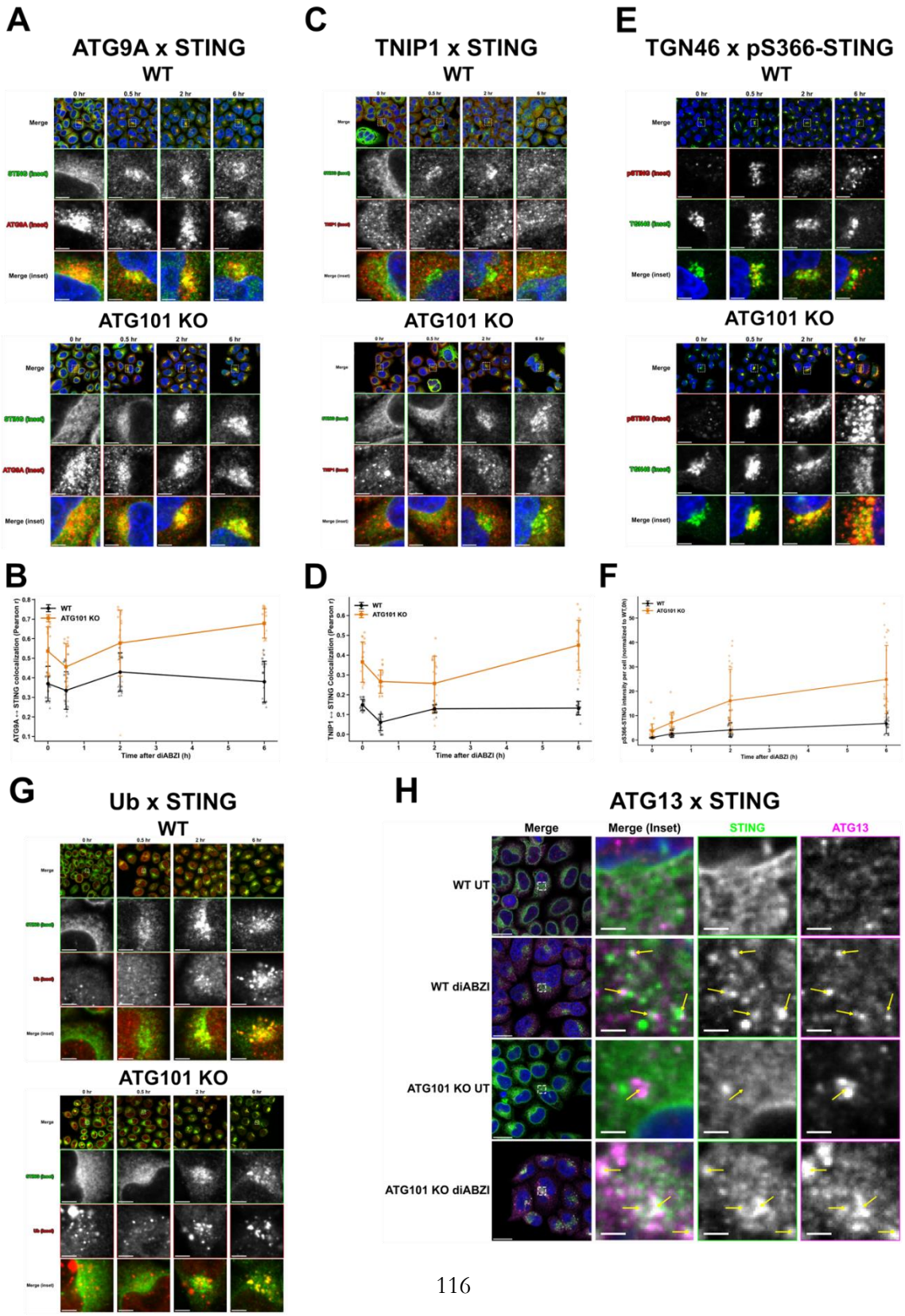
A
ATG9A x STING
WT
ATG101 KO
C
TNIP1 x STING
WT
ATG101 KO
E
TGN46 x pS366-STING
WT
ATG101 KO
B
D
F
G
Ub x STING
WT
ATG101 KO
H
ATG13 x STING
Merge
Merge (Inset)
STING
ATG13
WT UT
WT diABZI
ATG101 KO UT
ATG101 KO diABZI

Figure 4. Loss of ATG101 leads to the accumulation of autophagy markers at STING vesicles and phosphorylated STING. ***(A)*** *Representative live cell spinning disk microscopy images of WT and ATG101 KO HeLa^{STING} cells exposed to diABZI for varying times and immunostained for STING and ATG9A. Main scale bar, 10 µm; inset, 4 µm.* ***(B)*** *Quantification of ATG9A-STING Pearson colocalization coefficient WT, Black; ATG101 KO, orange. The mean and S.D are shown for N=18 sites across two experimental replicates.* ***(C)*** *Representative live cell spinning disk microscopy images of WT and ATG101 KO HeLa^{STING} cells exposed to diABZI for varying times and immunostained for STING and TNIP1. Main scale bar, 10 µm; inset, 4 µm.* ***(D)*** *Quantification of TNIP1-STING Pearson colocalization. WT, Black; ATG101 KO, orange. The mean and S.D are shown for N=18 sites across two experimental replicates.* ***(E)*** *Representative live cell spinning disk microscopy images of WT and ATG101 KO HeLa^{STING} cells exposed to diABZI for varying times and immunostained for pS366-STING and TGN46. Brightness and contrast of the pSTING signal is identical for all images. Main scale bar, 10 µm; inset, 4 µm.* ***(F)*** *Quantification of total pSTING intensity per cell coefficient normalized to WT at 0 hr diABZI. WT, Black; ATG101 KO, orange. The mean and S.D are shown for N=18 sites across two experimental replicates.* ***(G)*** *Representative live cell spinning disk microscopy images of WT and ATG101 KO HeLa^{STING} cells exposed to diABZI for varying times and immunostained for STING and conjugated Ub (FK2). Main scale bar, 10 µm; inset, 4 µm.* ***(H)*** *Representative live cell spinning disk microscopy images of WT and ATG101 KO HeLa^{STING} cells exposed to diABZI for 6 hours and immunostained for STING and ATG13.*

Time-course assays indicated that ATG9A, ATG101, and ATG13 are important for STING degradation. Western blot analysis of STING degradation reports on both endolysosomal and proteasomal degradation, both of which have been observed to degrade STING.[70] To specifically report on endolysosomal degradation, we adapted the HaloTag processing assay to monitor STING clearance. If ligand-conjugated HaloTag-

STING is delivered to the endolysosome, the protease-resistant HaloTag accumulates as a lower band (~33 kDa) sensitive to V-ATPase activity as shown for LC3B and other substrates. The accumulation of the free HaloTag can be analyzed as a measure of STING delivery to the endolysosome (**Figure S2A**). HaloTag-STING-expressing WT, ATG101, ATG9A, ATG13, and FIP200 KO cells were labeled with Halo-TMR and treated for 16 h with diABZI or diABZI + BafA. In WT cells, diABZI induced the accumulation of a ~33 kDa fluorescent fragment, which was lost upon BafA addition (**Figure 2J-K**). This band was also observed 8 h post-diABZI treatment (**Figure S2B,C**). Comparison of the 8 h (**Figure S2B,C**) and 16 h (**Figure 2J,K**) confirms STING endolysosomal delivery is progressive, though a systematic kinetic analysis of HaloTag-STING process was not evaluated. We confirmed that the lower band was αHaloTag-positive and negative for αSTING, indicating that it is free HaloTag following lysosomal cleavage (**Figure S2D**). An increase in the lower free band to HaloTag-STING band was observed upon cGAMP treatment (**Figure S2E,F**). In ATG101 and ATG9A, and to a lesser extent ATG13 KO cells, this lower band was not strongly observed in untreated cells, and its accumulation was reduced upon diABZI treatment, indicating defective endolysosomal STING degradation (**Figure 2J,K**). In contrast, FIP200 KO did not abolish this band at basal levels, or its accumulation upon diABZI treatment (**Figure 2J,K**). Critically, ATG16L1 KO did not alter basal or diABZI-induced degradation of STING (**Figure S2G,H**), ruling out CASM/VAIL as the mechanism underlying STING endolysosomal delivery.

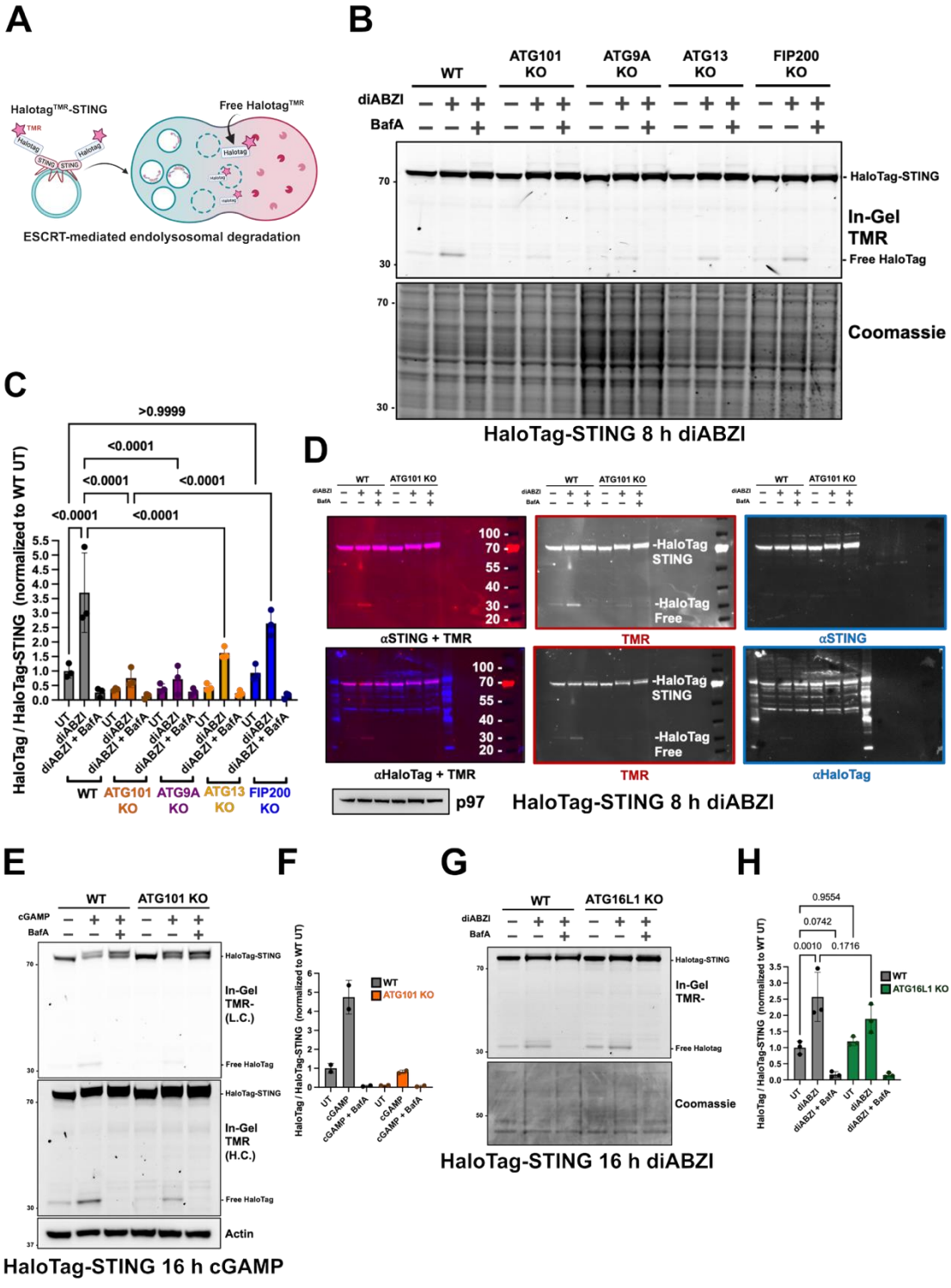
A
Halotag^TMR-STING
Free Halotag^TMR
ESCRT-mediated endolysosomal degradation
B
WT
ATG101 KO
ATG9A KO
ATG13 KO
FIP200 KO
diABZI
BafA
HaloTag-STING
In-Gel TMR
Free HaloTag
Coomassie
HaloTag-STING 8 h diABZI
C
HaloTag / HaloTag-STING (normalized to WT UT)
>0.9999
<0.0001
UT
diABZI
diABZI + BafA
WT
ATG101 KO
ATG9A KO
ATG13 KO
FIP200 KO
D
αSTING + TMR
TMR
αSTING
αHaloTag + TMR
p97
HaloTag-STING 8 h diABZI
E
cGAMP
BafA
HaloTag-STING
In-Gel TMR- (L.C.)
Free HaloTag
In-Gel TMR (H.C.)
Actin
HaloTag-STING 16 h cGAMP
F
G
diABZI
Halotag-STING
In-Gel TMR-
Coomassie
HaloTag-STING 16 h diABZI
H
0.9554
0.0742
0.0010
0.1716
WT
ATG16L1 KO

Figure S2. Validation and additional experiments using the HaloTag-STING processing assay. ***(A)*** *Cartoon detailing the basis of the HaloTag-STING processing assay.* ***(B)*** *In-gel fluorescence image of HaloTag-STING processing assay for WT and ATG101, ATG9A, ATG13, and FIP200 KO cells treated for 8 hours with diABZI or diABZI + BafA. Coomassie stain is used as a loading control* ***(C)*** *Quantification of HaloTag-STING processing in (B). N = 3 biological replicates.* ***(D)*** *Western blot analysis of WT and ATG101 KO HeLa expressing HaloTag-STING tagged with Halo-TMR and treated with diABZI or diABZI + BafA for 8 hours. The western blot was first probed for anti-STING demonstrating signal for the upper HaloTag-STING band, but not the lower processed free HaloTag band, which appears on the TMR fluorescence channel. Blots were stripped and reprobed for anti-HaloTag demonstrating overlapping signal with the TMR channel for both the HaloTag-STING band and lower processed free HaloTag band. p97 is used as a loading control* ***(E)*** *In-gel fluorescence image of HaloTag-STING processing assay for WT and ATG101 KO cells treated for 16 hours with 150 ug/mL of cGAMP. A subsequent western blot for actin is used as a loading control.* ***(F)*** *Quantification of HaloTag-STING processing in (E). N = 2 biological replicates.* ***(G)*** *In gel fluorescence image of HaloTag-STING processing assay for WT and ATG16l1 KO cells treated for 16 hours with diABZI. Coomassie stain is used as a loading control.* ***(H)*** *Quantification of HaloTag-STING processing in (G). N = 3 biological replicates. Data are presented as mean ± SD. (C,G: one-way ANOVA).*

3.3.6 LC3B AND ATG9A ARE NOT DEGRADED DURING STING SIGNALING.

Next, we followed LC3B processing after STING activation using HaloTag-LC3B in $HeLa^{STING}$. Upon diABZI treatment, both cell types form LC3B puncta (**Figure 2L**). LC3B colocalized with pS366-STING following diABZI treatment in WT and ATG101 KO cells (**Figure 2L**). LC3B had higher colocalization with pS366-STING in the ATG101 KO cell line treated with diABZI (**Figure 2M**). We next performed HaloTag-LC3B processing after STING activation. Treatment with diABZI induced LC3B lipidation (CASM); however, it did not increase LC3B degradation (**Figure 2N-O**).

LC3B-I to LC3B-II conversion and degradation was inhibited with BafA. ATG101 KO did not prevent LC3B lipidation, but reduced LC3B degradation (**Figure 2N-O**). Taken together, these results demonstrate that while activated STING undergoes endolysosomal degradation, conjugated LC3B colocalizing at these vesicles is not degraded and is recycled or degraded in the proteasome prior to STING degradation.

LC3B is thought to decorate ATG9A vesicles during canonical autophagy. We found that while endogenous ATG9A was recruited to LC3B positive structures upon diABZI treatment in both WT and ATG101 KO cells (**Figure S3A,B**). ATG9A appeared as vesicles positioned to the LC3B positive regions, rather than fully overlapping (**Figure S3A**). Given that ATG9A vesicles associate closely with STING/LC3B vesicles, we asked whether ATG9A itself was degraded using a HaloTag-ATG9A construct expressed in $HeLa^{STING}$. In WT cells at basal conditions, HaloTag-ATG9A appeared as a diffuse band above 100 kDa. A lower, "free" HaloTag band could be observed that slightly increased following 16 h of Torin1 treatment and lost with BafA treatment (**Figure S3C-D**). We confirmed that the free HaloTag band was HaloTag-positive but ATG9A-negative (**Figure S3I**). These data indicate that a fraction of ATG9A is trafficked to and degraded at the lysosome, but at a lower proportion than that of LC3B. ATG101 KO, but not FIP200 KO reduced levels of ATG9A degradation (**Figure S3C,E**). diABZI treatment for 16 h reduced levels of free HaloTag, suggesting that STING activation does not result in the ATG9A delivery to the lysosome (**Figure S3C,F**). Upon diABZI treatment, a distinct band was observed that was larger than free HaloTag, potentially an N-terminal fragment of ATG9A attached to HaloTag (**Figure S3C**). A time course of diABZI treatment showed that this cleaved band appeared after 8 hours (**Figure S3G**). This band was BafA insensitive, was induced by cGAMP, and was stabilized following proteasome inhibition. Nigericin, a Golgi-targeting K+ ionophore, induced N-terminal fragment (**Figure S3H**)[120]. Together, these data indicate that ATG9A is proteolytically processed upon STING activation. The cleavage is BafA-insensitive but proteasome-sensitive and induced by nigericin, suggesting it may reflect a general response to Golgi/endolysosomal stress rather than a STING-specific event.

The identity of this fragment and its functional significant remain to be determined (Chapter 5).

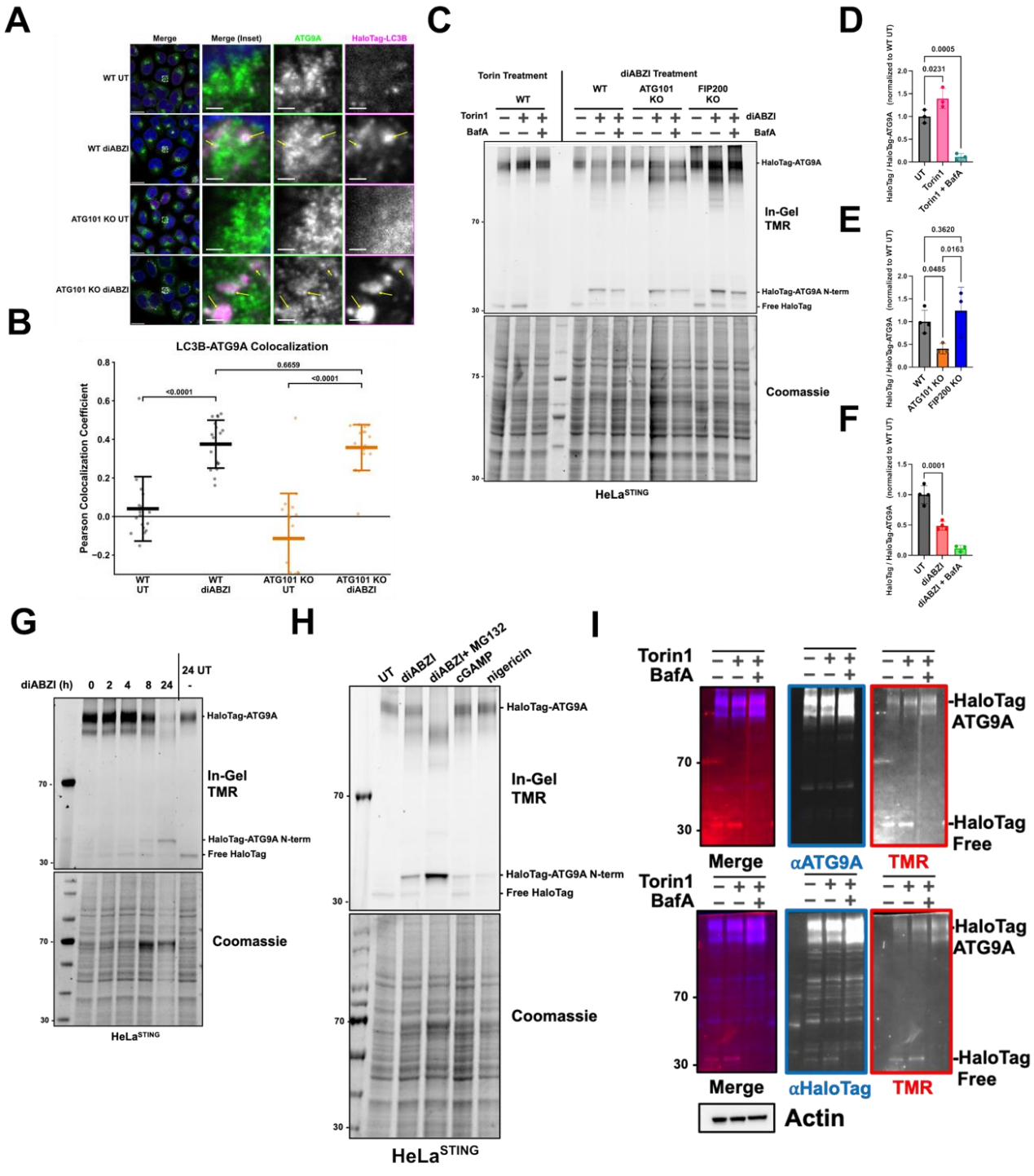

Figure S3. ATG9A is proteolytically processed, but not degraded in the endolysosome during STING activation. ***(A)*** *Representative live cell spinning disk microscopy images of HaloTAG-LC3B WT and ATG101 KO HeLa^{STING} cells control or exposed to diABZI for 6 hours and immunostained for ATG9A. Main scale bar, 10 µm; inset, 4 µm.* ***(B)*** *Pearson correlation coefficient of experiment in (A) for HaloTag-LC3B and ATG9A overlap in N = 18 sites across N = 2 biological replicates.* ***(C)*** *Representative In gel fluorescent image of a HaloTag-ATG9A processing assay. WT, ATG101 KO, or FIP200 KO HeLa^{STING} cells expressing HaloTag-ATG9A were treated with Halo-TMR before being treated with Torin1 or diABZI with or without Baf A for 16 hours. The upper HaloTag-ATG9A band is observed as a smear that increases with diABZI treatment. A lower Free HaloTag band sensitive to BafA is observed above 30KDa. A second proteolytically processed HaloTag band is observed upon diABZI treatment, and is insensitive to BafA. Coomassie stain is used as a loading control.* ***(D)*** *Quantification of HaloTag-ATG9A processing in WT Hela^{STING} cells treated with Torin1 or Torin1 + BafA for 16 hours. N = 3 biological replicates.* ***(E)*** *Quantification of basal HaloTag-ATG9A processing in WT, ATG101, and FIP200 KO Hela^{STING} cells. N = 3 biological replicates.* ***(F)*** *Quantification of HaloTag-ATG9A processing in WT Hela^{STING} cells treated with diABZI or diABZI + BafA. N = 3 biological replicates.* ***(G)*** *In gel fluorescent image of a HaloTag-ATG9A timecourse processing assay. WT Hela^{STING} cells were stained with Halo-TMR and treated with diABZI. Cells were collected at 0, 2, 4, 8 and 24 hours. An untreated control was collected at 24 hours. The accumulation of the lysosomally processed Free HaloTag band is observed over time, whereas the HaloTag N-Terminus fragment is only observed upon diABZI treatment.* ***(H)*** *In gel fluorescent image of a HaloTag-ATG9A processing assay. WT Hela^{STING} cells were stained with Halo-TMR and treated with diABZI, diABZI + 10 uM MG132, 60 ug/ml cGAMP, or 3 ug/ml nigericin for 16 hours. The accumulation of the HaloTag N-Terminus fragment is observed upon diABZI treatment, cGAMP, and to a lesser extent, nigericin. The HaloTag-ATG9A-n-terminal band is stabilized upon MG132 mediated inhibition of the proteasome. Coomassie stain is used as a loading control.* ***(I)*** *Western blot analysis of WT HeLa^{STING}*

expressing HaloTag-ATG9A tagged with Halo-TMR and treated with Torin1 or Torin1 + BafA for 8 hours. The western blot was first probed for αATG9A, demonstrating signal for the upper HaloTag-ATG9A band, but not the lower processed free HaloTag band, which appears on the TMR fluorescence channel. Blots were stripped and reprobed for αHaloTag demonstrating overlapping signal with the TMR channel for both the HaloTag-ATG9A band and lower processed free HaloTag band. Actin is used as a loading control. Data are presented as mean ± SD (B,D: one-way ANOVA).

3.3.7 SUBCELLULAR ORGANIZATION OF STING AND ATG9A VESICLES

Early work on STING trafficking identified STING trafficking with ATG9A at the Golgi body. We sought to determine the nature of STING's interaction with ATG9A using a series of super resolution imaging techniques. Using 3D spatial-detector array confocal microscopy we observed the HaloTag-STING, RFP-ATG9A, ATG101-GFP puncta after 5 hours of diABZI treatment. While at lower resolutions triple-positive spots appeared as unique puncta (Figure 5B), under super resolution conditions these spots appeared as multicolored clusters that associated with each other over time, but did not completely overlap (**Figure 5A**). We fixed cells at this stage and used Structured Illumination Microscopy (SIM) to prevent drift from optical filter switching during live cell imaging and improve resolution (**Figure 5B**). It is possible that STING could encounter ATG9A at the Golgi and co-traffic out in the same vesicle, or that ATG9A vesicles could fuse with STING vesicles in the post-Golgi compartment (**Figure 5D**). These imaging experiments indicate that STING vesicles instead form multi-vesicular clusters with ATG9A vesicles in trans, that also recruit ATG101. These compartments are observed as distinct separation of STING and ATG9A within such clusters (**Figure 5B,C**).

To examine the biophysical properties of these vesicles, we performed fluorescence recovery after photobleaching (FRAP) on diABZI-treated cells (5-7 h). By photobleaching ATG9A-ATG101 vesicles, we sought to determine if ATG101 bound to ATG9A could exchange with the cytosolic pool. ATG9A, a transmembrane protein, would not be expected to show extensive recovery. Neither RFP-ATG9A nor ATG101-

GFP strongly recovered to puncta after bleaching (**Figure S4A-C**). RFP-ATG9A and ATG101-GFP could be observed slowly entering in from adjacent structures, leading to a low apparent mobile fraction (A) and slow recovery times as indicated by low-rate constant (k) values (**Figure S4C**). In contrast, cytosolic ATG101-GFP readily recovered after bleaching, yielding higher A and k values (**Figure S4C,D**). These data indicate that ATG101 forms a long-lasting complex with ATG9A and is not in fast exchange with the cytosolic pool of ATG101. These data agree with recent reports that ATG101-ATG13 binding to ATG9A required a slow and energy intensive fold-switch resulting in slow on and off rates.[121]

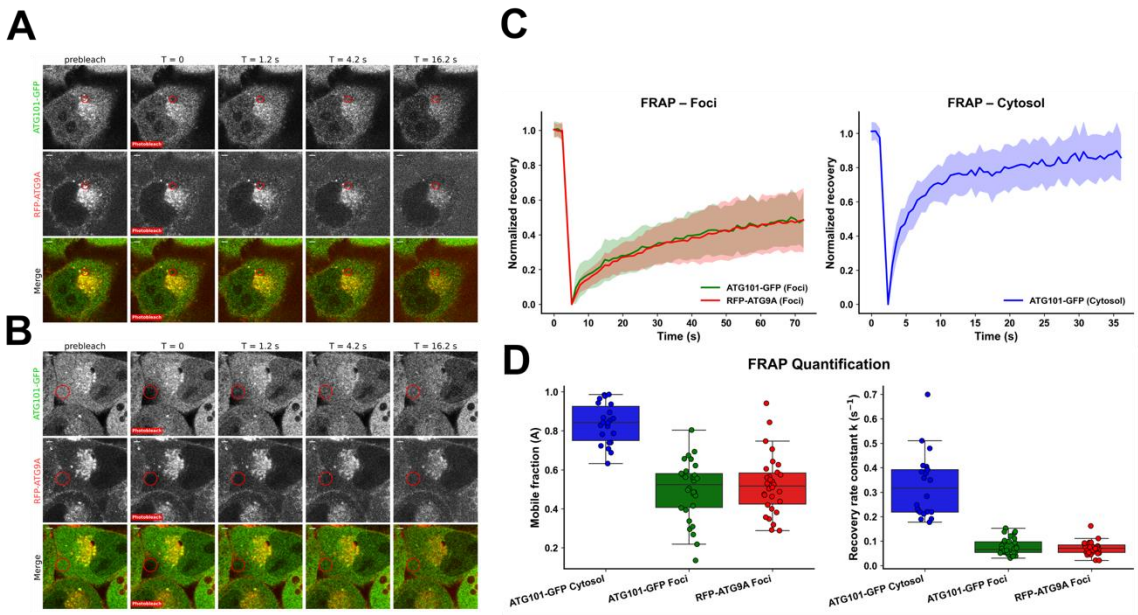

Figure S4. FRAP experiments suggest that ATG101-ATG9A form a stable complex in slow exchange with cytosolic ATG101 during STING signaling. ***(A)*** *Representative FRAP experiment of RFP-ATG9A/ATG101-GFP puncta or* ***(B)*** *cytosol in STING expressing HeLa cells after 5-7 hours of diABZI treatment. Cells were bleached at T = 0 seconds. Scale bar, 5 µm.* ***(C)*** *Quantification of RFP-ATG9A (red)/ATG101-GFP (green) puncta and ATG101-GFP (blue) cytosol FRAP traces. Colored lines and shaded represent the mean and standard deviation across N = 34 (puncta), N = 25 (cytosol) replicates.* ***(D)*** *Individual FRAP replicates were fit to exponential decay curves to*

determine the Mobile Fraction, A, and recovery rate constant, k. Box plots represent the median, first, second, third and fourth quartiles. Data with fitting parameters outside of the 95th percentile were excluded from the analysis.

We observed these clusters with HaloTag-STING and GFP-ATG9A vesicles in WT and ATG101 KO HeLa using live 3D SIM imaging after 5 hours of diABZI treatment. As in prior imaging, ATG9A was observed distinctly separated from STING in closely localized clusters (**Figure 5E**). In the absence of ATG101, large ATG9A-STING clusters were well defined and see migrating together (**Figure 5F**). We next asked what other markers were present at these stalled structures.

3.3.8 STING VESICLES REQUIRE THE ATG9A SUBCOMPLEX TO ENTER THE ENDOLYSOSOMAL PATHWAY

To understand how the ATG9A-ATG13-ATG101 complex suppresses activated STING and where STING stalls in its absence, we tracked STING post-Golgi localization after diABZI treatment in WT and ATG101 KO HeLa^{STING} using the trans-Golgi network protein TGN46. In WT cells, STING trafficked to the Golgi and subsequently exited for degradation, visualized as initial colocalization with TGN46 followed by delocalization (**Figure 5G-I**). In contrast, in ATG101 KO cells, STING entered the Golgi but remained colocalized with TGN46-positive vesicles that were detached from the main Golgi body apparent under higher-resolution confocal imaging (**Figure 5G-I**).

STING is thought to enter the endolysosomal pathway after exit from the Golgi, with its degradation being dependent on a series of Rabs and ESCRT complexes.[66,67,122] We tracked HaloTag-STING after diABZI with a series of Rabs and TSG101, a member of the ESCRT-I complex. As previously reported, STING colocalized with Rab11, a marker of the recycling endosome, with a peak after 4-6 hours and then began to decrease (**Figure 5J,K**). In the absence of ATG101 or ATG9A, STING colocalization with Rab11 was reduced (**Figure 5J,K S5A**). Rab11 condensed into the perinuclear region in all cells, however in ATG101/ATG9A KO cells Rab11 formed a dense

perinuclear structure surrounded by the previously observed stalled STING vesicles. A similar reduction in colocalization compared to WT HeLa was observed for the early endosome marker RAB5A, the late endosome marker RAB7A, and the ESCRT-I member TSG101 (**Figure S5B-G**). The consistent reduction in colocalization across sequential compartment markers, together with impaired lysosomal degradation (**Figure 2J,K**), is consistent with a block in endosomal entry (**Figure 5L**).

Together, these data support a model in which STING exiting the Golgi recruits ATG9A-positive vesicles, and the binding of ATG13-ATG101 to ATG9A, directs these vesicles to the endolysosomal pathway for STING degradation (**Figure 5M**). We term this pathway GLAD (Golgi-to-Lysosome ATG9A–ATG13–ATG101-Dependent degradation). In the absence of a functional GLAD pathway, active STING accumulates in post-Golgi vesicles and drives sustained NF-κB and type I IFN signaling.

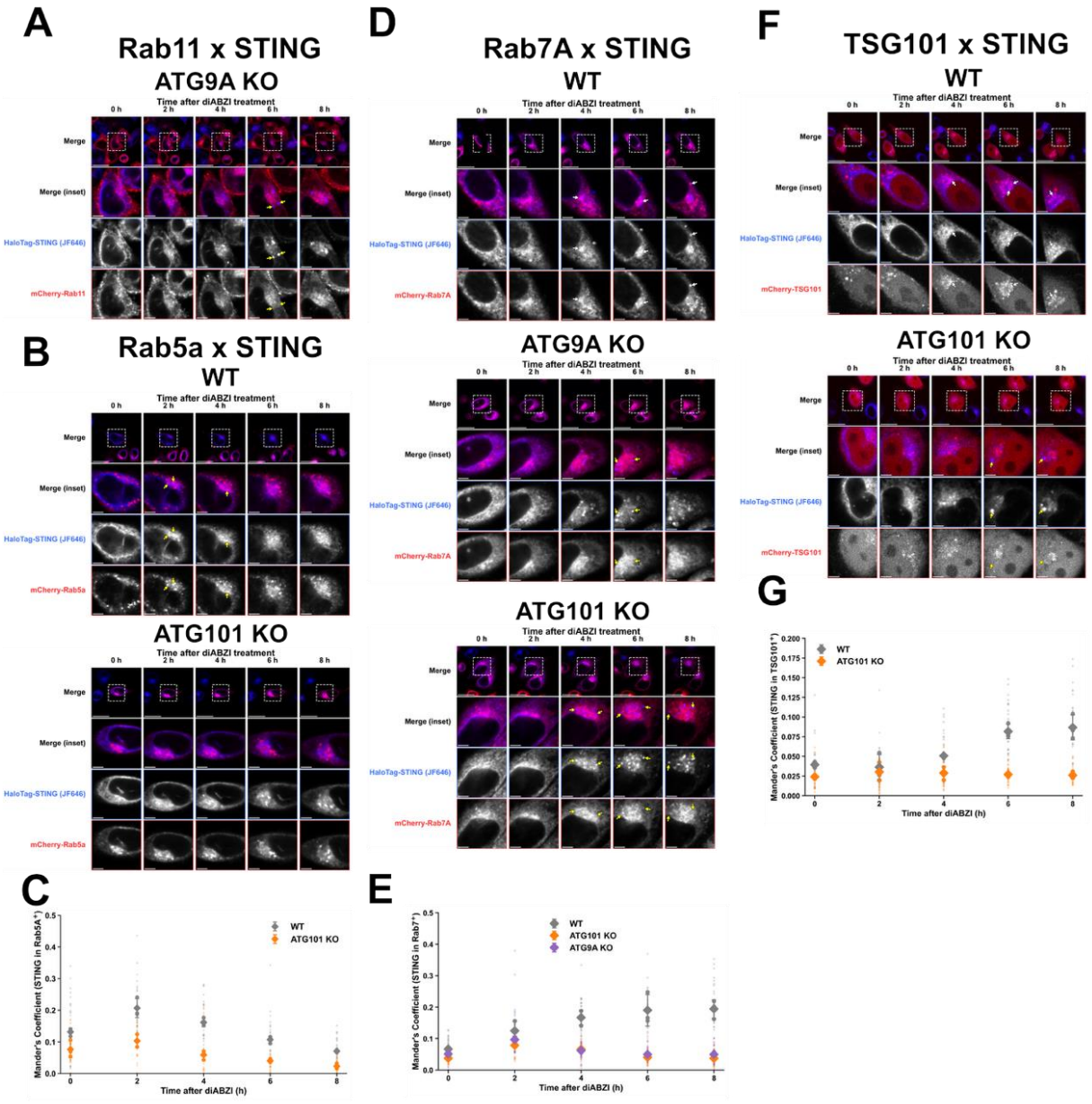

Figure S5. Loss of ATG9A subcomplex members prevents STING's trafficking into the endosome pathway. ***(A)*** *Representative live cell spinning disk microscopy of HeLa ATG9A KO expressing HaloTag-STING and mCherry-Rab11 treated with diABZI, quantified in Figure 5K.* ***(B)*** *Representative live cell spinning disk microscopy of HeLa ATG9A KO expressing HaloTag-STING and mCherry-Rab5a treated with diABZI* ***(C)*** *Quantification of STING colocalization within the Rab5a positive compartment at the*

indicated times after diABZI treatment. ***(D)*** *Representative live cell spinning disk microscopy of HeLa WT, ATG9A KO, and ATG101 KO cells expressing HaloTag-STING and mCherry-Rab7A treated with diABZI.* ***(E)*** *Quantification of STING colocalization within the Rab7A positive compartment at the indicated times after diABZI treatment.* ***(F)*** *Representative live cell spinning disk microscopy of HeLa WT and ATG101 KO cells expressing HaloTag-STING and mCherry-TSG101 treated with diABZI.* ***(G)*** *Quantification of STING colocalization within the TSG101 positive compartment at the indicated times after diABZI treatment. For C,E, and G, N = 3 biological replicates with 10 random sites imaged per replicate. For A,C,E Main scale bar, 20 µm; inset, 4 µm.*

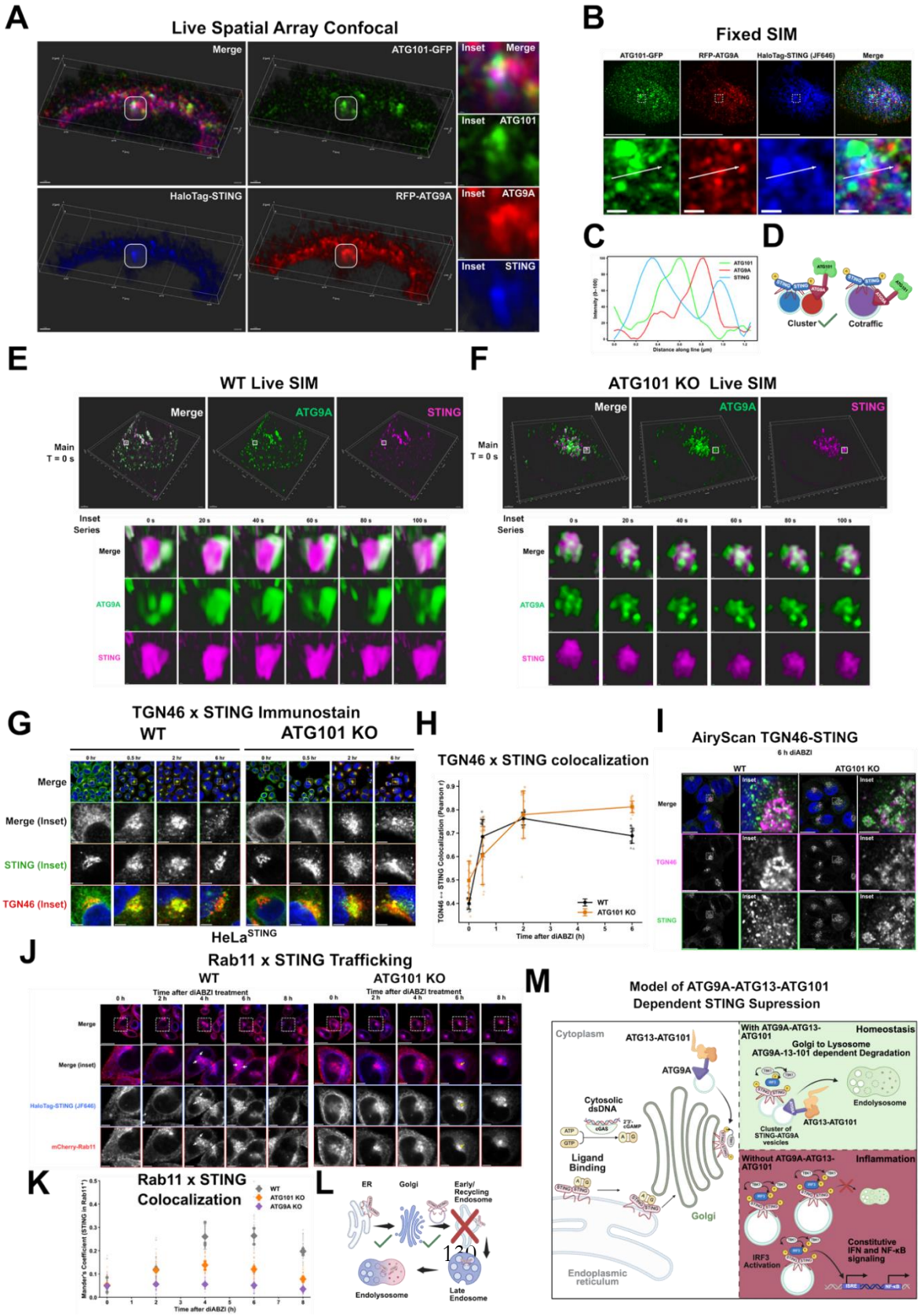
A
Live Spatial Array Confocal
Merge
ATG101-GFP
Inset Merge
Inset ATG101
HaloTag-STING
RFP-ATG9A
Inset ATG9A
Inset STING
B
Fixed SIM
ATG101-GFP
RFP-ATG9A
HaloTag-STING (JF646)
Merge
C
ATG101
ATG9A
STING
Distance along line (µm)
D
Cluster
Cotraffic
E
WT Live SIM
Main
T = 0 s
Merge
ATG9A
STING
Inset
Series
0 s
20 s
40 s
60 s
80 s
100 s
F
ATG101 KO Live SIM
G
TGN46 x STING Immunostain
WT
ATG101 KO
0 hr
0.5 hr
2 hr
4 hr
Merge
Merge (Inset)
STING (Inset)
TGN46 (Inset)
HeLa STING
H
TGN46 x STING colocalization
TGN46 ↔ STING Colocalization (Pearson r)
Time after diABZI (h)
WT
ATG101 KO
I
AiryScan TGN46-STING
6 h diABZI
WT
ATG101 KO
Merge
TGN46
STING
Inset
J
Rab11 x STING Trafficking
WT
ATG101 KO
Time after diABZI treatment
0 h
2 h
4 h
6 h
8 h
Merge
Merge (Inset)
HaloTag-STING (JF646)
mCherry-Rab11
K
Rab11 x STING
Colocalization
Mander's Coefficient (STING in Rab11+)
Time after diABZI (h)
WT
ATG101 KO
ATG9A KO
L
ER
Golgi
Early/
Recycling
Endosome
Endolysosome
Late
Endosome
M
Model of ATG9A-ATG13-ATG101
Dependent STING Supression
Cytoplasm
ATG13-ATG101
ATG9A
Cytosolic
dsDNA
cGAS
2'3' cGAMP
ATP
GTP
Ligand
Binding
Golgi
Endoplasmic
reticulum
With ATG9A-ATG13-ATG101
Homeostasis
Golgi to Lysosome
ATG9A-13-101 dependent Degradation
Endolysosome
Cluster of STING-ATG9A vesicles
Without ATG9A-ATG13-ATG101
Inflammation
IRF3
Activation
Constitutive
IFN and NF-κB
signaling
ISRE
NF-κB

Figure 5. ATG9A vesicles form multivesicular clusters with STING, that requires ATG101 to direct STING's entry into the endolysosomal pathway. ***(A)*** *Representative 3D spatial array confocal live cell imaging still from Video S1 of an ATG9A-ATG101-STING positive multivesicular cluster. HeLa cells expressing HaloTag-STING, RFP-ATG9A, and ATG101-GFP were treated with diABZI for 5 hours. Main scale bar, 1 µm; inset, 0.2 µm* ***(B)*** *Representative Structured Illumination Microscopy of HeLa cells expressing HaloTag-STING, RFP-ATG9A, and ATG101-GFP were treated with diABZI for 6 hours before fixation. Main scale bar, 10 µm; inset, 0.5 µm.* ***(C)*** *Representative line scan from (B). All channels max intensity are normalized to 1.* ***(D)*** *Potential models of STING and ATG9A vesicle trafficking.* ***(E)*** *Simultaneous SIM volume imaging of HaloTag-STING and GFP-ATG9A expressing HeLa WT showing the progression of a STING-ATG9A cluster. Main scale bar, 3 µm; inset, 0.3 µm.* ***(F)*** *Simultaneous SIM volume imaging of HaloTag-STING and GFP-ATG9A expressing HeLa ATG101 KO showing the progression of a STING-ATG9A cluster. Main scale bar, 2 µm; inset, 0.1 µm.* ***(G)*** *Representative live cell spinning disk imaging of a diABZI time-course experiment in WT and ATG101 KO cells expressing BFP-P2A-STING. Cells were immunostained for TGN46 (trans-Golgi marker) and STING. DAPI was used as a nuclear stain. Main scale bar, 20 µm; insets, 4 µm.* ***(H)*** *Quantification of TGN46 and STING colocalization using the Pearson correlation coefficient for the time-course shown in (G) in WT (black) and ATG101 KO (orange). Small points represent N =18 random sites measured across two independent experiments for each timepoint.* ***(I)*** *Representative Airyscan confocal image of WT and ATG101 KO HeLa^{STING} cells treated with diABZI for 6 hours and immunostained for STING and TGN46. Main scale bar, 20 µm; inset, 3 µm.* ***(J)*** *Live cell spinning disk microscopy of HeLa WT, and ATG101 KO cells expressing HaloTag-STING and mCherry-Rab11 treated with diABZI.* ***(K)*** *Quantification of STING colocalization within the Rab11 positive compartment at the indicated times after diABZI treatment. N = 3 biological replicates with 10 random sites imaged per replicate.* ***(L)*** *Model of STING's trafficking in WT cell and where stalling occurs in ATG101/9A KO cells.* ***(M)*** *Cartoon model of homeostatic STING signaling*

and in the absence of the ATG9A-13-101 subcomplex. Low basal levels of cytosolic DNA activate cGAS which synthesizes 2',3'-cGAMP, resulting in the trafficking of STING from the ER to the Golgi. STING associates with independent ATG9A vesicles at the trans-Golgi and is exported in vesicles that recruit ATG13-ATG101. The stable ATG9A-ATG13-ATG101 complex results in the trafficking of STING vesicles to the endosome where STING is ultimately degraded by the lysosome via an ESCRT-dependent manner. In the absence of the functioning ATG9A-ATG13-ATG101, STING trafficking from the Golgi to Lysosome, and subsequent degradation, is impaired leading to accumulation of active STING vesicles mediating NF-κB and Type-I IFN activation and driving chronic inflammation.

3.4 DISCUSSION

This chapter identifies a Golgi-to-lysosome degradation pathway, GLAD, through which the ATG9A–ATG13–ATG101 complex mediates the post-Golgi trafficking and lysosomal degradation of activated STING. This function is independent of FIP200, canonical autophagy, and the ATG8 lipidation machinery, although both GLAD and canonical autophagy depend on the interaction of ATG13–ATG101 with ATG9A. Notably, GLAD selectively degrades STING without co-degrading LC3B conjugated to adjacent membranes, distinguishing it from bulk lysosomal engulfment of STING-containing vesicles.

These findings resolve a long-standing mystery in the STING trafficking field. Termination of STING signaling is a well-studied process[64,122,123]. Previous work showed that STING colocalized with ATG9A and that loss of ATG9A enhanced pathway activation[124]. However, since no double-membrane autophagosome was observed, and other autophagy proteins (ATG16L1, ATG7, and ULK1) were not critical, this was interpreted to be an autophagy-independent function of ATG9A. Subsequent work demonstrated that while a fraction of STING could be degraded by the proteasome, most STING is degraded at the lysosome.[70] FIP200 loss did not impair STING degradation[71] and STING lysosomal delivery was attributed to the ESCRT

pathway[66,122,123]. Our data provide a molecular explanation for ATG9A's role: ATG9A acts in concert with the ATG13-ATG101 HORMA dimer to direct STING toward the endolysosomal pathway. The dispensability of FIP200 and ATG16L1, demonstrated by the HaloTag-STING processing assays, further distinguishes GLAD from both canonical autophagy and VAIL/CASM. While this thesis was in preparation, another report found that ATG9A is involved in STING degradation, reinterpreting prior results in a mouse model demonstrating that keratinocyte-specific ATG9A KO leads to inflammatory skin disease.[125,126] Our model is in agreement that ATG9A KO disrupts STING degradation, however our data demonstrate this is not dependent on ATG8-lipidation machinery and instead requires the ATG13-ATG101 HORMA dimer binding to ATG9A's HDIR motif, as established in Chapter 2. ATG9A has repeatedly emerged as the top hit in genetic screens for STING degradation, yet its precise role remained unclear.[54,66,127] Our work establishes that ATG9A's immune regulatory function requires its interaction with ATG13 and ATG101, rather than ATG9A alone, as the functional unit.

Super-resolution and structured illumination microscopy revealed that STING and ATG9A vesicles form multivesicular clusters in trans, associating closely without fully merging. FRAP experiments demonstrated that ATG101 bound to ATG9A is not in rapid exchange with the cytosolic pool, consistent with the slow kinetics of the ATG13–ATG101 conformational switch[121]. These observations support a model in which ATG9A-positive vesicles dock alongside STING vesicles and, through ATG13–ATG101-dependent mechanisms, license their entry into the endolysosomal system. ATG101 KO produces a more severe STING trafficking defect than ATG13 KO, paralleling the autophagy severity hierarchy in Chapter 2. Separately, diABZI-induced LC3B lipidation occurs independently of ATG101 and does not result in LC3B endolysosomal degradation, dissociating STING-induced CASM from GLAD. The precise molecular mechanism, substrate specificity, and evolutionary implications of GLAD are explored in Chapter 5.

The clinical relevance of GLAD is supported by cancer genomics analyses. ATG101 is upregulated in multiple cancers and has been identified as a negative prognostic marker in hepatocellular carcinoma (The Cancer Genome Atlas alias: LIHC), where high expression is associated with reduced survival outcomes[128]. ATG9A and ATG13, but not FIP200, expression are similarly associated with reduced survival in this cancer subtype (**Figure S6A-B**). High ATG101 expression correlates with reduced immune cell (CD8+ T-cells and dendritic cells) infiltration, and reduced response to immune checkpoint inhibitors (ICI) as measured by the Tumor Immune Dysfunction and Exclusion (TIDE) score (**Figure S6C-D**). In genome-wide CRISPR screens, ATG9A and ATG101 KO sensitized tumor cells to immune clearance[129], and a ULK1/2 inhibitor that degrades ATG13 was found to reduce tumor burden in a mouse model of pancreatic ductal adenocarcinoma (PDAC)[130]. These data are consistent with tumors exploiting the GLAD pathway to suppress STING-mediated immunosurveillance.

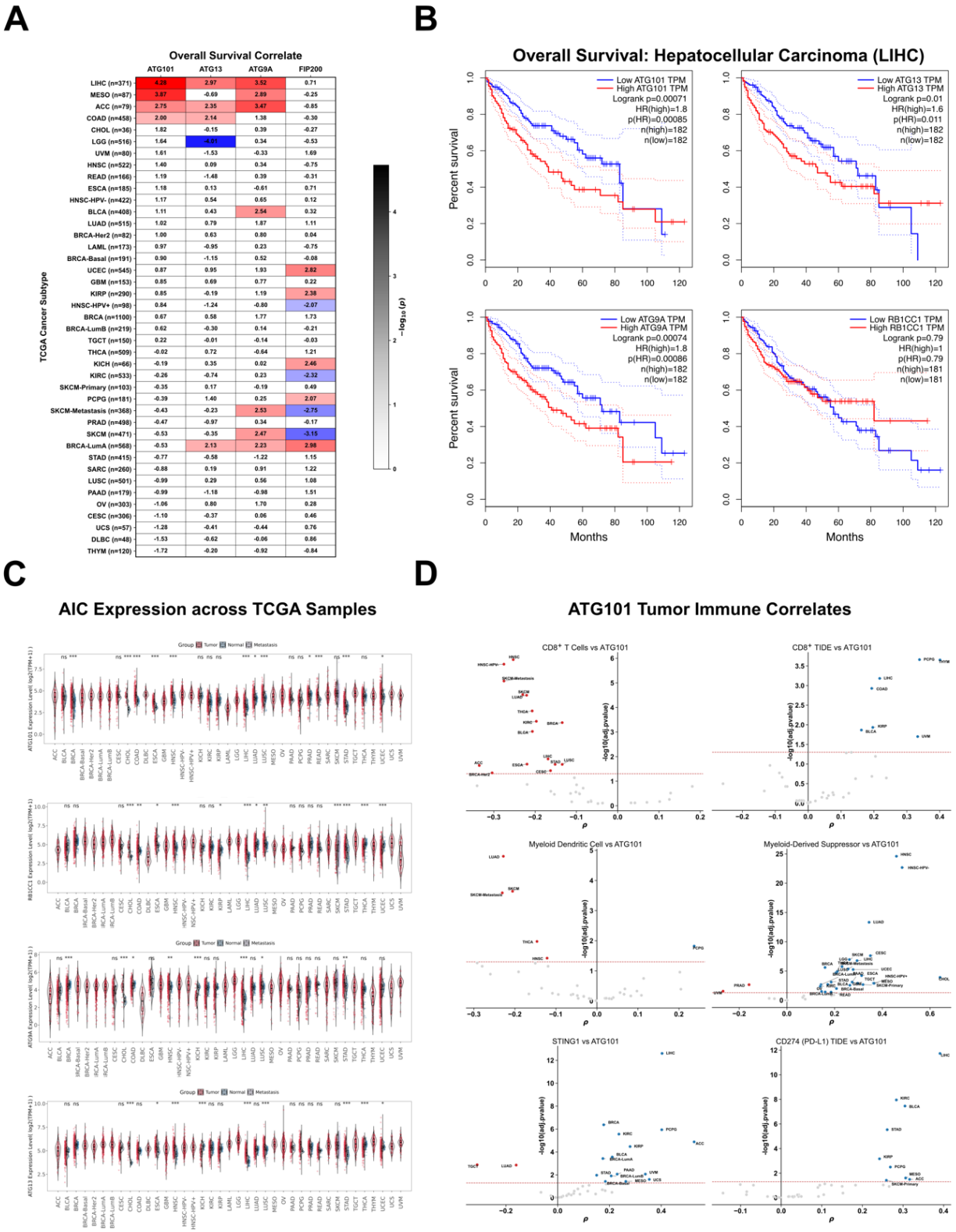
A
Overall Survival Correlate
ATG101
ATG13
ATG9A
FIP200
LIHC (n=371) 4.28 2.97 3.52 0.71
MESO (n=87) 3.87 -0.69 2.89 -0.25
ACC (n=79) 2.75 2.35 3.47 -0.85
COAD (n=458) 2.00 2.14 1.38 -0.30
CHOL (n=36) 1.82 -0.15 0.39 -0.27
LGG (n=516) 1.64 -4.01 0.34 -0.53
UVM (n=80) 1.61 -1.53 -0.33 1.69
HNSC (n=522) 1.40 0.09 0.34 -0.75
READ (n=166) 1.19 -1.48 0.39 -0.31
ESCA (n=185) 1.18 0.13 -0.61 0.71
HNSC-HPV- (n=422) 1.17 0.54 0.65 0.12
BLCA (n=408) 1.11 0.43 2.54 0.32
LUAD (n=515) 1.02 0.79 1.87 1.11
BRCA-Her2 (n=82) 1.00 0.63 0.80 0.04
LAML (n=173) 0.97 -0.95 0.23 -0.75
BRCA-Basal (n=191) 0.90 -1.15 0.52 -0.08
UCEC (n=545) 0.87 0.95 1.93 2.82
GBM (n=153) 0.85 0.69 0.77 0.22
KIRP (n=290) 0.85 -0.19 1.19 2.38
HNSC-HPV+ (n=98) 0.84 -1.24 -0.80 -2.07
BRCA (n=1100) 0.67 0.58 1.77 1.73
BRCA-LumB (n=219) 0.62 -0.30 0.14 -0.21
TGCT (n=150) 0.22 -0.01 -0.14 -0.03
THCA (n=509) -0.02 0.72 -0.64 1.21
KICH (n=66) -0.19 0.35 0.02 2.46
KIRC (n=533) -0.26 -0.74 0.23 -2.32
SKCM-Primary (n=103) -0.35 0.17 -0.19 0.49
PCPG (n=181) -0.39 1.40 0.25 2.07
SKCM-Metastasis (n=368) -0.43 -0.23 2.53 -2.75
PRAD (n=498) -0.47 -0.97 0.34 -0.17
SKCM (n=471) -0.53 -0.35 2.47 -3.15
BRCA-LumA (n=568) -0.53 2.13 2.23 2.98
STAD (n=415) -0.77 -0.58 -1.22 1.15
SARC (n=260) -0.88 0.19 0.91 1.22
LUSC (n=501) -0.99 0.29 0.56 1.08
PAAD (n=179) -0.99 -1.18 -0.98 1.51
OV (n=303) -1.06 0.80 1.70 0.28
CESC (n=306) -1.10 -0.37 0.06 0.46
UCS (n=57) -1.28 -0.41 -0.44 0.76
DLBC (n=48) -1.53 -0.62 -0.06 0.86
THYM (n=120) -1.72 -0.20 -0.92 -0.84
TCGA Cancer Subtype
−log10 (p)
B
Overall Survival: Hepatocellular Carcinoma (LIHC)
Low ATG101 TPM
High ATG101 TPM
Logrank p=0.00071
HR(high)=1.8
p(HR)=0.00085
n(high)=182
n(low)=182
Low ATG13 TPM
High ATG13 TPM
Logrank p=0.01
HR(high)=1.6
p(HR)=0.011
n(high)=182
n(low)=182
Low ATG9A TPM
High ATG9A TPM
Logrank p=0.00074
HR(high)=1.8
p(HR)=0.00086
n(high)=182
n(low)=182
Low RB1CC1 TPM
High RB1CC1 TPM
Logrank p=0.79
HR(high)=1
p(HR)=0.79
n(high)=181
n(low)=181
Percent survival
Months
C
AIC Expression across TCGA Samples
Group Tumor Normal Metastasis
ATG101 Expression Level(log2(TPM+1))
RB1CC1 Expression Level(log2(TPM+1))
ATG9A Expression Level(log2(TPM+1))
ATG13 Expression Level(log2(TPM+1))
D
ATG101 Tumor Immune Correlates
CD8+ T Cells vs ATG101
CD8+ TIDE vs ATG101
Myeloid Dendritic Cell vs ATG101
Myeloid-Derived Suppressor vs ATG101
STING1 vs ATG101
CD274 (PD-L1) TIDE vs ATG101
-log10(adj.pvalue)
ρ

Figure S6. ATG101 and GLAD components are associated with poor cancer prognosis and tumor immune dysfunction. ***(A)*** *Heatmap of overall survival correlations with AIC components gene expression in the TCGA database. Heatmap numbers indicate the Cox proportional hazard model survival outcome. Red indicates a significant negative survival correlation whereas blue indicates a significant positive survival correlation in a given TCGA cancer subtype. Color darkness is proportional to the -Log10 of the adjusted p-value. GLAD components, but not RB1CC1 (FIP200) are negatively associated with survival in a subset of cancers.* ***(B)*** *Kaplan-Meier survival curves for TCGA Hepatocellular Carcinoma (LIHC) cases. Patients were stratified by high or low expression of the gene of interest (50th percentiles). The Hazard Ratio (HR) is calculated for each comparison. GLAD complex components, but not RB1CC1 (FIP200) are associated with reduced survival in LIHC.* ***(C)*** *Expression of AIC components in tumor tissue (red) and matched controls (blue) across all TCGA tumor samples. NS P > 0.05, *P ≤ 0.05, **P ≤ 0.01, ***P ≤ 0.001, ****P ≤ 0.0001 (B,D: Student's T-test; N: one-way ANOVA).* ***(D)*** *Immune cell infiltration, Tumor Immune Dysfunction and Exclusion (TIDE), and immune gene correlations with ATG101 expression across the TCGA database. ρ is the Spearman's rank correlation coefficient. Tumor subtypes with significant (adjusted P-value ≤ 0.05) negative correlation are colored in red while positive correlations are denoted in blue. ATG101 expression is associated with poor CD8+ and myeloid dendritic cell infiltration. ATG101 expression is conversely associated with a higher TIDE CD8 dysfunction score and increased infiltration of myeloid-derived suppressor cells. ATG101 expression correlates with both STING1 mRNA expression and the PD-L1 TIDE score; these two correlations are most significant in the LIHC subtype.*

In summary, this chapter establishes GLAD as an autophagy-independent pathway for STING degradation and, together with Chapter 2, defines a previously unrecognized function for autophagy initiation machinery in the spatial regulation of innate immune signaling. Limitations include reliance on overexpressed STING constructs in HeLa

cells and the unresolved mechanism by which ATG13–ATG101 directs endolysosomal entry, both of which are addressed in Chapter 5.

3.5 METHODS

Cell culture

HeLa S3 cells (ATCC CCL-2.2; RRID:CVCL_0058), HEK293T (ATCC CRL-3216), MCF-7, K562, and THP-1 cells were used in this study. HeLa S3, HEK293T, and MCF-7 cells were cultured at 37°C in a humidified 5% CO^2 atmosphere in Dulbecco's Modified Eagle Medium (DMEM; Sigma-Aldrich) supplemented with 10% non-heat-inactivated fetal bovine serum (FBS; R&D Systems) and 1% penicillin-streptomycin (Gibco). Adherent cells were passaged every 2–3 days using 1× TrypLE Express (phenol red-free; Gibco). THP-1 and K562 cells were cultured under identical conditions in RPMI-1640 medium (Corning) supplemented with 10% non-heat-inactivated FBS, 1% penicillin-streptomycin, and 2 mM L-glutamine. THP-1 cells were maintained at a density of 3×10^5 cells/mL at each passage without differentiation induction. All cell lines were used below passage 8. STR authentication was not performed. All cell lines were tested monthly for mycoplasma contamination using the MycoAlert Mycoplasma Detection Kit (Lonza) and consistently tested negative.

Additional cell lines used in this chapter include $HeLa^{STING}$ (HeLa S3 stably expressing BFP-P2A-STING; Addgene #102586), ATG101 KO $HeLa^{STING}$, ATG13 KO $HeLa^{STING}$, ATG9A KO $HeLa^{STING}$, and FIP200 KO $HeLa^{STING}$. ATG101/cGAS DKO, ATG101/STING DKO, and ATG101/TBK1 DKO lines were generated by sequential CRISPR-Cas9 editing. The TBK1 KO line was previously described (Lazarou et al., 2015).

Generation of stable cell lines

Stable cell lines were generated using lentiviral and retroviral transduction. For lentiviral production, HEK293T cells were seeded in 6-well plates and transfected with pHDM-G (0.2 μg), CAG4RTR2 (0.6 μg), CAGGHIVgpco (0.6 μg), and the plasmid construct

containing the gene of interest using polyethyleneimine (PEI; Polysciences) at a 3:1 PEI:DNA ratio (w/w) in serum-free DMEM. For retroviral production, HEK293T cells were similarly transfected with pUMVC (0.4 µg) and VSV-G (0.8 µg) alongside the gene of interest construct using the same PEI:DNA ratio. In both cases, 9 µg PEI was diluted in 150 µL serum-free DMEM prior to addition to cells. Media were replaced 16 hours post-transfection, and viral supernatants were harvested 48 h post-transfection and filtered through 0.45 µm syringe filters (WHA9914-2504, Cytiva) to remove contaminating cells. Viral supernatants were used crude without further concentration.

Target cells were seeded at 50,000 cells/well in 12-well plates and transduced by spinfection with 500 µL virus-containing media supplemented with 8 µg/mL polybrene (Sigma-Aldrich) at 800 × *g* for 45 minutes at 16°C. Transduced cells were selected with 5 µg/mL puromycin (Thermo Scientific) for 72 hours to establish stable integrants. The cells were then expanded and sorted by fluorescence-activated cell sorting (FACS) to additionally select for infected cells and normalize protein expression across individual cells.

Plasmids used in this chapter included: pTRIP-SFFV-mTagBFP-2A-STING (Addgene #102586), pTRIP-SFFV-HaloTag-STING, pMXs-puro-HaloTag7-ATG9A, pMRX-IP-HaloTag7-LC3 (Addgene #184899; gift from Noboru Mizushima), ATG101-GFP (generated by Gibson assembly), pMXs-puro-RFP-ATG9A, GFP-ATG9A (generated by replacing RFP in pMXs-puro-RFP-ATG9A; Addgene #60609), pHAGE-Flag-Parkin, pHAGE-mtKeima, pHAGE-mCherry-Rab5a, pHAGE-mCherry-Rab7A, pHAGE-mCherry-Rab11, and pHAGE-mCherry-TSG101.

CRISPR-Cas9 genome editing

Knockout (KO) cell lines were generated in-house using CRISPR-Cas9. Cells were either transfected with a Cas9 plasmid encoding the appropriate sgRNA and carrying a puromycin resistance marker, followed by selection with 5 µg/mL puromycin, or transfected with a GFP-tagged Cas9 plasmid encoding the appropriate sgRNA, after which GFP-positive cells were isolated by single-cell fluorescence-activated cell sorting

(FACS) 48 h post-transfection. In both cases, 20 clones per target were screened. KO cell lines for ULK1, FIP200, ATG13, ATG101, ATG9A, ATG16L1, cGAS, STING, and TBK1 were generated in HeLa S3 cells. The ULK1/2 double knockout (DKO) was generated by sequential CRISPR-Cas9 editing of ULK2 in the ULK1 KO background. The FIP200/ATG101, ATG101/cGAS, ATG101/STING, and ATG101/TBK1 DKO lines were similarly generated by sequential editing. The FIP200 KO line was previously described (Vargas et al., 2019), the ATG16L1 KO line was previously described (Fischer et al., 2020), and the TBK1 KO line was previously described (Lazarou et al., 2015). All KO cell lines were validated by Western blot.

Doxycycline-inducible shRNA knockdown

Doxycycline (dox)-inducible shRNA knockdown was performed in THP-1 cells using the pLKO-Tet-On lentiviral vector (Addgene #98398). shRNA sequences targeting ATG101, ATG9A, and ATG13 were cloned into the vector by restriction cloning. A non-targeting (NT) shRNA was used as a control. THP-1 cells were transduced and selected as described above. For knockdown induction, cells were treated with doxycycline for 72 hours before experimental treatments or collection.

Genomic PCR for CRISPR knockout validation

Genomic DNA was extracted from cell pellets using the QuickExtract DNA Extraction Solution (Qiagen) according to the manufacturer's instructions. PCR was performed using Q5 High-Fidelity DNA Polymerase (New England Biolabs) with primers flanking the CRISPR-targeted region, designed to amplify a ~500–1000 bp product. Each 25 µL reaction contained 12.5 µL of 2× Q5 Master Mix, 0.5 µM each primer, and ~50 ng of genomic DNA. PCR cycling conditions were: initial denaturation at 98 °C for 30 s, followed by 30 cycles of 98 °C for 10 s, 58 °C for 20 s, and 72 °C for 30 s, with a final extension at 72 °C for 2 min. Products were run on a 1.5% agarose gel stained with SYBR Safe, purified by gel clean-up, and sent for Sanger sequencing of the amplified product containing indels.

Conditioned media experiment

To assess whether the ATG101 KO-induced immune response is cell-autonomous, conditioned media transfer experiments were performed. ATG101 KO cells were cultured for 48 hours, after which the culture media was collected and directly transferred without filtering or additional processing to replace the media on WT HeLa S3 cells. WT HeLa cells were cultured in the conditioned media for 24 hours before lysis and Western blot analysis for interferon-stimulated gene products.

Cell viability assay

Cells were seeded at 400 cells per well in each well of a white 384-well plate (Greiner 781080). Thirty microliters of DMEM supplemented with glucose (4.5 mg/mL), 10% FBS, and 1% penicillin-streptomycin was used as the culture medium. Following a 24-hour incubation at 37°C and 5% CO^2, the cells were treated with the designated compound (cisplatin, KU57788, or doxorubicin) with DMSO concentration no more than 0.5% and four biological replicates per condition. The cells were incubated with compounds for 24 or 48 hours, and then cell viability was assessed by the addition of 30 µL of CellTiter-Glo reagent (G7573, Promega). The cells were incubated for 10 min at room temperature, and luminescence was measured using a BioTek Synergy Neo Microplate Reader. Cell viability for each well was calculated by comparing the percentage of viable treated cells to the DMSO control (i.e., 0 µM compound). IC_{50} values were calculated from eight replicates collected in at least two separate experiments via nonlinear regression in GraphPad Prism 10.

Microscopy-based micronuclei assay

Cells were plated at 10,000 cells per well in 96-well plates (655086, Greiner) and incubated overnight. The following day, live cells were stained with Hoechst dye for 10 minutes at 37°C, followed by three 5-minute washes with PBS. Imaging was performed at 40× magnification using an ImageXpress Micro Confocal Plate Reader (Molecular Devices). Ten images were acquired and averaged per well, with each cell line imaged in triplicate wells. Two imaging channels were used: DAPI (excitation at 377 nm) and brightfield. Image analysis was conducted using MetaXpress software (Version

6.7.1.157). The number of micronuclei and total number of cells were counted, and the percentage of cells containing micronuclei was calculated.

For dsDNA-induced micronuclei drug treatment experiments, cells were plated at 250,000 cells per well in 6-well plates and treated with 200 nM doxorubicin (Sigma, Cat# D1515) for 24 hours. Cells were then trypsinized, counted, and replated at 10,000 cells per well into 96-well plates (655086, Greiner) in media containing 200 nM doxorubicin. Cells were imaged at 24 and 48 hours post-plating. Quantification was performed as described above.

ELISA

2',3'-Cyclic GAMP ELISA (K067; Arbor Assays) was performed according to the manufacturer's instructions to quantify intracellular cGAMP levels in WT, ATG101 KO, ATG101 KO + ATG101-GFP, ATG13 KO, and FIP200 KO cells. The absorbance of the ELISA plate was measured using a BioTek Synergy Neo2 Microplate Reader with Gen5 software.

Quantitative PCR

Total RNA was extracted from 800,000 cells using the Direct-zol RNA MicroPrep kit (R2062, Zymo Research). One microgram of total RNA was used for cDNA synthesis via the High-Capacity cDNA Reverse Transcription Kit (4368814, Thermo Fisher Scientific) as per the manufacturer's protocol. Quantitative PCR was performed using Power SYBR Green PCR Master Mix (4368577, Thermo Fisher Scientific). Fold changes in RNA expression were calculated using the ΔΔCt method compared to actin as a loading control. Where indicated, cells were treated with cGAMP (60 µg/mL; MedChemExpress) for 8 hours prior to RNA extraction. RT-qPCR primers for IFIT3, TNF-α, IL-6, and IFNβ are provided in Supplementary Table X.

Protein gels and Western blots

Cells were plated in six-well plates at a density of 400,000 cells per well and incubated overnight. Cells were harvested using TrypLE Express (12604-013, Thermo Fisher

Scientific) and pelleted by centrifugation. Cell pellets were washed with phosphate-buffered saline (PBS) and lysed in radioimmunoprecipitation assay (RIPA) buffer (50 mM Tris, 150 mM NaCl, 0.1% SDS, 0.5% sodium deoxycholate, 1% Triton X-100) supplemented with EDTA-free broad-spectrum protease inhibitors (Thermo Fisher Scientific) for 15 minutes on ice. Lysates were cleared by centrifugation at 20,000 × *g* for 15 minutes at 4°C, and soluble fractions were collected. Protein concentration was determined using the BCA assay (Thermo Fisher Scientific). Samples were diluted 1:4 in 4× SDS loading buffer, denatured at 95°C for 5 minutes, and briefly centrifuged. Five to ten micrograms of protein per sample was resolved on 4–20% Mini-PROTEAN TGX gels (Bio-Rad) at 150 V for 60 minutes, or on 4–12% Bis-Tris gels in MOPS running buffer where indicated. Proteins were transferred to nitrocellulose membranes using the Trans-Blot Turbo Transfer System (Bio-Rad) for 10 minutes. Membranes were stained with Ponceau S (Thermo Scientific) for 5 minutes at room temperature, washed with deionized water, and imaged using a ChemiDoc MP Imaging System (Bio-Rad). Membranes were washed in TBS-T (Tris-buffered saline + 0.1% Tween-20) and blocked for 1 hour at room temperature in 5% nonfat milk in TBS-T. Primary antibody incubation was performed overnight at 4°C in 2.5% nonfat milk in TBS-T at the concentrations listed below. Membranes were washed three times for 5 minutes with TBS-T and incubated for 1 hour at room temperature with goat anti-mouse or goat anti-rabbit HRP-conjugated secondary antibodies (1706515 and 1706516, Bio-Rad; RRID:AB_11125142 and RRID:AB_11125547) diluted 1:3000 in 2.5% nonfat milk in TBS-T. Membranes were washed three times with TBS-T and imaged using Immobilon ECL Ultra Western HRP Substrate (WBKLS0500, MilliporeSigma) and a ChemiDoc MP Imaging System (Bio-Rad). Densitometry analysis was performed using ImageLab version 6.1 (RRID:SCR_014210). All densitometry was first normalized to Ponceau S staining and then to the WT condition set at 1, unless otherwise noted.

For STING signaling timecourse experiments, HeLa^{STING} cells were treated with 1 μM diABZI (MedChemExpress) and collected at the indicated time points. pS366-STING and pS172-TBK1 levels were normalized to peak activation at 1 h post-diABZI. For

THP-1 shRNA experiments, cells were treated with doxycycline for 72 hours before adding diABZI for the indicated times.

HaloTag processing assays

Cells expressing HaloTag fusion proteins (HaloTag-STING, HaloTag-LC3B, or HaloTag-ATG9A) were plated at 200,000 cells per well in 12-well plates. The next day, cells were incubated with media containing 100 nM Halo-TMR ligand (G8252A, Promega) for 20 minutes. Cells were washed three times with PBS before experimental treatments. Treatments included diABZI (1 μM), cGAMP (150 μg/mL), nigericin (3 μg/mL), Torin1 (250 nM), and/or bafilomycin A1 (BafA; 100 nM, Selleckchem) for the durations indicated in the figure legends. For proteasome inhibition experiments, MG132 (10 μM, Selleckchem) was used. Following a PBS wash, cells were directly lysed on plate in 1× LDS sample buffer supplemented with cOmplete Protease Inhibitor cocktail (Roche), and boiled immediately at 99 °C for 10 min. Protein quantitation per sample was obtained using the Pierce BCA protein assay kit (Thermo Fisher). β-Mercaptoethanol (BME; Sigma) was added to each sample at 5% v/v with blue loading dye just before gel loading. Twenty micrograms of total protein per sample was loaded into wells of 4–12% Bis-Tris gels (GenScript) and separated in MOPS buffer run at 125 V until the dye front reached the bottom of the gel. Gels were directly imaged on a Bio-Rad ChemiDoc imaging system using the rhodamine channel. Gels were subsequently stained with Coomassie (Sigma) as a loading control or used for downstream immunoblotting.

For HaloTag-STING and HaloTag-LC3B processing, the intensity of the lower “free” HaloTag band was normalized to the upper HaloTag-fusion band. For HaloTag-ATG9A, two processed bands were observed: a BafA-sensitive lysosomally processed free HaloTag band and a BafA-insensitive proteolytically processed N-terminal HaloTag fragment that appeared upon diABZI treatment. HaloTag-STING was validated by sequential probing with anti-STING and anti-HaloTag antibodies. HaloTag-ATG9A was similarly validated with anti-ATG9A and anti-HaloTag antibodies.

Live cell spinning disk microscopy

Cells were imaged on a Nikon Ti-2 CSU-W1 spinning disk confocal system operated by Nikon Elements AR microscope imaging software using a 40× water objective (NA 1.15) with the automated TI2-N-WID water immersion dispenser. The microscope is equipped with a live cell chamber set to 37°C and 5% CO^2 with constant humidity. Cells were imaged in P96-1.5H-N, Coverslip #1.5H 96-well imaging plates (Cellvis). HaloTag labeling was performed by incubating cells with JF646-Halo ligand (Promega) at 200 nM for 20 minutes in warm media, before washing 3× with HBSS. For STING activation experiments, cells were treated with diABZI (1 μM) and imaged every 60 minutes. For endosomal trafficking experiments, cells co-expressing HaloTag-STING and mCherry-tagged Rab markers (Rab5a, Rab7A, Rab11, or TSG101) were similarly imaged over a diABZI timecourse.

Immunofluorescence

Cells seeded in 96-well imaging plates or 8-well chamber slides (Cellvis C8-1.5H-N) were fixed with 4% warm paraformaldehyde (PFA) in PBS for 10 minutes, washed three times with PBS, permeabilized with 0.1% Triton X-100 in PBS for 5 minutes, and blocked with 3% goat serum and 1% BSA in PBS for one hour. Cells were then incubated overnight in 1:200 or 1:500 dilution of primary antibodies in blocking solution on a rocker at 4°C. Cells were washed three times, incubated with a 1:1000 dilution of Alexa Fluor 568- or Alexa Fluor 647-conjugated secondary antibodies for one hour at room temperature in blocking solution on a rocker, then washed three times before imaging. Cells were imaged on either the Nikon Ti-2 CSU-W1 spinning disk confocal system using a 40× water objective (NA 1.15), or a Zeiss 980 using a 63× oil lens with Airyscan. DAPI was used as a nuclear stain where indicated.

Transmission electron microscopy

HeLa cells were fixed in 2.5% glutaraldehyde and 2 mM calcium chloride in 0.1 M sodium cacodylate buffer (pH 7.4) for one hour at room temperature. Fixed cells were rinsed three times in cacodylate buffer and postfixed on ice for one hour with 1%

osmium tetroxide and 1% potassium ferrocyanide in cacodylate buffer. After rinsing in cacodylate buffer and then 0.1 N acetate buffer (pH 5.0–5.2), cells were en bloc stained with 1% uranyl acetate in acetate buffer overnight at 4 °C. Samples were then rinsed in acetate buffer, dehydrated through a graded ethanol series, infiltrated with EmBED812 epoxy resin (Electron Microscopy Sciences, Hatfield, PA, USA) using the manufacturer's hard resin formulation, and polymerized at 60 °C for 48 hours. Ultrathin sections (60–70 nm) were cut using an ultramicrotome equipped with a diamond knife, collected on formvar-coated copper grids, and post-stained with Reynold's lead citrate. Sections were imaged on a transmission electron microscope operated at 120 kV, and images were acquired using a digital CMOS camera. Vesicle size and morphology were assessed from acquired images by manual annotation and measurement.

Fluorescence recovery after photobleaching (FRAP)

ATG101 KO HeLa cells expressing ATG101-GFP, RFP-ATG9A, and HaloTag-STING were plated at a density of 15,000 cells per well on 8-well chambered glass bottom slides. Cells were treated with 1 μM diABZI for 5–7 hours before FRAP analysis and imaged using a Zeiss 980 Airyscan-equipped confocal microscope. For FRAP analysis of foci, the bleach area was set with a radius of 1 μm at 1.67 FPS. Sites were selected, imaged for 4 frames, and bleached with the 488 and 555 nm lasers for 3 seconds before recording. To estimate parameters for the faster-diffusing cytosolic fraction, the radius was set to 3 μm at 2 FPS. Data were processed using the Zeiss Blue FRAP analysis module and custom Python scripts.

FRAP experiments were analyzed using a ratio-of-ratios normalization to correct for both photobleaching during acquisition and variations in fluorescence intensity across cells. For each time series, fluorescence intensities were extracted from a bleached region of interest (ROI; R1) and a non-bleached control ROI within the same cell (R2). The raw R1/R2 intensity ratio was first normalized to the mean of the pre-bleach frames to yield a pre-bleach baseline of 1. The post-bleach minimum was then estimated by averaging the first frames immediately following the bleach event, and traces were

linearly rescaled such that the post-bleach value corresponded to 0 and the pre-bleach baseline to 1.

Normalized recovery curves were fit to a single-exponential recovery model of the form $I(t) = A(1 - e^{-kt})$, where I(t) is the normalized fluorescence intensity at time t, A represents the mobile fraction, and k is the apparent recovery rate constant. Time was defined relative to the bleach frame, such that t = 0 corresponds to the bleach event. Nonlinear least-squares fitting was performed using SciPy, and goodness-of-fit was assessed by calculation of the coefficient of determination (R^2). The recovery half-time ($t_{1/2}$) was calculated from the fitted rate constant as $t_{1/2} = \ln(2)/k$. For population-level analyses, recovery curves from independent cells were averaged (mean ± standard deviation), and fit parameters were pooled across replicates. Outliers exceeding the 95th percentile within each experimental group were excluded prior to statistical analysis.

Colocalization and image analysis

Colocalization analysis was performed using custom Python scripts. Mander's overlap coefficients were used to determine the fraction of STING or ATG9A overlapping with ATG101-positive puncta, with thresholds automatically set by Otsu's method. Pearson's correlation coefficient was used to assess signal overlap between two channels (e.g., STING–LAMP1, STING–TGN46, STING–ATG9A, ATG9A–ATG101, pSTING–LC3B). For quantification of STING structures, at least 300 cells were measured per genotype across three biological replicates. For Rab colocalization timecourse experiments, at least 10 random sites per replicate were imaged across three biological replicates. Total pSTING intensity per cell was normalized to the WT at 0 h diABZI condition.

Label-free DIA proteomics

Cells (10×10^7) were harvested and prepared using the EasyPep Mini MS Sample Prep Kit (A4006, Thermo Fisher Scientific) according to the manufacturer's instructions in four biological replicates per genotype. Peptide concentration was measured via the Pierce Quantitative Fluorometric Peptide Assay (Cat #23290, Thermo Fisher Scientific).

Mass spectrometry sample preparation

For digestion, 25 µL of 50 mM HEPES was added to dilute 10 M urea, followed by 1 µL TCEP (500 mM) and 3 µL CAA (500 mM), incubated for 20 and 15 min shaking at 750 rpm at 37°C, respectively. Two microliters of Lys-C (100 ng/µL, Wako) was added and incubated for 4 hours at 750 rpm at 37°C, followed by dilution with 375 µL HEPES buffer (50 mM) and 5 µL $CaCl_2$ (100 mM). Three microliters of trypsin (100 ng/µL, Thermo Scientific) was added and incubated overnight. Peptides were desalted with Pierce C18 spin columns (Thermo Fisher Scientific) and dried by vacuum centrifugation. Samples were reconstituted in Solvent A (97.8% H_2O, 2% ACN, 0.2% formic acid).

LC-MS/MS experiments were performed using an EASY-nLC 1000 (Thermo Fisher Scientific) connected to a QExactive HF mass spectrometer operated in data-independent acquisition (DIA) mode. The sample (1 µg) in 0.1% formic acid solution was loaded onto an Aurora UHPLC Column (25 cm × 75 µm, 1.6 µm C18, AUR225075C18A, IonOpticks) and separated over 136 min at a flow rate of 0.35 µL/min with the following gradient: 2–6% Solvent B (7.5 min), 6–25% B (82.5 min), 25–40% B (30 min), 40–98% B (1 min), and 98% B (15 min). Solvent A consisted of 97.9% H_2O, 2% ACN, and 0.1% formic acid, and Solvent B consisted of 19.9% H_2O, 80% ACN, and 0.1% formic acid. MS1 scans were acquired in the Orbitrap at 120,000 resolution with a scan range of 350–1500 *m/z*. Ion source settings were: ion source type, NSI; spray voltage, 2400 V; ion transfer tube temperature, 275 °C. System control and data collection were performed by Xcalibur software. The mass spectrometry proteomics data have been deposited to the ProteomeXchange Consortium via the PRIDE partner repository with the dataset identifier PXD058150.

Proteomic data analysis

Proteomic analysis was performed using Proteome Discoverer 3.5 (Thermo Scientific), the *H. sapiens* UniProt database, and SequestHT with Percolator validation. Percolator FDRs were 0.01 (strict) and 0.05 (relaxed). Peptide FDRs were 0.01 (strict) and 0.05

(relaxed), with medium confidence and a minimum peptide length of 6. Carbamidomethyl (C) was a static modification, while oxidation (M) was dynamic. Additional N-terminal modifications included acetyl (protein N-term), Met-loss (protein N-term M), and Met-loss + acetyl (protein N-term M). P-values were calculated using independent t-tests, and data were sum-normalized to protein abundance, then normalized to bait protein abundance.

TCGA and bioinformatics analysis

Gene expression and clinical data were obtained from The Cancer Genome Atlas (TCGA) database. Cox proportional hazard models were used to assess the association between AIC component gene expression and overall survival across TCGA cancer subtypes. Kaplan-Meier survival curves were generated by stratifying patients by high or low expression of the gene of interest at the 50th percentile, and hazard ratios (HR) were calculated. Tumor Immune Dysfunction and Exclusion (TIDE) analysis was performed to assess immune dysfunction and exclusion scores. Spearman's rank correlation coefficients (ρ) were calculated to determine correlations between ATG101 expression and immune cell infiltration, STING1 mRNA expression, and PD-L1 TIDE scores across TCGA cancer subtypes. All bioinformatics analyses were performed using custom Python scripts.

Antibodies and reagents

Primary antibodies used for Western blotting included: ATG101 (13492S; CST, 1:1000; RRID:AB_2798234), ATG13 (13273; CST, 1:1000; RRID:AB_2798169), FIP200/RB1CC1 (17250-1-AP; ProteinTech, 1:1000; RRID:AB_10666428), LC3B (PM036; MBL, 1:1000; RRID:AB_2274121), NBR1 (16004-1-AP; ProteinTech, 1:1000; RRID:AB_2251178), p62 (PM045; MBL, 1:1000; RRID:AB_1279301), STING (13647; CST, 1:1000; RRID:AB_2732796), pSTING S366 (19781; CST, 1:500; RRID:AB_2737062), TBK1 (3013; CST, 1:1000; RRID:AB_2199749), pTBK1 S172 (5483; CST, 1:500; RRID:AB_10693472), cGAS (15102; CST, 1:1000; RRID:AB_2732795), IRF3 (4302; CST, 1:1000; RRID:AB_1904036), pIRF3 S396

(4947; CST, 1:500; RRID:AB_823547), IFIT1 (14769; CST, 1:1000; RRID:AB_2783869), IFIT3 (87781; CST, 1:1000; RRID:AB_3717248), ATG9A (ab108338; Abcam, 1:1000; RRID:AB_10863880), HaloTag (G9281; Promega, 1:1000; RRID:AB_713650), p97 (MA1-21412; Thermo Fisher, 1:1000; RRID:AB_557663), and GAPDH (60004-1-Ig; ProteinTech, 1:10000).

Primary antibodies used for immunofluorescence included: STING (13647; CST), calnexin, GM130 (610823; BD Biosciences; RRID:AB_398142), LAMP1, ATG13, pSTING S366 (19781; CST; RRID:AB_2737062), TGN46 (ProteinTech), ATG9A (ab108338; Abcam; RRID:AB_10863880), TNIP1, ubiquitin/FK2, and RAB7A. Secondary antibodies for immunofluorescence were Alexa Fluor 568- and Alexa Fluor 647-conjugated antibodies used at 1:1000.

Secondary antibodies for Western blotting included goat anti-rabbit IgG-HRP conjugate (170-6515; Bio-Rad; RRID:AB_11125142) and goat anti-mouse IgG-HRP conjugate (170-6516; Bio-Rad; RRID:AB_11125547), diluted 1:3000.

The following reagents were used: diABZI (HY-112921B, MedChemExpress), cGAMP (HY-12512, MedChemExpress), Torin1 (HY-13003, MedChemExpress), GSK8612 TBK1 inhibitor (HY-111941, MedChemExpress), bafilomycin A1 (S1413, Selleckchem), oligomycin (HY-100558, MedChemExpress), antimycin A (1397-94-0, USB Corporation), Q-VD-OPh (AC982001, Abochem), cisplatin (HY-17394, MedChemExpress), KU57788, doxorubicin (D1515, Sigma), MG132 (S2619, Selleckchem), nigericin, doxycycline, Halo-TMR ligand (G8252A, Promega), JF646-Halo ligand (Promega), Ponceau S stain (161470250, Thermo Scientific), and Coomassie stain (B-0630, Sigma).

Statistical analysis

Statistical analyses were performed and graphed using GraphPad Prism Version 10.2.3 (RRID:SCR_002798) or custom Python scripts. In most cases, significance was calculated with either a one-way or two-way ANOVA test with appropriate multiple

comparison tests; an unpaired, two-tailed *t* test was performed when comparing two groups. For TEM data analysis, a chi-square with Fisher's exact test was performed; 95% confidence intervals were estimated through bootstrapping with 1000 replicates. Error bars are reported as mean ± SD. Images and blots shown are representative of at least three biological replicates unless otherwise noted in the figure legends. Significance levels are indicated as: *P ≤ 0.05, **P ≤ 0.01, ***P ≤ 0.001, ****P ≤ 0.0001.

3.6 REFERENCES

1. Whiteley, A. T. *et al.* Bacterial cGAS-like enzymes synthesize diverse nucleotide signals. *Nature* **567**, 194–199 (2019).
2. Morehouse, B. R. *et al.* STING cyclic dinucleotide sensing originated in bacteria. *Nature* **586**, 429–433 (2020).
3. Slavik, K. M. & Kranzusch, P. J. CBASS to cGAS-STING: The Origins and Mechanisms of Nucleotide Second Messenger Immune Signaling. *Annu. Rev. Virol.* **10**, 423–453 (2023).
4. Cohen, D. *et al.* Cyclic GMP–AMP signalling protects bacteria against viral infection. *Nature* **574**, 691–695 (2019).
5. Margolis, S. R., Wilson, S. C. & Vance, R. E. Evolutionary Origins of cGAS-STING Signaling. *Trends Immunol.* **38**, 733–743 (2017).
6. Tanaka, Y. & Chen, Z. J. STING Specifies IRF3 Phosphorylation by TBK1 in the Cytosolic DNA Signaling Pathway. *Sci. Signal.* **5**, ra20–ra20 (2012).
7. Yum, S., Li, M., Fang, Y. & Chen, Z. J. TBK1 recruitment to STING activates both IRF3 and NF-κB that mediate immune defense against tumors and viral infections. *Proc. Natl. Acad. Sci.* **118**, e2100225118 (2021).
8. Jeltema, D., Abbott, K. & Yan, N. STING trafficking as a new dimension of immune signaling. *J. Exp. Med.* **220**, e20220990 (2023).
9. Rotem, Z., Cox, R. A. & Isaacs, A. Inhibition of Virus Multiplication by Foreign Nucleic Acid. *Nature* **197**, 564–566 (1963).
10. Zhang, X. *et al.* Cyclic GMP-AMP Containing Mixed Phosphodiester Linkages Is An Endogenous High-Affinity Ligand for STING. *Mol. Cell* **51**, 226–235 (2013).

11. Ablasser, A. *et al.* cGAS produces a 2′-5′-linked cyclic dinucleotide second messenger that activates STING. *Nature* **498**, 380–384 (2013).
12. Gao, P. *et al.* Cyclic [G(2′,5′)pA(3′,5′)p] Is the Metazoan Second Messenger Produced by DNA-Activated Cyclic GMP-AMP Synthase. *Cell* **153**, 1094–1107 (2013).
13. Diner, E. J. *et al.* The innate immune DNA sensor cGAS produces a non-canonical cyclic-di-nucleotide that activates human STING. *Cell Rep.* **3**, 1355–1361 (2013).
14. Sun, L., Wu, J., Du, F., Chen, X. & Chen, Z. J. Cyclic GMP-AMP synthase is a cytosolic DNA sensor that activates the type I interferon pathway. *Science* **339**, 786–791 (2013).
15. Ishikawa, H. & Barber, G. N. STING is an endoplasmic reticulum adaptor that facilitates innate immune signalling. *Nature* **455**, 674–678 (2008).
16. Burdette, D. L. *et al.* STING is a direct innate immune sensor of cyclic di-GMP. *Nature* **478**, 515–518 (2011).
17. Zhong, B. *et al.* The Adaptor Protein MITA Links Virus-Sensing Receptors to IRF3 Transcription Factor Activation. *Immunity* **29**, 538–550 (2008).
18. Sun, W. *et al.* ERIS, an endoplasmic reticulum IFN stimulator, activates innate immune signaling through dimerization. *Proc. Natl. Acad. Sci.* **106**, 8653–8658 (2009).
19. Gao, P. *et al.* Structure-Function Analysis of STING Activation by c[G(2′,5′)pA(3′,5′)p] and Targeting by Antiviral DMXAA. *Cell* **154**, 748–762 (2013).
20. Fitzgerald, K. A. *et al.* IKKε and TBK1 are essential components of the IRF3 signaling pathway. *Nat. Immunol.* **4**, 491–496 (2003).
21. West, A. P. *et al.* Mitochondrial DNA stress primes the antiviral innate immune response. *Nature* **520**, 553–557 (2015).
22. Riley, J. S. *et al.* Mitochondrial inner membrane permeabilisation enables mtDNA release during apoptosis. *EMBO J.* **37**, e99238 (2018).
23. Mackenzie, K. J. *et al.* cGAS surveillance of micronuclei links genome instability to innate immunity. *Nature* **548**, 461–465 (2017).
24. Dou, Z. *et al.* Cytoplasmic chromatin triggers inflammation in senescence and cancer. *Nature* **550**, 402–406 (2017).

25. Glück, S. *et al.* Innate immune sensing of cytosolic chromatin fragments through cGAS promotes senescence. *Nat. Cell Biol.* **19**, 1061–1070 (2017).
26. Dou, Z. *et al.* Autophagy mediates degradation of nuclear lamina. *Nature* **527**, 105–109 (2015).
27. Volkman, H. E., Cambier, S., Gray, E. E. & Stetson, D. B. Tight nuclear tethering of cGAS is essential for preventing autoreactivity. *eLife* **8**, e47491 (2019).
28. Michalski, S. *et al.* Structural basis for sequestration and autoinhibition of cGAS by chromatin. *Nature* **587**, 678–682 (2020).
29. Barnett, K. C. *et al.* Phosphoinositide Interactions Position cGAS at the Plasma Membrane to Ensure Efficient Distinction between Self- and Viral DNA. *Cell* **176**, 1432-1446.e11 (2019).
30. Kato, H. *et al.* Differential roles of MDA5 and RIG-I helicases in the recognition of RNA viruses. *Nature* **441**, 101–105 (2006).
31. Hornung, V. *et al.* 5'-Triphosphate RNA Is the Ligand for RIG-I. *Science* **314**, 994–997 (2006).
32. Ishikawa, H., Ma, Z. & Barber, G. N. STING regulates intracellular DNA-mediated, type I interferon-dependent innate immunity. *Nature* **461**, 788–792 (2009).
33. Ablasser, A. *et al.* RIG-I-dependent sensing of poly(dA:dT) through the induction of an RNA polymerase III–transcribed RNA intermediate. *Nat. Immunol.* **10**, 1065–1072 (2009).
34. Chiu, Y.-H., MacMillan, J. B. & Chen, Z. J. RNA Polymerase III Detects Cytosolic DNA and Induces Type I Interferons through the RIG-I Pathway. *Cell* **138**, 576–591 (2009).
35. Huang, Y.-H., Liu, X.-Y., Du, X.-X., Jiang, Z.-F. & Su, X.-D. The structural basis for the sensing and binding of cyclic di-GMP by STING. *Nat. Struct. Mol. Biol.* **19**, 728–730 (2012).
36. Ouyang, S. *et al.* Structural Analysis of the STING Adaptor Protein Reveals a Hydrophobic Dimer Interface and Mode of Cyclic di-GMP Binding. *Immunity* **36**, 1073–1086 (2012).
37. Yin, Q. *et al.* Cyclic di-GMP Sensing via the Innate Immune Signaling Protein STING. *Mol. Cell* **46**, 735–745 (2012).

38. Shu, C., Yi, G., Watts, T., Kao, C. C. & Li, P. Structure of STING bound to cyclic di-GMP reveals the mechanism of cyclic dinucleotide recognition by the immune system. *Nat. Struct. Mol. Biol.* **19**, 722–724 (2012).
39. Liu, S. *et al.* The mechanism of STING autoinhibition and activation. *Mol. Cell* **83**, 1502-1518.e10 (2023).
40. Shang, G., Zhang, C., Chen, Z. J., Bai, X. & Zhang, X. Cryo-EM structures of STING reveal its mechanism of activation by cyclic GMP–AMP. *Nature* **567**, 389–393 (2019).
41. Ergun, S. L., Fernandez, D., Weiss, T. M. & Li, L. STING Polymer Structure Reveals Mechanisms for Activation, Hyperactivation, and Inhibition. *Cell* **178**, 290-301.e10 (2019).
42. Zhang, C. *et al.* Structural basis of STING binding with and phosphorylation by TBK1. *Nature* **567**, 394–398 (2019).
43. Zhao, B. *et al.* A conserved PLPLRT/SD motif of STING mediates the recruitment and activation of TBK1. *Nature* **569**, 718–722 (2019).
44. Liu, S. *et al.* Phosphorylation of innate immune adaptor proteins MAVS, STING, and TRIF induces IRF3 activation. *Science* **347**, aaa2630 (2015).
45. Lu, D. *et al.* Activation of STING by targeting a pocket in the transmembrane domain. *Nature* **604**, 557–562 (2022).
46. Li, J. *et al.* Activation of human STING by a molecular glue-like compound. *Nat. Chem. Biol.* **20**, 365–372 (2024).
47. Srikanth, S. *et al.* The Ca2+ sensor STIM1 regulates the type I interferon response by retaining the signaling adaptor STING at the endoplasmic reticulum. *Nat. Immunol.* **20**, 152–162 (2019).
48. Picard, C. *et al.* STIM1 mutation associated with a syndrome of immunodeficiency and autoimmunity. *N. Engl. J. Med.* **360**, 1971–1980 (2009).
49. Pokatayev, V. *et al.* Homeostatic regulation of STING protein at the resting state by stabilizer TOLLIP. *Nat. Immunol.* **21**, 158–167 (2020).
50. Jønsson, K. L. *et al.* IFI16 is required for DNA sensing in human macrophages by promoting production and function of cGAMP. *Nat. Commun.* **8**, 14391 (2017).

51. Lepelley, A. *et al.* Mutations in COPA lead to abnormal trafficking of STING to the Golgi and interferon signaling. *J. Exp. Med.* **217**, e20200600 (2020).
52. Deng, Z. *et al.* A defect in COPI-mediated transport of STING causes immune dysregulation in COPA syndrome. *J. Exp. Med.* **217**, e20201045 (2020).
53. Mukai, K. *et al.* Homeostatic regulation of STING by retrograde membrane traffic to the ER. *Nat. Commun.* **12**, 61 (2021).
54. Gui, X. *et al.* Autophagy induction via STING trafficking is a primordial function of the cGAS pathway. *Nature* **567**, 262–266 (2019).
55. Ogawa, E., Mukai, K., Saito, K., Arai, H. & Taguchi, T. The binding of TBK1 to STING requires exocytic membrane traffic from the ER. *Biochem. Biophys. Res. Commun.* **503**, 138–145 (2018).
56. Zhang, B. *et al.* STEEP mediates STING ER exit and activation of signaling. *Nat. Immunol.* **21**, 868–879 (2020).
57. Ma, M. *et al.* TAK1 is an essential kinase for STING trafficking. *Mol. Cell* **83**, 3885-3903.e5 (2023).
58. Ran, Y. *et al.* YIPF5 Is Essential for Innate Immunity to DNA Virus and Facilitates COPII-Dependent STING Trafficking. *J. Immunol.* **203**, 1560–1570 (2019).
59. Luo, W.-W. *et al.* iRhom2 is essential for innate immunity to DNA viruses by mediating trafficking and stability of the adaptor STING. *Nat. Immunol.* **17**, 1057–1066 (2016).
60. Mukai, K. *et al.* Activation of STING requires palmitoylation at the Golgi. *Nat. Commun.* **7**, 11932 (2016).
61. Haag, S. M. *et al.* Targeting STING with covalent small-molecule inhibitors. *Nature* **559**, 269–273 (2018).
62. Shu, H.-B. & Wang, Y.-Y. Adding to the STING. *Immunity* **41**, 871–873 (2014).
63. Poddar, S. *et al.* ArfGAP2 promotes STING proton channel activity, cytokine transit, and autoinflammation. *Cell* https://doi.org/10.1016/j.cell.2025.01.027 (2025) doi:10.1016/j.cell.2025.01.027.

64. Liu, Y. *et al.* Clathrin-associated AP-1 controls termination of STING signalling. *Nature* **610**, 761–767 (2022).
65. Chu, T.-T. *et al.* Tonic prime-boost of STING signalling mediates Niemann–Pick disease type C. *Nature* **596**, 570–575 (2021).
66. Gentili, M. *et al.* ESCRT-dependent STING degradation inhibits steady-state and cGAMP-induced signalling. *Nat. Commun.* **14**, 611 (2023).
67. Tu, X. *et al.* Interruption of post-Golgi STING trafficking activates tonic interferon signaling. *Nat. Commun.* **13**, 6977 (2022).
68. Dobbs, N. *et al.* STING Activation by Translocation from the ER Is Associated with Infection and Autoinflammatory Disease. *Cell Host Microbe* **18**, 157–168 (2015).
69. Yang, J.-S. *et al.* ARFGAP1 promotes the formation of COPI vesicles, suggesting function as a component of the coat. *J. Cell Biol.* **159**, 69–78 (2002).
70. Gonugunta, V. K. *et al.* Trafficking-Mediated STING Degradation Requires Sorting to Acidified Endolysosomes and Can Be Targeted to Enhance Anti-tumor Response. *Cell Rep.* **21**, 3234–3242 (2017).
71. Fischer, T. D., Wang, C., Padman, B. S., Lazarou, M. & Youle, R. J. STING induces LC3B lipidation onto single-membrane vesicles via the V-ATPase and ATG16L1-WD40 domain. *J. Cell Biol.* **219**, e202009128 (2020).
72. Liu, D. *et al.* STING directly activates autophagy to tune the innate immune response. *Cell Death Differ.* **26**, 1735–1749 (2019).
73. Gaidt, M. M. *et al.* The DNA Inflammasome in Human Myeloid Cells Is Initiated by a STING-Cell Death Program Upstream of NLRP3. *Cell* **171**, 1110-1124.e18 (2017).
74. Konno, H., Konno, K. & Barber, G. N. Cyclic Dinucleotides Trigger ULK1 (ATG1) Phosphorylation of STING to Prevent Sustained Innate Immune Signaling. *Cell* **155**, 688–698 (2013).
75. Prabakaran, T. *et al.* Attenuation of cGAS-STING signaling is mediated by a p62/SQSTM1-dependent autophagy pathway activated by TBK1. *EMBO J.* **37**, e97858 (2018).

76. Cheng, J. *et al.* Autophagy regulates MAVS signaling activation in a phosphorylation-dependent manner in microglia. *Cell Death Differ.* **24**, 276–287 (2017).
77. Lim, J. & Murthy, A. Controlling inflammation by selective autophagy. *Cell Death Differ.* **25**, 825–827 (2018).
78. Watson, R. O., Manzanillo, P. S. & Cox, J. S. Extracellular M. tuberculosis DNA Targets Bacteria for Autophagy by Activating the Host DNA-Sensing Pathway. *Cell* **150**, 803–815 (2012).
79. Moretti, J. *et al.* STING Senses Microbial Viability to Orchestrate Stress-Mediated Autophagy of the Endoplasmic Reticulum. *Cell* **171**, 809-823.e13 (2017).
80. Decout, A., Katz, J. D., Venkatraman, S. & Ablasser, A. The cGAS–STING pathway as a therapeutic target in inflammatory diseases. *Nat. Rev. Immunol.* **21**, 548–569 (2021).
81. Crow, Y. J. *et al.* Mutations in the gene encoding the 3′-5′ DNA exonuclease TREX1 cause Aicardi-Goutières syndrome at the AGS1 locus. *Nat. Genet.* **38**, 917–920 (2006).
82. Stetson, D. B., Ko, J. S., Heidmann, T. & Medzhitov, R. Trex1 Prevents Cell-Intrinsic Initiation of Autoimmunity. *Cell* **134**, 587–598 (2008).
83. Gao, D. *et al.* Activation of cyclic GMP-AMP synthase by self-DNA causes autoimmune diseases. *Proc. Natl. Acad. Sci.* **112**, E5699–E5705 (2015).
84. Gray, E. E., Treuting, P. M., Woodward, J. J. & Stetson, D. B. cGAS is required for lethal autoimmune disease in the Trex1-deficient mouse model of Aicardi-Goutieres Syndrome. *J Immunol.* **195**, 1939–1943 (2015).
85. Lopez-Mosqueda, J. *et al.* SPRTN is a mammalian DNA-binding metalloprotease that resolves DNA-protein crosslinks. *eLife* **5**, e21491 (2016).
86. Lessel, D. *et al.* Mutations in SPRTN cause early onset hepatocellular carcinoma, genomic instability and progeroid features. *Nat. Genet.* **46**, 1239–1244 (2014).
87. Maskey, R. S. *et al.* Spartan deficiency causes genomic instability and progeroid phenotypes. *Nat. Commun.* **5**, 5744 (2014).

88. Tomaskovic, I. *et al.* DNA-protein cross-links promote cGAS-STING–driven premature aging and embryonic lethality. *Science* **391**, eadx9445 (2026).
89. Liu, Y. *et al.* Activated STING in a Vascular and Pulmonary Syndrome. *N. Engl. J. Med.* **371**, 507–518 (2014).
90. McCauley, M. E. *et al.* C9orf72 in myeloid cells suppresses STING-induced inflammation. *Nature* **585**, 96–101 (2020).
91. Yu, C.-H. *et al.* TDP-43 Triggers Mitochondrial DNA Release via mPTP to Activate cGAS/STING in ALS. *Cell* **183**, 636-649.e18 (2020).
92. Song, S. *et al.* Decreased expression of STING predicts poor prognosis in patients with gastric cancer. *Sci. Rep.* **7**, 39858 (2017).
93. Vashi, N. & Bakhoum, S. F. The Evolution of STING Signaling and Its Involvement in Cancer. *Trends Biochem. Sci.* **46**, 446–460 (2021).
94. Ramanjulu, J. M. *et al.* Design of amidobenzimidazole STING receptor agonists with systemic activity. *Nature* **564**, 439–443 (2018).
95. Demaria, O. *et al.* STING activation of tumor endothelial cells initiates spontaneous and therapeutic antitumor immunity. *Proc. Natl. Acad. Sci. U. S. A.* **112**, 15408–15413 (2015).
96. Corrales, L. *et al.* Direct activation of STING in the tumor microenvironment leads to potent and systemic tumor regression and immunity. *Cell Rep.* **11**, 1018–1030 (2015).
97. Ager, C. R. *et al.* Discovery of IACS-8803 and IACS-8779, potent agonists of stimulator of interferon genes (STING) with robust systemic antitumor efficacy. *Bioorg. Med. Chem. Lett.* **29**, 126640 (2019).
98. Meric-Bernstam, F. *et al.* Phase I Dose-Escalation Trial of MIW815 (ADU-S100), an Intratumoral STING Agonist, in Patients with Advanced/Metastatic Solid Tumors or Lymphomas. *Clin. Cancer Res* **28**, 677–688 (2022).
99. Curran, E. *et al.* STING pathway activation stimulates potent immunity against acute myeloid leukemia. *Cell Rep.* **15**, 2357–2366 (2016).
100. Kawai, T. & Akira, S. The role of pattern-recognition receptors in innate immunity: update on Toll-like receptors. *Nat. Immunol.* **11**, 373–384 (2010).
101. Wu, J. & Chen, Z. J. Innate Immune Sensing and Signaling of Cytosolic Nucleic Acids. *Annu. Rev. Immunol.* **32**, 461–488 (2014).

102. Theofilopoulos, A., Baccala, R., Beutler, B. & Kono, D. TYPE I Interferons (alpha/beta) in immunity and autoimmunity. *Annu. Rev. Immunol.* **23**, 307–336 (2005).
103. Ivashkiv, L. B. & Donlin, L. T. Regulation of type I interferon responses. *Nat. Rev. Immunol.* **14**, 36–49 (2014).
104. Schoggins, J. W. *et al.* A diverse range of gene products are effectors of the type I interferon antiviral response. *Nature* **472**, 481–485 (2011).
105. Diamond, M. S. & Farzan, M. The broad-spectrum antiviral functions of IFIT and IFITM proteins. *Nat. Rev. Immunol.* **13**, 46–57 (2013).
106. Hui, D. J., Bhasker, C. R., Merrick, W. C. & Sen, G. C. Viral Stress-inducible Protein p56 Inhibits Translation by Blocking the Interaction of eIF3 with the Ternary Complex eIF2·GTP·Met-tRNAi. *J. Biol. Chem.* **278**, 39477–39482 (2003).
107. Bluyssen, H. A. R., Vlietstra, R. J., Van Der Made, A. & Trapman, J. The interferon-stimulated gene 54 K promoter contains two adjacent functional interferon-stimulated response elements of different strength, which act synergistically for maximal interferon-α inducibility. *Eur. J. Biochem.* **220**, 395–402 (1994).
108. Pichlmair, A. *et al.* IFIT1 is an antiviral protein that recognizes 5′-triphosphate RNA. *Nat. Immunol.* **12**, 624–630 (2011).
109. Zhou, X. *et al.* Interferon Induced *IFIT* Family Genes in Host Antiviral Defense. *Int. J. Biol. Sci.* **9**, 200–208 (2013).
110. Tran, V. *et al.* Influenza virus repurposes the antiviral protein IFIT2 to promote translation of viral mRNAs. *Nat. Microbiol.* **5**, 1490–1503 (2020).
111. Daffis, S. *et al.* 2′-O methylation of the viral mRNA cap evades host restriction by IFIT family members. *Nature* **468**, 452–456 (2010).
112. Schlütermann, D. *et al.* FIP200 controls the TBK1 activation threshold at SQSTM1/p62-positive condensates. *Sci. Rep.* **11**, 13863 (2021).
113. Yuan, S. & Straub, A. C. STING inhibition enables efficient plasmid-based gene expression in primary vascular cells: A simple and cost-effective transfection protocol. *PLOS ONE* **19**, e0303472 (2024).
114. Apel, F. *et al.* The cytosolic DNA sensor cGAS recognizes neutrophil extracellular traps. *Sci. Signal.* **14**, eaax7942 (2021).

115. De Mingo Pulido, Á. *et al.* The inhibitory receptor TIM-3 limits activation of the cGAS-STING pathway in intra-tumoral dendritic cells by suppressing extracellular DNA uptake. *Immunity* **54**, 1154-1167.e7 (2021).
116. Hammerschlag, R., Stone, G. C., Bolen, F. A., Lindsey, J. D. & Ellisman, M. H. Evidence that all newly synthesized proteins destined for fast axonal transport pass through the Golgi apparatus. *J. Cell Biol.* **93**, 568–575 (1982).
117. Zhang, G. F., Driouich, A. & Staehelin, L. A. Effect of monensin on plant Golgi: re-examination of the monensin-induced changes in cisternal architecture and functional activities of the Golgi apparatus of sycamore suspension-cultured cells. *J. Cell Sci.* **104**, 819–831 (1993).
118. Liu, B. *et al.* Human STING is a proton channel. *Science* **381**, 508–514 (2023).
119. Xun, J. *et al.* A conserved ion channel function of STING mediates noncanonical autophagy and cell death. *EMBO Rep.* **25**, 544–569 (2024).
120. Katsnelson, M. A., Rucker, L. G., Russo, H. M. & Dubyak, G. R. K+ Efflux Agonists Induce NLRP3 Inflammasome Activation Independently of Ca2+ Signaling. *J. Immunol.* **194**, 3937–3952 (2015).
121. Nguyen, A. *et al.* Metamorphic proteins at the basis of human autophagy initiation and lipid transfer. *Mol. Cell* **83**, 2077–2090 (2023).
122. Kuchitsu, Y. *et al.* STING signalling is terminated through ESCRT-dependent microautophagy of vesicles originating from recycling endosomes. *Nat. Cell Biol.* **25**, 453–466 (2023).
123. Balka, K. R. *et al.* Termination of STING responses is mediated via ESCRT-dependent degradation. *EMBO J.* **42**, e112712 (2023).
124. Saitoh, T. *et al.* Atg9a controls dsDNA-driven dynamic translocation of STING and the innate immune response. *Proc. Natl. Acad. Sci. U. S. A.* **106**, 20842–20846 (2009).
125. Priem, D. *et al.* ATG9A-mediated autophagy prevents inflammatory skin disease by limiting TNFR1-driven STING activation and ZBP1-dependent cell death. *Immunity* **58**, 2972-2988.e6 (2025).
126. Huyghe, J. *et al.* ATG9A prevents TNF cytotoxicity by an unconventional lysosomal targeting pathway. *Science* **378**, 1201–1207 (2022).

127. Gentili, M. *et al.* Classification and functional characterization of regulators of intracellular STING trafficking identified by genome-wide optical pooled screening. *bioRxiv* 2024.04.07.588166 (2024) doi:10.1101/2024.04.07.588166.
128. Wang, B. *et al.* ATG101-related signature predicts prognosis and therapeutic option in hepatocellular carcinoma. *Sci. Rep.* **12**, 18066 (2022).
129. Lawson, K. A. *et al.* Functional genomic landscape of cancer-intrinsic evasion of killing by T cells. *Nature* **586**, 120–126 (2020).
130. Hagan, P. M. *et al*. ULK1/2 Inhibitors that Degrade ATG13 Effectively Target KRAS-Mutant Cancers. 2025.10.14.682402 Preprint at https://doi.org/10.1101/2025.10.14.682402 (2025).

Chapter 4

HSBP1 IS A DYNAMICALLY REGULATED SCAFFOLD THAT INTERACTS WITH THE FIP200 COILED-COIL REGION

4.1 ABSTRACT

Autophagy initiation requires the ULK1 complex comprising ULK1, FIP200, ATG13, and ATG101. Heat Shock Factor Binding Protein 1 (HSBP1) is a conserved trimeric coiled-coil protein that regulates the heat shock response and the formation of the WASH complex. Here, we identify HSBP1 as a FIP200 interactor that is associated with the coiled-coil and leucine-zipper region, independently of ULK1, ATG13, and ATG101. HSBP1 interactome profiling reveals associations with ATG16L1, EEA1, and other coiled-coil scaffold proteins including CROCC and CCHCR1 indicating a role in organizing multimeric assemblies. Mechanistically, HSBP1 is an intrinsically unstable protein that undergoes rapid proteasome-dependent degradation in response to mTOR inhibition, nutrient starvation, and mitophagy induction – independent of lysosomal-mediated autophagy or FIP200. Cycloheximide chase experiments reveal that HSBP1 has a basal half-life of 30-40 minutes, indicating constitutive turnover under normal conditions. This work identifies HSBP1 as a dynamically regulated coiled-coil scaffold associated with autophagy initiation complexes and identifies proteasomal degradation as a regulatory mechanism that rapidly depletes HSBP1 during metabolic stress.

4.2 INTRODUCTION

Chapters 2 and 3 established that the ATG9A-ATG13-ATG101 supercomplex mediates a Golgi-to-lysosome trafficking pathway for STING, operating independently of FIP200 and canonical autophagy. This finding reveals a fundamental principle: the AIC is not a single functional entity but rather a modular assembly whose discrete subsets of components have evolved specialized and independent cellular roles. The ATG13–ATG101 arm, acting through ATG9A, governs a specific aspect of innate immune homeostasis. This raises a fundamental question: does FIP200 perform unique functions?

The unbiased proteomic analyses of AIC KO lines, detailed in Chapter 2, offer a clue. Unlike the innate immune signatures seen in ATG101 and ATG13 KOs, the FIP200 KO displayed a distinct proteomic profile characterized by downregulation of pathways related to protein phosphorylation and extracellular matrix organization. These signatures were exclusive to the FIP200 KO, reflecting FIP200-specific roles in kinase signaling and cell adhesion networks. Such findings align with FIP200's initial identification as a focal adhesion kinase (FAK)-interacting protein and suggest that FIP200 orchestrates cellular processes beyond autophagy, distinct from the AIC.

Proteomic analysis of the endogenous FIP200 interactome identified HSBP1 (Heat Shock Factor Binding Protein 1) as the top-enriched interactor beyond canonical AIC members, providing a candidate through which FIP200 may exert functions distinct from the ATG13–ATG101 arm. This chapter investigates whether HSBP1 constitutes a bona fide FIP200 interactor by elucidating the structural basis, specificity, and functional implications of this interaction. I characterize the HSBP1 interactome and uncover an unexpected mechanism regulating HSBP1 during autophagy and metabolic stress. Together with the findings from Chapters 1 through 3, this work supports a model in which ULK1 complex submodules have evolved discrete downstream functions: ATG101 and ATG13, acting through ATG9A, govern innate immune homeostasis, whereas FIP200, through interactions with HSBP1 and other coiled-coil scaffold

proteins, organizes a separate regulatory layer coordinating vesicular trafficking and membrane assembly.

4.2.1 FIP200 DOMAIN ARCHITECTURE

FIP200 is a 1,594-residue protein organized into four regions: a dimeric N-terminal domain (NTD, residues 1–639); an intrinsically disordered region (IDR, 639–737); a central coiled-coil (CC, 737–1,498) containing a leucine zipper motif (LZ, 1286–1413); and a C-terminal region containing the containing the dimeric "Claw" domain (residues 1,498–1,594)[1–3] (**Figure 1**). This architecture physically separates FIP200's two major functional surfaces: the NTD, which scaffolds the ULK1 kinase complex, and the CC C-terminus together with the Claw, which collectively form a multi-site cargo receptor docking platform[4]. Crystal and cryo-EM structures have revealed how these regions operate through mechanistically distinct interaction modes, reviewed below.

Beyond canonical receptor interactions, FIP200 also responds to organelle-specific stress signals through structurally unresolved mechanisms. In response to cellular stress, Ca^{2+} release from the endoplasmic reticulum (ER), FIP200 interacts directly with ER-localized factors to promote localized autophagosome formation. Phosphorylation of FIP200 near ER Ca^{2+} leak sites facilitates autophagosome formation independently of upstream autophagy activation signals[5].

4.2.2 THE NTD: SCAFFOLDING THE AIC

Cryo-EM and HDX-MS established that the FIP200 NTD forms a C-shaped dimer ~20 nm across that asymmetrically associates with single copies of ATG13, ATG101, and ULK1[2,6]. ATG13's C-terminal IDR binds the NTD directly, and mutations disrupting this contact abolish mitophagy. The NTD bears structural similarity to the scaffold domain of TBK1, suggesting a shared evolutionary origin between the two kinase-organizing platforms[2]. Negative stain electron microscopy of full-length FIP200 shows the CC project away from the NTD as a long flexible arm, physically separating ULK1

complex assembly at the NTD from cargo receptor engagement at the distal CC and Claw[3].

4.2.3 THE CLAW: A PHOSPHO-REGULATED AUTOPHAGY CARGO RECEPTOR HUB

The Claw domain (residues ~1,498–1,594) presents a conserved hydrophobic pocket flanked by positively charged residues that serves as the binding site for short linear motifs termed FIP200-interacting regions (FIRs)[7,8]. All structurally characterized Claw ligands engage this binding pocket and their binding is frequently enhanced by phosphorylation.

p62/SQSTM1 residues 326–380 engage the Claw in a phosphorylation-enhanced manner. Further, this interaction is mutually exclusive with LC3B binding, providing temporal coordination during autophagosome formation[9]. The CCPG1 FIR/Claw co-crystal structure provided the first atomical view of a canonical FIR peptide engaged in the Claw pocket, showing a 2:2 stoichiometry with TBK1-mediated phosphorylation of Ser104 substantially increasing affinity[8,10]. Optineurin (OPTN) follows the same molecular logic: TBK1 phosphorylation of Ser177 within OPTN's LIR converts it to a functional FIR, directly coupling TBK1 kinase activity during mitophagy to FIP200 recruitment. Several ALS- and glaucoma-associated OPTN mutations map to the FIP200-OPTN contact surface, highlighting a direct link between FIP200's scaffolding function and disease biology[11,12]. TNIP1 inverts this logic, functioning as a competitive brake: TBK1-mediated phosphorylation of Ser122/Ser123 on TNIP1 enables it to outcompete autophagy receptors for the FIP200 Claw, releasing FIP200 from the autophagosome to allow expansion[13,14]. Finally, ATG16L1 engages the Claw (residues 1,564–1,582) through anti-parallel β-sheet complementation[15,16].

The Claw pocket is thus a single structural surface serving as a competitive hub for multiple ligands with phosphorylation state biasing selectivity at any given moment[8,17].

4.2.4 THE COILED-COIL RECEPTOR PLATFORM

The distal portion of the FIP200 CC (residues ~1,286–1,441, encompassing the LZ) provides a structurally independent binding surface for domains of NDP52 and TAX1BP1, operating through a mechanism entirely distinct from FIR/pocket recognition[4,18,19]. Crystal structures of NDP52/FIP200 CC and TAX1BP1/FIP200 CC reveal that both receptors use their SKICH domains and a common set of interface residues to engage the same dimeric CC surface[17,19].

The HSBP1-binding region identified in this chapter (residues 826–1,594, spanning the CC and LZ) overlaps with both the NDP52 binding site (1,351–1,441) and the TAX1BP1 SKICH-binding region (1,343–1,395), positioning HSBP1 as a potential participant in the competitive receptor exchange occurring at this surface — a possibility explored further in the Discussion.

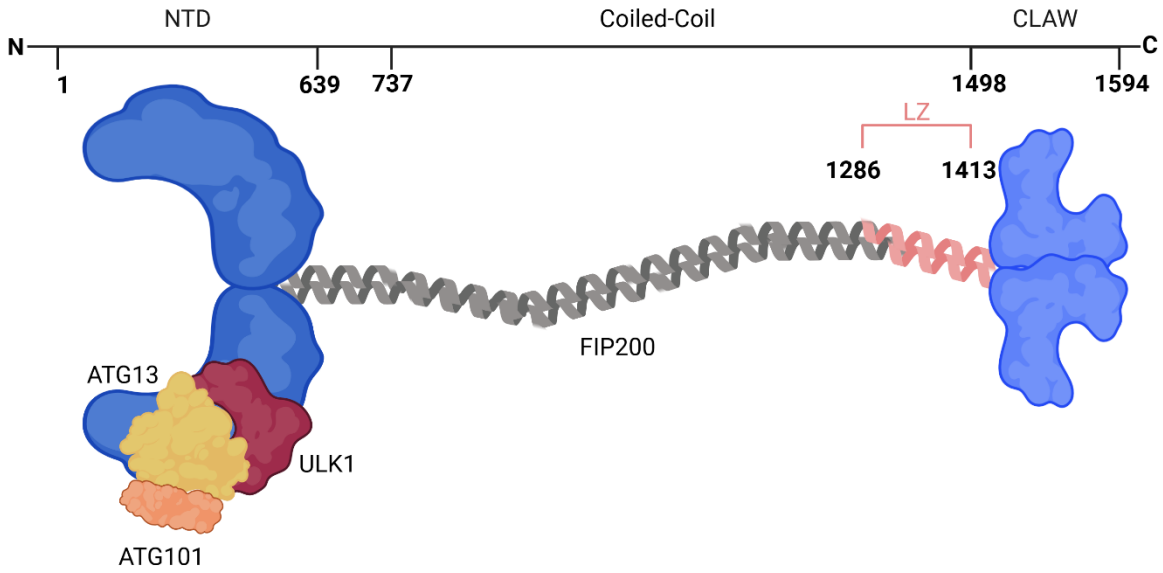

Figure 1. Domain architecture of FIP200 and its interaction with the AIC. *FIP200 (1,594 residues) is organized into an N-terminal domain (NTD, residues 1–639), a central coiled-coil region (Coiled-Coil, residues 737–1,498), and a C-terminal Claw domain (CLAW, residues 1,498–1,594). The leucine zipper motif (LZ, residues 1,286–1,413, pink) is embedded within the distal coiled-coil. The NTD scaffolds the AIC by engaging ATG13 (yellow), ATG101 (orange), and ULK1 (red), while the coiled-coil and*

Claw provide structurally independent binding surfaces for autophagy cargo receptors and downstream effectors. The coiled-coil and LZ region overlaps with the HSBP1-binding region identified in this chapter (see Section 4.3.3). Structural representations are based on published cryo-EM and crystal structures.

4.2.5 HSBP1

HSBP1 is a small, highly conserved 76-amino-acid protein composed of two hydrophobic heptad repeats that form a parallel trimeric coiled-coil structure, which can further oligomerize into hexamers[20,21]. This coiled-coil architecture enables HSBP1 to regulate other proteins through direct coiled-coil interactions.[22] Structure-function modeling indicates that HSBP1 is predominantly trimeric in solution and can modulate protein complex assembly by engaging coiled-coil domains in partner proteins[20]. Early reports described HSBP1 as nuclear-localized; however, steady-state HSBP1 is predominantly cytoplasmic with nuclear translocation occurring during specific cellular stress[23].

HSBP1 was initially characterized as a negative regulator of heat shock response through its interaction with heat shock factor 1 (HSF1)[23]. HSBP1 binds active HSF1 trimers and inhibits their DNA-binding activity, suppressing heat shock target gene expression. HSBP1 interacts with heat shock protein 70 (HSP70) when HSF1 is inactive.[23] Consistent with this repressive function, HSBP1 overexpression blocks heat shock response activation. *Hsbp1*-deficient mice exhibit early embryonic lethality and the limited analysis of these embryos revealed increased Hsf1 activity and elevated Hsp expression, confirming HSBP1 is an essential developmental regulator of heat shock signaling[24].

More recently, HSBP1 has been identified as an assembly factor for the Wiskott-Aldrich syndrome protein and SCAR homolog (WASH) complex, revealing a broader role in organized coiled-coil protein containing complexes.[22] HSBP1 stabilizes formation of the WASH Complex via interaction with CCDC53 (formerly WASHC3), mediated by stabilizing salt bridges between the coiled-coil regions. Mechanistically, HSBP1

dissociates CCDC53 homotrimers to promote ternary complex formation with WASH and FAM21, which is required for actin polymerization on endosomes. HSBP1 depletion phenocopies WASH complex loss, resulting in defects in focal adhesion, cell polarity, and cell migration. This work established that HSBP1 functions as a coiled-coil assembly factor capable of remodeling oligomeric protein complexes.

Despite repeated identification of HSBP1 in immunoprecipitation-mass spectrometry (IP-MS) studies of the ULK1 complex[25–27], its role in autophagy initiation remains unclear. Recent work demonstrates that HSBP1 stabilizes ULK1 complex subunits, including ATG13 and FIP200, and promotes proper complex assembly. HSBP1 depletion reduces the number of ATG13 puncta and the accumulation of LC3-II during starvation, indicating a role in autophagy initiation even if bulk autophagic flux is not entirely abolished.[28]

In vivo, Hsbp1 has essential developmental roles beyond cell culture systems. Mice KO studies show preimplantation lethality and zebrafish morphants exhibit defects in germ layer formation and neural crest specification.[24] These observations suggest that HSBP1 contributes to developmental signaling pathways, including Wnt-mediated patterning.

In sum, although HSBP1 has been shown to repeatedly interact and co-purify with the ULK1 complex, its function in autophagy remains only partially understood. Emerging evidence indicates that HSBP1 is a multifunctional coiled-coil assembly factor that stabilizes diverse protein complexes involved in stress responses, cytoskeletal dynamics, and autophagy initiation. We sought to define the biochemical and functional consequences of the HSBP1-FIP200 interaction.

4.3 RESULTS

4.3.1 ENDOGENOUS FIP200 INTERACTOME CONFIRMS HSBP1 AS AN INTERACTOR

Prior interactome studies of AIC components in HEK293T[26] and mouse embryonic fibroblasts[25,27] established IP-MS as a productive approach for identifying AIC-associated proteins. Applying this strategy to endogenous FIP200, we identify novel

interactors with critical downstream functions. Using CRISPR-edited HeLa cells expressing N-terminal HA-tagged FIP200, we performed an HA-tag IP-MS and confirmed robust enrichment of FIP200 with ULK1, ATG13, and ATG101 (**Figure 2A**), validating the approach. Additional autophagy components, including ATG5 and ATG16L1, were enriched. Strikingly, HSBP1 was the top-enriched interactor beyond core ULK1 complex members (**Figure 2A**). Cross-validation with prior datasets confirmed the presence of HSBP1 in IPs using other ULK1 complex components, various FIP200 tags, and multiple mammalian cell types[25–27].

4.3.2 HSBP1 INTERACTS SPECIFICALLY WITH FIP200 NOT OTHER AIC COMPONENTS

To confirm this interaction, we generated a stable HeLa cell line co-expressing HA-FIP200 and C-terminal V5-tagged HSBP1 (HSBP1-V5). HA-IP confirmed co-enrichment of HSBP1-V5 with HA-FIP200, along with endogenous AIC components, as expected (**Figure 2B**). Reciprocal pull-down with V5, to enrich for HSBP1 specific interactors, pulled down HA and FIP200, but not AIC components ULK1, ATG13, or ATG101 (**Figure 2C,E**). The autophagy cargo receptors NBR1, p62, and LC3 were not detected by immunoprecipitation (**Figure 2D**). Stable HSBP1-V5 expression did not alter levels of AIC subunits (FIP200, ATG13, ATG101), autophagy cargo receptors (NBR1, p62), or LC3 (**Figure 3**), confirming that HSBP1 overexpression does not perturb AIC complex stability or basal autophagy flux and validating this cell line for interaction studies. Proximity labeling studies investigated the interactome of individual AIC components, providing additional evidence that HSBP1 uniquely interacts with FIP200 and not with other AIC components[27]. Taken together, these data demonstrate that HSBP1 interacts specifically with FIP200, independently of the broader AIC, and defines a pool of FIP200 that is not associated with AIC components or autophagy cargo receptors.

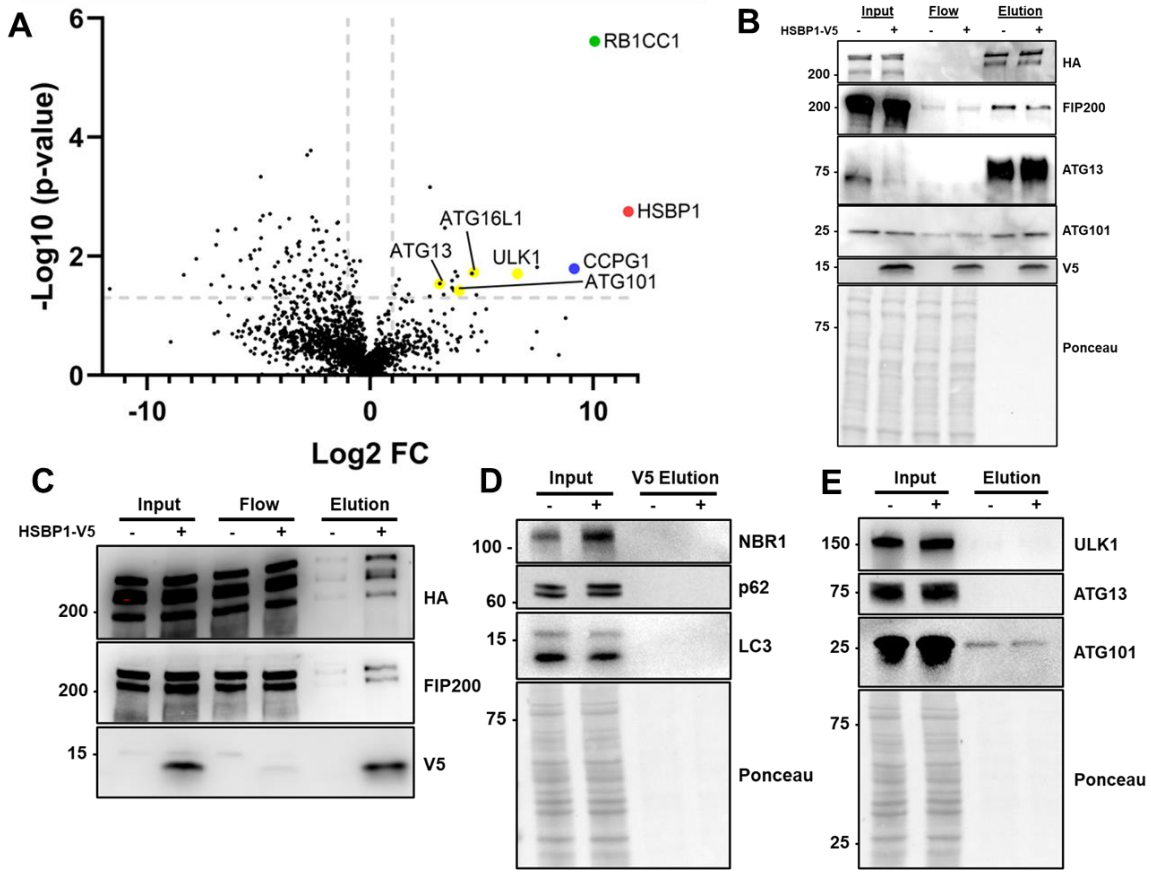

Figure 2. HSBP1 is a selective interactor of FIP200 identified by proteomics. (A) *Volcano plot of HA-FIP200 IP-MS from CRISPR-edited HA–FIP200 HeLa cells compared to parental controls. Log2 fold change (x-axis) is plotted against −log10(p-value) (y-axis). RB1CC1/FIP200 (green) is the most significantly enriched protein, confirming efficient bait enrichment. Known AIC components ATG13, ULK1, ATG16L1, and ATG101 (yellow) and the autophagy receptor CCPG1 (blue) are enriched. Endogenous HSBP1 (red) is the top-enriched interactor beyond canonical AIC members. Dashed lines indicate significance thresholds.* ***(B)*** *HA immunoprecipitation from HA–FIP200 HeLa cells with (+) or without (−) stable HSBP1-V5 expression. Western blotting of input, flowthrough (Flow), and HA-IP elution confirms co-enrichment of endogenous ATG13 and ATG101 with HA–FIP200, as expected. HSBP1-V5 is also co-precipitated, biochemically validating the interaction observed by IP-MS in (A). Ponceau S stain is the loading control.* ***(C)*** *Reciprocal V5 immunoprecipitation*

from stable HSBP1-V5-expressing HA–FIP200 HeLa cells. V5-IP elution demonstrates co-enrichment of HA and FIP200 with HSBP1-V5, confirming the interaction from the HSBP1 side. ***(D)*** *Immunoblot of input and V5-IP eluates probed for the autophagy cargo receptors NBR1 and p62/SQSTM1 and the autophagy marker LC3. None are detected in the V5-IP elution, indicating that HSBP1 does not associate with autophagy substrates. Ponceau stain is the loading control.* ***(E)*** *Immunoblot of input and V5-IP eluates probed for AIC subunits ULK1, ATG13, and ATG101. All three are present in the input but absent from the V5-IP elution, demonstrating that HSBP1 interacts with FIP200 independently of the broader AIC. Ponceau S stain is the loading control.*

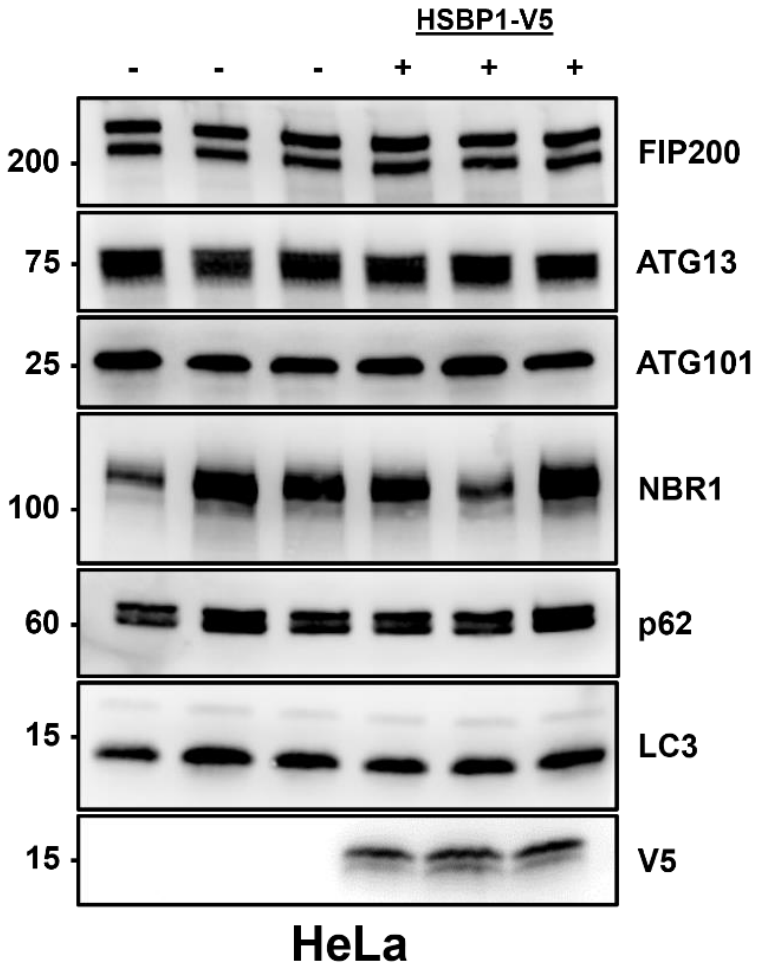

Figure 3. HSBP1-V5 overexpression does not alter AIC subunit levels or autophagy markers. *Western blot of whole-cell lysates from HeLa cells with (+) or without (−) stable HSBP1-V5 expression. Blots were probed for AIC subunits (FIP200, ATG13, ATG101), autophagy cargo receptors (NBR1, p62/SQSTM1), and the autophagy marker LC3. No detectable changes in protein levels are observed upon HSBP1-V5 stable expression, confirming that HSBP1 overexpression does not perturb AIC complex stability or basal autophagy flux. V5 blot confirms HSBP1-V5 expression stably expressing samples.*

4.3.3 MAPPING HSBP1-FIP200 INTERACTION TO THE FIP200 COILED-COIL REGION

Evidence from the literature shows that the N-terminus of FIP200 interacts with the ULK1 complex, while the Claw domain interacts with autophagy cargo[1,6,29]. To map the FIP200 HSBP1-binding region, we co-transfected FIP200-KO HeLa cells with HSBP1-V5 and various HA-FIP200 truncation constructs: full-length FIP200 (FL), two C-terminal fragments (C1: 826–1594; C2: 1300–1594), an N-terminal fragment (1–825), and a ΔClaw mutant (1–1490) (**Figure 4A**). V5-IP revealed strong interaction with FL, C1, C2, and ΔClaw mutants, but not the N-terminal fragment (**Figure 4B**). Critically, the interaction with the ΔClaw mutant demonstrates that the Claw domain is dispensable for HSBP1 binding. Since HSBP1 bound both C1 (826-1594) and C2 (1300-1594) but not the N-terminal fragment (1-825) and binding was maintained in the ΔClaw mutant (1-1490), the data narrow the HSBP1-binding region to residues 1300–1594, spanning the distal coiled-coil and leucin zipper domains (**Figure 4C**). This region overlaps with the NDP52-binding surface on FIP200 (residues 1351-1441)[4]. An earlier study mapped ATG16L1 binding to FIP200 residues 1315-1413, which would fall within the HSBP1-binding region[30], however a subsequent crystal structure revealed that the critical ATG16L1-FIP200 contacts instead depend on Claw residues 1564-1582[15]. This distinction underscores that HSBP1 engages FIP200 through a mechanistically distinct, non-Claw interface.

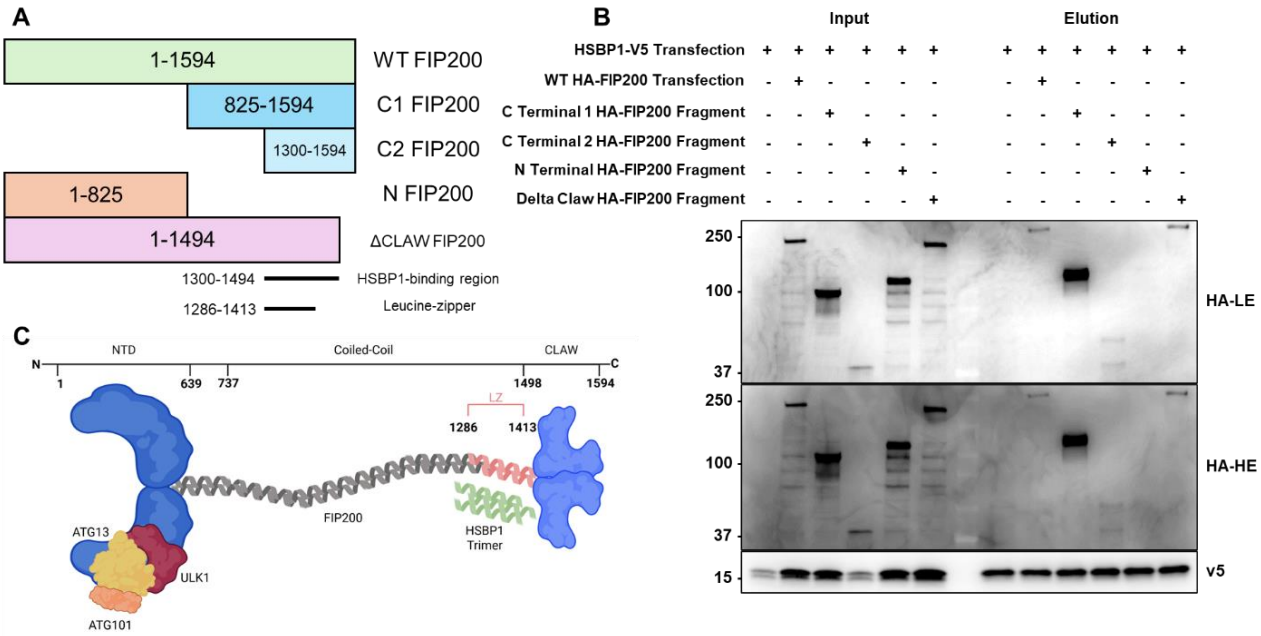

Figure 4. HSBP1 interacts with the FIP200 coiled-coil and leucine zipper region. (A) *Schematic of HA-tagged full-length FIP200 (WT, residues 1–1594) and truncation constructs used for domain mapping: C-terminal fragment 1 (C1, 825–1594), C-terminal fragment 2 (C2, 1300–1594), N-terminal fragment (N, 1–825), and a Claw deletion mutant (ΔCLAW, 1–1494). The mapped HSBP1-binding region (residues 1300–1494) and leucine zipper motif (residues 1371–1391) are indicated.* ***(B)*** *V5 immunoprecipitation following co-transfection of HSBP1-V5 with full-length or truncated HA–FIP200 constructs into FIP200 KO HeLa cells. Western blotting of inputs and V5-IP eluates demonstrates that HSBP1-V5 co-precipitates WT, C1, C2, and ΔCLAW FIP200, but not the N-terminal fragment, mapping the interaction to the coiled-coil region distal to the NTD. HA blots are shown at low exposure (LE) and high exposure (HE) to resolve differential binding across fragments. V5 blot confirms equivalent HSBP1-V5 expression and immunoprecipitation across conditions.* ***(C)*** *Structural model of FIP200 domain architecture showing the NTD (residues 1–639), coiled-coil (737–1498), leucine zipper (LZ, 1286–1413), and Claw domain (1498–1594). The AIC components ATG13 (yellow), ULK1 (red), and ATG101 (orange) engage*

the NTD, while the HSBP1 trimer (green) associates with the distal coiled-coil and LZ region, illustrating the spatial separation between AIC scaffolding and HSBP1 binding.

4.3.4 ALPHAFOLD3 PREDICTS A DIRECT COILED-COIL INTERACTION BETWEEN FIP200 AND HSBP1

To define the structural basis of the FIP200–HSBP1 interaction mapped (**Section 4.3.3**), we used AlphaFold3 to model trimeric HSBP1 in complex with dimeric full-length FIP200. Consistent with prior evidence that HSBP1 forms a coiled-coil homotrimer, the top-ranked model positioned HSBP1 along the distal coiled-coil region of FIP200, consistent with the domain mapping data, and spatially separated from the NTD that binds AIC components (**Figure 5A–C**). Per-residue confidence (pLDDT) was high across the coiled-coil regions of both proteins, including the predicted interaction (**Figure 5B**). The predicted interaction was characterized by hydrophobic packing between the coiled-coil domains (**Figure 5C**). Modeling of the minimal mapped binding region (residues 1300–1494) with HSBP1 recapitulated this interface with high confidence, consistent with the biochemical data (**Figure 4B**) showing that this region is sufficient for HSBP1 binding (**Figure 5D–F**). At the interface, FIP200 hydrophobic residues L1367, I1368, L1371 are positioned to contact HSBP1 residues M30, I34, and I35. These residues represent candidate sites for future mutagenesis to selectively disrupt the interaction without perturbing established functional domains within the FIP200 NTD or Claw.

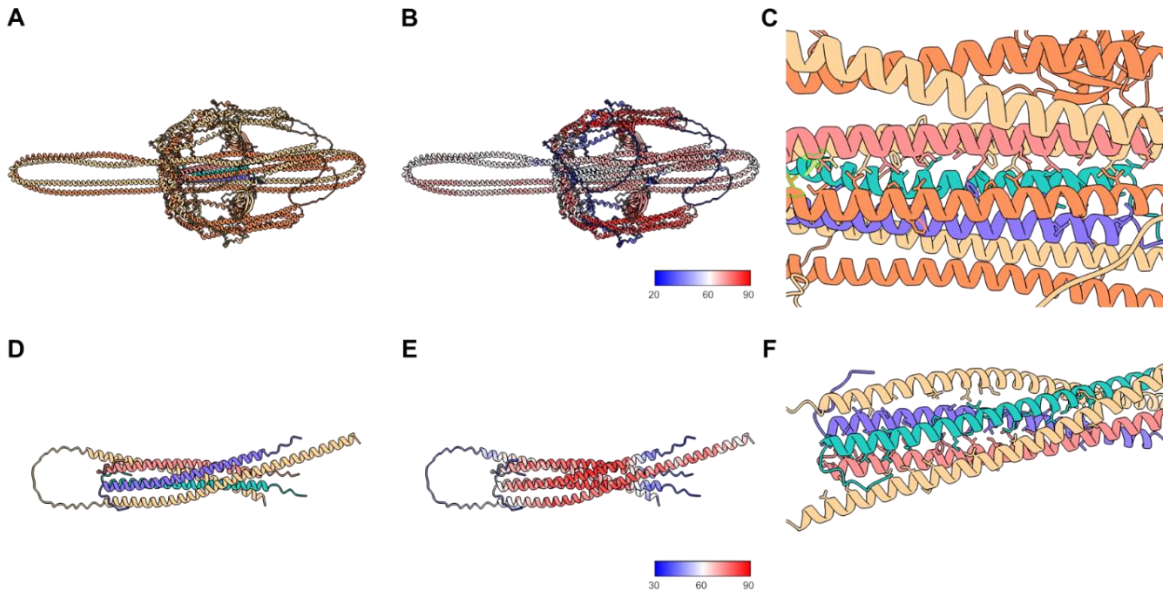

Figure 5. AlphaFold3 predicts a direct coiled-coil interaction between FIP200 and HSBP1. ***(A)*** *AlphaFold3-predicted structure of full-length dimeric FIP200 in complex with trimeric HSBP1, colored by chain. FIP200 chains (orange/salmon) form an extended coiled-coil dimer with flanking NTD and Claw domains, while the HSBP1 trimer (teal, purple, green) engages the distal coiled-coil region, consistent with the domain mapping data in Figure 3.* ***(B)*** *Same model colored by pLDDT score. The coiled-coil regions of both FIP200 and HSBP1 show high confidence (red), while flexible loops and terminal regions display lower confidence (blue). Scale indicates pLDDT values from 20 (low, blue) to 90 (high, red).* ***(C)*** *Zoomed view of the predicted FIP200–HSBP1 binding interface. HSBP1 trimer helices intercalate with the FIP200 coiled-coil, with hydrophobic side chains displayed at the interface, suggesting the interaction is mediated by hydrophobic packing between coiled-coil domains.* ***(d)*** *AlphaFold3-predicted structure of the dimeric FIP200 HSBP1-binding region (residues 1300–1494) in complex with trimeric HSBP1, colored by chain. FIP200 chains (orange/salmon) and HSBP1 trimer chains (teal, purple, pink) form a coiled-coil interaction consistent with the full-length prediction in (a).* ***(E)*** *Same model colored by pLDDT score. The interaction interface retains high confidence (red) despite the absence of flanking domains. Scale indicates pLDDT values from 30 (low, blue) to 90 (high, red).* ***(F)***

Zoomed view of the predicted interface showing hydrophobic contacts at the FIP200–HSBP1 contact surface. The recapitulation of the interaction using only the minimal mapped binding region confirms that residues 1300–1494 are sufficient for HSBP1 engagement independently of the NTD and Claw. All predictions were generated using AlphaFold3 with human protein sequences obtained from UniProt. Structures were visualized in UCSF ChimeraX.

4.3.5 HSBP1 INTERACTOME ENRICHES FIP200 AND COMPONENTS OF THE AUTOPHAGY CONJUGATION MACHINERY

To characterize the HSBP1 interactome, we performed V5-IP-MS from HeLa cells stably expressing HSBP1-V5 (S3 HSBP1-V5) and compared protein enrichment profiles to parental S3 cells lacking V5 expression. Western blot of IP fractions confirmed that HSBP1-V5 and endogenous FIP200 were enriched in the V5 eluate, while AIC subunits ULK1 and ATG101 were detected in the input and flowthrough, but absent in the eluate. (**Figure 6A**). Volcano plot analysis of the IP-MS data identified FIP200 among the significantly enriched proteins, confirming the specific interaction between HSBP1 and FIP200 (**Figure 6B**). Consistent with results from HA-FIP200 HeLa cells (**Figure 2C–E**), HSBP1-V5 did not co-precipitate AIC subunits, autophagy cargo receptors (NBR1, p62/SQSTM1), or LC3 (**Figure 7A**), confirming that the selective FIP200 interaction is maintained across independent cell lines. Beyond FIP200, HSBP1-V5 enriched components of the autophagy conjugation machinery – ATG5, ATG7, ATG12, and ATG16L1, as well as the early endosome tethering factor, EEA1 (**Figure 6B-D**). Western blot validation confirmed specific enrichment of ATG16L1 and EEA1 in the HSBP1-V5 eluate (**Figure 6C**). Comparison of significantly enriched proteins from HA-FIP200 and HSBP1-V5 interactomes revealed limited overlap, with RB1CC1/FIP200 highly enriched in both datasets as expected for reciprocal interactors, and ATG16L1 and ATG5 shared between the two interactomes (**Figure 7B**). The largely distinct enrichment profiles indicate that HSBP1 associates with a separate set of proteins relative to FIP200. Notably, ATG16L1 and EEA1 both contain coiled-coil regions,

hinting at a coiled-coil interaction interface with HSBP1[31]. These results suggest a potential link between HSBP1, FIP200, and downstream autophagy machinery.

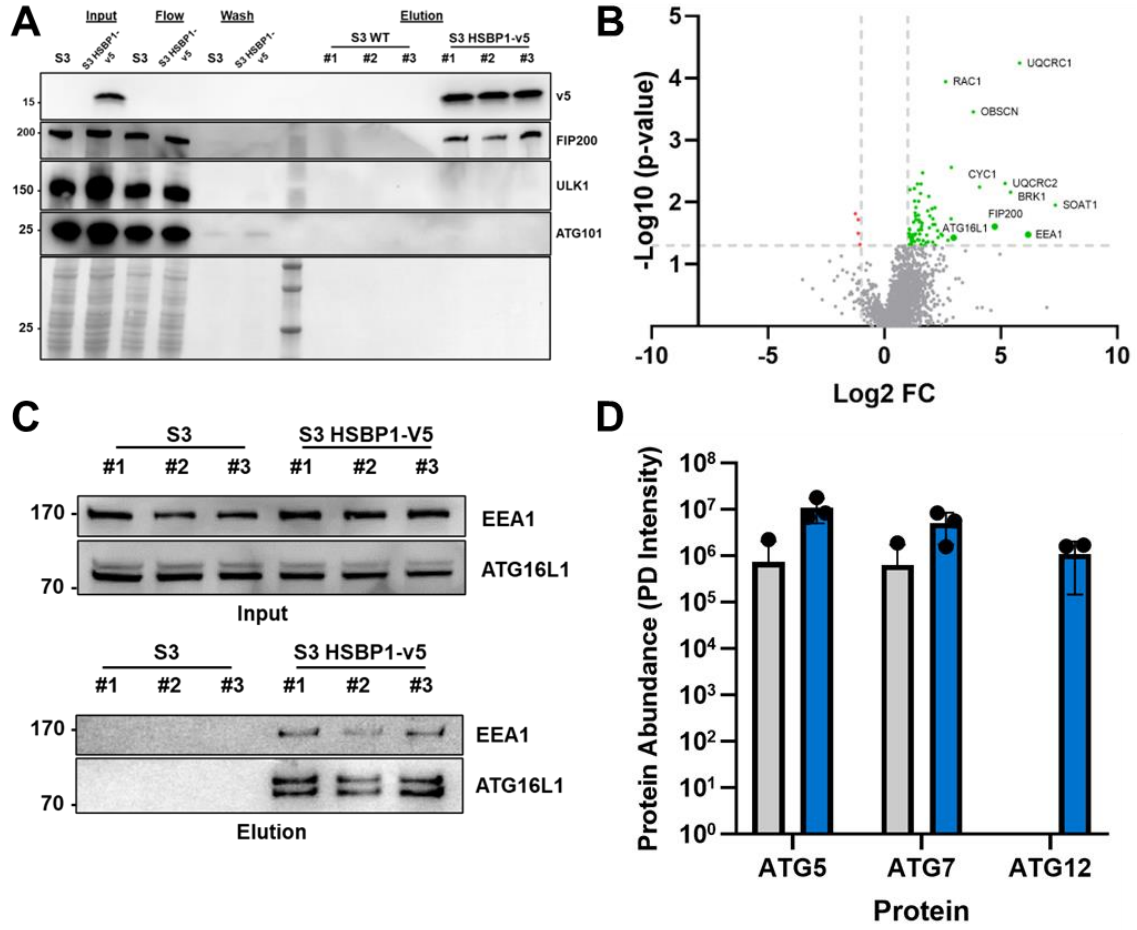

Figure 6. HSBP1-V5 interactome profiling identifies FIP200 and components of the autophagy conjugation machinery. ***(A)*** *Western blot of V5 immunoprecipitation fractions from stable HSBP1-V5-expressing HeLa S3 cells (S3 HSBP1-V5). Fractions include total input, unbound flowthrough, wash, and V5 elution. HSBP1-V5 and endogenous FIP200 are enriched in the V5 eluate, confirming successful bait capture and co-precipitation of FIP200. Immunoblots probed for AIC subunits ATG101 and ULK1 confirm both are detected in input and flowthrough but absent from the V5 eluate, indicating these components are not stably associated with HSBP1.* ***(B)*** *Volcano plot of differential protein enrichment from V5-IP-MS comparing S3 HSBP1-V5 to parental S3 HeLa cells. Log2 fold change (x-axis) is plotted against −log10(p-value) (y-axis).*

Significantly enriched proteins (log2FC ≥ 1 or ≤ −1, −log10(p-value) ≥ 1.3; unadjusted two-sided t-test) are shown in green. Select enriched proteins are labeled. ***(C)*** *Western blot validation of selected interactors from V5-IP eluates of parental S3 and S3 HSBP1-V5 cells. ATG16L1 and EEA1 are specifically enriched in the HSBP1-V5 eluate.* ***(D)*** *Protein abundance (Proteome Discoverer intensity) of autophagy conjugation machinery components ATG5, ATG7, and ATG12 in V5-IP eluates from parental S3 (grey) and S3 HSBP1-V5 (blue) cells. Individual data points are shown with bars representing the mean.*

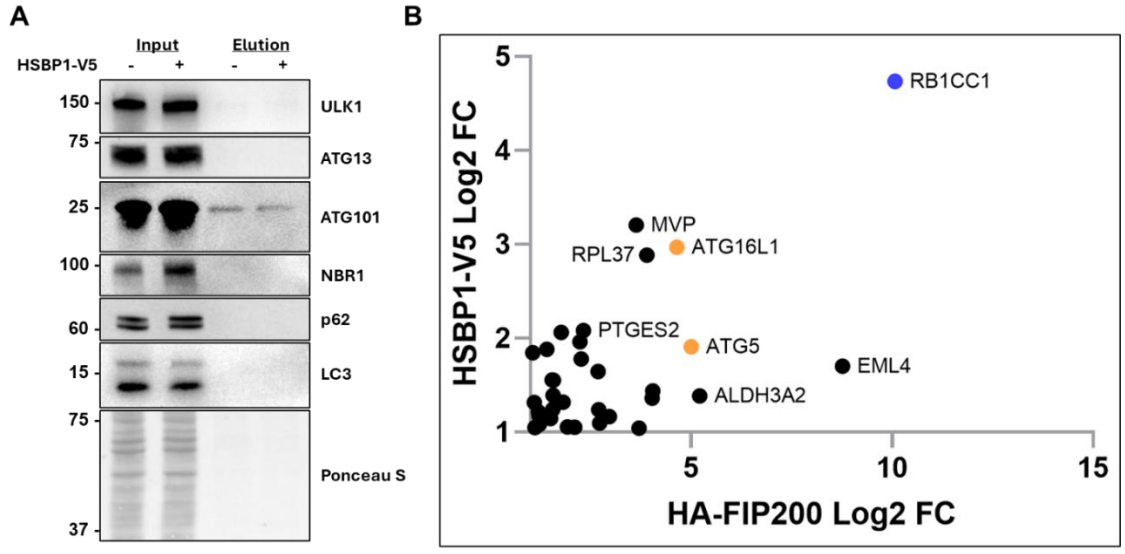

Figure 7. HSBP1-V5 does not co-precipitate AIC subunits or autophagy cargo receptors, and comparison of HSBP1 and FIP200 interactomes. ***(a)*** *Immunoblot of input and V5-IP eluates from parental S3 (−) and stable S3–HSBP1-V5 (+) HeLa cells probed for AIC subunits (ULK1, ATG13, ATG101), autophagy cargo receptors (NBR1, p62/SQSTM1), and the autophagy marker LC3. All proteins are detected in the input but absent from the V5-IP eluate, confirming that HSBP1 does not stably associate with the broader AIC or autophagy substrates. Ponceau S stain is the loading control.* ***(b)*** *Scatter plot comparing log2 fold change enrichment of significantly enriched proteins from HA-FIP200 IP-MS (x-axis) and HSBP1-V5 IP-MS (y-axis). RB1CC1/FIP200 (blue) is highly enriched in both datasets, consistent with HSBP1 and FIP200 being reciprocal interactors. ATG16L1 and ATG5 (orange) are shared between both interactomes. The limited overlap between datasets indicates that HSBP1 associates with a largely distinct set of proteins relative to FIP200.*

4.3.6 HSBP1 INTERACTS WITH NOVEL COILED-COIL PROTEINS

Among the most enriched proteins in the HSBP1-V5 IP were CCHCR1 and CROCC, both consistently detected across all HSBP1-V5 replicates and absent in parental control, indicating reproducible and specific enrichment (not shown). Coiled-coil prediction

using MultiCoil2 indicated that both proteins contain extensive coiled-coil regions (not shown)[32]. Similarly, ATG16L1 contains a well-characterized coiled-coil region. Notably, all three proteins are reported to form obligate homodimers[33–35], analogous to FIP200.

To assess whether these associations could be mediated by coiled-coil interactions, we used AlphaFold3 to model trimeric HSBP1 in complex with full-length dimeric ATG16L1, CCHCR1, and CROCC. For ATG16L1, a coiled-coil region spanning residues 79-232 was predicted, with the HSBP1 interaction localized to residues 124-179. In all cases, the top-ranked models supported direct coiled-coil-mediated interfaces between trimeric HSBP1 and the respective dimers, consistent with the enrichment observed in IP-MS (**Figure 8**). Together, these results support a model in which HSBP1 preferentially interacts with coiled-coil proteins that form higher-order oligomeric assemblies.

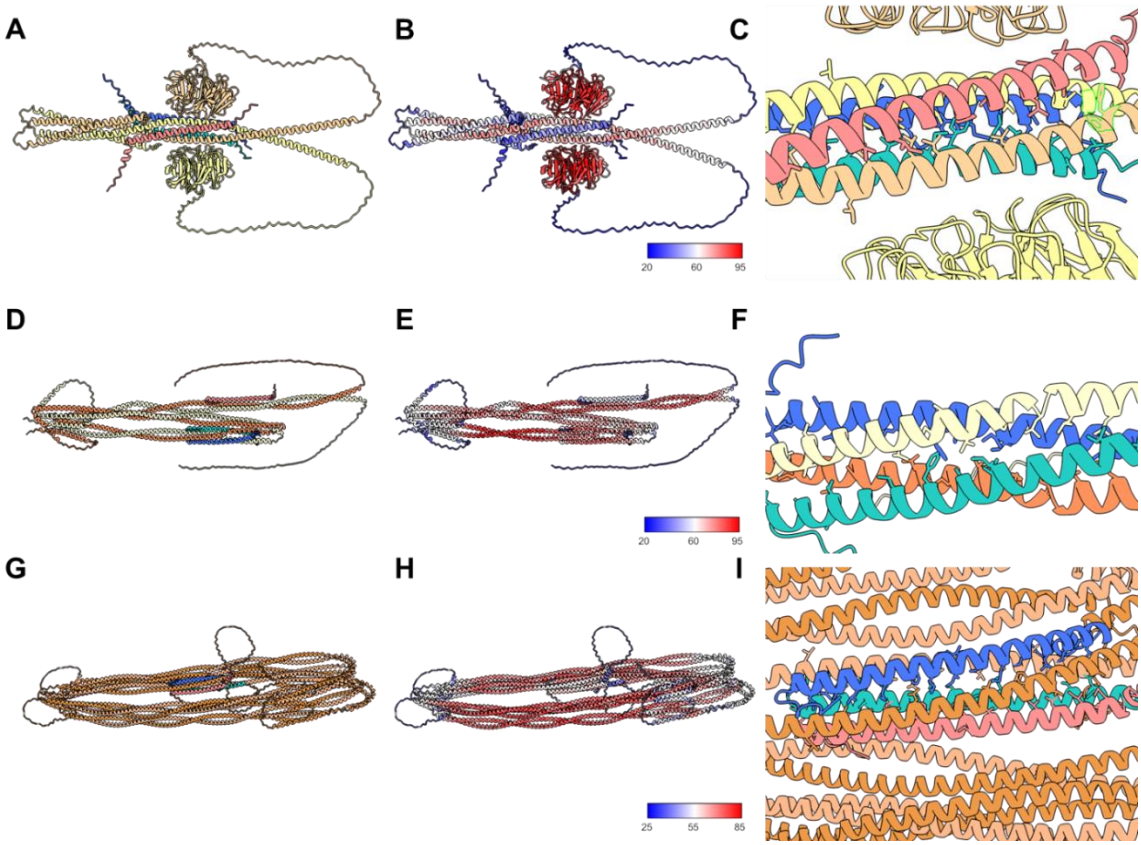

Figure 8. AlphaFold3 predicts coiled-coil-mediated interactions between HSBP1 and multiple interactome hits. *AlphaFold3-predicted structures of trimeric HSBP1 in complex with dimeric coiled-coil proteins identified in the HSBP1-V5 IP-MS (Figure 4). For each complex, three views are shown: chain coloring (left), pLDDT confidence scoring (center), and a zoomed view of the predicted binding interface with hydrophobic side chains displayed (right).* ***(A–C)*** *Dimeric ATG16L1 (orange/yellow) in complex with trimeric HSBP1 (teal, pink, green). The HSBP1 trimer engages the ATG16L1 coiled-coil domain, distal to the C-terminal WD40 repeat domain. pLDDT scale: 20–95.* ***(D–F)*** *Dimeric CCHCR1 (orange/salmon) in complex with trimeric HSBP1 (teal, blue, pink). pLDDT scale: 20–95.* ***(G–I)*** *Dimeric CROCC (orange) in complex with trimeric HSBP1 (teal, blue, green). pLDDT scale: 25–85. Across all three complexes, HSBP1 engages the coiled-coil regions of the partner protein through hydrophobic packing, consistent with a general coiled-coil interaction mode. pLDDT coloring indicates high confidence (red) at the interaction interfaces. All predictions were generated using AlphaFold3 with human protein sequences obtained from UniProt. Structures were visualized in UCSF ChimeraX.*

4.3.7 HSBP1 IS RAPIDLY DEGRADED DURING METABOLIC STRESS INDEPENDENT OF AUTOPHAGY

In HSBP1-V5^{HeLa}, autophagy activation triggered rapid HSBP1 loss. Treatment with the mTOR inhibitor Torin1 or amino acid starvation (HBSS) resulted in approximately 70–80% reduction in HSBP1-V5 abundance within 1 hour relative to untreated control (**Figure 9A-E**). Endogenous HSBP1 could not be evaluated due to insufficient antibody detection. The rapid kinetics indicate post-translational regulation in response to metabolic stress.

To assess autophagy dependence, we combined autophagy induction with lysosomal inhibition using bafilomycin A1 (BafA). Torin1 or HBSS induced p62 turnover, confirming autophagy activation, while BafA blocked p62 degradation, verifying lysosomal inhibition. BafA treatment did not stabilize HSBP1-V5, indicating that

degradation occurs independently of autophagy. In FIP200 KO cells, Torin1–induced HSBP1-V5 degradation was comparable to wild-type, while p62 turnover was abolished (**Figure 9F**). These results establish that HSBP1 degradation under metabolic stress occurs independently of canonical autophagy.

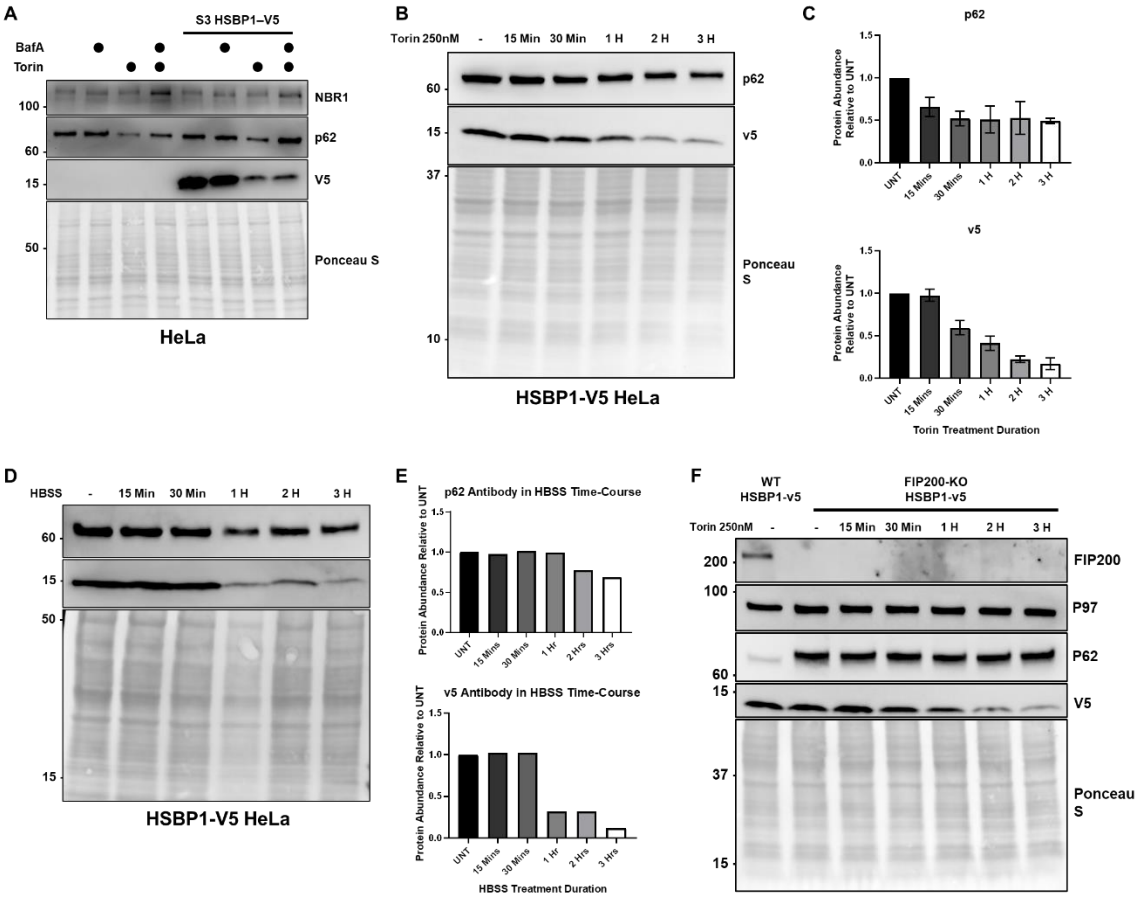

Figure 9. HSBP1 is rapidly degraded during metabolic stress independently of autophagy. *(**A**) S3 WT and S3 HSBP1-V5 HeLa cells were treated with 300 nM bafilomycin A1 (BafA), 250 nM Torin1, or both. Lysates were immunoblotted for NBR1, p62, and V5 (HSBP1). HSBP1-V5 was degraded upon autophagy activation with Torin1. (**B**) HSBP1-V5 HeLa cells were treated with 250 nM Torin1 for the indicated times. Cell lysates were immunoblotted for p62 and V5 (HSBP1). Ponceau S staining served as a loading control. (**C**) Quantification of (B) p62 and V5 protein abundance relative to*

*untreated (UNT) control (mean ± SD; n = 3 biological replicates). (**D**) HSBP1-V5 HeLa cells were subjected to amino acid starvation (HBSS) for the indicated times. Lysates were immunoblotted for p62 and V5. (**E**) Quantification of (D) p62 and V5 protein abundance relative to UNT (mean ± SD; n = 3). (**F**) FIP200 KO HSBP1-V5 HeLa cells were treated with Torin1. HSBP1-V5 degradation was comparable to wild-type cells, while p62 turnover was abolished, confirming autophagy-independent degradation.*

4.3.8 HSBP1 IS AN INTRINSICALLY UNSTABLE PROTEIN DEGRADED IN A PROTEASOME- AND P97-DEPENDENT MANNER

We next investigated proteasomal involvement in HSBP1-V5 degradation. Proteasome inhibition with MG132 treatment[37] was confirmed by accumulation of K48 poly-ubiquitination, the canonical signal for proteasomal degradation[38]. MG132 treatment stabilized HSBP1-V5, resulting in a 2-fold increase in HSBP1-V5 (**Figure 10A,B**). p97, also known as VCP, is an AAA+ ATPase that extracts ubiquitinated proteins from cellular structures and delivers them to the proteasome for degradation[39]. p97 inhibition with CB-5339[40] led to K48-linked polyubiquitin accumulation and stabilized HSBP1-V5 during Torin-1 treatment, indicating that HSBP1 turnover relies on both the proteasome and p97 (**Figure 10C**).

To measure protein stability, we performed cycloheximide (CHX) chase experiments to monitor protein degradation in the absence of new protein synthesis. HSBP1-V5 levels decreased by ~70% within 1 hour and ~90% by 3 hours, corresponding to an apparent half-life of 30-40 minutes (**Figure 10D**). In contrast, p62 and p97 remained largely stable over the same period (~60% and p97 ~90% of initial levels, respectively), confirming that HSBP1 is uniquely short-lived.

Collectively, these findings demonstrate that HSBP1 is an intrinsically unstable protein whose levels are maintained by continuous synthesis and regulated by a p97-dependent ubiquitin-proteasome degradation, independent of canonical autophagy.

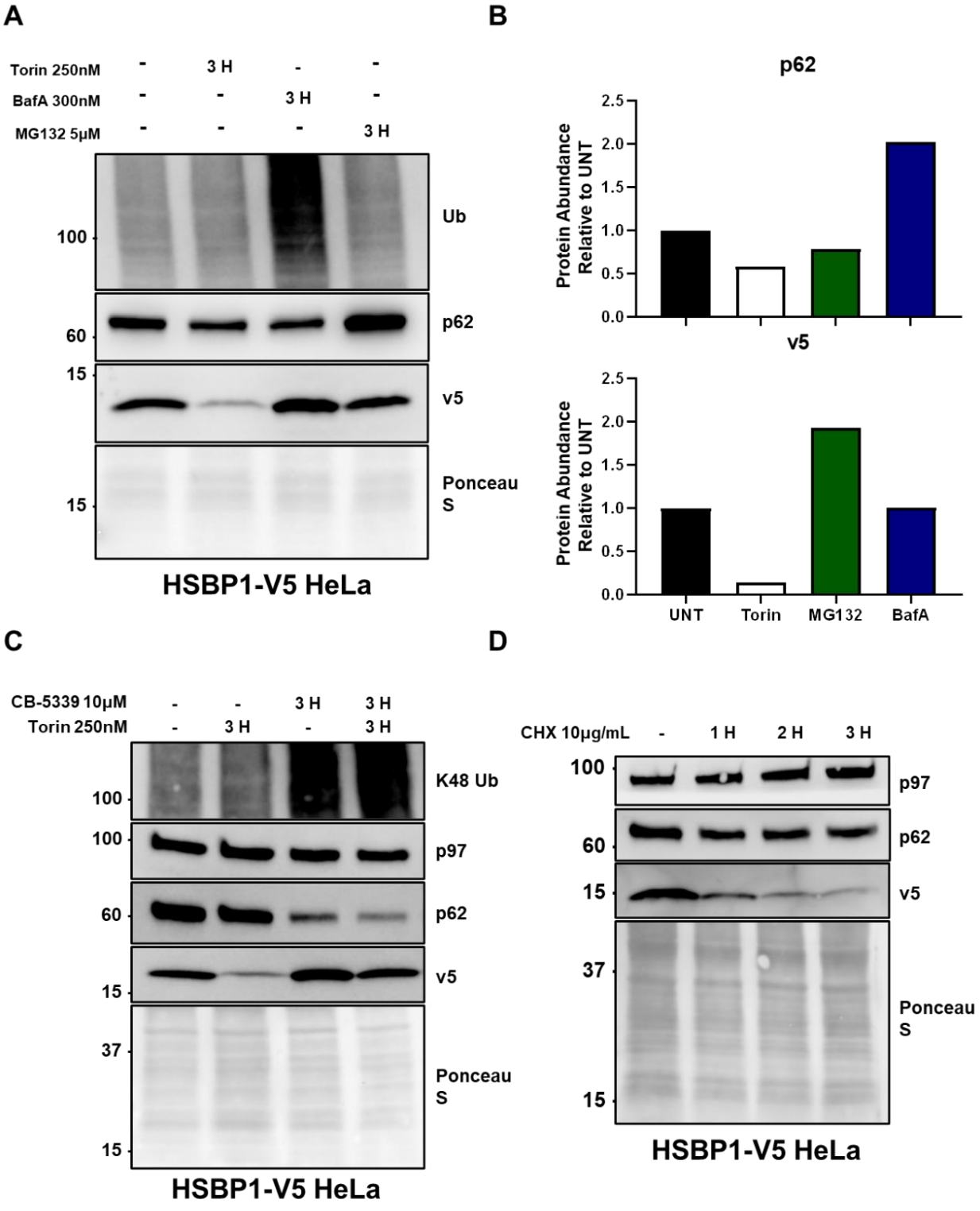
A
Torin 250nM - 3 H - -
BafA 300nM - - 3 H -
MG132 5μM - - - 3 H
100
60
15
15
Ub
p62
v5
Ponceau S
HSBP1-V5 HeLa
B
p62
Protein Abundance Relative to UNT
2.5
2.0
1.5
1.0
0.5
0.0
v5
Protein Abundance Relative to UNT
UNT
Torin
MG132
BafA
C
CB-5339 10μM - - 3 H 3 H
Torin 250nM - 3 H - 3 H
100
100
60
15
37
15
K48 Ub
p97
p62
v5
Ponceau S
HSBP1-V5 HeLa
D
CHX 10μg/mL - 1 H 2 H 3 H
100
60
15
37
15
p97
p62
v5
Ponceau S
HSBP1-V5 HeLa

Figure 10. HSBP1 is an intrinsically short-lived protein degraded through a p97- and proteasome-dependent pathway. (A) *HSBP1-V5 HeLa cells were treated with 250 nM Torin1 (3 h), 300 nM bafilomycin A1 (BafA; 3 h), or 5 µM MG132 (3 h) as indicated. Lysates were immunoblotted for ubiquitin (Ub), p62, and V5. Ponceau S staining served as a loading control. (**B**) Quantification of (A) V5 and p62 protein abundance relative to UNT. BafA treatment did not prevent HSBP1-V5 degradation, whereas MG132 stabilized HSBP1-V5. (**C**) HSBP1-V5 HeLa cells were treated with 10 µM CB-5339 (p97 inhibitor; 3 h) and/or 250 nM Torin1 (3 h) as indicated. Lysates were immunoblotted for K48-linked polyubiquitin, p97, p62, and V5. (**D**) HSBP1-V5 HeLa cells were treated with 10 µg/mL cycloheximide (CHX) for the indicated times. Lysates were immunoblotted for p97, p62, and V5. HSBP1-V5 exhibited an apparent half-life of 30-40 minutes, in contrast to the comparatively stable p62 and p97.*

4.3.9 PROTEOMICS CONFIRMS PROTEASOME-DEPENDENT, AUTOPHAGY-INDEPENDENT REGULATION OF ENDOGENOUS HSBP1

The biochemical characterization of HSBP1 stability in Figure 6 and 7 relied on overexpressed and tagged HSBP1, as reliable antibodies for endogenous HSBP1 detection were not available. To confirm these findings at the endogenous level, we performed quantitative proteomic profiling of WT HeLa S3 cells treated for 3 h with pharmacologic perturbations targeting the proteasome (MG132), autophagy (Torin1), or lysosomal acidification (BafA), relative to DMSO control. Western blot analysis confirmed the efficacy of each treatment: MG132 induced accumulation of K48-linked polyubiquitinated proteins, BafA elevated p62 and LC3-II levels consistent with impaired lysosomal degradation, and Torin1 promoted conversion of LC3-I to LC3-II indicative of autophagy induction (**Figure 11**). As expected, autophagy cargo receptors and LC3/GABARAP family proteins accumulated with BafA but not Torin1 at the proteome level, validating the pharmacological conditions and confirming that the decrease in HSBP1 upon Torin1 treatment is not attributable to autophagic clearance (**Figure 12A**). Direct comparison of BafA versus Torin1 further highlighted the

divergent regulation of autophagy substrates and HSBP1 across these conditions (**Figure 12B**).

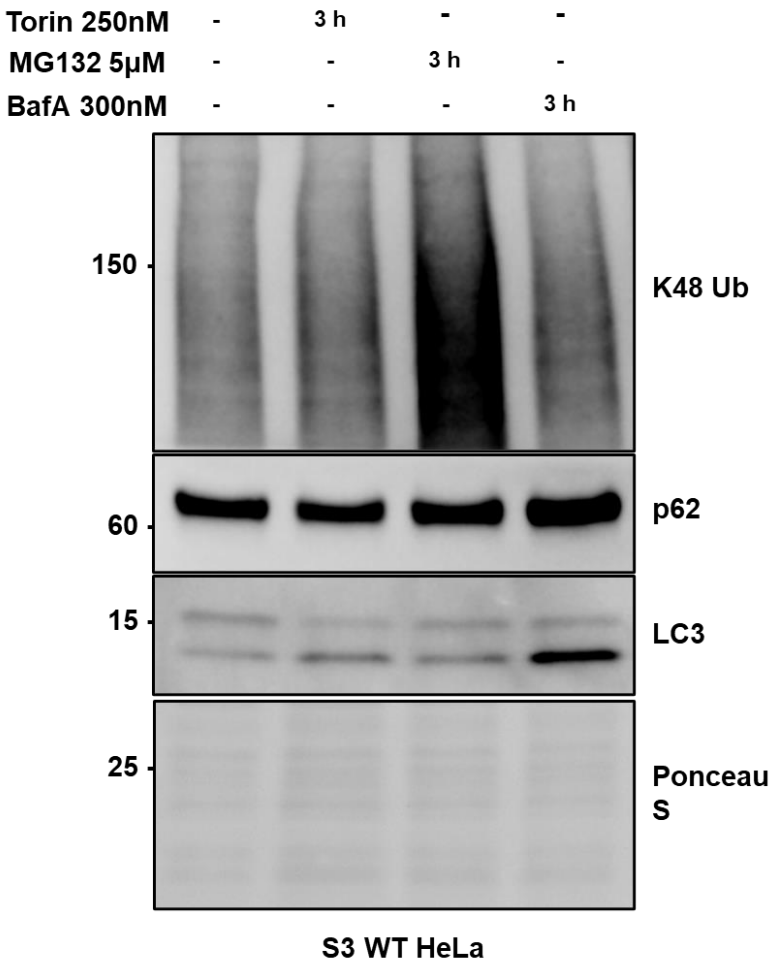

Figure 11. Validation of pharmacological treatment efficacy. *Western blots of wild-type HeLa S3 cells treated for 3 h with DMSO, Torin1, MG132, or BafA. From top to bottom: K48-linked polyubiquitin, p62/SQSTM1, LC3, and Ponceau S (loading control). Accumulation of K48-linked polyubiquitinated proteins under MG132 confirms effective proteasome inhibition. Elevated p62 levels under BafA are consistent with impaired lysosomal degradation. LC3 blotting reveals a shift from LC3-I to LC3-II with Torin1, indicating autophagy induction, and accumulation of LC3-II with BafA, consistent with blocked autophagic flux.*

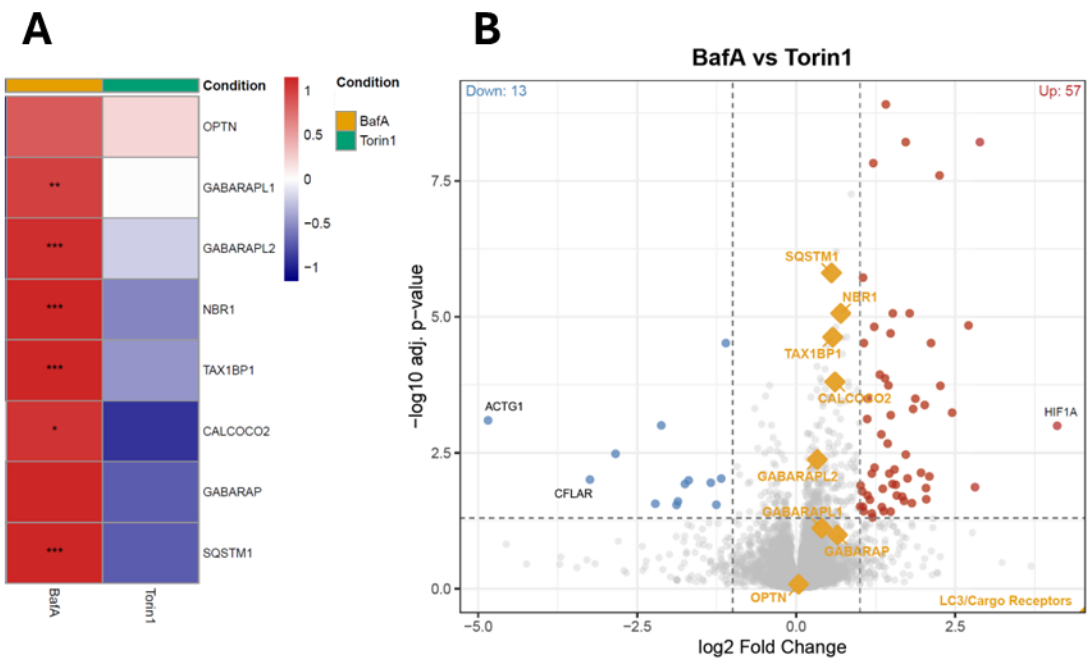

Figure 12. Autophagy cargo receptors and LC3/GABARAP family proteins accumulate under BafA but not Torin1 treatment. (A) *Heatmap showing log2 fold change relative to DMSO for selected autophagy cargo receptors and LC3/GABARAP family proteins across DMSO, BafA, and Torin1 conditions in wild-type HeLa S3 cells treated for 3 h (n = 4 biological replicates per condition). Asterisks denote significant differences versus DMSO by t-test (*p < 0.05, **p < 0.01, ***p < 0.001).* ***(B)*** *Volcano plot of differential protein abundance comparing BafA versus Torin1 (log2 fold change, x-axis; −log10 adjusted p-value, y-axis). Significantly decreased (adjusted p < 0.05, log2FC < −1) and increased (adjusted p < 0.05, log2FC > 1) proteins are colored blue and red, respectively. LC3/GABARAP family members and cargo receptors are highlighted as orange diamonds and labeled. Dashed lines indicate significance thresholds. The number of significantly changed proteins is indicated in the upper corners.*

Consistent with the biochemical data, HSBP1 showed decreased abundance with Torin1, increased abundance with MG132, and no significant change with BafA, confirming that

endogenous HSBP1 is rapidly degraded in a proteasome-dependent manner upon mTOR inhibition, independently of lysosomal turnover (**Figure 13**).

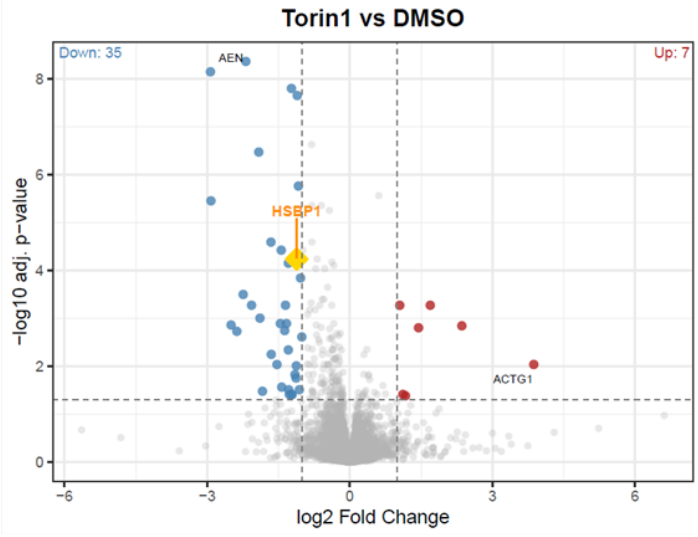
Torin1 vs DMSO
Down: 35
Up: 7
AEN
HSBP1
ACTG1
−log10 adj. p−value
log2 Fold Change

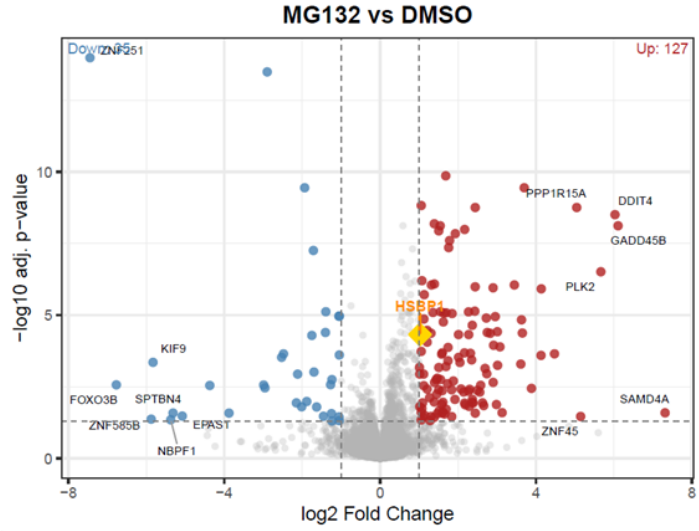
MG132 vs DMSO
Up: 127
PPP1R15A
DDIT4
GADD45B
PLK2
HSBP1
KIF9
FOXO3B
SPTBN4
ZNF585B
EPAST
NBPF1
SAMD4A
ZNF45
−log10 adj. p−value
log2 Fold Change

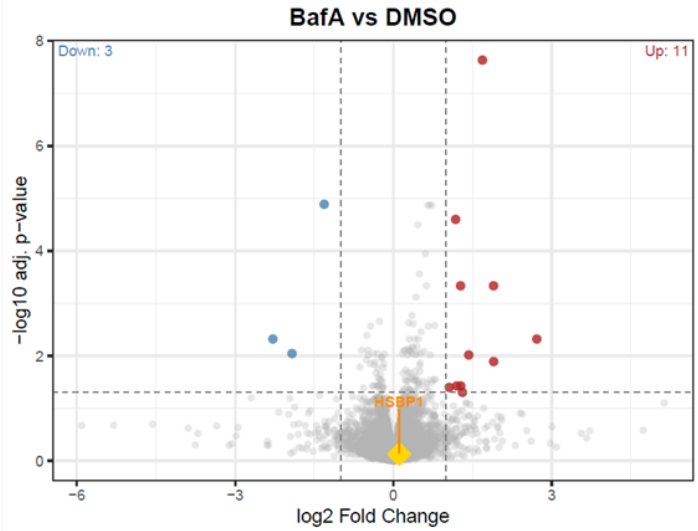
BafA vs DMSO
Down: 3
Up: 11
HSBP1
−log10 adj. p−value
log2 Fold Change

Figure 13. Differential protein abundance following 3 h drug treatment in wild-type HeLa S3 cells. *Volcano plots show log2 fold change (x-axis) versus −log10 adjusted p-value (y-axis) for all detected proteins after Torin1, MG132, or BafA treatment relative to DMSO control (n = 4 biological replicates per condition). Significantly decreased proteins (adjusted p < 0.05, log2FC < −1) are colored blue, and significantly increased proteins (adjusted p < 0.05, log2FC > 1) are colored red; non-significant proteins are shown in grey. HSBP1 is highlighted with a yellow diamond, showing decreased abundance with Torin1, increased abundance with MG132, and no significant change with BafA. Dashed lines indicate significance thresholds (adjusted p = 0.05, |log2FC| = 1). The number of significantly increased and decreased proteins is indicated in the upper corners of each panel.*

Among the proteins that responded similarly to HSBP1 under Torin1 and MG132 treatment, we identified cell cycle and growth regulators (CCND3, ODC1, AZIN1), transcriptional modulators that inhibit differentiation (ID3, EID1, EID2), and factors associated with stress and apoptosis (OSGIN1, AEN) (**Figure 14**). The coordinated regulation of these proteins suggests predominant control via mTOR-dependent synthesis and proteasome-mediated degradation, rather than lysosomal turnover. Notably, many of these proteins are known to be short-lived and rapidly turned over, consistent with a rapidly regulated class whose abundance is tightly governed by coupled synthesis and degradation.

The coordinated regulation of these proteins, decreased by Torin1, increased by MG132, and largely unaffected by BafA, is consistent with a class of short-lied proteins whose steady-state abundance is governed by mTOR-dependent synthesis and constitutive proteasomal degradation. The implications of this co-regulated network are considered in the Discussion.

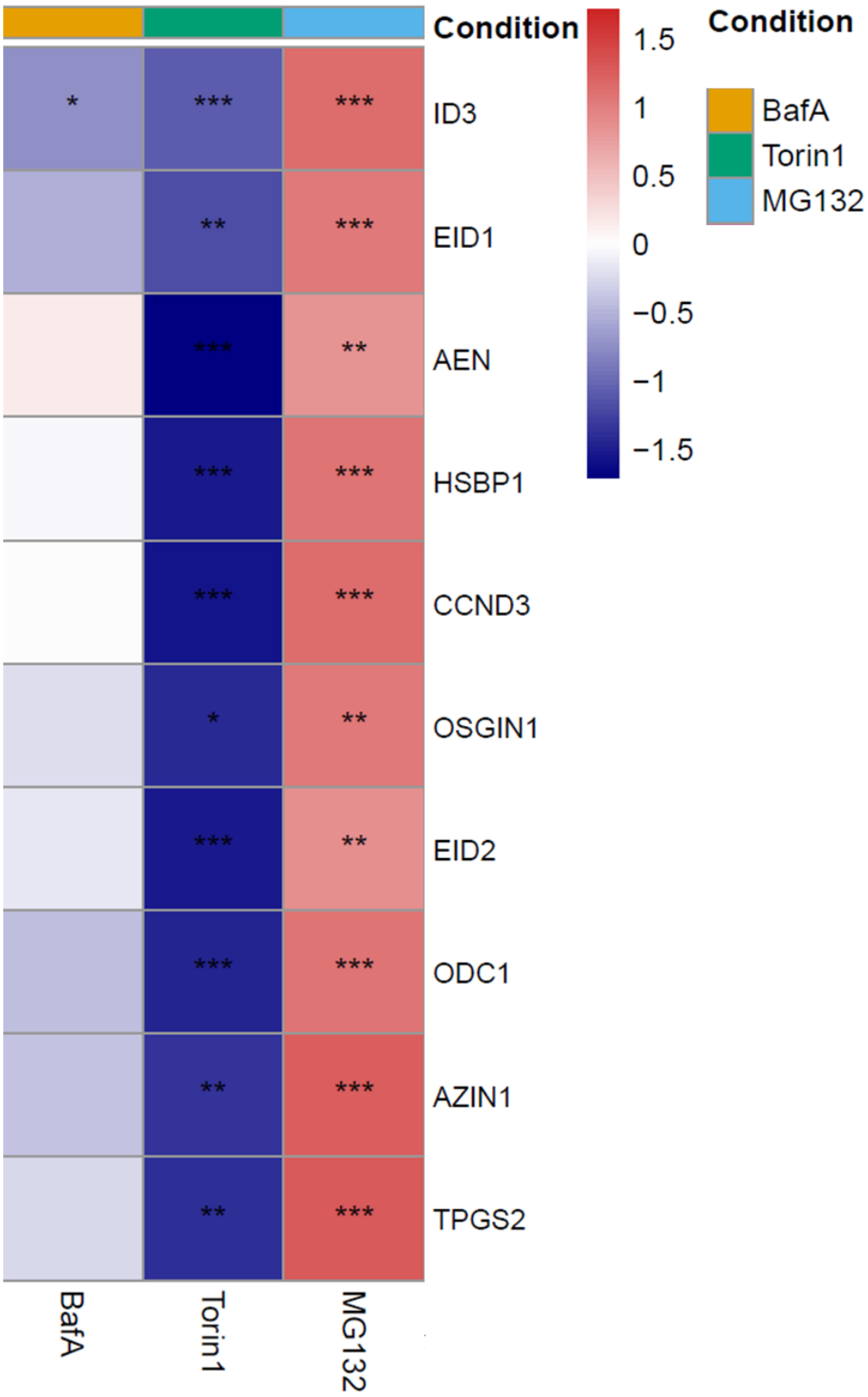
Condition
ID3
EID1
AEN
HSBP1
CCND3
OSGIN1
EID2
ODC1
AZIN1
TPGS2
BafA
Torin1
MG132
1.5
1
0.5
0
−0.5
−1
−1.5
Condition
BafA
Torin1
MG132

Figure 14. Proteins decreased by Torin1 and increased by MG132 suggest proteasomal degradation targets. *Heatmap showing log2 fold change relative to DMSO for selected proteins across BafA, Torin1, and MG132 conditions in wild-type HeLa S3 cells treated for 3 h (n = 4 biological replicates per condition). These proteins exhibit a shared pattern of decreased abundance with Torin1 and increased abundance with MG132, consistent with enhanced proteasomal turnover under mTOR inhibition. Asterisks denote significant differences versus DMSO by t-test (*p < 0.05, **p < 0.01, ***p < 0.001).*

4.4 DISCUSSION

We have identified and validated HSBP1 as a direct FIP200-binding protein that associates with the coiled-coil and leucine-zipper region, distinct from the N-terminal ULK1-binding domain and the C-terminal Claw domain. Notably, this region overlaps with binding sites for ATG16L1 and NDP52, raising the possibility that HSBP1 either competes with these factors or functions sequentially to regulate cargo recruitment. The detection of ATG5–ATG12–ATG7 conjugation machinery, EEA1, and ATG16L1 in the HSBP1 interactome suggests HSBP1 coordinates early autophagosome formation by linking FIP200 to vesicle trafficking and LC3 lipidation machinery through coiled-coil-mediated assemblies.

Beyond autophagy machinery, HSBP1 interacts with CCHCR1 and CROCC, coiled-coil scaffolds associated with centrosomes and cytoskeletal structures. This enrichment of homo-dimeric coiled-coil proteins suggests HSBP1 functions as a general coiled-coil assembly factor that modulates multimeric protein complexes across cellular compartments. This extends HSBP1's known role in HSF1 oligomer disruption and WASH complex assembly, positioning it as a regulator in coiled-coil-rich protein complexes.

Our data demonstrate that HSBP1 degradation occurs independently of lysosomal degradation and FIP200, indicating it is not cleared by autophagy but rather by active proteasomal targeting triggered by autophagy induction. The observation that HSBP1

undergoes proteasome-dependent degradation during autophagy induction presents an apparent paradox: why would a protein that associates with the autophagy initiation machinery be targeted for proteasomal degradation precisely when autophagy is activated? This finding is particularly striking given that autophagy and the ubiquitin-proteasome system are traditionally viewed as parallel, competing pathways for cellular protein homeostasis.

We propose three non-mutually exclusive models for the functional significance of HSBP1 degradation during autophagy induction. First, HSBP1 degradation may serve as a negative feedback mechanism to limit autophagy initiation. If HSBP1 stabilizes FIP200-containing complexes during autophagosome formation, its subsequent degradation could promote complex disassembly or recycling once initiation is complete. Second, HSBP1 may need to be cleared to allow engagement of competing FIP200 binding partners such as ATG16L1 or NDP52. In this model, HSBP1 degradation would function as a molecular switch, transitioning FIP200 from an HSBP1-bound "inactive" state to an “active” cargo-engaged state. Third, the rapid basal turnover of HSBP1 suggests that it functions as a dynamically regulated scaffold rather than a stable complex component. In this model, HSBP1 is a rapidly depletable buffer whose degradation during stress alters the availability of its coiled-coil binding partners, enabling functional remodeling of protein networks.

Emerging evidence suggests substantial crosstalk between the ubiquitin-proteasome system and autophagy: autophagy receptors (p62, NBR1) accumulate during proteasome inhibition and are themselves regulated by ubiquitination. The identity of the E3 ubiquitin ligase responsible for HSBP1 targeting remains unknown and represents a critical gap in understanding how metabolic stress signals are transduced to HSBP1 degradation. Similarly, whether HSBP1 degradation is constitutive and accelerated during stress, or requires stress-dependent post-translational modifications (e.g., phosphorylation by AMPK or stress kinases), remains to be determined. Identifying the upstream signals and ubiquitination machinery will be essential for understanding the functional consequences of HSBP1 removal during autophagy.

The proteomic analysis also revealed a cohort of proteins that share HSBP1's regulatory profile including cell cycle regulators (CCND3), polyamine metabolism components (ODC1, AZIN1), transcriptional repressors of differentiation (ID3, EID1, EID2), and stress-response factors (OSGIN1, AEN). This co-regulation suggests that HSBP1 may belong to a broader class of mTOR-sensitive, proteasome-cleared effectors whose rapid depletion may serve as a real-time readout of growth signaling status.

The rapid basal turnover of HSBP1 (half-life of 30-40 minutes) further suggests that HSBP1 functions as a dynamically regulated scaffold rather than a stable complex component. One possibility is that HSBP1 acts as a rapidly depletable buffer, whose removal during stress alters the availability of its coiled-coil binding partners, though whether this leads to functional remodeling of protein networks remains to be tested.

A key limitation of this work is that the functional consequences of HSBP1 loss on FIP200-dependent processes remain untested. While we have established the interaction, mapped its structural basis, and characterized the degradation mechanism, whether HSBP1 depletion alters autophagosome formation kinetics, cargo receptor engagement, or FIP200 complex composition has not been directly addressed.

Collectively, our findings position HSBP1 as a dynamically regulated coiled-coil scaffold whose rapid degradation during metabolic stress may alter the composition of FIP200-containing assemblies. We propose that HSBP1 stabilizes these assemblies under basal conditions and that its rapid clearance via p97-proteasome could permit engagement of competing FIP200 binding partners such as cargo receptors. Critical future experiments include identifying the E3 ligase responsible for HSBP1 ubiquitination, determining whether HSBP1 depletion affects cargo selectivity or autophagosome formation kinetics, and testing whether HSBP1's role in centrosomal and Golgi scaffolds reflects a general function in organizing coiled-coil networks across cellular compartments.

4.5 METHODS

Cell culture and generation of KO cell lines

HeLa S3 cells (ATCC CCL-2.2; RRID:CVCL_0058) were cultured at 37°C in a humidified 5% CO^2 atmosphere in Dulbecco's Modified Eagle Medium (DMEM; Sigma-Aldrich) supplemented with 10% non-heat-inactivated fetal bovine serum (FBS; R&D Systems) and 1% penicillin-streptomycin (Gibco). Adherent cells were passaged every 2–3 days using 1× TrypLE Express (phenol red-free; Gibco). All cell lines were used below passage 8. STR authentication was not performed. All cell lines were tested monthly for mycoplasma contamination using the MycoAlert Mycoplasma Detection Kit (Lonza) and consistently tested negative.

FIP200 KO HeLa S3 cells were generated by CRISPR-Cas9 as previously described (Vargas et al., 2019). Cells were either transfected with a Cas9 plasmid encoding the appropriate sgRNA and carrying a puromycin resistance marker, followed by selection with 5 µg/mL puromycin, or transfected with a GFP-tagged Cas9 plasmid encoding the appropriate sgRNA, after which GFP-positive cells were isolated by single-cell FACS 48 h post-transfection. In both cases, 20 clones per target were screened. All KO cell lines were validated by Western blot.

Generation of stable cell lines

Stable cell lines were generated using lentiviral and retroviral transduction. For lentiviral production, HEK293T cells were seeded in 6-well plates and transfected with pHDM-G (0.2 µg), CAG4RTR2 (0.6 µg), CAGGHIVgpco (0.6 µg), and the plasmid construct containing the gene of interest using polyethyleneimine (PEI; Polysciences) at a 3:1 PEI:DNA ratio (w/w) in serum-free DMEM. For retroviral production, HEK293T cells were similarly transfected with pUMVC (0.4 µg) and VSV-G (0.8 µg) alongside the gene of interest construct using the same PEI:DNA ratio. In both cases, 9 µg PEI was diluted in 150 µL serum-free DMEM prior to addition to cells. Media were replaced 16 hours post-transfection, and viral supernatants were harvested 48 h post-transfection and filtered through 0.45 µm syringe filters (WHA9914-2504, Cytiva) to remove contaminating cells. Viral supernatants were used crude without further concentration.

Target cells were seeded at 50,000 cells/well in 12-well plates and transduced by spinfection with 500 µL virus-containing media supplemented with 8 µg/mL polybrene (Sigma-Aldrich) at 800 × *g* for 45 minutes at 16°C. Transduced cells were selected with 5 µg/mL puromycin (Thermo Scientific) for 72 hours to establish stable integrants. The cells were then expanded and sorted by fluorescence-activated cell sorting (FACS) to additionally select for infected cells and normalize protein expression across individual cells.

Plasmids used in this study included HSBP1-V5 (Addgene #144637) and HA-FIP200 (Addgene #24303). HA-FIP200 truncation constructs were generated by mutagenesis as described below: full-length FIP200 (FL, residues 1–1594), C-terminal fragment 1 (C1, residues 826–1594), C-terminal fragment 2 (C2, residues 1299–1594), N-terminal fragment (N, residues 1–825), and ΔClaw mutant (residues 1–1490).

Mutagenesis

Site-directed mutagenesis of HA-FIP200 truncation constructs was performed using Q5® Hot Start High-Fidelity DNA Polymerase (NEB) according to the manufacturer's protocol with primer pairs designed to introduce deletions. Briefly, PCR reactions (50 µL) contained 1× Q5 reaction mix, 0.5 µM each primer, 1 ng of plasmid template, and 1 U of Q5 Hot Start polymerase. Thermocycling conditions were optimized according to primer T_m values, typically involving an initial denaturation at 98 °C for 30 s, followed by 25 cycles of 98 °C for 10 s, 55–65 °C for 15 s, and 72 °C for 30 s per kb, with a final extension at 72 °C for 2 min. Following amplification, 1 µL of the PCR product was treated with 1× KLD enzyme mix (NEB) containing T4 polynucleotide kinase, T4 DNA ligase, and DpnI for 15–60 min at room temperature to simultaneously phosphorylate, ligate, and digest parental methylated DNA. The reaction mixture was then transformed into chemically competent *E. coli* (NEB 5-alpha), and positive clones were verified by Sanger sequencing.

Transient transfections

For co-transfection experiments, FIP200 KO HeLa cells were cultured in 15-cm plates in DMEM supplemented with 10% FBS at 37°C in a humidified incubator with 5% CO^2 until reaching 75% confluency. A DNA-PEI complex was prepared by mixing 30 µg of plasmid DNA with 90 µg of polyethylenimine (PEI; 1 mg/mL stock; Polysciences) in 1.5 mL of Opti-MEM. The mixture was vortexed briefly and incubated at room temperature for 15 minutes to allow complex formation. The transfection mixture was then added dropwise to the cells, and the plate was gently swirled to ensure even distribution. Cells were incubated overnight before the media was replaced with fresh DMEM containing 10% FBS. Cells were harvested 24–48 hours post-transfection for downstream analyses.

Protein gels and Western blots

Cells were plated in six-well plates at a density of 400,000 cells per well and incubated overnight. Cells were harvested using TrypLE Express (12604-013, Thermo Fisher Scientific) and pelleted by centrifugation. Cell pellets were washed with phosphate-buffered saline (PBS) and lysed in radioimmunoprecipitation assay (RIPA) buffer (50 mM Tris, 150 mM NaCl, 0.1% SDS, 0.5% sodium deoxycholate, 1% Triton X-100) supplemented with EDTA-free broad-spectrum protease inhibitors (Thermo Fisher Scientific) for 15 minutes on ice. Lysates were cleared by centrifugation at 20,000 × *g* for 15 minutes at 4°C, and soluble fractions were collected. Protein concentration was determined using the BCA assay (Thermo Fisher Scientific). Samples were diluted 1:4 in 4× SDS loading buffer, denatured at 95°C for 5 minutes, and briefly centrifuged. Five to ten micrograms of protein per sample was resolved on 4–20% Mini-PROTEAN TGX gels (Bio-Rad) at 150 V for 60 minutes. Proteins were transferred to nitrocellulose membranes using the Trans-Blot Turbo Transfer System (Bio-Rad) for 10 minutes. Membranes were stained with Ponceau S (Thermo Scientific) for 5 minutes at room temperature, washed with deionized water, and imaged using a ChemiDoc MP Imaging System (Bio-Rad). Membranes were washed in TBS-T (Tris-buffered saline + 0.1% Tween-20) and blocked for 1 hour at room temperature in 5% nonfat milk in TBS-T. Primary antibody incubation was performed overnight at 4°C in 2.5% nonfat milk in

TBS-T at the concentrations listed below. Membranes were washed three times for 5 minutes with TBS-T and incubated for 1 hour at room temperature with goat anti-mouse or goat anti-rabbit HRP-conjugated secondary antibodies (1706515 and 1706516, Bio-Rad; RRID:AB_11125142 and RRID:AB_11125547) diluted 1:3000 in 2.5% nonfat milk in TBS-T. Membranes were washed three times with TBS-T and imaged using Immobilon ECL Ultra Western HRP Substrate (WBKLS0500, MilliporeSigma) and a ChemiDoc MP Imaging System (Bio-Rad). Densitometry analysis was performed using ImageLab version 6.1 (RRID:SCR_014210).

Pharmacological treatments

The following pharmacological treatments were used in this chapter: mTOR inhibition with Torin1 (250 nM; HY-13003, MedChemExpress), amino acid starvation with HBSS, proteasome inhibition with MG132 (10 μM; S2619, Selleckchem), p97/VCP inhibition with CB-5339 (10 μM), and lysosomal inhibition with bafilomycin A1 (300 nM; S1413, Selleckchem). Treatment durations are indicated in the figure legends.

Cycloheximide chase

To assess HSBP1 protein stability, HSBP1-V5 HeLa cells were treated with cycloheximide (CHX; 10 μg/mL) under nutrient-replete conditions. Cells were harvested at 0, 0.25, 0.5, 1, 2, and 3 h post-treatment. Lysates were analyzed by Western blot as described above. HSBP1 half-life was calculated from densitometry using ImageLab.

Immunoprecipitation

HeLa S3 and S3-HSBP1-V5 cells were cultured in 15-cm plates and harvested by trypsinization. Cell pellets were washed with PBS containing protease inhibitors, flash-frozen, and stored at –80 °C. Pellets were lysed in 40 mM HEPES (pH 7.5), 200 mM NaCl, 0.1% n-dodecyl-β-D-maltoside, 1 mM N-ethylmaleimide (HY-D0843, MedChemExpress), and protease inhibitors. Lysates were clarified by centrifugation at 16,600 × *g* for 15 min at 4 °C, and protein concentrations were determined by Bradford assay. Approximately 4 mg of lysate was incubated with 50 μL anti-V5 magnetic beads

per sample overnight at 4 °C with rotation. Beads were washed three times with lysis buffer and twice with 50 mM HEPES (pH 8.0), with the flow-through and first wash retained for Western blot analysis. For HA-FIP200 immunoprecipitation, the same protocol was followed using anti-HA magnetic beads. Bound proteins were digested on-bead with Lys-C for 4 h, followed by trypsin overnight at 37 °C. Peptides were acidified with trifluoroacetic acid, desalted using C18 spin columns, and dried prior to mass spectrometry analysis.

Immunoprecipitation mass spectrometry (IP-MS)

For digestion of IP eluates, 25 µL of 50 mM HEPES was added to dilute 10 M urea, followed by 1 µL TCEP (500 mM) and 3 µL CAA (500 mM), incubated for 20 and 15 min shaking at 750 rpm at 37°C, respectively. Two microliters of Lys-C (100 ng/µL, Wako) was added and incubated for 4 hours at 750 rpm at 37°C, followed by dilution with 375 µL HEPES buffer (50 mM) and 5 µL $CaCl_2$ (100 mM). Three microliters of trypsin (100 ng/µL, Thermo Scientific) was added and incubated overnight. Peptides were desalted with Pierce C18 spin columns (Thermo Fisher Scientific) and dried by vacuum centrifugation. Samples were reconstituted in Solvent A (97.8% H_2O, 2% ACN, 0.2% formic acid).

LC-MS/MS experiments were performed using an EASY-nLC 1000 (Thermo Fisher Scientific) connected to an Orbitrap Astral mass spectrometer (Thermo Fisher Scientific) equipped with a FAIMS Pro interface, operated in data-independent acquisition (DIA) mode. The sample (1 µg) in 0.1% formic acid solution was loaded onto an Aurora UHPLC Column (25 cm × 75 µm, 1.6 µm C18, AUR225075C18A, IonOpticks) and separated over 136 min at a flow rate of 0.35 µL/min with the following gradient: 2–6% Solvent B (7.5 min), 6–25% B (82.5 min), 25–40% B (30 min), 40–98% B (1 min), and 98% B (15 min). Solvent A consisted of 97.9% H_2O, 2% ACN, and 0.1% formic acid, and Solvent B consisted of 19.9% H_2O, 80% ACN, and 0.1% formic acid. MS1 scans were acquired in the Orbitrap analyzer at 500,000 resolution with a scan range of 350–1500 m/z. MS2 scans were acquired in the Astral analyzer. Ion source

settings were: ion source type, NSI; spray voltage, 2400 V; ion transfer tube temperature, 275 °C. System control and data collection were performed by Xcalibur software.

Proteomic analysis was performed using Proteome Discoverer 3.5 (Thermo Scientific), the *H. sapiens* UniProt database, and SequestHT with Percolator validation. Percolator FDRs were 0.01 (strict) and 0.05 (relaxed). Peptide FDRs were 0.01 (strict) and 0.05 (relaxed), with medium confidence and a minimum peptide length of 6. Carbamidomethyl (C) was a static modification, while oxidation (M) was dynamic. Additional N-terminal modifications included acetyl (protein N-term), Met-loss (protein N-term M), and Met-loss + acetyl (protein N-term M). P-values were calculated using independent t-tests, and data were sum-normalized to protein abundance, then normalized to bait protein abundance. Protein enrichment in tagged cell lines was compared to parental HeLa controls.

Protein expression and purification

Recombinant HSBP1 and FIP200 fragments (e.g., LZ-Claw, ΔClaw) were expressed in *E. coli* BL21 (DE3) cells. Cells were transformed with SUMO-tagged constructs and grown in LB medium at 37°C to an OD_{600} of ~0.6–0.8. Protein expression was induced with 0.5 mM IPTG at 18°C for 16 hours. Cells were harvested, resuspended in lysis buffer (50 mM Tris-HCl pH 8.0, 300 mM NaCl, 10 mM imidazole, 1 mM PMSF), and lysed by sonication on ice.

Lysates were clarified at 20,000 × *g* for 30 min at 4°C. SUMO-tagged proteins were purified using Ni^{2+}-NTA affinity chromatography (Qiagen), washed with 20 mM imidazole buffer, and eluted with 250 mM imidazole. SUMO tags were removed by SUMO protease digestion at 4°C overnight, followed by a second Ni^{2+}-NTA purification. Purified proteins were concentrated and exchanged into buffer suitable for nanoDSF/DLS analysis (50 mM HEPES pH 7.5, 150 mM NaCl). Purity was assessed by SDS-PAGE, and concentrations were determined by absorbance at 280 nm.

AlphaFold3 structural modeling

Protein–protein interactions involving HSBP1 were modeled using AlphaFold 3 via the AlphaFold Server (alphafoldserver.com). HSBP1 was modeled as a homotrimer, consistent with its known oligomeric state, in complex with candidate interacting proteins identified by IP-MS. Full-length human protein sequences were obtained from the UniProt database in FASTA format: HSBP1 (O75506), FIP200 (Q8TDY2), ATG16L1 isoform 1 (Q676U5-1), CROCC (Q5TZA2), and CCHCR1 (Q8TD31).

Full-length dimeric FIP200 was modeled in complex with full-length trimeric HSBP1. To refine the interaction interface, additional models were generated using truncated FIP200 constructs comprising the C-terminal region (residues 830–1594) and a minimal interaction region (residues 1300–1491), each in complex with trimeric HSBP1. Additional candidate interactions were modeled using full-length dimeric EEA1, ATG16L1, CROCC, and CCHCR1 in complex with trimeric HSBP1.

Predictions were generated using default AlphaFold 3 server parameters. For each complex, five models were produced. Models were ranked using the server-generated ranking score, which primarily reflects interface confidence (ipTM), and the top-ranked model was selected for downstream analysis. Model confidence was assessed using per-residue predicted Local Distance Difference Test (pLDDT) scores, global confidence metrics (pTM and ipTM), and Predicted Aligned Error (PAE) matrices. All modeled interfaces were interpreted as structural hypotheses requiring experimental validation.

Structural visualization

Structural visualization and analysis were performed in UCSF ChimeraX 1.10. Complexes were rendered using cartoon and surface representations, with individual chains colored distinctly. Predicted interaction interfaces were examined by visual inspection, with emphasis on regions of close contact and hydrophobic residues likely to mediate protein–protein interactions. pLDDT values were mapped onto structures using standard color schemes to visualize per-residue confidence.

Antibodies

Primary antibodies used for Western blotting included: LC3 (12741, clone D11; CST, 1:1000), ATG101 (13492; CST, 1:1000; RRID:AB_2798234), ATG13 (13273, clone D1G9; CST, 1:1000; RRID:AB_2798169), ULK1 (8054, clone D9K4; CST, 1:1000; RRID:AB_11178668), ULK2 (PA5-76450; Thermo Fisher, 1:1000), FIP200/RB1CC1 (17250-1-AP; ProteinTech, 1:1000; RRID:AB_10666428), NBR1 (16004-1-AP; ProteinTech, 1:1000; RRID:AB_2251178), p62 (PM045; MBL, 1:3000), ATG16L1 (8089, clone D6D5; CST, 1:1000), V5 (66007-1-Ig; ProteinTech, 1:1000), HA (51064-2-AP; ProteinTech, 1:1000), EEA1 (3288-1-AP; ProteinTech, 1:1000), K48-linked polyubiquitin (05-1307; Millipore), p97/VCP (MA3-004, clone 5; Thermo Fisher), and GAPDH (60004-1-Ig; ProteinTech, 1:10000).

Secondary antibodies included goat anti-rabbit IgG-HRP conjugate (170-6515; Bio-Rad; RRID:AB_11125142) and goat anti-mouse IgG-HRP conjugate (170-6516; Bio-Rad; RRID:AB_11125547), diluted 1:3000.

Statistical analysis

Statistical analyses were performed and graphed using GraphPad Prism Version 10.2.3 (RRID:SCR_002798). Significance was calculated with either a one-way or two-way ANOVA test with appropriate multiple comparison tests. Error bars are reported as mean ± SD for densitometry quantification, unless otherwise noted. Significance levels are indicated as: *P ≤ 0.05, **P ≤ 0.01, ***P ≤ 0.001. Images and blots shown are representative of at least two biological replicates as indicated in figure legends.

4.6 REFERENCES

1. Turco, E., Fischer, I. & Martens, S. *FIP200 Organizes the Autophagy Machinery at P62-Ubiquitin Condensates beyond Activation of the ULK1 Kinase*. http://biorxiv.org/lookup/doi/10.1101/2020.07.07.191189 (2020) doi:10.1101/2020.07.07.191189.
2. Shi, X. *et al.* ULK complex organization in autophagy by a C-shaped FIP200 N-terminal domain dimer. *J. Cell Biol.* **219**, e201911047 (2020).
3. Shi, X., Chang, C., Yokom, A. L., Jensen, L. E. & Hurley, J. H. The autophagy adaptor NDP52 and the FIP200 coiled-coil allosterically activate ULK1 complex membrane recruitment. *eLife* **9**, e59099 (2020).
4. Ravenhill, B. J. *et al.* The Cargo Receptor NDP52 Initiates Selective Autophagy by Recruiting the ULK Complex to Cytosol-Invading Bacteria. *Mol. Cell* **74**, 320-329.e6 (2019).
5. Zheng, Q. *et al.* Calcium transients on the ER surface trigger liquid-liquid phase separation of FIP200 to specify autophagosome initiation sites. *Cell* **185**, 4082-4098.e22 (2022).
6. Chen, M. *et al.* Structure and activation of the human autophagy-initiating ULK1C:PI3KC3-C1 supercomplex. *Nat. Struct. Mol. Biol.* **32**, 1596–1605 (2025).
7. Turco, E. *et al.* FIP200 Claw Domain Binding to p62 Promotes Autophagosome Formation at Ubiquitin Condensates. *Mol. Cell* **74**, 330-346.e11 (2019).
8. Zhou, Z. *et al.* Phosphorylation regulates the binding of autophagy receptors to FIP200 Claw domain for selective autophagy initiation. *Nat. Commun.* **12**, 1570 (2021).
9. Turco, E. *et al.* FIP200 Claw Domain Binding to p62 Promotes Autophagosome Formation at Ubiquitin Condensates. *Mol. Cell* **74**, 330-346.e11 (2019).
10. Smith, M. D. *et al.* CCPG1 Is a Non-canonical Autophagy Cargo Receptor Essential for ER-Phagy and Pancreatic ER Proteostasis. *Dev. Cell* **44**, 217-232.e11 (2018).

11. Maruyama, H. *et al.* Mutations of optineurin in amyotrophic lateral sclerosis. *Nature* **465**, 223–226 (2010).
12. Rezaie, T. *et al.* Adult-Onset Primary Open-Angle Glaucoma Caused by Mutations in Optineurin. *Science* **295**, 1077–1079 (2002).
13. Le Guerroué, F. *et al.* TNIP1 inhibits selective autophagy via bipartite interaction with LC3/GABARAP and TAX1BP1. *Mol. Cell* **83**, 927-941.e8 (2023).
14. Wu, S. *et al.* Structural basis for TNIP1 binding to FIP200 during mitophagy. *J. Biol. Chem.* **300**, 107605 (2024).
15. Gong, X. *et al.* Molecular bases of the interactions of ATG16L1 with FIP200 and ATG8 family proteins. *Nat. Commun.* **16**, 9035 (2025).
16. Gammoh, N., Florey, O., Overholtzer, M. & Jiang, X. Interaction between FIP200 and ATG16L1 distinguishes ULK1 complex–dependent and –independent autophagy. *Nat. Struct. Mol. Biol.* **20**, 144–149 (2013).
17. Fu, T. *et al.* Structural and biochemical advances on the recruitment of the autophagy-initiating ULK and TBK1 complexes by autophagy receptor NDP52. *Sci. Adv.* **7**, eabi6582 (2021).
18. Vargas, J. N. S. *et al.* Spatiotemporal Control of ULK1 Activation by NDP52 and TBK1 during Selective Autophagy. *Mol. Cell* **74**, 347-362.e6 (2019).
19. Zhang, M. *et al.* Mechanistic insights into the interactions of TAX1BP1 with RB1CC1 and mammalian ATG8 family proteins. *Proc. Natl. Acad. Sci.* **121**, e2315550121 (2024).
20. Tai, L.-J. *et al.* Structure-Function Analysis of the Heat Shock Factor-binding Protein Reveals a Protein Composed Solely of a Highly Conserved and Dynamic Coiled-coil Trimerization Domain. *J. Biol. Chem.* **277**, 735–745 (2002).
21. Liu, X. *et al.* Crystal structure of the hexamer of human heat shock factor binding protein 1. *Proteins Struct. Funct. Bioinforma.* **75**, 1–11 (2009).
22. Visweshwaran, S. P. *et al.* The trimeric coiled-coil HSBP1 protein promotes WASH complex assembly at centrosomes. *EMBO J.* **37**, e97706 (2018).
23. Satyal, S. H., Chen, D., Fox, S. G., Kramer, J. M. & Morimoto, R. I. Negative regulation of the heat shock transcriptional response by HSBP1. *Genes Dev.* **12**, 1962–1974 (1998).

24. Eroglu, B. *et al.* An essential role for heat shock transcription factor binding protein 1 (HSBP1) during early embryonic development. *Dev. Biol.* **386**, 448–460 (2014).
25. Schlütermann, D. *et al.* FIP200 controls the TBK1 activation threshold at SQSTM1/p62-positive condensates. *Sci. Rep.* **11**, 13863 (2021).
26. Hein, M. Y. *et al.* Global organelle profiling reveals subcellular localization and remodeling at proteome scale. 2023.12.18.572249 Preprint at https://doi.org/10.1101/2023.12.18.572249 (2023).
27. Sankar, D. S. *et al.* The ULK1 effector BAG2 regulates autophagy initiation by modulating AMBRA1 localization. *Cell Rep.* **43**, (2024).
28. Mauthe, M., Dinesh Kumar, N., Verlhac, P., van de Beek, N. & Reggiori, F. HSBP1 Is a Novel Interactor of FIP200 and ATG13 That Promotes Autophagy Initiation and Picornavirus Replication. *Front. Cell. Infect. Microbiol.* **11**, (2021).
29. Vargas, J. N. S. *et al.* Spatiotemporal Control of ULK1 Activation by NDP52 and TBK1 during Selective Autophagy. *Mol. Cell* **74**, 347-362.e6 (2019).
30. Nishimura, T. *et al.* FIP200 regulates targeting of Atg16L1 to the isolation membrane. *EMBO Rep.* **14**, 284–291 (2013).
31. Callaghan, J., Simonsen, A., Gaullier, J. M., Toh, B. H. & Stenmark, H. The endosome fusion regulator early-endosomal autoantigen 1 (EEA1) is a dimer. *Biochem. J.* **338**, 539–543 (1999).
32. Trigg, J., Gutwin, K., Keating, A. E. & Berger, B. Multicoil2: Predicting Coiled Coils and Their Oligomerization States from Sequence in the Twilight Zone. *PLOS ONE* **6**, e23519 (2011).
33. Parkhouse, R., Ebong, I.-O., Robinson, C. V. & Monie, T. P. The N-Terminal Region of the Human Autophagy Protein ATG16L1 Contains a Domain That Folds into a Helical Structure Consistent with Formation of a Coiled-Coil. *PLoS ONE* **8**, e76237 (2013).
34. Zhang, J., Wu, Q., Zhang, S., Sze, S. C. W. & Li, C. CCHCR1 links P-body proteins to the centrosome and is required for ciliogenesis through interacting with OFD1 and PCM1. *Cell. Mol. Biol. Lett.* **30**, 103 (2025).

35. Bahe, S., Stierhof, Y.-D., Wilkinson, C. J., Leiss, F. & Nigg, E. A. Rootletin forms centriole-associated filaments and functions in centrosome cohesion. *J. Cell Biol.* **171**, 27–33 (2005).
36. Hershko, A. The ubiquitin pathway for protein degradation. Trends Biochem. Sci. 16, 265–268 (1991).
37. Lee, D. H. & Goldberg, A. L. Proteasome Inhibitors Cause Induction of Heat Shock Proteins and Trehalose, Which Together Confer Thermotolerance in Saccharomyces cerevisiae. *Mol. Cell. Biol.* **18**, 30–38 (1998).
38. Komander, D. & Rape, M. The ubiquitin code. *Annu. Rev. Biochem.* **81**, 203–229 (2012).
39. Meyer, H., Bug, M. & Bremer, S. Emerging functions of the VCP/p97 AAA-ATPase in the ubiquitin system. *Nat. Cell Biol.* **14**, 117–123 (2012).
40. Roux, B. *et al.* Targeting acute myeloid leukemia dependency on VCP-mediated DNA repair through a selective second-generation small molecule inhibitor. *Sci. Transl. Med.* **13**, eabg1168 (2021).
41. Abramson, J. et al. Accurate structure prediction of biomolecular interactions with AlphaFold 3. *Nature* **630**, 493–500 (2024).
42. Pettersen, E. F. et al. UCSF ChimeraX: Structure visualization for researchers, educators, and developers. *Protein Sci. Publ. Protein Soc.* **30**, 70–82 (2021).

Chapter 5

CONCLUSIONS AND FUTURE DIRECTIONS

5.1 CONCLUSION

This work identifies a previously unrecognized functional architecture within the autophagy initiation complex (AIC), demonstrating that its components can operate in modular, functionally distinct assemblies independent of canonical autophagy. Specifically, the data support a model in which the ATG9A–ATG13–ATG101 submodule constitutes a dedicated membrane trafficking system that regulates Golgi-to-lysosome transport of activated STING, thereby controlling basal innate immune signaling.

Our starting point, unbiased proteomic profiling of AIC component KO lines, provided the discovery entry point: selective upregulation of type I interferon-stimulated genes in ATG101 and ATG13 knockout cells, but not in ULK1/2 or FIP200 knockouts. Much of the work that followed was to establish this finding as a real, rescuable, and generalizable cellular phenotype. HeLa cells, useful laboratory workhorses, are a unique cancer line that may not represent a generalizable cell context. The presence of this phenotype in HeLa, K562, THP-1, and MCF-7 cell lines establishes this as a conserved cellular response rather than a cell type-specific artifact.

Genetic and chemical dissection traced the interferon phenotype to a familiar immune nexus: STING homeostasis. In the absence of ATG13, ATG101, or ATG9A, active STING exits its first stop, the Golgi, but does not reach the lysosome. Instead, active STING accumulates in swollen post-Golgi vesicles. Mutational analysis demonstrated that the ATG101–ATG13 HORMA dimer and the ATG9A C-terminal HDIR motif are required for this trafficking function, genetically separating this pathway from canonical autophagy. Imaging further shows that the ATG9A–ATG13–ATG101 complex localizes to STING-containing vesicles at the post-Golgi stage, consistent with a direct role in vesicle maturation or sorting into the endolysosomal system.

In parallel, this work identifies HSBP1 as a direct, short-lived, proteasomally regulated interactor of FIP200. HSBP1 binds selectively to the FIP200 coiled-coil/leucine-zipper region independently of other AIC components and exhibits rapid turnover under basal and stress conditions. Its interactome is enriched for coiled-coil scaffold and vesicle-tethering proteins, suggesting a role in organizing higher-order assemblies. These findings position HSBP1 as a dynamically regulated factor that may modulate FIP200-dependent processes in response to metabolic state.

Together, these findings support a revised conceptual model of the AIC. Rather than a single integrated complex, the AIC is better understood as a modular platform: the ATG9A–ATG13–ATG101 submodule governs Golgi-to-lysosome trafficking and innate immune homeostasis, while FIP200 engages in parallel interactions, including HSBP1, to mediate distinct downstream processes. This modular organization provides a framework for understanding how conserved autophagy components have been repurposed to support diverse cellular functions beyond autophagosome biogenesis.

5.2 FUTURE DIRECTIONS

The findings described in this thesis raise four major areas for future investigation: (i) the molecular mechanism of GLAD, (ii) the substrate specificity of GLAD, (iii) the functional role of the FIP200–HSBP1 interaction, and (iv) the physiological and translational relevance of these pathways.

5.2.1 MECHANISM OF THE GLAD PATHWAY

The central challenge in understanding GLAD is disentangling the trafficking function of ATG9A–ATG13–ATG101 complex from its known role in canonical autophagy, lipid transfer, and membrane repair. Disrupting any one component risks confounding effects, therefore defining the GLAD pathway mechanism will require specifically isolating the GLAD-relevant activities of this complex.

Two non-mutually exclusive mechanistic models are consistent with our data.

In the first model, ATG9A's lipid scramblase activity drives membrane remodeling events required for ESCRT recruitment or multivesicular body (MVB) biogenesis. In this framework, the ATG13–ATG101 HORMA dimer functions to spatially regulate ATG9A activity at STING-containing membranes. In canonical autophagy, ATG9A vesicles serve as the seed membrane for the autophagosome[1]; in GLAD, this membrane contribution may instead facilitate endolysosomal entry. This model is supported by the requirement of the HDIR-HORMA interaction and the constitutive nature of ATG9A scramblase activity, which could be locally harnessed to promote membrane curvature or lipid redistribution necessary for downstream trafficking.

In the second model, the complex acts as a recruitment platform for machinery, such as ESCRT-III components[2]. Recent evidence that ATG9A physically interacts with ESCRT-III machinery, which is required for STING endolysosomal entry[3], supports this possibility. In this scenario, ATG13-ATG101 may mediate the recruitment of ESCRT machinery to post-Golgi vesicles.

These models can be distinguished experimentally by visualization of ESCRT recruitment in the presence and absence of ATG13–ATG101, as well as by testing the requirement for ATG9A scramblase activity using catalytically dead mutants.

A related mechanistic question concerns ATG101's contribution. ATG101 KO produces a more severe trafficking phenotype than ATG13 KO, suggesting that ATG101 may possess partially independent functions. Given that ATG101 can homodimerize and retain partial ATG9A binding independently of ATG13[4], targeted analysis of ATG101 homodimerization mutants and phospho-mutants may define its unique role within the GLAD pathway.

An additional observation requiring further investigation is the proteolytic processing of ATG9A during STING activation, which generates an N-terminal fragment stabilized by proteasome inhibition but insensitive to lysosomal inhibition (Chapter 3, Figure S2). This raises the possibility that ATG9A undergoes regulated processing during trafficking. Key experiments include characterizing this fragment by mapping the

cleavage site and testing the functional consequences of cleavage-resistant mutants on STING trafficking.

5.2.2 SUBSTRATE SCOPE OF GLAD

An open question is whether GLAD is specific to STING or functions as a broader Golgi-to-lysosome trafficking pathway. Previous studies have identified ATG9A-dependent, FIP200-independent degradation pathways for other cargoes such as NCOA4 and ferritin[5], and for a subset of K63-ubiquitinated proteins[6], suggesting the pathway is not STING-specific. Preliminary experiments exploring NCOA4 and ferritin in ATG101/ATG13 KO cells have been performed (unpublished) and these do not appear to be ATG9A-ATG13-ATG101 trafficking substrates. ATG9A vesicles contribute to lysosome homeostasis by trafficking cathepsin D and L from the TGN, mediated through AP-1 binding to the tyrosine sorting motif of ATG9A, raising the possibility that GLAD substrates may include other Golgi-to-lysosome cargo beyond immune signaling proteins[7].

Defining the substrate scope of GLAD will require a systematic approach. Proximity labeling strategies to identify cargo flux in wild-type versus GLAD KO cells could identify cargo that accumulate or fail to traffic in the absence of this pathway.

An ultimate goal is to define a targeting logic that defines GLAD substrates. Potential determinants include post-translational modification (e.g., ubiquitin linkage type) or lipid modifications (e.g., palmitoylation). Identifying a shared structural or modification-based feature of GLAD substrates would clarify whether this pathway operates through a known sorting signal or recognizes cargoes through a distinct mechanism.

Evolutionarily, the observation that HORMA domain proteins in bacteria regulate cGAS-like bacteriophage defense pathways[8] suggests that GLAD may represent an ancient HORMA–immune pathway connection that predates metazoan STING itself[9,10].

5.2.3 THE FIP200–HSBP1 AXIS

The HSBP1 findings are primarily biochemical and mechanistic at this stage; the functional consequences of HSBP1–FIP200 interaction for autophagy or membrane trafficking remain incompletely defined. The functional role of HSBP1 in relation to FIP200 remains to be defined. Two models are consistent with current data. In one, HSBP1 acts as a negative regulator of FIP200-dependent processes, with its degradation serving as a permissive step for autophagy initiation or membrane remodeling. In the alternative model, HSBP1 functions as a transient scaffold that is consumed during the assembly of higher-order protein complexes.

Distinguishing these models will require HSBP1 variants that are resistant to proteasomal degradation, for example through mutation of degradation motifs, followed by assessment of effects on FIP200 complex assembly, ATG13 puncta formation, and autophagosome nucleation. In parallel, acute depletion experiments combined with rescue by interaction-deficient mutants will clarify whether HSBP1's role is structural or regulatory.

HSBP1 interactome's enrichment for coiled-coil structural proteins raises the possibility that HSBP1 participates in organizing larger protein assemblies in response to stress. Determining whether HSBP1 regulates the assembly or stability of these coiled-coil complexes, for example through in vitro reconstitution with purified components, would clarify whether HSBP1 functions as a general coiled-coil assembly factor or has specificity for particular protein complexes.

5.2.4 PHYSIOLOGICAL AND TRANSLATIONAL CONTEXTS

A limitation of this work is that the GLAD pathway has been characterized primarily in cancer-derived cell lines, with its role in primary cells remaining to be established. Given the central role of STING signaling in innate immune cells, analysis in macrophages, dendritic cells, and other immune cell types will be important. Conditional KO models of ATG101 or ATG13 in relevant tissues, particularly in combination with STING-deficient background, would allow direct assessment of the pathway's function *in* vivo. Existing mouse models, such as keratinocyte-specific ATG9A KO mice that

develop STING-dependent inflammatory skin disease, provide a relevant model to test whether GLAD similarly impacts immune homeostasis.

From a translational perspective, modulation of this pathway may be therapeutically relevant. In cancer, high ATG101/ATG9A expression correlates with reduced immune cell infiltration and poor response to checkpoint immunotherapy in certain contexts. Genetic disruption of these components enhances immune-mediated tumor clearance in experimental models. These observations are consistent with a model in which tumor cells utilize GLAD-mediated STING trafficking to limit innate immune activation. Notably, a ULK1/2 inhibitor that promotes ATG13 degradation reduces tumor burden and enhances T-cell infiltration in a PDAC model, providing pharmacological proof-of-concept that disrupting GLAD components can potentiate anti-tumor immunity.

Targeting the HDIR-HORMA interface, necessary for GLAD activity, may represent a strategy to prolong STING signaling to enhance anti-tumor immunity, potentially in combination with STING agonists[11]. Conversely, hyperactivated STING contributes to autoimmune disorders such as SLE[12] and SAVI[13], suggesting that enhancing GLAD function could have therapeutic benefit in these contexts.

5.3 REFERENCES

1. Olivas, T. J. *et al*. ATG9 vesicles comprise the seed membrane of mammalian autophagosomes. *J. Cell Biol*. **222**, e202208088 (2023).
2. Takahashi, Y. *et al*. An autophagy assay reveals the ESCRT-III component CHMP2A as a regulator of phagophore closure. *Nat. Commun*. **9**, 2855 (2018).
3. Javed, R. *et al*. ATG9A facilitates the closure of mammalian autophagosomes. *J. Cell Biol*. **224**, e202404047 (2025).
4. Nguyen, A. *et al*. Metamorphic proteins at the basis of human autophagy initiation and lipid transfer. *Mol. Cell* **83**, 2077–2090 (2023).
5. Goodwin, J. M. *et al*. Autophagy-Independent Lysosomal Targeting Regulated by ULK1/2-FIP200 and ATG9. *Cell Rep*. **20**, 2341–2356 (2017).

6. Scavone, F., Lian, S., Eskelinen, E.-L., Cohen, R. E. & Yao, T. Trafficking of K63-polyubiquitin–modified membrane proteins in a macroautophagy-independent pathway is linked to ATG9A. *Mol. Biol. Cell* **36**, ar42 (2025).
7. Jia, S. *et al*. Mammalian Atg9 contributes to the post-Golgi transport of lysosomal hydrolases by interacting with adaptor protein-1. *FEBS Lett*. **591**, 4027–4038 (2017).
8. Ye, Q. *et al*. HORMA Domain Proteins and a Trip13-like ATPase Regulate Bacterial cGAS-like Enzymes to Mediate Bacteriophage Immunity. *Mol. Cell* **77**, 709-722.e7 (2020).
9. Margolis, S. R., Wilson, S. C. & Vance, R. E. Evolutionary Origins of cGAS-STING Signaling. *Trends Immunol*. **38**, 733–743 (2017).
10. Lai, Z. et al. Evolutionary diversification of the autophagy initiation complex: reduced Atg101 dependency and changes in Atg9 binding to Atg13. *Autophagy* https://doi.org/10.1080/15548627.2025.2559683 (2025) doi:10.1080/15548627.2025.2559683.
11. Harrington, K. J. et al. Phase I and II Clinical Studies of the STING Agonist Ulevostinag with and without Pembrolizumab in Participants with Advanced or Metastatic Solid Tumors or Lymphomas. *Clin. Cancer Res. Off. J. Am. Assoc. Cancer Res*. **31**, 3400–3411 (2025).
12. Postal, M. et al. Type I interferon in the pathogenesis of systemic lupus erythematosus. *Curr. Opin. Immunol*. **67**, 87–94 (2020).
13. Liu, Y. et al. Activated STING in a Vascular and Pulmonary Syndrome. *N. Engl. J. Med*. **371**, 507–518 (2014).